Unravelling mechanisms causing astrocytic uncoupling in epilepsy

Dissertation

zur

Erlangung des Doktorgrades (Dr. rer. nat)

der

Mathematisch-Naturwissenschaftlichen Fakultät

der

Rheinische Friedrich-Wilhelms-Universität Bonn

Vorgelegt von

Tushar Deshpande

aus

Akot

Bonn, 2017

Angefertigt mit Genehmigung der Mathematisch-Naturwissenschaftlichen Fakultät der
Rheinischen Friedrich-Wilhelms-Universität Bonn

1. Gutachter:	**Prof. Dr. Christian Steinhäuser** Institut für Zelluläre Neurowissenschaften Universität Bonn
2. Gutachter:	**Prof. Dr. Walter Witke** Institut für Genetik Universität Bonn

Tag der Promotion: 27.07.2017

Erscheinungsjahr: 2017

“If our brains were simple enough for us to understand them, we'd be so simple that we couldn't.”

- Emerson M. Pugh (1896-1981),
Carnegie Institute of Technology

Acknowledgements

At first, I would like to thank Prof. Dr. Christian Steinhäuser for giving me the opportunity to work on this exciting topic in his research group. Without his supervision and guidance, this work would not have been possible.

I am grateful to Prof. Dr. Walter Witke, Prof. Dr. med. Volkmar Gieselmann and Prof. Dr. Christa Müller for accepting my request to be part of the examination committee and for their time and efforts in reviewing this work.

My former supervisor Prof. Dr. Martin Theis deserves special mention here for introducing me to the field of transgenic animals and for his guidance during my initial days in the laboratory. I was fortunate to have a fruitful collaboration with Dr. Peter Bedner throughout this study. I am thankful to him, especially for the animal models used in this study. I owe my deepest sense of gratitude to Dr. Marc Sylvester, whose expertise in mass spectrometry was valuable for my thesis. His patience during the optimization of sample preparation protocol was commendable. I would like to thank Dr. Ronald Jabs for introducing me to the confocal microscopy. I am thankful to Dr. Gerhard Seifert for sharing his expertise in mice genotypes.

Special thanks go to Dr. Tingsong Li, for his cooperation during studies on human specimens. His insights on post-seizure neurogenesis were very helpful. I would like to express appreciation to Dr. Michel Herde and Prof. Dr. Christian Henneberger for scientific advice and help regarding expansion microscopy.

I am thankful to Anja Matijevic, Thomas Erdman and Berndt Gehrig for excellent technical support. I would like to express gratitude towards Dr. Ines Nauroth and Dr. Silke Künzel for their help in administrative matters.

It gives me immense pleasure to thank all the members of the laboratory Alberto, Aline, Björn, Camile, Catia, Daniel, Dimitri, Dilaware, Julia, Kirsten, Magda, Steffi and Zhou for excellent work environment.

Words are inadequate to express my gratitude towards my family and loved ones. Their understanding and support meant a lot to me.

Contents

Abbreviations

a.u.	arbitrary units
ACSF	artificial cerebrospinal fluid
AHS	Ammon's horn sclerosis
APS	ammonium persulfate
ATP	adenosine triphosphate
BBB	blood brain barrier
BCA	bicinchoninic acid assay
BrdU	5-bromo-2'-deoxyuridine
CA	cornu ammonis
CamKII	Ca^{2+}/calmodulin-dependent protein kinase II
cAMP	cyclic adenosine monophosphate
CDK	cyclin-dependent kinase
cGMP	cyclic guanosine monophosphate
CID	collision induced dissociation
CNS	central nervous system
CSF	cerebrospinal spinal fluid
DCX	doublecortin
DG	dentate gyrus
DKO	double knockout
EL	extracellular loop
ER	endoplasmic reticulum
GAPDH	glyceraldehyde 3-phosphate dehydrogenase
GCD	granule cell dispersion
GCL	granule cell layer
GFAP	glial fibrially acidic protein
HS	hippocampal sclerosis
IgG	immunoglobulin
IL	interleukin
ILAE	International League Against Epilepsy
IP	immunoprecipitation
IP3	inositol triphosphate 3
kDa	kilodalton
LC MS	liquid chromatography mass spectrometry
MAPK	mitogen activated protein kinase
MTLE	mesial temporal lobe epilepsy
NGS	normal goat serum
NO	nitric oxide
PAGE	polyacrylamide gel electrophoresis
PBS	phosphate-buffered saline
PFA	paraformaldehyde
PKA	protein kinase A
PKC	protein kinase C
PKG	protein kinase G
PTM	post translational modification
PVDF	polyvinylidene fluoride
RG	radial glia
SD	standard deviation
SDS	sodium dodecyl sulfate
SGZ	subgranular zone
SR	stratum radiatum
TBST	tris-buffered saline with Tween-20
TGFβ	transforming growth factor beta
TGN	trans-golgi network
TLR	toll-like receptor
TM	trans membrane
TNF	tumor necrosis factor
TUNEL	terminal deoxynucleotidyl transferase dUTP nick end labeling
WT	wild type
ZO	zonula occludens

1 Introduction

Epilepsy is a central nervous system disorder characterized by propensity of the brain to have spontaneous seizures. Astrocytes, which are the major non-neuronal cells in the brain, are increasingly being recognized as key players in epilepsy. Metabolic and electric coupling is a vital property of astrocytic networks in which the distribution of energy metabolites and ions takes place. Failure of this buffering function of the astrocytic network can result in seizures (Wallraff et al., 2006). Gap junctions formed by connexins are responsible for coupling among astrocytes. This coupling is completely absent in human temporal lobe epilepsy with sclerosis and its loss has been proposed as a focal contributor to epileptogenesis (Bedner et al., 2015). The principal purpose of this study was to find out the mechanism leading to astrocytic uncoupling in epilepsy, with a focus on connexins. This section gives a brief introduction to various aspects of this topic.

1.1 Astrocytes

Non-neuronal cells called glia exist throughout the central nervous system (CNS). Although the ratio of glia to neurons varies depending on the region of the brain and the species, according to most of the estimates glial number is at least equal to or exceeds that of neurons (Khakh and Sofroniew, 2015). Specialized glia called astrocytes constitute approximately 20 to 40% of the total numbers of cells in the mammalian brain. Astrocytes (from the Greek word ‘astro’ meaning star) derive their name from their star shaped appearance in Golgi stain. They have passive electrophysiological properties and unlike neurons are unable to generate action potential (Dallérac et al., 2013). Grey matter astrocytes termed protoplasmic have a roughly spherical and bushy appearance. Their processes enwrap numerous synapses and blood vessels. White matter astrocytes termed fibrous have long, thin, unbranched processes whose endfeet encircle the nodes of Ranvier. There exists a regional variation in the structure and functions of astrocytes. Astrocytes are a far more heterogeneous group of cells than was previously thought. Their crucial contribution to brain homeostasis and disease is now being progressively appreciated.

1.1.1 Physiological role of astrocytes

Glucose transporters present on the astrocytic endfeet enwrapping the blood vessels take up the blood glucose. It is converted to pyruvate through aerobic respiration and then to lactate by lactate dehydrogenase (Bélanger et al., 2011). Astrocytes convert and store some of the glucose into glycogen which acts as an energy substrate in case of hypoglycemia. Lactate is released into the extracellular space and then utilized by neurons as an energy substrate. In response to synaptic activity, astrocytes increase the uptake and metabolism of glucose to provide lactate to neurons. This model of neuroglial metabolic coupling is known as astrocyte-neuron lactate shuttle (Pellerin and Magistretti, 2012). In this model (Figure 1.1.1), astrocytes also take up glutamate released by neurons and convert it to glutamine using an enzyme glutamine synthetase. The uptake of glutamate mediated by specialized transporters on astrocytes is essential for the termination of its action in the synaptic cleft. The uptake also triggers glycolysis in astrocytes to generate ATP and lactate. Glutamine produced after degradation of glutamate in astrocytes can be recycled again for the production of glutamate. Thus, astrocytes play a significant role in brain energetics and glutamate turnover.

Astrocytes maintain the water, ion, pH, and transmitter homeostasis of the synaptic interstitial fluid by expressing a variety of channels and transporters (Sofroniew and Vinters, 2010). They exert a tight control on the extracellular potassium ion (K^+) levels with the help of Na^+K^+ ATPase, inward rectifying K^+ channels and gap junctional coupling (introduced in section 1.1.2). Such a control is essential to prevent the hyper-excitation of neurons following K^+ accumulation. Astrocytes not only take up neurotransmitters but also metabolize, synthesize and release them. The process of neurotransmitter release by astrocytes termed gliotransmission, modulates synaptic activity (Parpura and Zorec, 2010). Astrocytes via their endfeet constitute a component of the blood brain barrier. They release many vasoactive molecules that can influence the blood brain barrier permeability and the blood flow (Serlin et al., 2015a). Regulation of the blood flow by astrocytic endfeet is an important aspect of neurovascular coupling.

Glial fibrillary acid protein (GFAP), a component of astrocytic cytoskeleton, has become a prototypic marker for astrocytes. The stem cells in the neurogenic niches of the adult brain express GFAP (Kriegstein and Alvarez-Buylla, 2009). These GFAP expressing cells have a radial morphology and they remain active throughout life in the subventricular zone of the lateral ventricles and in the subgranular zone of the hippocampal dentate gyrus (DG), where they are the principal source of adult neurogenesis.

The newborn neurons generated from these cells integrate into the existing circuitry and are believed to play a role in learning and memory (Gonçalves et al., 2016).

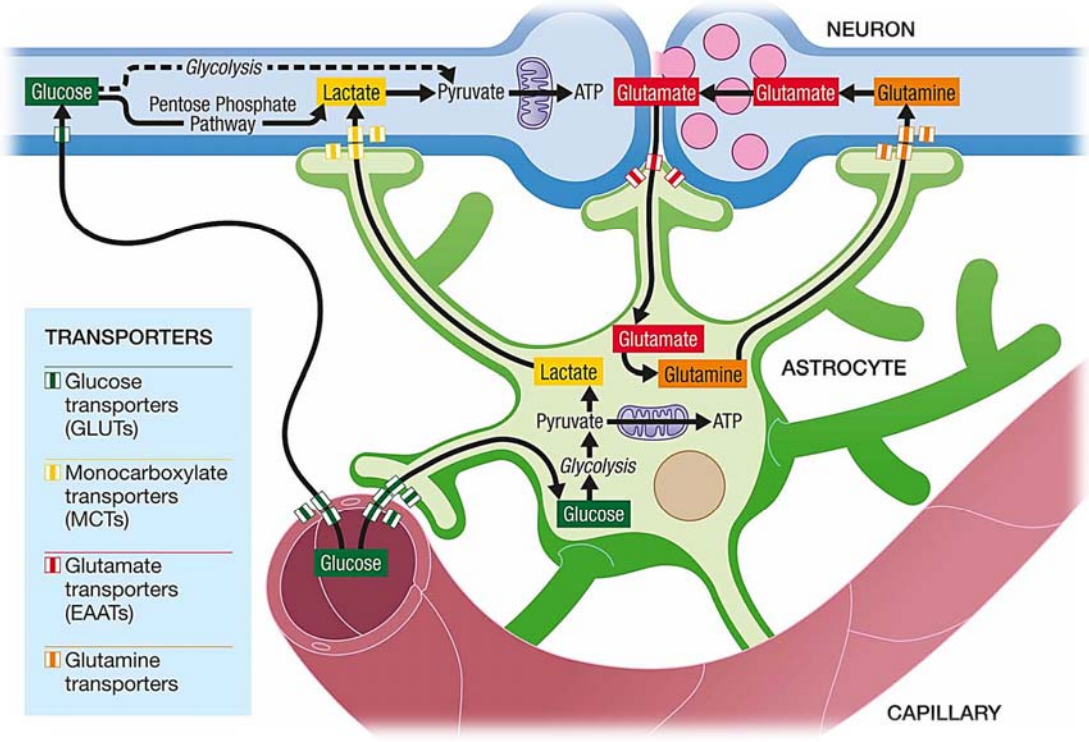

Figure 1.1.1: Schematic illustration of astrocyte-neuron lactate shuttle. Glutamate uptake by astrocytes triggers glycolysis which promotes glucose uptake by glucose transporters. Lactate and glutamine produced by astrocytes are transported to neurons. Figure adopted from (Demetrius et al., 2015).

1.1.2 Astrocytic coupling

Astrocytes are connected with each other via structures called gap junctions (introduced in section 1.2). Such a connectivity of astrocytes with the surrounding astrocytes results in the formation of a huge network through which transport of small molecules (~ 1 kDa) can take place (Scemes and Spray, 2009). The astrocytic network is often referred to as a functional syncytium. A syncytium is defined as a multinucleated mass of cytoplasm that is surrounded by a continuous plasma membrane with no individualized units (cells) (Scemes and Spray, 2003). According to this definition, astrocytes do not form a structural syncytium mainly because even in network, they retain their individual cellular structures. Under physiological conditions, there is very little interdigitation between astrocytic processes (Bushong et al., 2002). In rodent brain, each astrocytic domain includes ~ 140,000 synapses while in the human brain the number reaches up to ~2,000,000 synapses. These synapses are not shared with the

neighboring astrocytic domains (Oberheim et al., 2008). However, at the border zone between two astrocytes, gap junctions pave a way for intercellular transport allowing direct exchange of molecules from the cytosol of one cell to that of its coupled neighbours.

The passage of molecules across astrocytic gap junctions takes place by passive diffusion along the concentration gradient. The concentration gradients may be formed either through release of molecules at specific sites or through their uptake by subpopulation of cells. The gap junctions however exert certain resistance to the permeation. As a result, molecules dissipate only gradually through time and space through the networks (Scemes and Spray, 2003). There are many possible molecules that can be transported across astrocytic networks e.g. K^+, cyclic adenosine monophosphate (cAMP), inositol triphosphate (IP3), Ca^{2+}, glucose, glutamate etc. Depending on the molecule transported, different functions can be ascribed to astrocytic coupling. One of these functions is K^+ spatial buffering. The model of astrocyte-mediated K^+ spatial buffering was first proposed by Dick Orkand, John Nichols and Steve Kuffler (Orkand et al., 1966) (Kuffler et al., 1966) and thereafter confirmed by (Wallraff et al., 2006), (Pannasch et al., 2011) and (Bazzigaluppi et al., 2016). Through this mechanism, glial cells are suggested to remove the excess K^+ released at synaptic sites to regions of low extracellular K^+ (Figure 1.1.2 A). The K^+ flux is driven by the difference between the membrane potential (V_m) and the local K^+ equilibrium potential (E_K). In regions of $[K^+]_o$ increases, there is a net driving force causing K^+ uptake (Dallérac et al., 2013). This K^+ entry causes a local depolarization. K^+ is released at a location distant from the site of entry. It is important to note here that syncytial isopotentiality conferred by gap junctions facilitates all three critical steps in "K^+ spatial buffering": K^+ uptake, intercellular transfer and release (Ma et al., 2016). Astrocytic spatial buffering of K^+ has been proposed to be antiepileptic. Indeed, hippocampal slices from mice lacking astrocytic coupling were shown to have spontaneous epileptiform activity (Wallraff et al., 2006).

Astrocytic coupling contributes to the distribution of glucose and other metabolites from the perivascular space to distal synapses (Figure 1.1.2 B). This property called metabolic polarity endows the astrocytic syncytium with the capacity to ensure the transfer of metabolic intermediates from areas of production to areas of demand (Pellerin and Magistretti, 2012). In the absence of extracellular glucose, the distribution of exogenous glucose or lactate injected into an astrocyte maintains glutamatergic synaptic transmission and epileptiform activity only when the astrocytes in the network are connected by gap junctions (Rouach et al., 2008). This

aspect of astrocytic coupling facilitating the distribution of energy substrates to firing neurons has been viewed as pro-epileptic.

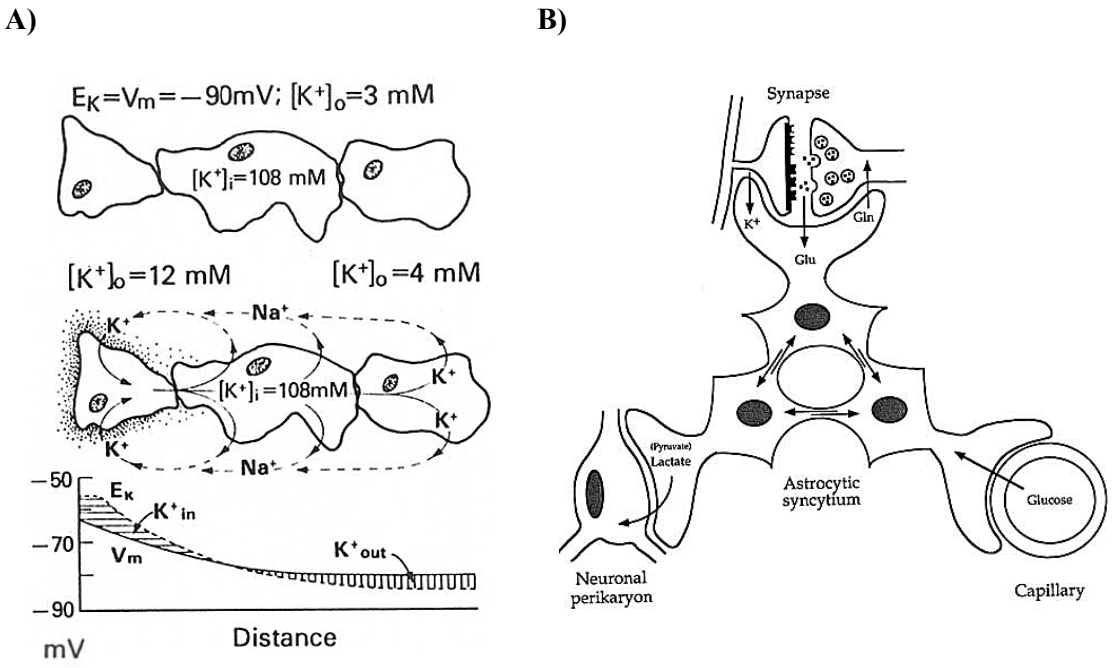

Figure 1.1.2: Physiological role of astrocytic coupling. A) K+ buffering. Increase in $[K]_o$ produces a local depolarization. The local difference in V_m and E_K drives the K^+ uptake in regions of elevated $[K]_o$ and K^+ outflow at distant regions. The intercellular currents are carried by K+ and extracellular currents are facilitated by other ions such as Na^+**.** Figure adopted from (Orkand, 1986). **B) Metabolic polarity of astrocytic network.** Astrocytes have various processes that make contact with capillaries, neuronal perikarya, or synapses. The distribution of metabolites through the network takes place in the direction of energy demand. Figure adopted from (Pellerin and Magistretti, 2012).

Astrocytic coupling modulates the synaptic strength also by facilitating the removal of glutamate and by controlling the extracellular space volume (Pannasch et al., 2011). These functions take place synergistically with K^+ buffering. The propagation of Ca^{2+} signal through the astrocytic network has also been documented and has been termed Ca^{2+} waves (Bazargani and Attwell, 2016). IP3 has been shown to mediate Ca^{2+} waves in astrocytic networks (Boitano et al., 1992). The speed of such Ca^{2+} waves in astrocytic cultures is ~ 20 µm/s while in spreading depression it is ~30 to 40 µm/s (Scemes and Giaume, 2006). Ca^{2+} waves in astrocytic cultures can take place even in the absence of neurons. Similarly, Ca^{2+} waves during spreading depression are independent of action potentials (Chuquet et al., 2007). A third, neuronal activity-dependent, faster type of Ca^{2+} wave (60 µm/s) has been shown to propagate through astrocytic network in vivo (Kuga et al., 2011). This wave named glissandi has been speculated

to mediate the activity-dependent, large-scale modulation of cerebral blood flow (Kuga et al., 2011).

There are three methods by which astrocytic coupling can be assessed. Simultaneous patch clamp recordings from two astrocytes are used to evaluate electrical coupling between them (Kettenmann and Ranson, 1988). In this method, a depolarizing current injected into one astrocyte also depolarizes the other if they are connected by gap junctions. For pairs of coupled cells, the strength of electrical coupling, termed the coupling coefficient is defined as the ratio of voltage changes in the coupled cell to that in the injected cell (Ma et al., 2016). Simultaneous patch clamp recordings are technically challenging and while using them, the spatial aspects of coupling need to be extracted from multiple recordings. A second method called fluorescence recovery after photobleaching (FRAP) involves bleaching of gap junction permeable dye in a single astrocyte and recording the recovery of fluorescence caused by diffusion of the dyes through gap junctions (Lee et al., 1994). The third and the most commonly used method utilizes injection of a tracer dye (for example biocytin) into a single astrocyte and measures its spread through the astrocytic network in a given time (Bedner et al., 2015).

1.2 Gap junctions

Gap junctions are specialized pore forming structures at the interface of two apposing membranes that connect the cytoplasms of the neighboring cells. The typical distance between the two apposing membranes harboring gap junctions is 2 to 4 nm (Oshima, 2014). In vertebrates, membrane proteins called connexins form the gap junctions. They are expressed in almost all differentiated cells except red blood cells, spermatozoa, and skeletal muscles (Sáez et al., 2003). Twenty one different isoforms of connexins have been detected in humans (Bedner et al., 2012). They are commonly named as prefix 'Cx' followed by their approximate predicted molecular weight in kilo Daltons e.g. Cx39. Cx43 and Cx30 are the main gap junctional proteins in astrocytes. Astrocytic expression of Cx26 has been reported but is still under debate (Bedner et al., 2012). In mouse hippocampus, the expression of Cx43 and its contribution to coupling exceeds that of Cx30.

1.2.1 Structure of gap junctions

A single gap junction channel comprises of 12 connexins. A connexin is a tetraspanning membrane protein with cytoplasmic N and C terminus and two extracellular loops (Figure 1.2.1.1). The transmembrane domains (TM1, TM2, TM3 and TM4) and the extracellular loops (E1L and E2L) are remarkably similar among connexins. The intracellular loop and C‑terminal tail are more variable, with the C‑terminal tail being the major determinant of connexin size, which can range from 23 to 62 kDa (Aasen et al., 2016). Six connexins oligomerize to form a connexon (also known as a hemichannel) and two connexons from the adjacent cells dock on each other to form a gap junction (Figure 1.2.1.1). A gap junction plaque may consist of 100 to 1000 densely packed gap junction channels. The transmembrane domains of connexins have α-helical structures while the extracellular loops are arranged in an anti-parallel β-sheet configuration. The extracellular loops are connected by three disulfide bridges considered essential for docking. The N terminal tail (aa 1 to 23) with one α-helix is shorter than the C-terminal tail. The intracellular loop and the C-terminal tails resist crystallographic resolution, indicating that they do not have an organized structure and are highly flexible. The C– terminal tail of Cx43 begins at aa 230 and ends at aa 382. It has a random coil structure with two short α-helices (Thévenin et al., 2013).

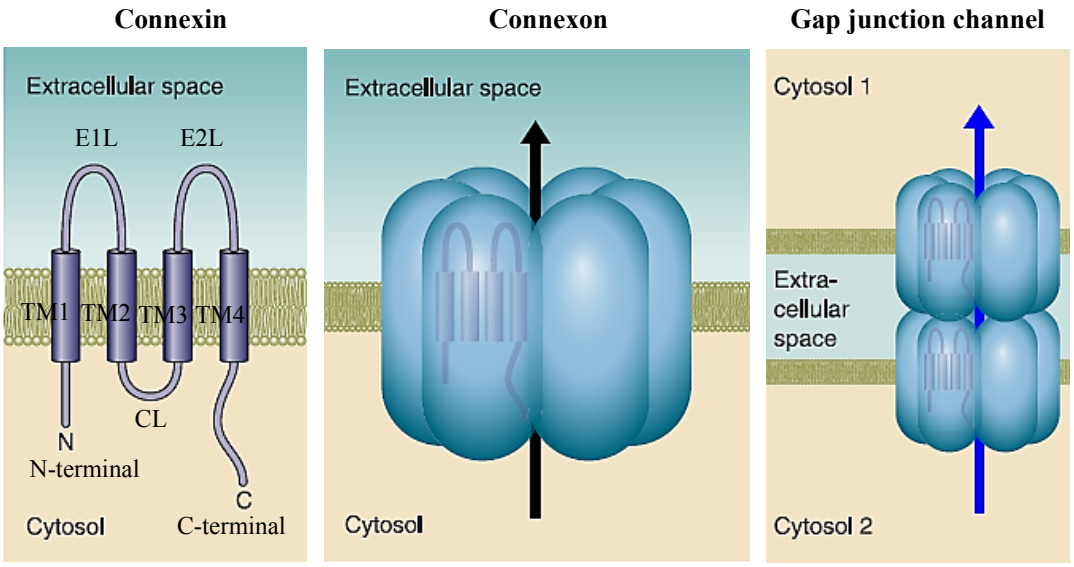

Figure 1.2.1.1: Structural organization of a gap junction channel. A connexin molecule spans the membrane four times (Transmembrane domain, TM 1 to TM 4). N-terminal, cytoplasmic loop (CL) and C terminal reside in the cytoplasm while the extracellular loops (E1L and E2L) project outside the cell. Six connexins oligomerize to form a connexon. A gap junction is formed when two connexons from adjacent cells dock on each other. Figure adopted from (Bosco et al., 2011).

All connexins in a connexon can be similar (homomeric) or dissimilar (heteromeric). The docked connexons in a gap junction can be of similar configuration (homotypic) or different configuration (heterotypic). The heteromeric compatibility of connexins can be predicted by a signature amino acid motif localized at the interface region where the cytosolic intracellular loop domain transitions into the third transmembrane domain (Koval et al., 2014) (Figure 1.2.1.2). In some connexins (e.g. Cx43), the motif in this region contains a conserved arginine or lysine residue (referred to as R type connexins) while other connexins have (e.g. Cx30) a di-tryptophan motif (W type connexins). In R type of connexins, because of the presence of arginine or lysine at a specific location, interaction with a monomer stabilizing protein Erp29 is favoured. This interaction delays the oligomerization till the trans-golgi network (Das et al., 2009). On the other hand, W type of connexins oligomerize in the endoplasmic reticulum. As a result, the likelihood of an R type connexin forming a heteromer with W type of connexin is very low. This implies that Cx43 and Cx30 are unlikely to form heteromers. The heterotypic (docking) compatibility on the other hand is indicated by motifs in the second extracellular loop domain (Koval et al., 2014) (Figure 1.2.1.2). There are two types of connexins based on the signature motifs in this region: group1 has lysine, arginine and asparagine while group 2 has only histidine in the signature motif. Thus, group1 connexons are probably incompatible in docking with group 2 connexons.

Cx43 and Cx30 both belong to group1 and hence their connexons can potentially dock to form a gap junction.

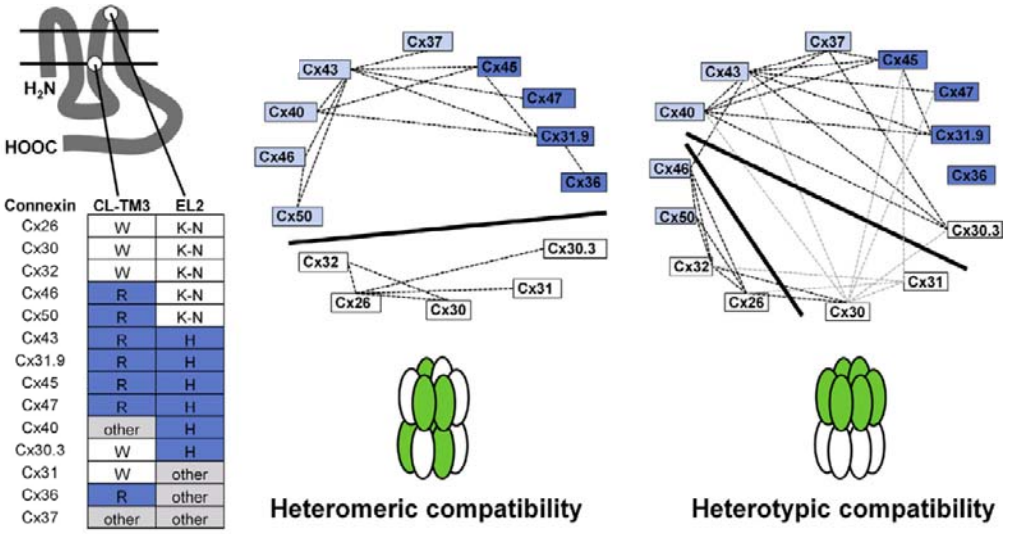

Figure 1.2.1.2: Molecular signatures predicting the heteromeric and heterotypic compatibility of connexins. Amino acids at the junction of transition from the cytoplasmic loop into the TM3 determine heteromeric compatibility while the amino acids in the extracellular loop 2 determine heterotypic compatibility. Accordingly, connexins with the possibility of heteromeric or heterotypic interactions are shown in the wheel diagrams. Faint dotted lines indicate weaker compatibility. Figure adopted from (Koval et al., 2014).

A high resolution (3.5˚A) crystal structure of Cx26 has been reported (Maeda et al., 2009). According to this model, the shape of a gap junction channel resembles that of a tsuzumi, a traditional Japanese drum (Figure 1.2.1.3 A). The structure (without C-terminal tail) has a height of 155 Å and an outer maximum diameter of 92 Å. The diameter of the hydrophilic channel is widest at the cytoplasmic surface (40 Å), narrows at the membrane/extracellular space interface forming the channel vestibule (14 Å), and widens again in the extracellular space (25 Å). The extracellular domains have a dual concentric β-barrel configuration with the E1L on the inner side of the pore connected through disulfide bridges with corresponding E2L on the outer side (Figure 1.2.1.3 B) (Nakagawa et al., 2010). Docking of the extracellular regions of opposite hemichannels entails an interdigitation of 6˚A and a rotation of 30˚. Such a structural arrangement creates an inter-cellular 'gap' of 40˚A (4 nm) between the apposed extracellular domains. E1L and E2L loops from one channel dock on to the corresponding E1L and E2L loops from another channel to create a tight seal (Nakagawa et al., 2010). All interactions in the docking of connexin channels are non-covalent and involve hydrogen bonds and salt bridges. N-terminal, TM1 and E1L form lining of the pore-proper. The intracellular regions of the TM1 and TM3 domains form the entrance of the channel. The N- terminal resides

inside the channel pore giving it a funnel shaped appearance and functions in voltage gating (also known as plug gating) (Oshima, 2014).

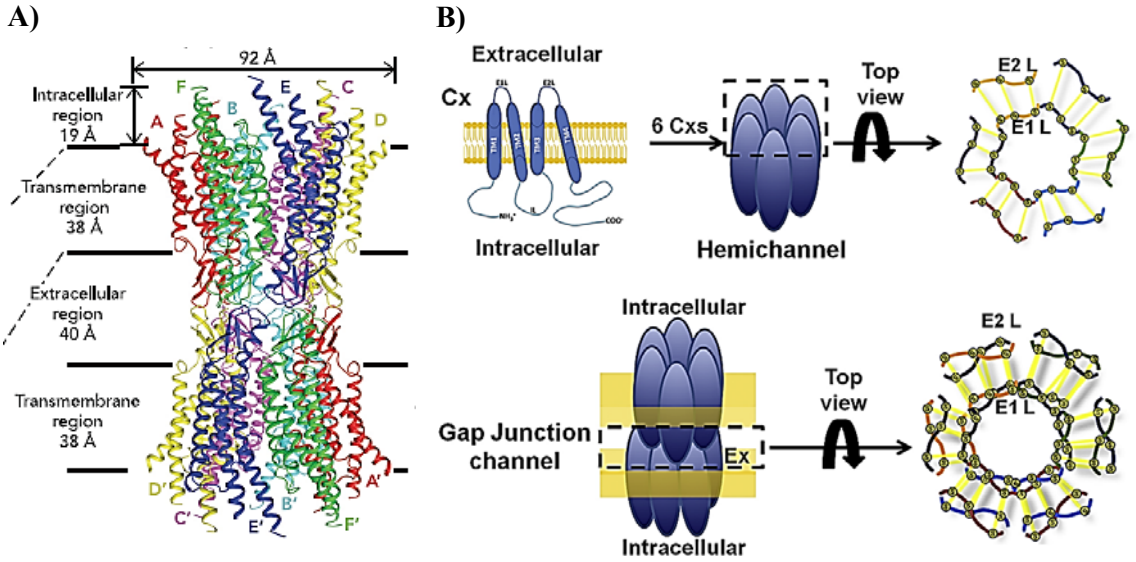

Figure 1.2.1.3: Crystal structure of a gap junction channel. A) Dimensions of a Cx26 gap junction channel**.** Differently coloured helices (tagged A to F) indicate individual Cx26 monomers in a gap junction channel. The gap between two membranes harbouring individual connexons is 40˚A (4 nm). Figure adopted from (Maeda et al., 2009). **B)** Top view of a connexon (upper panel) and a cross-sectional view of a gap junction channel (lower panel). The yellow lines denote disulfide bridges connecting two extracellular loops of an individual connexin monomer. Six extracellular loops 1 (E1L) line the inside of the channel pore while six extracellular loops 2 (E2L) form the outer wall of the pore. Figure adopted from (Riquelme et al., 2013).

1.2.2 Life cycle of connexins

Some connexin genes tend to cluster together within the genome. For example human chromosome 1 alone harbours genes for 8 connexins (Beyer and Berthoud, 2009). Genes for Cx43 and Cx30 are located respectively on chromosomes 6 and 13 in humans and on chromosomes 10 and 14 in mouse (Söhl and Willecke, 2003). The connexin genes have a uniform structure: with a 5' untranslated region, named exon 1, which is separated by an intron of variable length from exon 2 bearing the complete connexin encoding region and the 3' untranslated region (Beyer and Berthoud, 2009). The pattern of synthesis, oligomerization and plasma membrane translocation of connexins is similar to that of other membrane proteins although certain differences exist for Cx43 (Figure 1.2.2). The transcribed mRNAs are translated in rough endoplasmic reticulum into a full length protein. It is then inserted into the membrane of the endoplasmic reticulum (ER). Oligomerization takes place in the ER or in the trans-Golgi network (TGN). Cx43 is phosphorylated very early in its life cycle and its oligomerization takes place in the TGN unlike Cx30 which is oligomerized in ER.

After oligomerization, connexons can be delivered to the plasma membrane by two mechanisms. A minority of the connexons are directly inserted into the plasma membrane, in contrast to the majority of the connexons, which follow a secretory pathway (Salameh, 2006). The fully formed connexons pass the cisternae of the TGN and are transported in secretory vesicles to the plasma membrane. The transport of vesicles takes place along microtubular filaments. Once inserted into the plasma membranes, connexons appear to freely diffuse within the lipid bilayer (Laird, 2006). By lateral movement in the plane of the plasma membrane, the new connexons reach the outer rim of an already existing gap junction plaque causing growth of that plaque. The docking of connexons from the neighboring cells is facilitated by cadherins in a Ca^{2+} dependent manner. In case of Cx43, the size of the plaque is negatively regulated by its interaction with the zonula occludens -1 (ZO-1) protein. Interestingly, phosphorylation of Cx43 (discussed in detail in section 1.2.3) at S373 inhibits this interaction and results in larger plaques (Dunn and Lampe, 2014).

The half-life of connexins is shorter as compared with other structural membrane proteins. Cx30 (half-life > 12 h) appears to be more stable than Cx43 (half-life 1.5 to 5 h) (Kelly et al., 2015). Once a complete dodecameric gap junction channel has been formed, it cannot be separated into connexons again because of the tight seal between extracellular loops. Instead, it is internalized by one of the neighboring cells resulting in intracellular membrane vesicles called annular junctions (Thévenin et al., 2013). The process involves clathrin and other

relevant endocytic proteins like dynamin, actin and myosin. Ubiquitination of connexins is a vital signal for its internalization. Once internalized, most of the integral membrane proteins are degraded via a lysosomal pathway. Although connexins can be degraded by this pathway, many researchers have indicated a proteasomal pathway for connexin degradation (Falk et al., 2014) (VanSlyke and Musil, 2005) (Minogue et al., 2013). An autophagic degradation of internalized Cx43-based gap junctions has also been described (Iyyathurai et al., 2016).

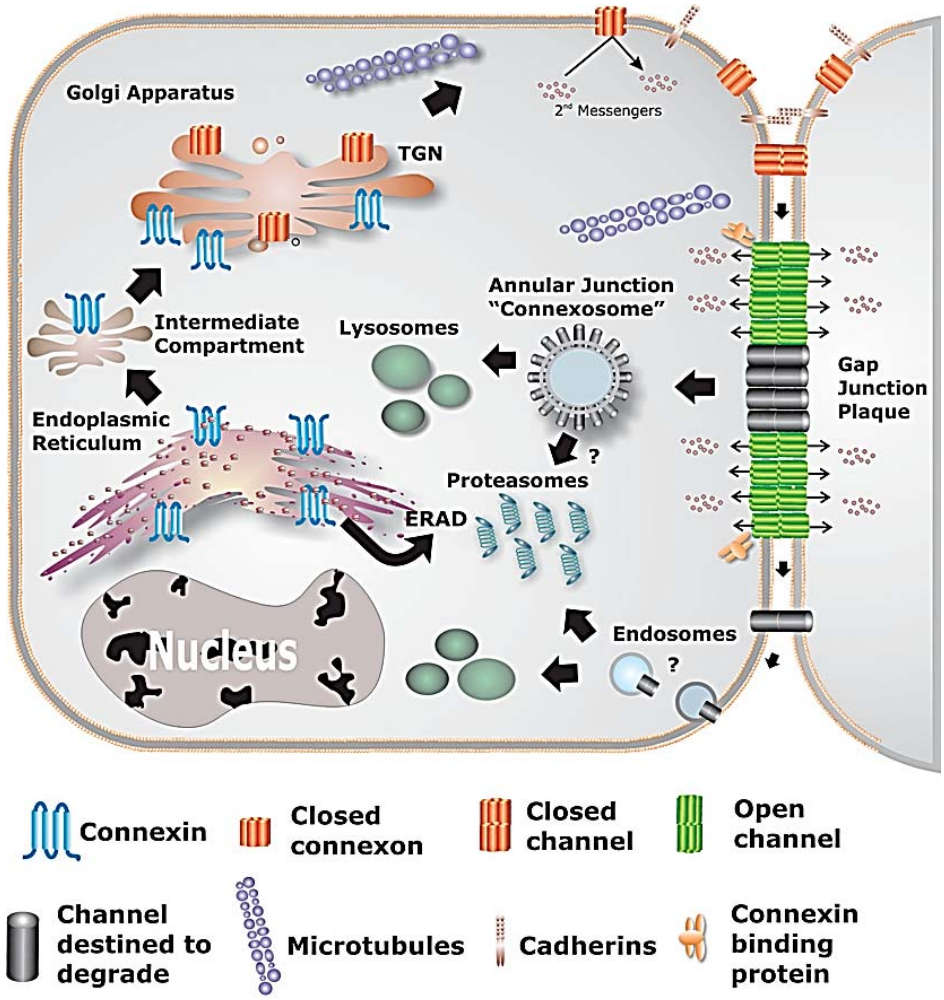

Figure 1.2.2: Life cycle of connexins. Connexins are continuously synthesized and degraded resulting in a very short half-life. After translation, they are folded and incorporated in the membrane of ER. Most of the oligomerized connexins (connexons) are transported to the plasma membrane in secretory vesicles guided by microtubules. After cadherin-assisted gap junction formation, many scaffolding proteins (like ZO-1) bind to the connexins. Internalization of gap junctions results in the formation of an annular junction (also known as connexosome) which can be degraded by proteasomal or lysosomal pathway. Figure adopted from (Laird, 2006).

1.2.3 Phosphorylation of Cx43

Phosphorylation is one of the most extensively studied post translational modifications in Cx43. Cx43 is a phosphoprotein presenting three bands on SDS PAGE namely the faster migrating P0 band and the slower migrating P1 and P2 bands. The P0 band is relatively non-phosphorylated as compared with the P1/P2 bands. Treatment with alkaline phosphatase merges all the bands at P0 (Musil et al., 1990). The 2-4 kDa shifts in the mobility of phosphorylated Cx43 is not caused by mere addition of phosphate groups. It is being gradually appreciated that conformational changes caused by specific phosphorylation result in the band shifts (Solan and Lampe, 2009). There are 21 putative phosphorylation sites in the C terminal region of Cx43. At least 19 of the 26 serines and 2 of the 6 tyrosines in the C-terminal region of Cx43 have been confirmed as sites for potential phosphorylation (Axelsen et al., 2013). Till this date, there are no confirmed reports about N-terminal, cytoplasmic loop or extracellular loop phosphorylations. Phosphorylation of Cx43 takes place very early in its life cycle. Cx43 phosphorylation can occur within 15 min after its synthesis in the rough endoplasmic reticulum (Crow et al., 1990). This event is deemed to be important for its subsequent oligomerization and transport to the plasma membrane. Even the assembly of connexins into gap junctions is affected by C-terminal phosphorylation (Cooper and Lampe, 2002). Although phosphorylation is an important process in the life cycle of Cx43, it is not absolutely essential for the formation of gap junctions. This is highlighted by the fact that C-terminal truncated Cx43 still forms gap junctions albeit with different permeability and electrical properties (Fishman et al., 1991).

Various kinases and their respective target sites are displayed in Figure 1.2.3.1. It is important to note here that not all the phosphorylation events take place simultaneously. In fact some of the phosphorylated sites prevent the phosphorylation of other sites. Many of the kinases have overlapping specificity. Nevertheless, phosphorylation at each site of Cx43 can be viewed as a regulatory process affecting a particular aspect of its function. Phosphorylation of S364/S365 by protein kinase A (PKA) is considered crucial for connexin trafficking towards plasma membrane (Solan and Lampe, 2007). Phosphorylation on these residues results in the formation of a P1 band on the Western blot. S365 phosphorylation has also been suggested to perform a “gatekeeper” function causing a conformational change that prevents protein kinase C (PKC)-induced phosphorylation of S368 (Solan et al., 2007). PKC-mediated phosphorylation of Cx43 at S368 has been shown to shift the unitary conductance of Cx43 channels to a lower than normal value (from 100 pS to 50 pS) (Lampe et al., 2000). This is known to take place in the S and G2/M phase of the cell cycle leading to reduced gap junctional coupling (Solan et al., 2003).

Axelsen et al., however have linked dephosphorylation of S368 together with S297 with electrical uncoupling in cardiac ischemia (Axelsen et al., 2006). Recently, phosphorylation of S368 by PKCδ has been shown to induce gap junction internalization (Cone et al., 2014).

Casein kinase 1 mediated phosphorylation at S325, S328, and S330 results in increased assembly of connexons as gap junctions (Cooper and Lampe, 2002). In fact Cx43 phosphorylated at these residues has been revealed to be exclusively located in gap junction plaques. On Western blot, these changes are reflected in the formation of a P2 band. Consistent with this information, phosphorylation at S325, S328, and S330 is drastically reduced in ischemic hearts which show Cx43 dislocalization from the intercalated discs (also known as gap junction remodeling) (Lampe et al., 2006). To assess the impact of constitutive phosphorylation or dephosphorylation of these sites on the gap junctional remodeling, Remo et al., developed transgenic mice in which S325, S328, and S330 were replaced either with alanine (S3A mice mimicking constitutive dephosphorylation) or with glutamate (S3E mice mimicking constitutive phosphorylation) (Remo et al., 2011). S3A mice showed deleterious effects on cardiac gap junction formation and functions, developed electric remodeling, and were highly susceptible to inducible arrhythmias. On the other hand, S3E mice were resistant to acute and chronic pathological gap junction remodeling and displayed diminished susceptibility to the induction of ventricular arrhythmias. Interestingly, the S3A construct of Cx43 failed to form P2 bands while S3E construct showed prominent P2 bands (Remo et al., 2011).

Mitogen activated protein kinase (MAPK)-mediated phosphorylation of Cx43 at S255, S262, and S279/S282 is known to hamper gap junctional communication by two mechanisms. These phosphorylations either decrease the open probability of gap junction channels or they induce gap junction internalization (Thévenin et al., 2013). Some reports also indicate an interplay between MAPK and PKC (Sirnes et al., 2009). Remarkably, S262 which is also phosphorylated by cyclin-dependent kinase-2 (CDK-2) during mitosis has been shown to regulate DNA synthesis (Doble et al., 2004). Thus, there exists considerable interplay and cross reactivity among kinases phosphorylating Cx43. This is further exemplified by Src kinases which phosphorylate Cx43 at T247 and T265 (resulting in reduced channel conductance ultimately leading to channel closure) but can also induce phosphorylation at S255 and 279/S282 (Axelsen et al., 2013). The conductance of gap junction channels is also reduced upon protein kinase G-induced phosphorylation at S257 (Kwak et al., 1995).

Akt or protein kinase B phosphorylate S369 and S373 of Cx43. Phosphorylation at S373 inhibits ZO-1-Cx43 interaction and increases plaque size (Dunn and Lampe, 2014). Apart from these kinases, CamK II has been predicted to phosphorylate Cx43 at multiple sites based on in vitro assays at Cx43 peptides, but direct in vivo evidence of CamK II-mediated Cx43 phosphorylation is still lacking (Huang et al., 2011). Although phosphorylation at S296, S297 and S306 has been shown to take place, there is no clear direct information about kinases phosphorylating these sites (Axelsen et al., 2006) (Axelsen et al., 2013) (Pogoda et al., 2016).

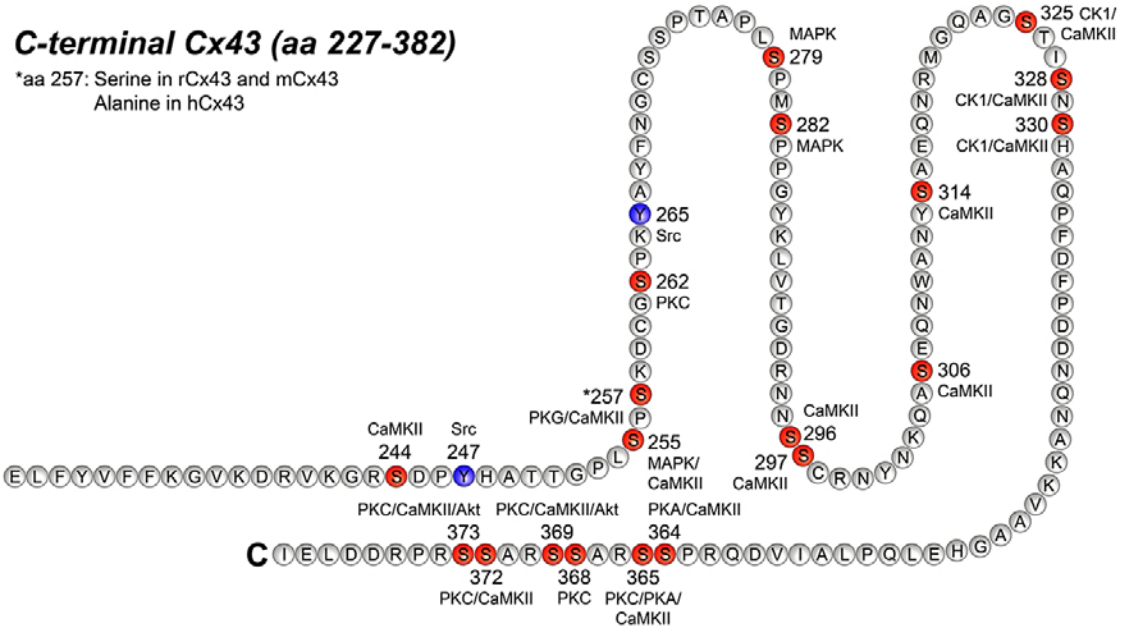

Figure 1.2.2.1: Summary of Cx43 phosphorylation sites. Schematic diagram showing the C-terminal tail of Cx43 with putative phosphorylation sites and their respective kinases. Tyrosines are shown in blue while serines are shown in red. Figure adopted from (Axelsen et al., 2013).

There are two principal approaches for investigating phosphorylation of Cx43 in a disease state. In a hypothesis driven approach, a specific kinase targetting a particular site of Cx43 is postulated based on the available literature. This site then can be assessed with phospho-specific antibodies or by site directed mutagenesis. Although simple and direct, the hypothesis-driven approach has severe limitations given the complexity of Cx43 phosphorylation. Another strategy is a systems approach involving powerful phosphoproteomics provided by mass spectrometry (Chen et al., 2013). Principal advantage of this strategy is that global changes in Cx43 phosphorylation can be detected with a high degree of accuracy. These changes can be correlated with the state of gap junctional coupling. The first step in proteomic analysis involves reducing the isolated proteins to peptides with an endoproteinase such as trypsin.

Most modern-day MS systems are comprised of 4 major components: 1) High performance liquid chromatography (HPLC) 2) ion source, 3) mass analyzer and 4) detector (Figure 1.2.2.2 A). HPLC separates the peptides based on their retention time in a chromatographic column. The peptides are then ionized either by electrospray ionization or matrix associated laser desorption. The ionized peptides are fragmented by introducing intermolecular collisions with a neutral gas. This process, called collision-induced dissociation (CID) breaks the peptides through the lowest energy pathway producing either C-terminal (designated as x-, y- or z- ions) or N-terminal ions (a-, b-, or c-ion) (Figure 1.2.2.2 B). The fragment ions are further analyzed in a mass analyzer which separates them according to their mass/charge (m/z) ratio. The detector records the separated peptide fragments and gives readouts in the form of a mass spectrum which is intensity vs. m/z plot. The identification of peptides is based on database searches. Any post-translational modification (for example phosphorylation) will alter the m/z ratio and therefore can be detected (Chen et al., 2013).

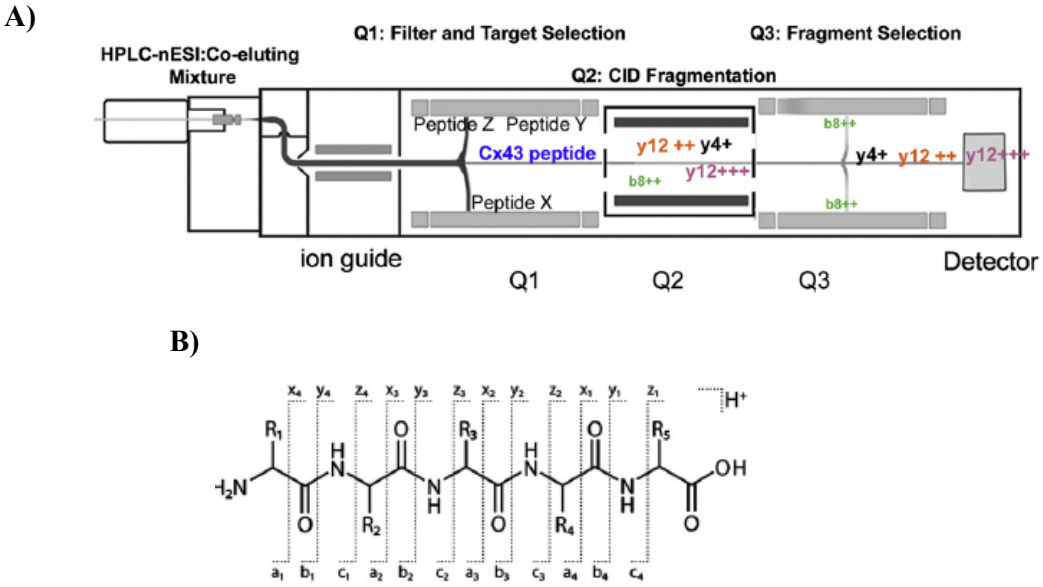

Figure 1.2.2.2: Mass spectrometry. A) An overview of a mass analyzer. During a multiple-reaction monitoring run, cell Q1 selects peptides based on m/z for transfer to the Q2 CID collision cell. Product ions, called transitions, are then specifically selected as they pass through a Q3 isolation window. Each set of transitions at a given LC-elution time uniquely identifies a target protein. **B)** Peptide fragments are named as per the convention shown in the figure. The cleavage results in C- (x-, y-, z-) or N-terminal (a-, b-, c-) ions. (Figure adopted from Chen et al., 2013).

1.3 Epilepsy

Epilepsy is a brain state that supports repeated, unprovoked seizures which are unusual, paroxysmal changes in the electrical activity of the brain (Goldberg and Coulter, 2013). At any given time, it is estimated that ~50 million individuals worldwide have a diagnosis of epilepsy posing an immense socioeconomic challenge (Birbeck, 2010). Seizures can be classified into two clinically useful categories: partial and generalized. The classification of epilepsies has been based on whether or not a focal brain abnormality could be identified (localization related vs. generalized epilepsies) and whether or not a cause could be identified (symptomatic vs. idiopathic) (Shorvon, 2011). Temporal lobe epilepsy (TLE) is the most common form of adult localization-related epilepsy. Hippocampal onset accounts for at least 80% of all temporal lobe seizures (hence called mesial temporal lobe epilepsy (MTLE)) (Tatum, 2012). In MTLE syndrome, ~56% of the cases present a condition termed hippocampal sclerosis (MTLE-HS) (Thom, 2014). Although increasingly being understood at the molecular level, epileptogenesis is extremely complex process posing a challenge for the effective pharmacotherapy. Indeed, ~40% of the total epilepsy cases are pharmacoresistant warranting a resective surgery (Alexopoulos, 2013). MTLE-HS is the most common feature encountered in epilepsy surgeries.

1.3.1 MTLE-HS

Hippocampal sclerosis is a combination of atrophy and astrogliosis mainly of the hippocampus but may include amygdala, parahippocampal gyrus, and the enterorhinal cortex (Tatum, 2012). It is frequently bilateral. Anatomically, the hippocampus is a medial temporal lobe structure that runs along a dorsal (septal)-to ventral (temporal) axis in rodents, corresponding to a posterior-to‑anterior axis in humans (Figure 1.3.1.1 A) (Strange et al., 2014). The term ‘hippocampus’ often encompasses the Ammon’s horn and the dentate gyrus (DG) together. The Ammon’s horn is separated into three main parts: CA1, CA2, and CA3 (CA stands for *Cornu Ammonis*). Each of these parts consists of four layers: *stratum oriens, stratum pyramidale, stratum radiatum* and *stratum lacunosum moleculare*. The pyramidal cells in the *Cornu Ammonis* are packed into a layer called *stratum pyramidale*, in contrast to the neocortex in which pyramidal cells are spread over several layers. The DG on the other hand contains no pyramidal cells, but is densely packed with smaller granule cells. These granule cells project their dendrites into the molecular layer and their axons into the hilus. The axons from the neurons of the entorhinal cortex form synapses with dentate granule cells through the perforant pathway.

The granule cells in turn send signals to the pyramidal cells in CA3 through the mossy fibres. CA3 pyramidal neurons transmit the signals to CA1 pyramidal neurons through Schaffer collaterals. CA1 pyramidal neurons provide feed-back to deep-layer neurons of the entorhinal cortex. The CA3 also receives direct projections from entorhinal cortex (Figure 1.3.1.1 B) (Moser et al., 2014). The hippocampus plays a vital role in the formation of episodic and spatial memory. Through its interactions with brain structures associated with emotion, it is implicated in emotional behaviour as well (Strange et al., 2014). It is also one of the two sites in the mature brain where neurogenesis takes place (Gonçalves et al., 2016).

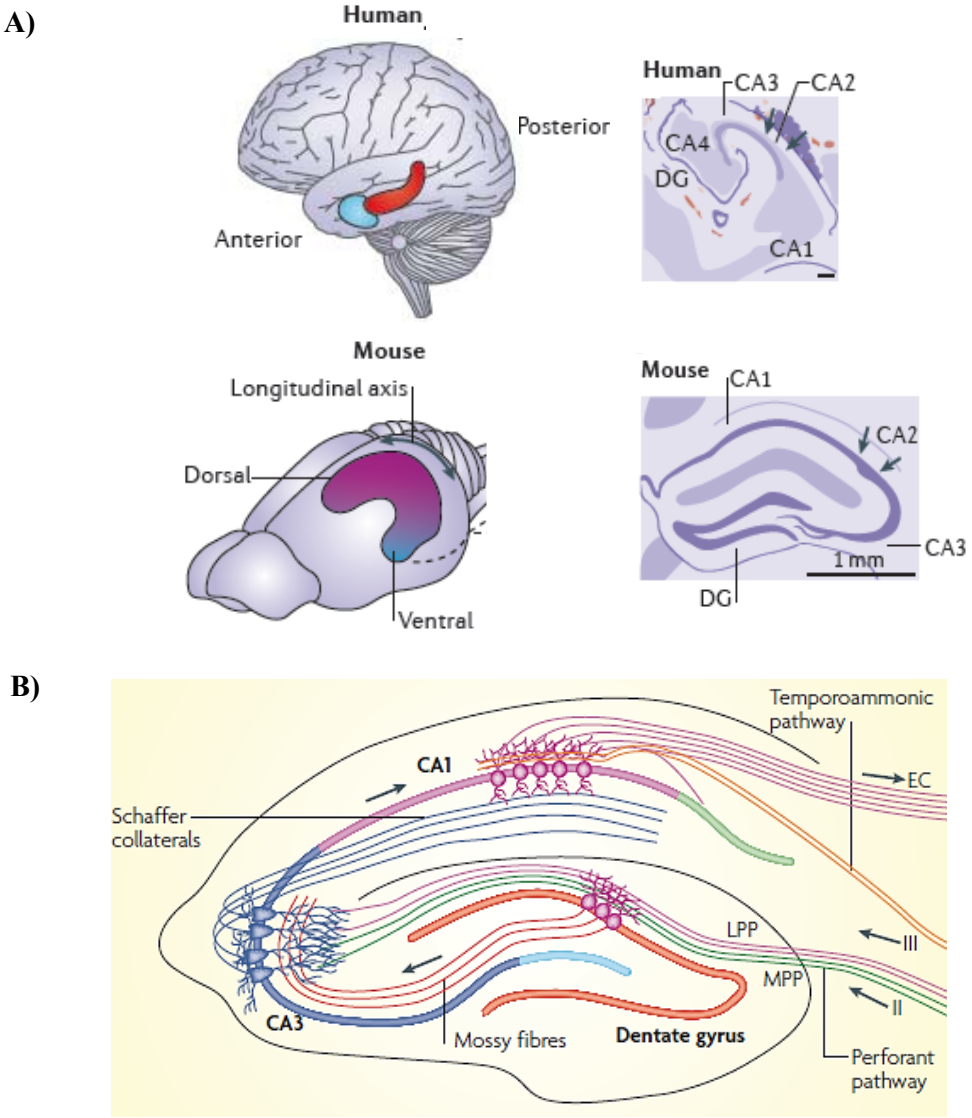

Figure 1.3.1.1: Position and structure of hippocampus. A) Relative positions of human and mouse hippocampi in respective brains. Schematic diagram of coronal sections show DG and different subdivisions of the Ammon's horn. Figure adopted from (Strange et al., 2014) **B)** Schematic diagram displaying the hippocampal circuitry. The hippocampus receives inputs from entorhinal cortex (EC) via the perforant and temporoammonic pathway and also sends signals to the EC from CA1 pyramidal

neurons. Mossy fibres originate in the hilus and form synapses with CA3 pyramidal neurons which through Schaffer collaterals relay information to CA1 pyramidal neurons. Figure adopted from (Deng et al., 2010).

It has been long recognized that the hippocampus has a low threshold for seizures (McIntyre and Racine, 1986). Animal experiments and clinical observations congregate to support the concept that the hippocampus plays a critical role in the generation of epileptiform activities (Schwartzkroin, 1994). This is especially evident in drug resistant MTLE in which surgical resection of hippocampus results in seizure control in 60 to 80% of the patients within 2 years (Blümcke et al., 2013). Most of these patients display HS. The striking characteristic of HS seen in histopathologic examination is loss of pyramidal neurons which can take place in any subdivision of the Ammon's horn. This cell loss is associated with strong astrogliosis, appearing as a dense intermingled network of intensely immunostained GFAP-positive processes. The International league against epilepsy (ILAE) has classified MTLE-HS into three categories (Blümcke et al., 2013). ILAE type 1 displays severe neuronal cell loss mainly in the CA1 and CA4 regions, ILAE type 2 has neuronal cell loss only in CA1, while loss of only CA4 neurons is termed ILAE type 3 (Figure 1.3.1.2). Type 1 represents the classical or typical MTLE-HS while type 2 and 3 are atypical. All of these types demonstrate intense gliosis which together with hippocampal atrophy hardens the tissue. Granule cell dispersion (GCD) is another remarkable feature observed in 40-50% of MTLE-HS patients (Thom, 2014). GCD has been associated with early onset of epilepsy and febrile seizures as well as with longer duration of seizures (Blümcke et al., 2009). There is conflicting data about the predictive value of GCD for post-surgical success (da Costa Neves et al., 2013) (Blümcke et al., 2009a) (Thom et al., 2010). Experimental models of epilepsy suggest that deficiency of reelin rather than seizure-induced neurogenesis contributes to GCD (Haas and Frotscher, 2010). Somatic translocation of already existing mature granule cells has also been proposed as a mechanism of GCD (Murphy and Danzer, 2011). In HS, mossy fibre collaterals send recurrent projections into the molecular layer to make excitatory synaptic contact with apical dendrites and spines of granule cells (Sutula et al., 1989). This 'mossy-fibre sprouting' has a potential to synchronize the firing neurons during seizures. It has been correlated with the extent of neuronal loss and GCD (Schmeiser et al., 2017). Although mossy fibre sprouting is observed extensively in HS, its contribution to epileptogenesis is still not clear (Thom, 2014).

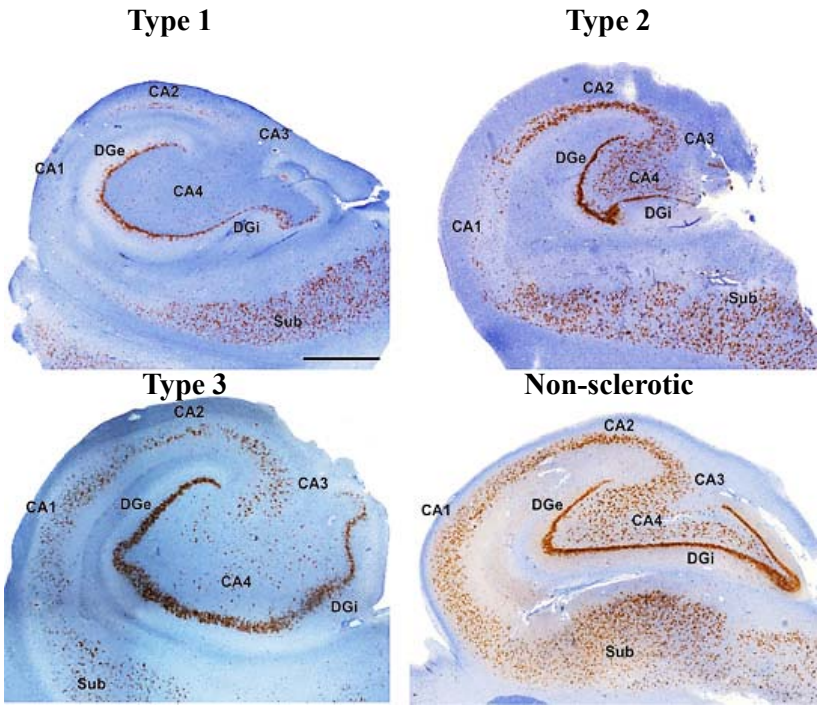

Figure 1.3.1.2: ILAE classification of MTLE-HS. NeuN immunohistochemistry with hematoxylin counterstaining in surgically resected human hippocampi demonstrating subtypes of MTLE-HS. The non-sclerotic tissue serves as a control. All MTLE-HS subtypes display neuronal loss that differs in pattern of location. Type 1 (also known as classical or typical HS) shows neuronal loss in the CA1 and CA4 regions. Type 2 (prominent neuronal loss only in CA1) and type 2 (prominent neuronal loss only in CA4) are atypical MTLE-HS. Scale bar 1mm. Figure adopted from (Blümcke et al., 2013).

1.3.2 Role of astrocytes in epilepsy

The contribution of astrocytes to epileptogenesis can be envisaged from the physiological functions played by them. Astrocyte-mediated metabolic supply sustaining neuronal firing is viewed as pro-epileptic (Rouach et al., 2002). On the other hand, astrocytic contribution to ion, water and neurotransmitter homeostasis is perceived as anti-epileptic. Remarkably, this homeostatic function of astrocytes is perturbed in epilepsy (Figure 1.3.2). Seizure activity leads to an upsurge in extracellular K^+ which in MTLE-HS is ineffectively regulated partly because of the downregulation of astrocyte Kir4.1 channels and reduction in extracellular space volume (Heuser et al., 2012). This downregulation of Kir4.1 channels is reflected in reduced inward rectifying currents (Hinterkeuser et al., 2000). The resultant accumulation of extracellular K^+ is expected to exacerbate seizures (Walz, 2000). Interestingly, mutations in the Kir4.1 encoding gene (*KCNJ10*) along with mutations in the aquaporin 4 gene have been linked with MTLE (Heuser et al., 2010). Aquaporins facilitate water movement across the membrane along the osmotic gradients.

Aquaporin 4, a predominant water channel in the brain is dislocalized from its position in perivascular end feet due to dystrophin down regulation in MTLE-HS (Eid et al., 2005). Its total expression is however increased (Lee et al., 2004). These alterations in aquaporin expression pattern are expected to disturb not only water but also K^+ homeostasis owing to the fact that the uptake of K^+ drives water flux into the cell. Furthermore, in experimental epilepsy, the perivascular dislocalization of aquaporin takes place even before the chronic phase indicating that it is not mere a consequence but rather can be a contributing factor to the process of epileptogenesis (Alvestad et al., 2013).

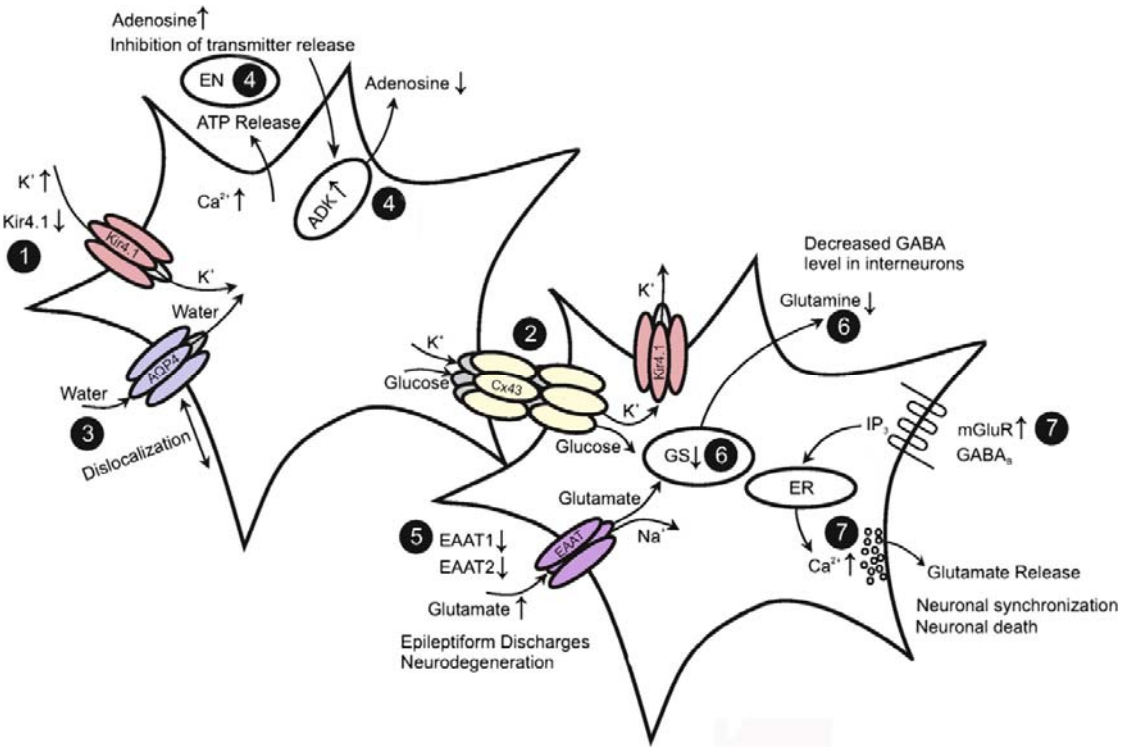

Figure 1.3.2: Disruption of astrocytic functions in epilepsy. Schematic representation of various aspects of astrocytic changes labelled in numbers. 1) Downregulation of Kir 4.1 channels. 2) Reduced astrocytic gap junctional coupling. Cx43 gap junctions under physiological conditions distribute ions and metabolites in the astrocytic network. 3) Dislocalization of aquaporin 4 4) Upregulation of adenosime kinase (ADK) resulting in reduced extracellular adenosine. However Ca^{2+} induced ATP release can result in increased adenosine levels by endonucleases (EN). 5) Downregulation of glutamate transporters (EAAT1 and EAAT2). 6) Reduced supply of glutamine by astrocytes due to reduced glutamine synthetase (GS). 7) Upregulation of metabotropic glutamate receptors causing increased Ca^{2+} mediated glutamate release. Figure adopted from (Steinhäuser et al., 2016).

Astrocytic glutamate transporters are mainly responsible for removal of synaptic glutamate and cessation of its action on neurons which would otherwise continue to fire (Tanaka et al., 1997).

Uncontrolled glutamate-induced neuronal excitation would ultimately result in their death termed as excitotoxicity (Gl, 1992). Thus, through glutamate transporters, astrocytes prevent excitotoxicity. The reports on expression levels of these transporters in epilepsy however are inconsistent (Steinhäuser et al., 2016). Nevertheless, increased glutamate levels in epilepsy have unequivocally been reported (During and Spencer, 1993) (Glass and Dragunow, 1995)(Cavus et al., 2005). These increased glutamate levels can be partially explained by the loss of astrocytic glutamine synthetase that converts glutamate into glutamine (Eid et al., 2004). Such an impairment of the glutamate–glutamine cycling in astrocytes can lead to cytosolic glutamate buildup which can impede the operation of glutamate transporters, ultimately leading to extracellular glutamate accumulation. Another explanation for increased extracellular glutamate can be astrocytic Ca^{2+} -mediated release of glutamate (Carmignoto and Haydon, 2012). Astrocytes respond to synaptic activity by increasing intracellular Ca^{2+} through various ionotropic and metabotropic receptors many of which are upregulated after seizures (Aronica et al., 2000). The elevation of astrocytic Ca^{2+} is then reflected in gliotransmission of glutamate, ATP, D-serine, prostaglandins and cytokines, all of which are known to modulate synaptic activity (Bezzi and Volterra, 2001).

Astrocytes in MTLE-HS undergo dramatic changes and acquire an atypical phenotype suggesting their crucial role in the pathogenesis of epilepsy. The most apparent astrocytic change in MTLE-HS is the morphology. Astrocytes in physiological state retain their anatomical domains and there is very little interdigitation in their processes (Bushong et al., 2002). However, seizure induced abolition of astrocytic domains have been demonstrated in mice (Oberheim et al., 2008). In human MTLE-HS, astrocyte-like cells expressing the markers GFAP and S100β show atypical morphology. Their intense GFAP labelling with a mesh-like network makes identification of a cell body difficult without co-labelling with S100β. Although these cells display a complex current pattern resembling that of an NG2 cell, they do not express the NG2 cell marker PGFRα (Bedner et al., 2015). In response to glutamate, they show linear current voltage relationship, indicating the presence of ionotropic receptors. The glutamate induced inward currents in these astrocytes are incompletely blocked by glutamate receptor blockers indicating co-expression of glutamate receptors and transporters. They are also completely devoid of astrocytic coupling (discussed in section 1.3.3) supporting the notion of lack of *bona fide* astrocytes in MTLE-HS (Bedner et al., 2015).

1.3.3 Astrocytic uncoupling in epilepsy

A tracer injected into an astrocyte spreads throughout the astrocytic network if individual cells of the network are gap junction coupled. Such a coupling although present in MTLE without sclerosis, is completely absent in MTLE-HS (Bedner et al., 2015). In order to investigate the time course of this phenomenon in epileptogenesis, a mouse model of epilepsy involving intracortical injection of kainate over the right hippocampus was developed. Such an injection resulted in status epilepticus (0 to 12 h) followed by a seizure free latent phase (till ~5 d) and thereafter a phase of spontaneous seizures (chronic phase). In this mouse model, three months after the kainate injection, the hippocampus on the injected side (ipsilateral) displayed many features of MTLE-HS. Importantly, the ipsilateral astrocytes were devoid of gap junctional coupling. Uncoupling continued to exist at 6 months and 9 months post injection. This uncoupling of astrocytes was however found to evolve gradually. As early as 4 h after kainate injection, the astrocytes lost ~50% of their coupling network when compared with the astrocytes from the non-injected side (contralateral). Interestingly, at this time point, late stage apoptosis in neurons was absent. As expected, astrocytic uncoupling in the ipsilateral hippocampus resulted in dysregulation of extracellular K^+ (Bedner et al., 2015).

After losing 50% of coupling at 4 h post injection, the ipsilateral astrocytes continued to remain so till 5 d. At this time point, the majority of mice were still in the latent phase. Thus, astrocytic uncoupling observed initially, preceded the phase of spontaneous seizures highlighting its role in epileptogenesis. An important mechanistic insight into the uncoupling phenomenon was obtained when kainate injection failed to cause uncoupling in toll-like receptor 4 (TLR-4) knock-out mice (Bedner et al., 2015). Toll-like receptor 4 is expressed in astrocytes and is known to mediate downstream effects of inflammation. Indeed, the inflammatory cytokines tumor necrosis factor α (TNFα) and interleukin 1β (IL-1β) were able to uncouple astrocytes (Bedner et al., 2015). It was not though clear how these changes affected the gap junctions in astrocytes.

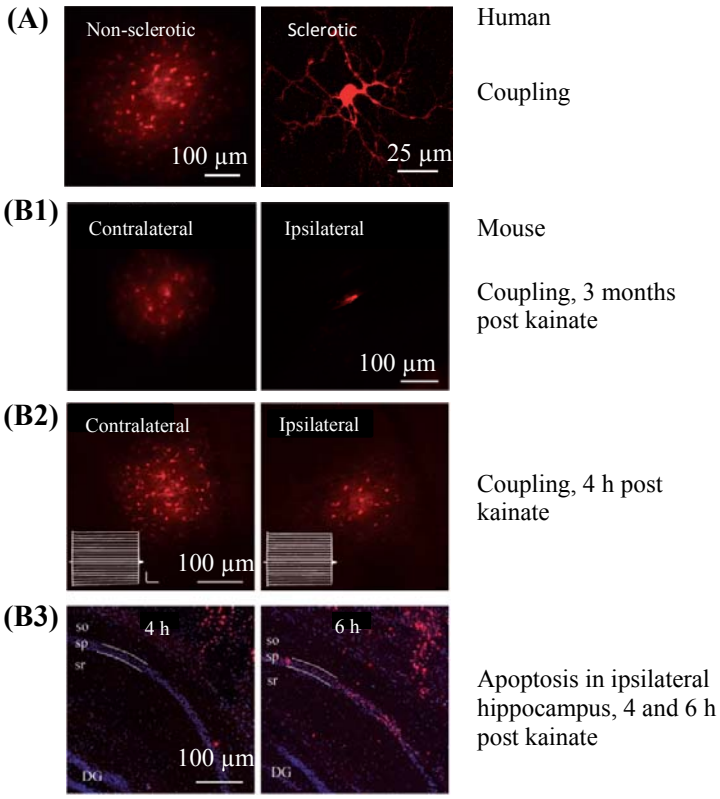

Figure 1.3.3: Astrocytic uncoupling in human and experimental epilepsy. Astrocytic coupling was assessed with biocytin-spread in human and mouse hippocampi. Human MTLE-HS (A) and mouse ipsilateral hippocampus 3 months post kainate injection (B1) were completely devoid of coupling. 4 h post kainate injection, coupling in the ipsilateral hippocampus was reduced by ~50% (B2). However, there were no TUNEL positive cells, indicating absence of late stage apoptosis (B3). TUNEL-positive cells begin to appear at 6 h post injection (B3). Figure adopted from Bedner at al., 2015.

2 Aims of the study

Gap junction-mediated astrocytic coupling which plays an important role in the physiological functions of astrocytes, is lost in epilepsy (Bedner et al., 2015). An obvious implication of the widespread uncoupling in astrocytes is disturbed ion and neurotransmitter homeostasis. Accumulation of extracellular K^+ and glutamate as a result of astrocytic uncoupling is expected to generate and sustain spontaneous epileptiform activity. Accordingly, strategies targeting a prevention of astrocytic uncoupling or rescue of astrocytic coupling in epilepsy have therapeutic potential. In order to devise such a strategy, an understanding of the molecular modifications in gap junctions leading to uncoupling is indispensable. Cx43 and Cx30, which form gap junctions in astrocytes, are subject of dynamic regulation throughout their life cycles. Little is known about the seizure induced alterations in astrocytic connexins resulting in uncoupling. Knowledge of these alterations can shed a light on the molecular basis of astrocytic uncoupling and thereby help in formulating preventive or rescue strategies for the same. Therefore, the main aim of this study was to unravel seizure induced modifications in astrocytic connexins which lead to uncoupling. In order to achieve this goal, the study was divided into three main objectives.

(I) Pattern of connexin expression, distribution and phosphorylation in hippocampi from epilepsy patients: This part of the study was intended at exploring connexins in the context of hippocampal sclerosis. Previous studies assessing astrocytic connexin expression in epilepsy patients were inconsistent and inconclusive regarding the functional outcome (Coulter and Steinhäuser, 2015) as they did not consider the distribution and phosphorylation of connexin. The present study was designed to overcome these limitations by utilizing cellular fractionation, phospho-specific antibodies and expansion microscopy techniques.

(II) Evaluating whether the abovementioned parameters from human specimens are recapitulated in the mouse model of epilepsy: An experimental animal of epilepsy in mouse can be extremely useful for examining the time course of events in epileptogenesis. The relevance of an animal model is depicted by its resemblance with the human condition. The mouse model involving intracortical injection of kainate employed by Bedner et al., was used for the present study as well. In this model, three months after kainate injection, the morphological features and astrocytic uncoupling in the mouse hippocampus are similar to those observed in human epilepsy (Bedner et al., 2015). Consequently, to mimic the findings

from human specimens (Objective I), the three months' time point was assessed in the mouse model.

(III) Investigating connexins in the early phase of the mouse model of epilepsy: In the mouse model, astrocytic uncoupling is observed as early as 4 h post injection without any detectable neuronal death. The level of uncoupling remained at approximately the same level in mice which were in the latent phase at day 5 post injection (Bedner et al., 2015). Thus, the uncoupling takes place before the onset of spontaneous seizures, indicating its potential role in epileptogenesis. Understanding molecular mechanisms of astrocytic uncoupling in the early phase of epilepsy might be useful in the understanding of epileptogenesis itself. In order to unravel these mechanisms, astrocytic connexins were investigated in the early phase of the mouse model of epilepsy.

All these three objectives were aimed at finding out what seizure does to astrocytic connexins. Another objective was aimed to evaluate how astrocytic connexins contribute to post seizure GCD and neurogenesis. For this purpose, mice with astrocytic deletion of connexins and fate mapping techniques were utilized.

3 Materials and Methods

3.1 Biological specimens

3.1.1 Hippocampal specimens from patients

A total of 38 hippocampal specimens were obtained from patients with pharmacoresistant MTLE and were divided into two broad categories based on prior histopathological diagnosis. The first category involved 19 specimens, hereafter referred to as the sclerotic group, and revealed hippocampal sclerosis characterized by severe neuronal loss, atrophy and intense GFAP immunoreactivity in the Ammon's horn. The other 19 patients constituted the 'non-sclerotic group' as they did not show any significant hippocampal atrophy or neuronal death. However, mild to moderate astrogliosis and/or microglia activation was present in many of the specimens in the non-sclerotic group (Table 3.1.1). In all patients, the generation of temporal lobe seizures had been traced to the hippocampus as shown by non-invasive and invasive diagnostics described elsewhere (Elger et al., 1993)(Behrens et al., 1994). Informed consents were obtained from all patients for additional morphological studies. All procedures were approved by the ethics committee of Bonn University Medical center and conform to standards set by the Declaration of Helsinki (1989). For immunohistochemistry, specimens were fixed in 4% paraformaldehyde (PFA) (pH 7.4) for 12 h at 4˚C. For Western blotting, specimens were snap frozen in liquid nitrogen for 5 min and then were stored at -80˚C until further use.

Table 3.1.1: Patient information

AHS: Ammon's Horn Sclerosis, F: female, M: male

Category	Patient	Gender	Age (Years)	Diagnosis
Sclerotic	1	F	28	AHS
	3	F	11	AHS
	5	F	20	AHS
	7	F	27	AHS
	9	M	21	AHS
	11	M	18	AHS + Dysembryoplastic neuroepithelial tumour
	13	M	24	AHS
	15	M	17	AHS (Endfolium sclerosis)
	17	M	31	AHS
	19	M	35	AHS
	21	M	48	AHS
	23	F	50	AHS
	25	F	22	AHS
	27	F	48	AHS
	29	M	40	AHS
	31	F	41	AHS
	33	M	26	AHS
	35	F	17	AHS
	37	M	51	AHS
Non-sclerotic	2	M	16	Middle cerebral artery infarction right
	4	M	10	Multifocal dysplasia of the left hemisphere
	6	F	43	Glioblastoma multiforme
	8	F	8	Rasmussen encephalitis
	10	F	47	Rasmussen encephalitis
	12	M	3	Rasmussen encephalitis
	14	M	19	Loss of grey-white matter differentiation
	16	M	11	Rasmussen encephalitis
	18	M	21	Loss of grey-white matter differentiation
	20	M	48	Non-AHS
	22	M	11	Dysembryoplastic neuroepithelial tumour
	24	F	30	Rolando-epilepsy
	26	M	38	Focal cortical dysplasia
	28	M	13	Ganglioglioma
	30	M	18	Reactive astrogliosis
	32	M	22	Focal cortical dysplasia
	34	M	47	Cavernous hemangioma
	36	F	24	Dysembryoplastic neuroepithelial tumour
	38			Glioblastoma multiforme, no epilepsy

3.1.2 Animals

Maintenance and handling of animals was according to the local government regulations. Experiments were approved by the state office of North-Westphalia, (LANUV approval number 84-02.04.2015.A393). Mice were kept under standard housing conditions (12 h/12 h dark-light cycle, food and water ad libitum). Wild-type mice (FVB and Black 6 background) and transgenic mice lacking Cx30 and Cx43 in GFAP-positive cells ($Cx30^{-/-}$/Cx43fl/fl-hGFAP-Cre mice) of 90-120 d age were used. The MTLE animal model was established by unilateral intracortical kainate injection as described before (Bedner et al., 2015). All kainate injections were performed by Dr. P. Bedner, Institute of Cellular Neurosciences, Bonn. Briefly, the mice were anesthetized (medetomidine (0.3 mg/kg, i.p.) and ketamine (40 mg/kg, i.p.)) and placed in a stereotaxic frame equipped with a manual microinjection unit (TSE Systems GmbH, Bad Homburg, Germany). Seventy nl of a 20 mM solution of kainate (Tocris, Bristol, UK) in 0.9% sterile NaCl were stereotactically injected into the neocortex just above the right dorsal hippocampus. The stereotactic coordinates were 1.9 mm posterior to bregma, 1.5 mm from midline and 1.7 mm from the skull surface. Control mice were given injections of 70 nl saline under the same conditions. After injection the scalp incision was sutured and anesthesia stopped with atipamezol (300 mg/kg, i.p.). Brains from these mice were perfusion fixed with 4% PFA at the following time points: 4 h, 5 d, 1 month and 3 months. For Western blotting, entire hippocampi from the dorsal region of the temporal lobe were harvested at the following time points post kainate injection: 4 h, 5 d, and 3 months. The harvested tissues were snap frozen in liquid nitrogen followed by storage at -80 ºC until further use.

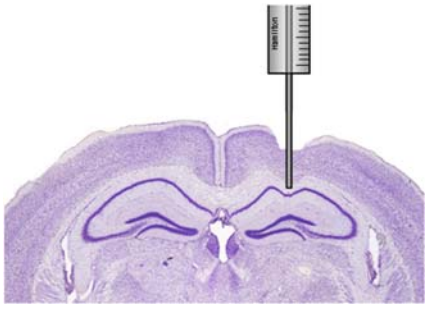

Stereotactical coordinates
Anteroposterior (AP) = -1.9 mm Lateral (Right) = 1.5 mm
Dorsoventral = 1.7 mm

Figure 3.1.2: Schematic diagram illustrating intracortical kainate injection

3.2 Materials

3.2.1 Chemicals, solutions and reagents

Product	Company
Acetic acid	Sigma Aldrich, Munich, Germany
Acetonitrile	Sigma Aldrich, Munich, Germany
Acrylamide solution (Rotiphorese Gel 30 (37, 5:1)	Carl Roth, Karlsruhe, Germany
Albumin fraction V	AppliChem, Darmstadt, Germany
Ammonium bicarbonate	Sigma Aldrich, Munich, Germany
5-Bromo-2′-deoxyuridine (BrdU)	Sigma Aldrich, Munich, Germany
Dithiothreitol (DTT)	Carl Roth, Karlsruhe, Germany
Ethanol	Carl Roth, Karlsruhe, Germany
Gel Code blue safe protein stain	Pierce (Now Thermo Scientific Waltham, MA, USA)
Hoechst 33258	Sigma Aldrich, Munich, Germany
Iodoacetamide	Sigma Aldrich, Munich, Germany
Isopropanol	Carl Roth, Karlsruhe, Germany
Ketamine 10%	Bela Pharma, Vechta, Germany
Methanol	Carl Roth, Karlsruhe, Germany
Milk powder (non-fat)	Carl Roth, Karlsruhe, Germany
NativeMark™ Unstained Protein Standard	Invitrogen (Now Thermo Scientific Waltham, MA, USA)
Normal Goat Serum (NGS)	Chemicon (Now Merck Millipore, Darmstadt, Germany)
Normal Donkey Serum (NDS)	Carl Roth, Karlsruhe, Germany
PageRuler	Thermo Scientific Waltham, MA, USA
Paraformaldehyde	Sigma Aldrich, Munich, Germany
Permafluor mounting medium	Thermo Scientific Waltham, MA, USA
Phosphate Buffered Saline	Gibco (Now Thermo Scientific Waltham, MA, USA)
Protease and phosphatase inhibitor cocktail	Pierce (Now Thermo Scientific Waltham, MA, USA)
Protein A beads	Invitrogen (Now Thermo Scientific Waltham, MA, USA)
Roti-Load buffer (Laemli buffer 4x)	Carl Roth, Karlsruhe, Germany
TritonX-100	Sigma Aldrich, Munich, Germany
Tween-20	AppliChem, Darmstadt, Germany
Tetramethylethylenediamine (TEMED)	Carl Roth, Karlsruhe, Germany
Xylazine	Ceva, Dusseldorf, Germany

3.2.2 Kits

Product (Company)	Purpose
BCA assay kit (Pierce, now Thermo Scientific)	Estimation of protein concentration
Plasma membrane protein extraction Kit (Abcam)	Isolation of plasma membrane proteins
Click-iT® TUNEL Alexa Fluor® Imaging Assay (Invitrogen, now Thermo Scientific)	Detection of apoptosis
WesternBright® Sirius HRP substrate (Advansta)	Substrate for visualizing HRP activity

3.2.3 General materials

Material	Company
Gloves	Ansell ltd, Staffordshire, UK
Mice surgery equipment	Fine Science Tools (F.S.T), Germany
Microscopic slides	Thermoscientific, Braunsweig, Germany
Pasteur pippetts	Carl-Roth, Karlsruhe, Germany
Pipette tips	Greiner GmbH, Frickenhausen, Germany
Native Protein gels (4-16 %)	Invitrogen/Thermo Scientific, Waltham, MA, USA
PVDF membrane	Millipore, Schwalbach, Germany
Sterile filters	Millipore, Schwalbach, Germany
Syringes, Venofix safety	Braun, Melsungen, Germany
Whatman paper	Whatman International, Maidstone, UK

3.2.4 Softwares

Software	Application	Company
Gene Tools	Quantification of Western blots	Genegnome , UK
ImageJ	Image analysis	NIH, USA
Proteome Discoverer	MS Raw data processing	Thermo Fisher Scientific, USA
Mascot	Peptide identification	Matrix Science Ltd, UK
Huygens Essential	Deconvolution	Scientific Volume Imaging

3.2.5 Instruments

Instrument	Company
Centrifuge 5424	Eppendorf, Hamburg, Germany
DynaMag magnet	Invitrogen (Now Thermo Scientific Waltham, USA)
Gene Gnome Imaging system	Synaptics ltd. Cambridge, England
Heat block	VWR, Darmstadt, Germany
SP8® Laser Scanning Microscope	Leica Microsystems, Wetzlar, Germany
Mini-Protean 3 Cell	Biorad, Munich, Germany
Mini-Trans blot Cell	Biorad, Munich, Germany
pH meter	Mettler Toledo, Giessen, Germany
Rotator PTR-30	Grant Bio
SDS gel electrophoresis power supply	Bio-Rad
Shaker	Grant-Bio, UK
Vibratome VT1200S	Leica, Nussloch, Germany
Vortexer	VWR, Darmstadt, Germany
Weighing balance	Acculab, Sartorius group, Germany
Western Blotting power supply	Biorad, Munich, Germany
4˚C Refrigerator	Liebherr, Biberach, Germany
-20˚C Freezer	Liebherr, Biberach, Germany
-80˚C Freezer	Thermo Scientific, Bonn, Germany

3.2.6 Buffers for polyacrylamide gel

Contents for two gels of 1.55 mm thickness	Stacking gel	Resolving gel	
	4%	10%	12.50%
Rotiphorese gel 30	1.66 ml	6.66 ml	8.33 ml
50 mM Tris buffer (pH 6.8)	2.5 ml		
150 mM Tris buffer (pH 8.8)		5 ml	5 ml
Distilled water	5.63 ml	7.92 ml	6.25 ml
TEMED	10 µl	20 µl	20 µl
APS (10 %)	100 µl	200 µl	200 µl
SDS	100 µl	200 µl	200 µl

3.2.7 Buffers for electrophoresis and Western blotting

Buffer	Concentration	Composition
Protein lysis buffer (RIPA buffer, modified) (pH adjusted to 7.4) sterile-filtered, stored at -20°C	50 mM	Tris-base
	150 mM	NaCl
	0.5 % v/v	Nonidet P-40 (NP40)
	0.5 % w/v	Sodium Deoxycholate
	1 % v/v	TritonX-100
Plasma membrane protein buffer (4 % Dodecyl maltoside) (pH adjusted to 7.4)	50 mM	Bis-Tris
	40 mM	NaCl
	4%	Dodecyl maltoside
SDS-running buffer (pH 8.3)	0.25 M	Tris-base
	1.92 M	Glycine
	1 % v/v	SDS
Transfer buffer (pH 8.3)	0.25 M	Tris-base
	1.92 M	Glycine
Tris-buffered saline with Tween-20 (TBST) (pH adjusted to 7.4)	0.25 M	Tris-base
	150 mM	NaCl
	0.05 % v/v	Tween 20

3.2.8 Buffers for Blue Native PAGE

Buffer	Concentration	Composition
Anode buffer (pH adjusted to 7)	50 mM	Bis-Tris
Cathode buffer (pH adjusted to 7)	50 mM	Tricine
	15 mM	Bis-Tris
	0.02%	Coomassie G 250
Cathode buffer/10 (pH adjusted to 7)	50 mM	Tricine
	15 mM	Bis-Tris
	0.002%	Coomassie G 250

3.2.9 Buffers for expansion microscopy

Monomer solution

Chemicals	Concentration (%)	Volume (ml) for 9.4 ml
38 % Sodium acrylate	8.6	2.25
50% Acrylamide	2.5	0.5
2 % N,N′-Methylenebisacrylamide	0.15	0.75
29.2% Sodium chloride	11.7	4
1x PBS	10	1
Deionized water		0.9

Gelling solution

Chemicals	Concentration (%)	Volume (µl) for 300 µl)
Monomer solution		282
0.5% 4-hydroxy-TEMPO	0.01	6
10% TEMED	0.2	6
10% APS	0.2	6

Digestion buffer

Chemicals	Concentration	Volume (µl) for 5 ml
Tris pH 8.0	50 mM	250
0.5M EDTA	1 mM	10
10% Triton X-100	0.50%	250
8 M Guanidine-HCl	0.8 M	500
Proteinase K	16 units/mL	100
Deionized water		3890

3.2.10 Primary antibodies

IF: Immunofluorescence, IB: Immunoblotting

Antigen	Species	Dilution ratio	Company/Reference
BrdU	rat	IF 1: 500	AbD Serotec
CD31	Mouse	IF 1: 200	Abcam
	Goat	IF 1: 200	R&D systems
Cx43 360-382	rabbit	IF 1: 500	Custom made (Perbioscience)
		IB 1: 1000	
Cx43 363-382	rabbit	IF 1: 500	Sigma
		IB 1: 1000	
Cx43NT1	mouse	IB 1: 200	FHCRC
Cx43 phospho S262	rabbit	IB 1: 1000	Santa Cruz Biotech

Cx43 phospho S255	rabbit	IB 1: 1000	Santa Cruz Biotech
Cx43 phospho S368	rabbit	IB 1: 1000	Invitrogen
Cx30	rabbit	IF 1: 500	Invitrogen
		IB 1: 250	
DCX	goat	IF 1: 100	Santa Cruz Biotech
GAPDH	mouse	IB 1: 5000	Abcam
GFAP	mouse	IF 1: 500	Chemicon
	rabbit	IF 1: 500	Dako
		IB 1: 1000	
Iba1	rabbit	IF 1: 500	Dako
Prox1	rabbit	IF 1: 2500	Chemicon
NG2	Mouse	IF 1: 100	Millipore
PDGFR β	Goat	IF 1: 600	RD systems
S100 β	Mouse	IF 1: 1000	Abcam
	Rabbit	IF 1: 500	Abcam

3.2.11 Secondary antibodies

IF: Immunofluorescence, IB: Immunoblotting

Product	Species	Dilution ratio	Company
Anti-mouse HRP	sheep	IB 1: 6000	GE Healthcare
Anti-rabbit HRP	donkey	IB 1: 6000	GE Healthcare
Anti-rat biotinylated	donkey	IF 1: 500	Jackson Immunoresearch
Alexa fluor 488	donkey anti-goat	IF 1: 200	Invitrogen
Alexa fluor 488	goat anti-mouse	IF 1: 500	Invitrogen
Alexa fluor 488	goat anti-rabbit	IF 1: 500	Invitrogen
Alexa fluor 488	donkey anti-rabbit	IF 1: 500	Invitrogen
Alexa fluor 594	goat anti-mouse	IF 1: 500	Invitrogen
Alexa fluor 594	goat anti-rabbit	IF 1: 500	Invitrogen
Alexa fluor 594	donkey anti-goat	IF 1: 500	Invitrogen
Alexa fluor 647	donkey anti-rabbit	IF 1: 300	Invitrogen
Alexa fluor 647	goat anti-mouse	IF 1: 500	Invitrogen
Alexa fluor 647	goat anti-rabbit	IF 1: 500	Invitrogen
Alexa fluor 568	donkey anti-goat	IF 1: 200	Jackson ImmunoResearch
Biotin	donkey anti-rabbit	IF 1: 200	Jackson ImmunoResearch
Streptavidin (Alexa Fluor 647)		IF 1: 500	Jackson ImmunoResearch

3.3 Methods

3.3.1 Fixation and sectioning of brains

Mice were perfusion fixed as follows. They were first anesthetized with intraperitoneal injection (100 µl each) of Xylazine and Ketamine (in the ratio 3:2). Using small scissors, the ribcage was opened up and the pericardium was exposed. A 25-G needle connected with PBS and PFA sources was inserted into the left ventricle. An incision was made into the right ventricle in order to make an exit for the blood flow. 20 ml PBS (pH 7.4) was slowly injected into the left ventricle to remove blood, followed by further pumping of 20 ml 4% PFA for fixation. After perfusion, the brains were isolated by opening up the skull and then were fixed again in 4% PFA overnight at 4°C. The next day, brains were transferred in vials containing PBS and stored until further use. They were cut into 40 µm thick coronal sections with the help of a vibratome. The sections were stored in PBS containing 0.01% sodium azide.

Human hippocampal specimens obtained during surgeries (performed at the Department of Neurosurgery, University Clinic, Bonn) were fixed in 4% PFA overnight followed by storage in PBS. They were cut into 20 µm thick sections with the help of a vibratome. For expansion microscopy, 60 µm thick sections were made. The sections were stored in PBS containing 0.01% sodium azide.

3.3.2 General procedure for immunohistochemistry

Brain slices prepared as described in 3.3.1 were washed 3 times (5 min each time) with PBS to remove the sodium azide and residual PFA. After permeabilization and blocking (2 h, room temperature) with 0.5% Triton X-100 and 10% normal goat serum (NGS) (or 10% normal donkey serum, NDS) in PBS, the sections were incubated overnight (4°C) in 5% NGS (or NDS) in PBS containing 0.1% Triton X-100 and primary antibodies (listed in Table 3.2.10). After washing three times with PBS (5 min each time), the sections were incubated with secondary antibodies conjugated with Alexa Fluor® 488, Alexa Fluor® 594 or Alexa Fluor ®647 (Invitrogen, dilution 1:500 each) in PBS with 2% NGS (or 2% NDS) and 0.1% Triton X-100 for 1.5 h at room temperature. For immunostaining of PDGFRβ and CD31, NGS in the blocking solutions was replaced by NDS, and the secondary antibodies were also changed accordingly. For the immunostaining of albumin, no serum was used in the blocking solutions. For the histochemical detection of the vasculature in the hippocampus, biotinylated lycopersicon esculentum (tomato) lectin (Vector laboratories) was used. In brief, after overnight incubation with primary antibodies, the diluted lectin (dilution 1:100) was added to

the sections and incubated for 30 min at room temperature, then the mixture of streptavidin coupled with Alexa Fluor ®647 (1:500, Invitrogen) and other appropriate secondary antibodies was added to the sections. Sections were washed three times after each incubation. Alternatively, CD31 was used to visualize the vasculature.

3.3.3 Expansion microscopy

(Performed in collaboration with Dr. M. Herde, Institute of Cellular Nuerosciences, Bonn).
The expansion microscopy protocol with conventional primary and secondary antibodies was adopted from Chen et al., 2015 and Chozinski et al., 2016 (Chen et al., 2015)(Chozinski et al., 2016). A schematic procedure is depicted in Figure 3.3.3. Hippocampal slices were stained as described in section 3.3.2. For Cx43 labelling, biotinylated anti-rabbit secondary antibody was used. The sections were then incubated with 1 mM methylacrylic acid-NHS (Sigma Aldrich) linker for 1 h. After washing in PBS 3 times, sections were incubated with monomer solution containing 8.6% sodium acrylate, 2.5% acrylamide, 2% N, N′-Methylenebisacrylamide and 29.2% sodium chloride in PBS for 45 min. A gelling solution was prepared by adding APS (0.2 %), TEMED (0.2 %) and 4-hydroxy-TEMPO (0.01 %) to the monomer solution. Slices were placed in the gelling solution on a glass slide and the preparation was covered with a coverslip. After 2 h of incubation at 37°C, the coverslip was removed and the excess gel around the slice was removed. The gel pieces containing the tissue slices were incubated overnight at 37˚C in a digestion buffer containing 50 mM Tris, 0.5 % Triton-X100, 1 mM EDTA, 0.8 M guanidine hydrochloride and 16 U/ml of proteinase K (pH 8). The next day, the digestion buffer was removed and the gel pieces were incubated with streptavidin coupled with Alexa 647 for 1.5 h. They were then washed with deionized water. After five washes (2.5 h), slices were transferred to a custom mounting chamber filled with distilled water, mounted by superglueing its edges to the chamber's bottom and sealed with a coverslip on the top. All imaging was performed on a Leica SP8 confocal microscope using a 40x/1.1NA objective and hybrid detectors. The expansion factor was determined by measuring gel sizes before and after expansion. Images were deconvolved with Huygens Essential® (Scientific Volume Imaging).

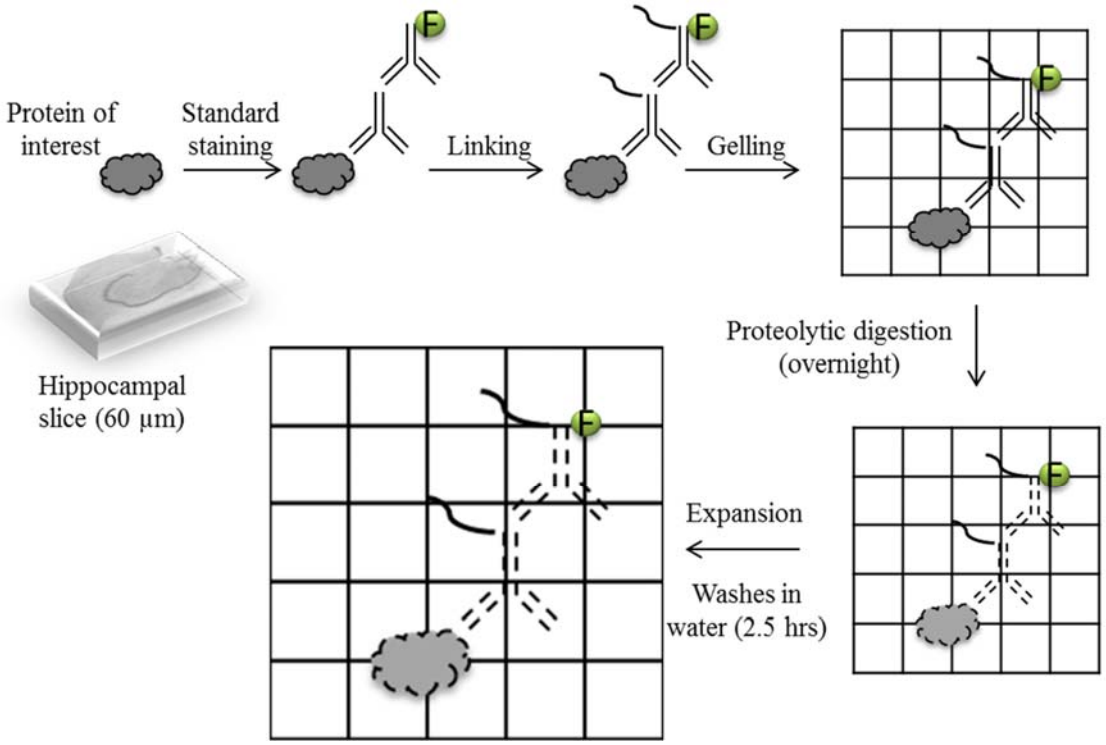

Figure 3.3.3: Schematic diagram describing expansion microscopy. Prior to the linking step, a standard protocol for immunohistochemistry was followed. Expansion was carried out by washing the gel-containing tissue slices in deionized water. F stands for the fluorophore attached to a secondary antibody.

3.3.4 TUNEL assay for detection of apoptotic cells

Terminal deoxynucleotidyl transferase dUTP nick end labeling (TUNEL) was performed with the Click-iT® TUNEL Alexa Fluor Imaging Assay (Invitrogen) according to the manufacturer's instructions. Briefly, 15 µm cryostat cut sections were placed on Superfrost® plus glass slides. They were then fixed with acetone for 2 min at room temperature (alternatively with 4% PFA for 15 min), air dried and a hydrophobic barrier (Roti-Liquid Barrier Marker, Roth) was applied around the sections, followed by wash with PBS. Sections were permeabilized with 0.25% Triton X-100 in PBS. A positive control was prepared by incubating some of the sections with DNAse I for 30 min at room temperature. TdT reaction cocktail was prepared by mixing the following components:

TdT reaction buffer (Component A):	94 µl
EdUTP (Component B):	2 µl
TdT (Component C):	4 µl
Total:	100 µl

The reaction was allowed to take place for 1 h at 37˚C after which it was terminated by removing the reaction cocktail and washing the sections twice with 3% BSA in PBS for 2 min each time. Click-iT® reaction cocktail, in which the sections were incubated for 30 min at room temperature, was prepared as follows:

Click-iT reaction buffer (Component D):	97.5 µl
Click-iT reaction buffer additive (Component E):	2.5 µl
	100 µl

The reaction was terminated by removing the reaction cocktail and washing the sections 3 times with 3% BSA in PBS for 2 min each time.

For GFAP staining, sections were blocked with 5% NGS, 0.125% TritonX-100 in 1x PBS (pH 7.4) for 1 hr at room temperature and incubated with mouse GFAP antibody (1:400) in 2% NGS, 0.125% TritonX-100 in 1x PBS (pH 7.4) for 1h at RT. The sections were washed three times for 5 min each with 1x PBS followed by incubation with goat anti mouse Alexa Fluor 488 (1:500) secondary antibody in 2% NGS, 0.125 % TritonX-100 in 1x PBS (pH 7.4) for 1h at room tempreature. Sections were washed three times with 1x PBS for 5 min each, followed by staining for nuclei with Draq5 (1:1000, Biostatus ltd, Leicestershire, UK) in 1x PBS for 10 min at room temperature followed by two short washes, drying of the sections and mounting using Permafluor® mounting medium.

3.3.5 BrdU administration and staining procedure

Mice were given BrdU (1 mg/ml) through drinking water containing 1% sucrose for 14 days post intracortical kainate injection. BrdU administration was started 24 h after the kainate injection. From the 16th day after kainate injection, mice were given normal drinking water (Figure 3.3.5). They were perfused and the brains were processed as described in 3.3.1. Before immunostaining an antigen retrieval procedure was performed. Briefly, sections were incubated with 2 N HCl for 30 min. After washing with PBS, any remaining HCl in the sections was neutralized by incubating the sections in 0.1 M borate buffer for 10 min. The sections were

immunostained as outlined in section 3.3.2. Normal donkey serum was used as a blocking agent in all solutions. Rat anti- BrdU antibody was used at the concentration of 1:500. Donkey anti-rat secondary antibody coupled with Alexa 594 was used to visualize BrdU incorporated into the nuclei.

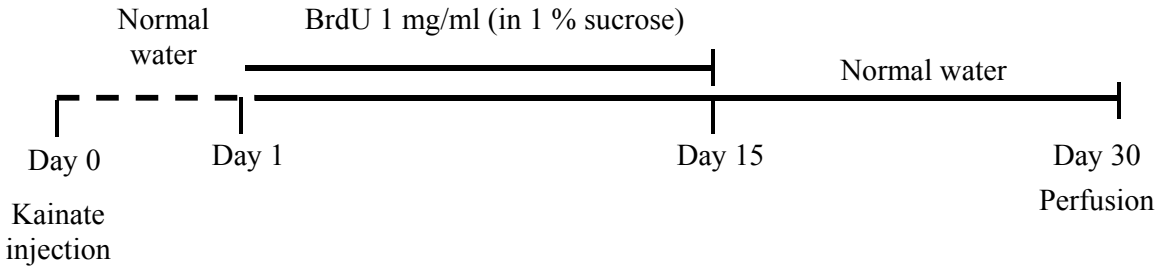

Figure 3.3.5: Design of the experiment for BrdU-based assessment of cell proliferation. BrdU solution was freshly prepared every 5 days and it was protected from light.

3.3.6 Image acquisition and cell counting

A laser confocal microscope (Leica SP8®) was used to acquire all the images. For cell counting, 63x or 40x magnification images were taken while for Cx43 stereology, only 63 x magnification was used with an optical thickness of 1 µm. 1024 x 1024 pixel frame was used in all of the images. Images intended for fluorescence intensity and stereological analysis were acquired with the Leica HyD hybrid® detector in a standard mode. Other images were acquired with a photo-multiplier tube (PMT) detector. 184.52 X 184.52 X 30 μm^3 counting boxes (boxes 1, 2 and 3 in Figure 3.3.6) were positioned in the SR region of CA1 for cell counting (for example astrocytes, microglia, and endothelial cells) or for Cx43 stereology. Cell counting in the DG (for example granule cells, newly generated neurons and astrocytes) was performed in 290 x 290 x 8 μm^3 counting boxes (boxes 4, 5 and 6 in Figure 3.3.6). The first counting box in the DG was positioned 250 µm away from the tip of the granule cell layer as shown in Figure 3.3.6. The cell numbers (or values for any other parameter) were averaged across all boxes in the same region.

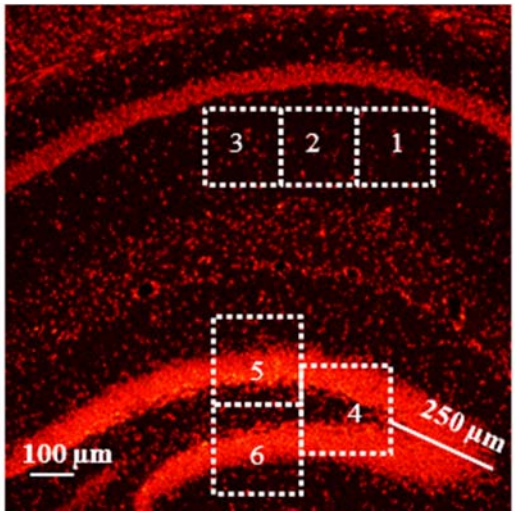

Figure 3.3.6: Positions of the counting boxes. Hoechst fluorescence image showing cell nuclei in the hippocampus. Boxes with the dotted lines represent the region of interests in which cell counting or Cx43 stereological analysis was performed. Values from the boxes 1, 2 and 3 were used to get the mean value for the CA1 region. Similarly, values from the boxes 4, 5 and 6 were used to get the mean value for the DG region.

3.3.7 Stereology

A point counting method was used to quantify the vascular density (Rigau et al., 2007). The resulting parameter called 'point count' is influenced not only by the number of vessels present in a given area but also by the size and tortuosity of the vessels. Briefly, a 5 x 5 grid was superposed onto the digitized image of the CA1 region (including all layers of the CA1) (Figure 3.3.7 A). The numbers of intersections made by blood vessels with this grid were counted. At least three sections (slices) were used per mouse or patient. The point counts were first averaged across sections and then across mice or patients. Cx43 immunostaining was analyzed to extract the plaque dimensions. Confocal images acquired at constant settings were used to extract the following parameters using the image analysis software Fiji (Schindelin et al., 2012): average fluorescence intensity, the area occupied by the Cx43 signal, average plaque size, plaque number and the distribution ratio. Images were converted into 8-bit format and were thresholded at 3 different values 55-255, 75-255 and 90-255. All of these thresholding conditions maintained the statistical inference between the experimental groups. Therefore, the intermediate thresholding condition (75-255) was used for further analysis. The values were recorded for each optical plane and then averaged across all the planes in a slice from mouse or a patient. Mean pixel intensity and the distribution ratio was measured in non-thresholded, 12-bit images. Pixel intensities or grey values were measured in arbitrary units (a.u.).

The distribution ratio was calculated as the ratio of average Cx43 intensities around the blood vessels to the intensities in the rest of the tissue. The region around the blood vessel was defined as a 5 µm wide rim from the innermost margin of Cx43 around blood vessel into the brain parenchyma (Figure 3.3.7 B). For each mouse or patient, these values were obtained from 3 slices and then they were averaged.

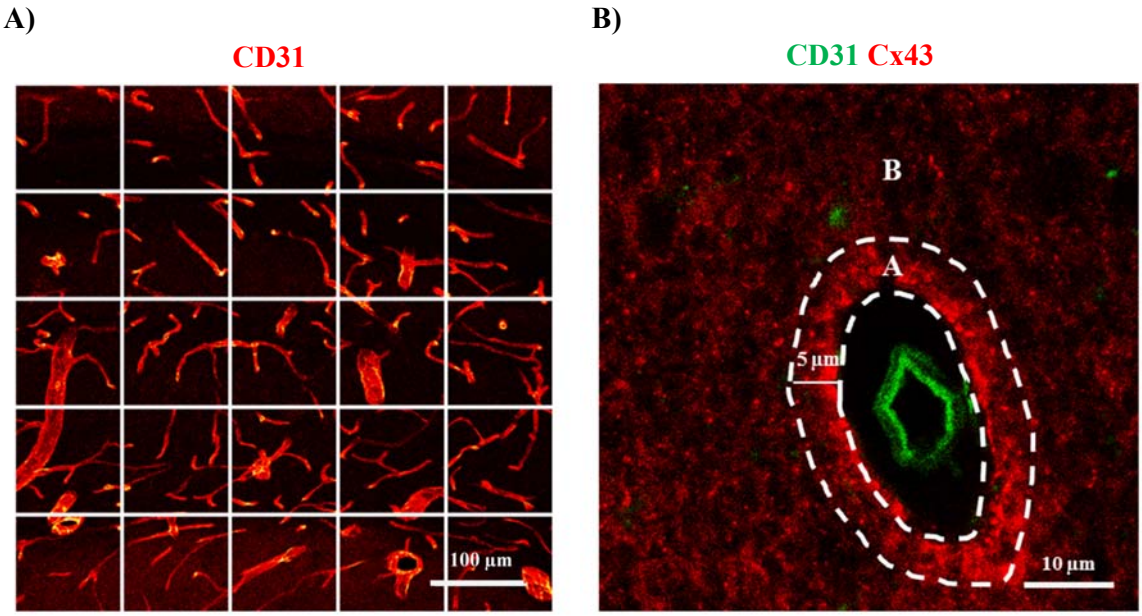

Figure 3.3.7: Examples of point count and distribution ratio estimation. A) A 5 x 5 grid superimposed on an image displaying CD31 positive blood vessels in the CA1 region. A point count is the number of intersections made by the blood vessels with the superimposed grid. **B)** CD31-Cx43 immunostaining displaying the regions of interests, A (5 µM thick rim around the blood vessel) and B (rest of the image without region A). The distribution ratio is defined as the ratio of mean Cx43 fluorescence intensity in region A to that in region B.

3.3.8 Preparation of total cellular protein lysates (whole-cell protein lysates)

Dorsal hippocampi from mice or surgically resected hippocampal specimens from epilepsy patients were snap frozen in liquid nitrogen and stored at -80˚C until further use. The tissues were homogenized with the help of a plastic or glass pestle in a modified RIPA buffer (containing 150 mM NaCl, 50 mM Tris, 1% Triton X-100, 0.5% sodium Deoxycholate, 0.5% NP-40, pH 7.4). Halt® protease and phosphatase inhibitor cocktail was added in 1:10 v/v ratio. The resultant cell suspension was sonicated in a bath sonicator three times for 30 s each, with incubation on ice for one min after each sonication. The lysates were then passed through a prechilled 27 gauge syringe 5 times. Protein concentration was measured using a BCA assay kit (Pierce/Thermo Scientific). Proteins were aliquoted and stored at -80˚C.

3.3.9 Plasma membrane protein isolation

Plasma membrane-associated proteins were isolated from mouse or human hippocampi using 'Plasma Membrane Protein Extraction Kit' (Abcam) as per the manufacturer's instructions. Halt® protease and phosphatase inhibitor cocktail was added to all buffers in the kit (1:10 v/v ratio). The tissues were homogenized in the homogenization buffer supplied with the kit. The homogenized tissue suspension was sonicated in supersonic bath 3 times for 30 s each. The sonications were interspaced with incubations on ice for 1 min. The resultant lysate was centrifuged at 11000xG for 30 min. The supernatant contained the cytoplasmic fraction while the pellet contained the total membrane fraction. The pellet was then extracted with the two partially miscible polymer solutions provided with the kit. The plasma membrane proteins are enriched in the upper phase of the polymer mixture. After series of extractions and centrifugations, a final pellet enriched in plasma membrane proteins was obtained. This pellet was dissolved in 4% didodecyl maltoside in 50 mM Bis-Tris buffer containing 'Halt® Protease and Phosphatase Inhibitor Single-Use Cocktail' (Thermo Scientific) and then stored at -80˚C.

3.3.10 SDS PAGE and Western blotting

Five µg (plasma membrane fraction) or 30 µg (total cellular lysate) of protein from each sample was subjected to 4-12.5% SDS PAGE. The separated proteins were transferred to PVDF membranes by the electrophoretic wet transfer method (100 V for 2 h). The blotted membranes were blocked with 5% non-fat milk in TBST for 1 h followed by overnight incubation with primary antibodies in 2.5% milk. The next day, after 3 times washings in TBST, the membranes were probed with ECL™ anti-rabbit or anti-mouse IgG, HRP-linked $F(ab)_2$ fragment (Amersham, dilution 1:5000) in 2.5% milk for 1 h. For phospho-specific antibodies, the albumin fraction V (pH 7) was used as a blocking agent in all the steps at the same concentrations as that of milk. WesternBright Sirius® Chemiluminescent substrate (Advansta) was used to visualize the blots by GeneGnomeXRQ® imager (Syngene). Densitometry was performed using GeneTools (Syngene). Band intensities of proteins of interest were normalized with loading control intensities (GAPDH for total cellular proteins and cadherin for plasma membrane fraction).

3.3.11 Blue Native PAGE

A Blue native PAGE protocol as reported by Wittig et al., (Wittig et al., 2006) was adopted with some modifications. Five µg of plasma membrane protein lysate (prepared in 4% dodecyl maltoside) was suspended in 10% glycerol and 5% coomassie G 250. The ratio of detergent (dodecyl maltoside) to dye (coomassie G 250) was adjusted to 4:1 with diluent 4% dodecyl maltoside. Native gels with a gradient of 4 to 16% and a XCell SureLock® Mini-Cell apparatus were used for electrophoresis. The inner chamber of the apparatus was filled with cathode buffer containing 0.02% coomassie G 250 while the outer chamber was filled with anode buffer. A constant voltage of 75 V was applied across the electrodes. After the dye front reached 1/3 of total gel length, the inner chamber was refilled with cathode buffer containing 0.01% coomassie G 250. The run was allowed to continue until the dye front reached the end of the gel. Separated proteins on the gel were blotted on PVDF membranes as described in section 3.3.10.

3.3.12 Immunoprecipitation and isolation of Cx43

The sample preparation workflow is illustrated in figure 3.3.12. Homogenization buffer supplied with the 'Plasma Membrane Protein Extraction Kit' (Abcam) was used to homogenize the dorsal hippocampi (one dorsal hippocampus is equal to approximately half of the whole hippocampus from one hemisphere). Halt® protease and phosphatase inhibitor cocktail was added to all buffers in the kit (1:10 v/v ratio). The homogenized tissue suspension (350 µl/half hippocampus) was sonicated in supersonic slat 3 times for 30 s each. The sonications were interrupted with incubations on ice for 1 min. The resultant lysate was centrifuged at 11000 G for 30 min. The supernatant contained the cytoplasmic fraction while the pellet contained the total membrane fraction. The total membrane fraction pellet was dissolved in 200 µl of modified RIPA buffer (containing 150 mM NaCl, 50 mM Tris, 1% Triton X-100, 0.5% sodium Deoxycholate, 0.5% NP-40, pH 7.4). The membrane fractions of dorsal hippocampi from two mice were pooled together. Membrane fractions from the ipsilateral dorsal hippocampus from one mouse were always pooled with the corresponding ipsilateral hippocampus of another mouse. Similar pooling was followed for contralateral hippocampi. Such pooled membrane lysates were stored at -80˚C until immunoprecipitation.

One-hundred µl of custom-made anti-Cx43 antibody was coupled with 6 mg of Protein A magnetic beads for 1 h. Membrane lysates from two dorsal hippocampi (total volume 400 µl) were added to the bead-antibody mixture and the total volume was adjusted to 700 µl with

modified RIPA buffer. All buffers used for immunoprecipitation contained Halt® protease and phosphatase inhibitor cocktail in a 1:10 v/v ratio. The bead-antibody-lysate mixture was incubated on a rotar for 1 h. The supernatant was then removed with magnetic separation and stored at -80˚C. The beads were washed 5 times with PBS.

The washed beads were heated with 12 µl Laemmli buffer and 36 µl modified RIPA buffer for 10 min at 65˚C. The eluate was separated from beads with the help of a magnet. The entire 48 µl of eluate was subjected to SDS PAGE (4-10% gel). After electrophoretic separation of proteins, the gel was washed 3 times in distilled water and then was stained with colloidal coomassie G 250 (Gel Code blue, Pierce/ Thermo Scientific) with overnight incubation. The next day, the gel was photographed with the help of a GeneGnomeXRQ® imager (Syngene). Bands corresponding to 40 kDa were excised with the help of a scalpel blade and then were submitted to mass-spectrometric analysis.

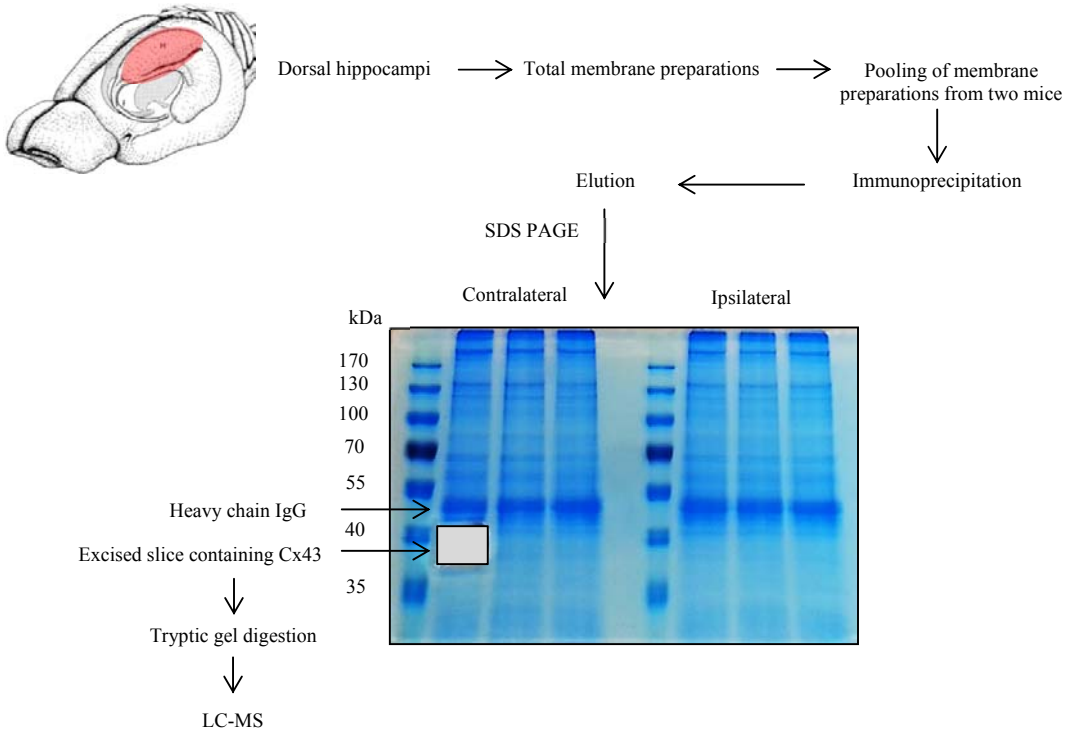

Figure 3.3.12: Schematic diagram showing sample preparation workflow for mass-spectrometry. The eluates obtained from immunoprecipitation reaction were subjected to SDS PAGE and the gel was stained with Coomassie G250. The strong band between 40 and 55 kDa represents the heavy chain of IgG antibody that was used for immunoprecipitation. Bands at 40 kDa were carved out and were subjected to tryptic digestion. (Brain image adapted and modified from Amaral and Witter, 1995)

3.3.13 In-gel digestion

(Performed by Dr. B. Gehrig, Institute of Biochemistry and Molecular Biology, Bonn University)

Gel slices in the molecular weight range of Cx43 were cut into smaller pieces and then were subjected to tryptic in-gel digestion. In brief, proteins were reduced with 20 mM DTT, slices were washed with 100 mM ammonium bicarbonate, and proteins were alkylated with 40 mM iodoacetamide. The slices were washed again and dehydrated with acetonitrile. Slices were dried in a vacuum concentrator and incubated with 400 ng sequencing grade trypsin (at 37°C) overnight. The peptide extract was dried in a vacuum concentrator and stored at -20°C.

3.3.14 Liquid chromatography-Mass-Spectrometry (LC-MS) analysis

(Performed by Dr. M. Sylvester, Institute of Biochemistry and Molecular Biology, Bonn University)

Dried peptides were dissolved in 10 µl of 0.1% formic acid (solvent A). Three µl were injected onto a C18 trap column (self-packed, 20 mm length, 100 µm inner diameter, ReproSil-Pur 120 C18-AQ, 5 µm, Dr. Maisch GmbH, Ammerbuch-Entringen, Germany). Bound peptides were eluted onto a C18 analytical column (200 mm length, 75 µm inner diameter, 1.9 µm particles, NanoSeparations, Nieuwkoop, Netherlands). Peptides were separated over a linear gradient from 6% to 35% solvent B (80% acetonitrile, 0.1% formic acid) within 87 min at a flow rate of 320 nl/min. The nanoHPLC was coupled online to an LTQ Orbitrap Velos mass spectrometer (Thermo Fisher Scientific, Bremen, Germany). Peptide ions between 330 and 1600 m/z were scanned in the orbitrap detector with a resolution of 30,000 (maximum fill time 400 ms, AGC target 106). The 25 most intense precursor ions (threshold intensity 3000) were subjected to collision induced dissociation with multiple stage activation and fragments analyzed in the linear ion trap. Fragmented peptide ions were excluded from repeat analysis for 15 s.

Raw data processing and analysis of database searches were performed with Proteome Discoverer software 2.1.0.81 (Thermo Fisher Scientific). Peptide identification was done with an in-house Mascot server version 2.5.1 (Matrix Science Ltd, London, UK) from Proteome Discoverer. MS2 data were searched against mouse sequences from SwissProt (release 2012_07) and a minimized Cx43 database for increased sensitivity. Precursor Ion m/z tolerance was 9 ppm, fragment ion tolerance 0.5 Da. b- and y-ion series were included. Tryptic peptides with up to two missed cleavages were searched. Carbamidomethylation was set as a static modification of cysteines. The following dynamic modifications were allowed:

phosphorylation of serine, threonine, and tyrosine, oxidation of methionine, and the acetylation of the protein N-terminus. The ptmRS1.4 node was used for scoring of the phospho site assignments. Spectra without high confident matches were sent to a second round Mascot search with semitryptic specificity and 11 ppm mass tolerance.

Mascot results from searches against SwissProt were sent to the percolator algorithm version 2.05 as implemented in Proteome Discoverer 2.1. Low scoring identifications and phospho-localizations were inspected manually. Chromatographic peak areas of phosphopeptides were calculated in Proteome Discoverer. Peak areas of peptides with the same assigned site were summed and normalized to total Cx43 (the sum of the top 3 Cx43 peptides' chromatographic peak areas).

3.3.15 Statistics

Data are given as mean ± standard deviation (SD). All error bars represent standard deviation. The difference between groups was tested for significance using the Student's t-test or ANOVA followed by Tukey's post hoc analysis. Non-normal data sets (determined by Grubb's test) were analyzed by non-parametric tests, followed by post hoc Dunn's test. The level of significance was set at $P < 0.05$.

4 Results

Short half- life and extensive post-translational modification of connexins have profound influence on the extent of gap junctional coupling mediated by them. Cx43 and Cx30 mediate gap junctional coupling in astrocytes. In order to investigate the molecular mechanism leading to astrocytic uncoupling in epilepsy, it is imperative to study these connexins at various stages of epilepsy. Since the contribution of Cx43 to the astrocytic coupling in hippocampus is more than that of Cx30 (Gosejacob et al., 2011), the former was the major focus of this investigation.

4.1 Molecular alterations associated with astrocytic uncoupling in human hippocampal specimens

Lack of intercellular coupling is a prominent feature of astrocytes in the sclerotic hippocampus (Bedner et al., 2015). There have been inconsistent reports about the expression pattern of connexins in hippocampal specimens obtained from epileptic patients (Steinhäuser et al., 2012). Therefore, total connexin expression levels could not be correlated with the observed astrocytic uncoupling. Moreover, previous studies lacked the information about cellular distribution and phosphorylation of Cx43 in human specimens (Mylvaganam et al., 2014). These aspects of connexin expression along with their functional relevance were investigated in hippocampal specimens obtained from 38 patients suffering from pharmacoresistant temporal lobe epilepsy. These specimens were divided into two groups: sclerotic (total 19) and non-sclerotic (total 19), based on histological diagnosis.

4.1.1 Number S100β-positive cells are increased in the sclerotic hippocampus

Astrocytes in the sclerotic hippocampus are known to undergo profound alterations (Coulter and Steinhäuser, 2015). The term astrogliosis encompasses increases in both, the number and size of astrocytes (Sofroniew and Vinters, 2010). The numbers of astrocytes in the CA1 region were counted and compared between sclerotic and non-sclerotic hippocampi. Coronal sections of the brain were stained with mouse monoclonal anti-S100β and rabbit polyclonal anti-GFAP antibodies. Identification of an astrocyte was based on colocalization of GFAP and S100β immunolabelling. Confocal images revealed that most of the GFAP-positive cells were co-labelled with S100β (Figure 4.1.1 A).

However, not all S100β-positive cells were GFAP-positive. In the sclerotic hippocampus, GFAP immunoreactivity was intense and diffuse with intermingled fibres. In this case, recognition of a putative astrocytic cell body was possible only with S100β labelling. Numbers of S100β-positive cells per counting box were significantly higher in the sclerotic group (26.4 ± 2 in non-sclerotic vs. 38.22 ± 3.5 in sclerotic hippocampus, N = 3, $p < 0.01$) (Figure 4.1.1 B).

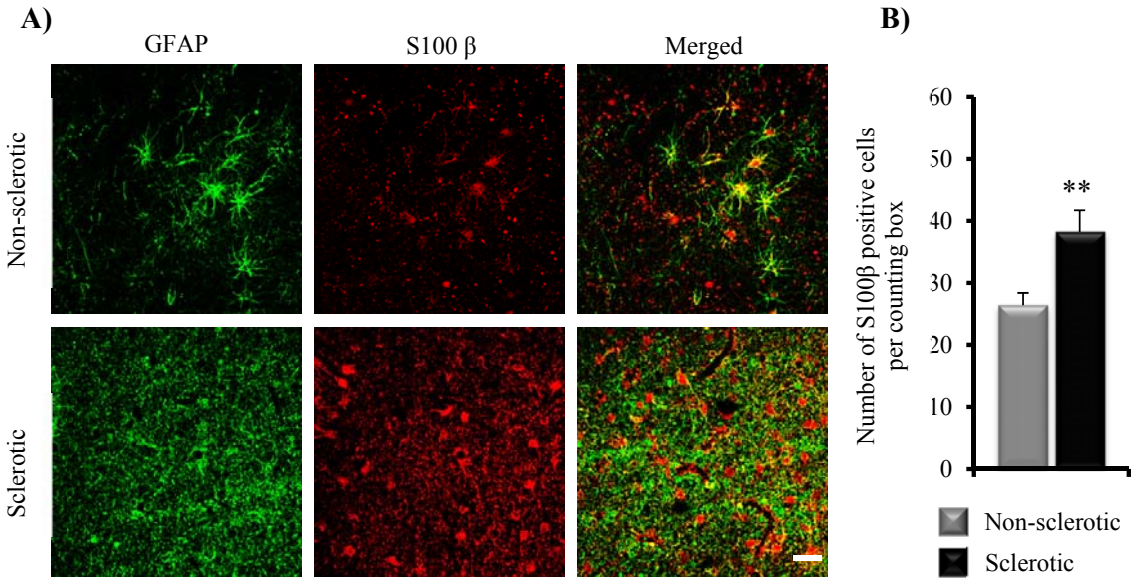

Figure 4.1.1: Astrocytic markers in human hippocampal specimens. A) S100β and GFAP co-immunostaining. Representative images from the sclerotic and non-sclerotic CA1 regions of human specimens are shown. All GFAP positive cells were also S100β positive. Scale bar, 25 µm. B) The bar graph shows that the numbers of S100β positive cells per counting box were significantly higher in the sclerotic hippocampus. Three counting boxes of dimension 184.52 x184.52 x20 μm^3 were positioned in the stratum radiatum of each specimen for counting. (** $p < 0.01$, N = 3 per group).

4.1.2 Cx43 expression is augmented and is preferentially located around blood vessels in sclerosis

Plasma membrane associated connexins are essentially hexamers which can dock with hexamers from neighboring cells to form gap junctions or remain in un-docked (hemichannel) configuration. They are present not only at the junctions between two astrocytic processes, but also in the astrocytic end-feet surrounding blood vessels where they facilitate transport of metabolites from perivascular space to distal places of neuronal activity (Rouach et al., 2008). Connexins in the astrocytic end-feet whether in hemichannel or in gap junctional assemblies, are important components of neurovascular coupling.

Therefore, their distribution at the vascular interface was examined. Antibody staining showed higher Cx43 immunoreactivity in the sclerotic vs. non-sclerotic CA1 region (non-sclerotic, 99.75 ± 40.26 a.u.; sclerotic, 183.03 ± 64.15 a.u.). The enhanced expression was also reflected in the total area occupied by Cx43 immunolabeled structures, which were much larger in the sclerotic CA1 region (468.01 ± 426.55 μm^2) as compared with non-sclerotic (37.88 ± 30.31 μm^2) (N = 6 per group). Thus, the area occupied by Cx43 in sclerotic CA1 was 1235.51 ± 1126.06% that of Cx43 in non-sclerotic (Figure 4.1.2 B). In sclerosis, Cx43 expression was non-uniformly distributed. Immunoreactivity was preferentially seen around blood vessels (Figure 4.1.2 A). To get a quantitative measure of the distinctive pattern of Cx43 immunoreactivity, a distribution ratio was defined as the ratio of the mean Cx43 staining intensity around blood vessels to the mean intensity of the remaining CA1 area (Chapter 3, section 3.3.7). In non-sclerotic specimens this ratio was 1.07 ± 0.24 (N = 6), suggesting a uniform distribution of Cx43. In contrast, a ratio of 1.83 ± 0.47 (N = 6) was obtained in the sclerotic CA1 region, confirming the non-uniform immunoreactivity pattern. Most of the perivascular Cx43 immunoreactivity was not co-localized with the blood vessel marker lectin (Figure 4.1.2 A). To further characterize the Cx43 staining patterns, Cx43 plaque number and average size were determined. In sclerotic CA1, both of these parameters exceeded those in the non-sclerotic CA1 region (plaque numbers, 5493.84 ± 3992.15 vs. 885.05 ± 708.49; average plaque size, 0.06 ± 0.09 μm^2 vs. 0.04 ± 0.004 μm^2, respectively).

A)

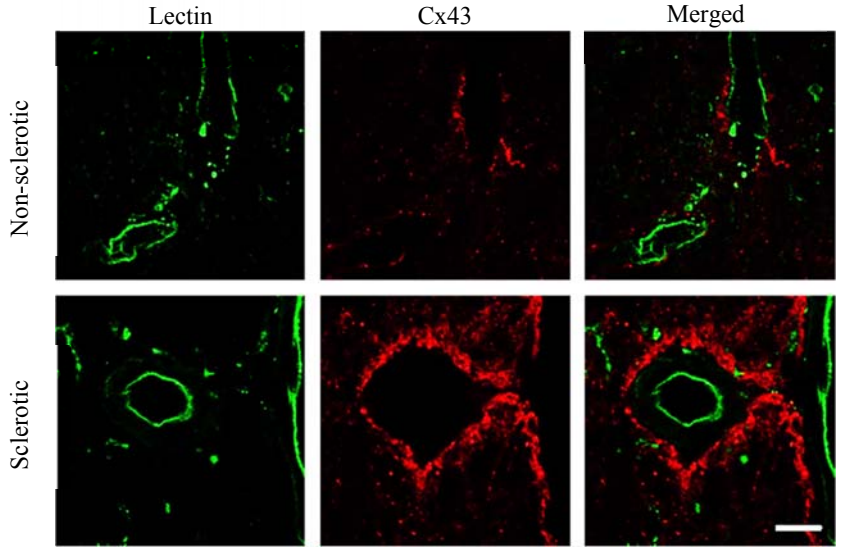

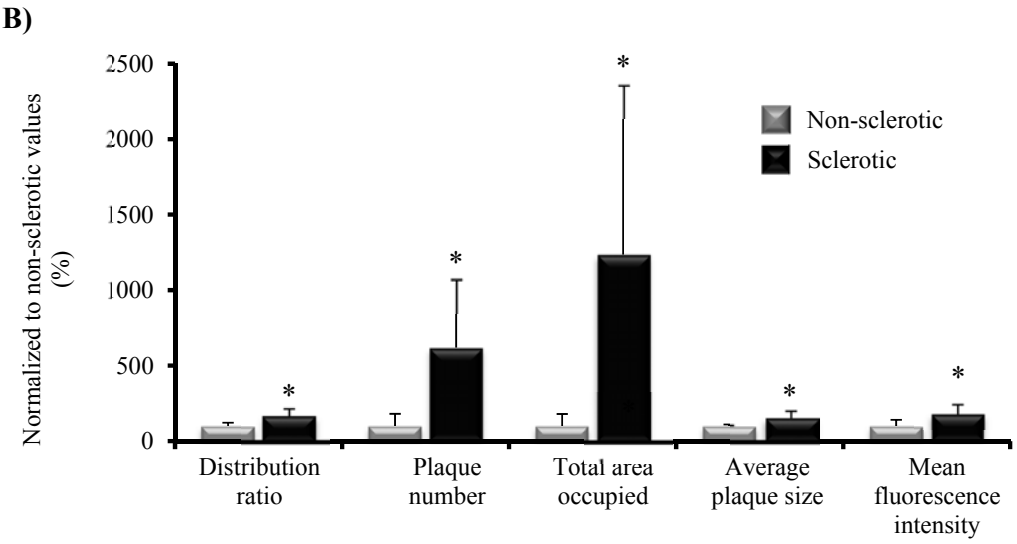

Figure 4.1.2: Cx43 expression and stereology in human hippocampal specimens. A) Lectin and Cx43 immunostaining. Single stack images were taken from the CA1 region of sclerotic and non-sclerotic hippocampi. Note the up-regulation and distribution of Cx43 around the lectin positive blood vessels. Cx43 was not co localized with lectin. Scale bar, 10 µm. **B)** Bar graph showing the quantification of the Cx43 plaques. There was a significant increase in the total number of plaques (620.74 ± 451.06%), area occupied by plaques (1235.51 ± 1126.06%), average plaque size (156.43 ± 42.86%) and average fluorescence intensity (183.49 ± 64.31%) in the sclerotic hippocampus. The distribution ratio was also significantly elevated in the sclerotic hippocampus (170.88 ± 43.55%) indicating altered distribution of Cx43. All values are expressed as a percentage over non-sclerotic (* $p < 0.05$, N = 6 per group).

4.1.3 Cellular localization of Cx43 in the human epileptic hippocampus

In the central nervous system, Cx43 is expressed mainly in astrocytes. Pericytes, which are part of the brain-vascular interface have been described to express Cx43 at least in retinal pericyte cultures (Li et al., 2003). Therefore, co-localization Cx43 with pericyte markers NG2 and PDGFRβ was assessed. Most of the Cx43 immunoreactivity was not found to be co-localized with either of these markers (Figure 4.1.3 A and B). Cx43 accumulation around the endothelial cells observed earlier (Figure 4.1.2) was also evident around pericytes as both of these cells have the same basement membrane (Abbott et al., 2006). Thus, majority of perivascular Cx43 puncta were not localized in endothelial cells or pericytes, leaving the possibility of its expression in astrocytic endfeet only. Indeed, the redistributed Cx43 around the vasculature was present in close proximity with S100β (Figure 4.1.3 C). Although S100β, which is a cytosolic protein, has mainly been used to visualize the cell body and main processes of astrocytes, this protein can also be used to visualize end-feet (Söderqvist et al., 2015) (Steiner et al., 2007).

Altogether, this data indicated that the up-regulated Cx43 in the vicinity of vasculature is not extra-astrocytic but it is present in astrocytic endfeet.

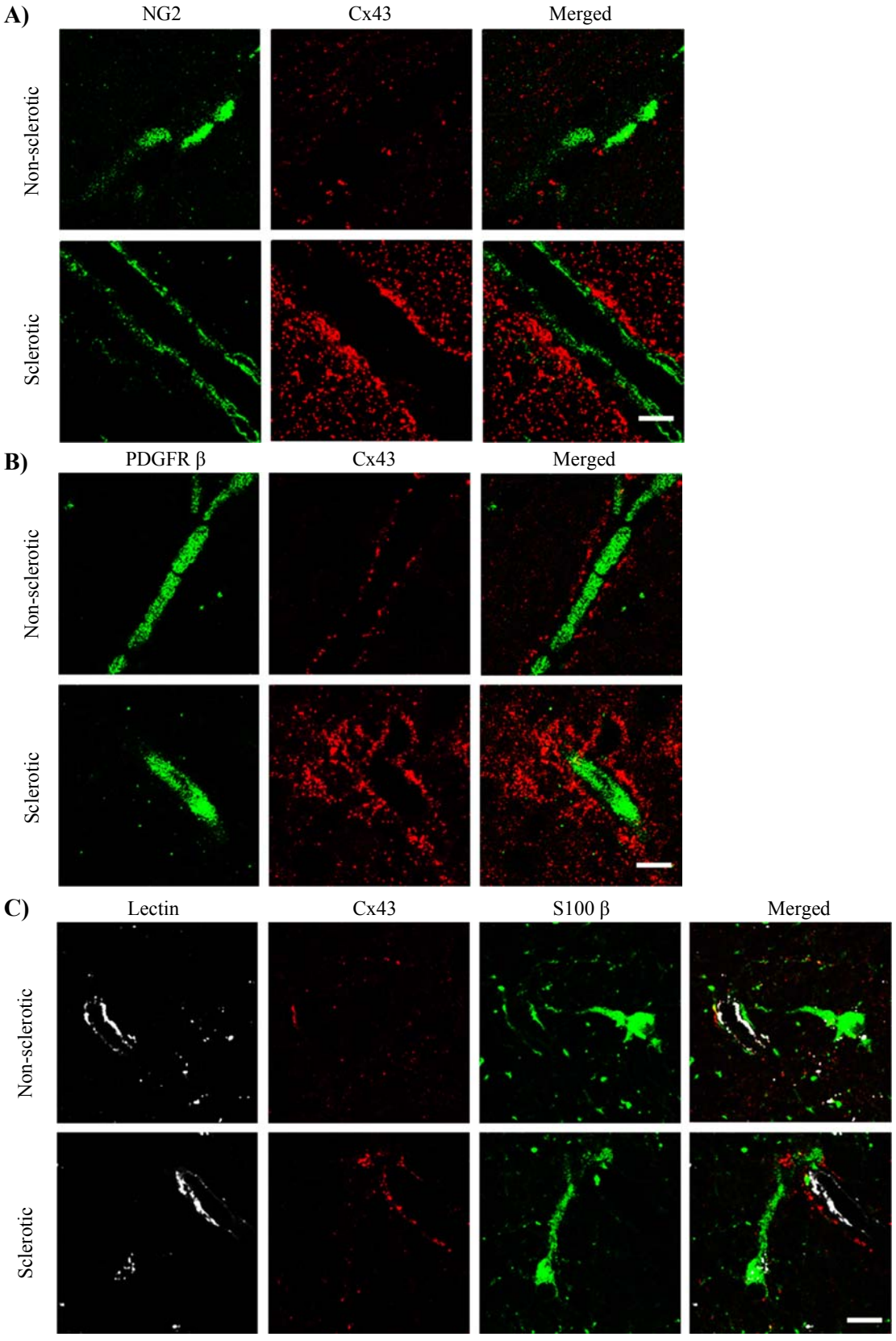

Figure 4.1.3: Cellular localization of Cx43 in the CA1 region. A) Cx43 and NG2 immunostaining. Cx43 was not co-localized with NG2. Some Cx43 puncta were seen in close contact with NG2 positive pericytes. **B)** Cx43 and PDGFRβ immunostaining. Note the distribution of Cx43 around PDGFRβ positive pericytes. Cx43 did not co-localize with PDGFRβ. **C)** Cx43, S100β and Lectin immunostaining. S100β positive astrocytic end-feet surround the lectin positive blood vessels in both non-sclerotic and sclerotic hippocampi. In the sclerotic hippocampus, Cx43 expression around the blood vessels was increased and it was in close proximity with S100β. Scale bar, 10 µm.

4.1.4 Expansion microscopy revealed a detailed structure of the blood vessel–gap junction interface

As described in section 4.1.1 and 4.1.2, the sclerotic CA1 region was characterized by a mesh-like appearance of diffuse GFAP staining and enhanced accumulation of Cx43 around blood vessels, respectively. Confocal microscopy images shown in Figure 4.1.3 indicated that most of the Cx43 immunoreactivity was astrocytic. However, this conventional diffraction limited microscopy was unable to resolve the fine details of blood vessel-gap junction interface. In order to circumvent this limitation, a recently developed expansion microscopy (ExM) technique was employed (Chen et al., 2015)(Chozinski et al., 2016). Briefly, this technique involves embedding the immunostained tissue slices in a polyacrylamide gel followed by enzymatic digestion and expansion in deionized water. An expansion factor defined as the ratio of gel dimensions after and before expansion was determined for each specimen (average expansion factor 4.57 ± 0.67, N = 16). There was no difference in the average expansion factors of sclerotic and non-sclerotic specimens (4.36 ± 0.75, N =8 for sclerotic vs. 4.74 ± 0.53, N =8 for non-sclerotic). ExM allowed assignment of the location of Cx43 with respect to the vessel and endfoot in much detail than with the standard confocal microscopy (Figure 4.1.4.1). Most of the Cx43 in the perivascular space was found to be present on the parenchymal side of the astrocytic endfoot (Figure 4.1.4.1, arrows) as GFAP or S100β separated the Cx43 signal from the vessel wall. Cx43 formed large plaques around blood vessels in both, the sclerotic and the non-sclerotic CA1 regions. However, in the sclerotic CA1, the accumulation of Cx43 was more pronounced as compared to that in the non-sclerotic condition. Importantly, many of the Cx43 puncta were found to be hemmed between GFAP positive processes (solid arrows, Figure 4.1.4.2) even in the sclerotic specimens. A minor proportion of Cx43 immunoreactivity of relatively smaller puncta size was found to be present in close association with endothelial cells (dotted-arrows, Figure 4.1.4.2 and Figure 4.1.4.3). Pericytes on the other hand faced large Cx43 plaques mainly on the parenchymal side (solid arrows, Figure 4.1.4.3).

It can be concluded that, although the majority of perivascular Cx43 immunoreactivity was astrocytic, a minor endothelial and pericytic expression of Cx43 cannot be ruled out.

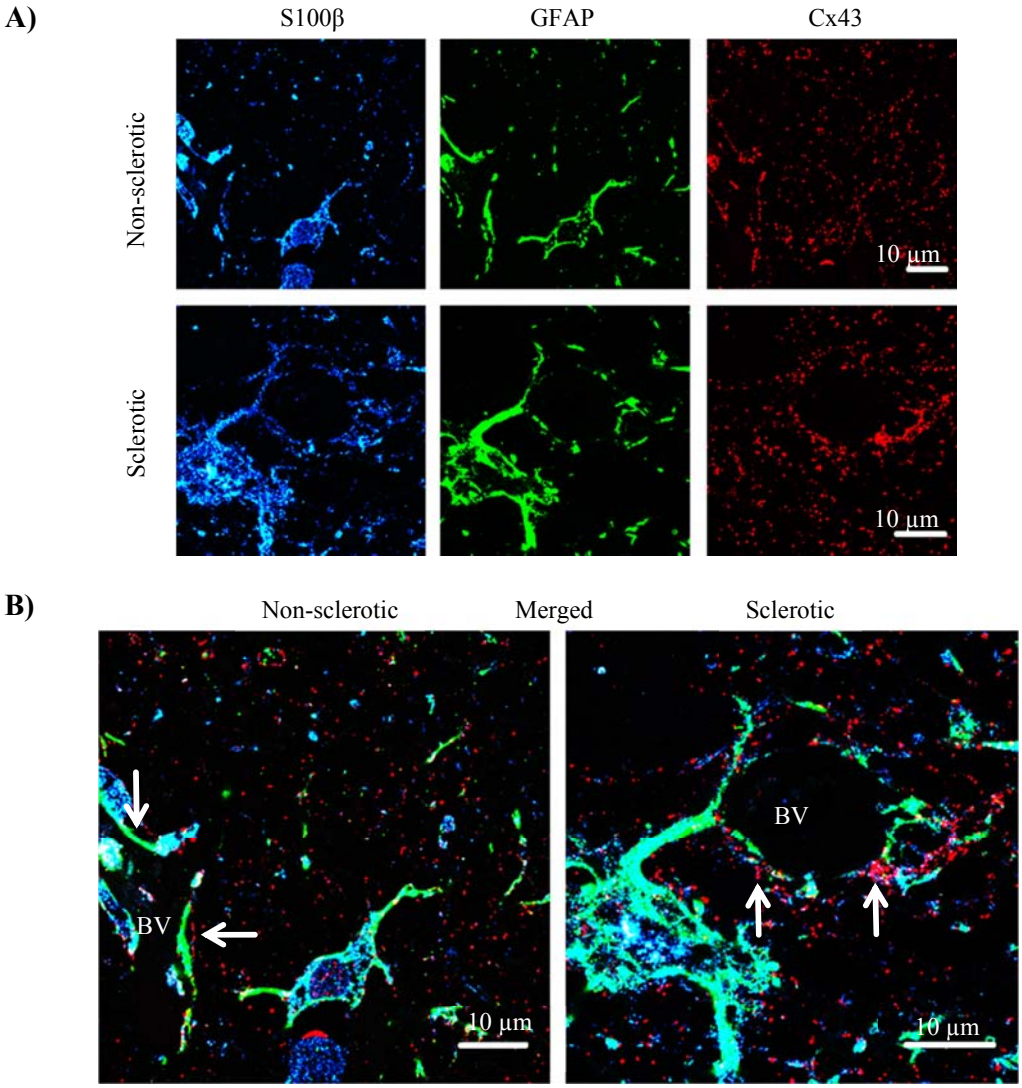

Figure 4.1.4.1: Expansion microscopy images displaying S100β-GFAP-Cx43 immunostaining in the CA1 region. Panel A) shows individual channels while panel B) shows merged images. Blood vessels (BV) were identified by observing each specimen in bright-field mode of the microscope. Astrocytic cell bodies with endfeet approaching a blood vessel can be seen in non-sclerotic and sclerotic specimens. Cx43 formed large plaques near endfeet. Their accumulation in perivascular space was increased in the sclerotic tissue. In both of the hippocampi, majority of the Cx43 plaques were localized on the parenchymal sides of the endfeet (arrows). The scale bars show expansion adjusted distances in µm.

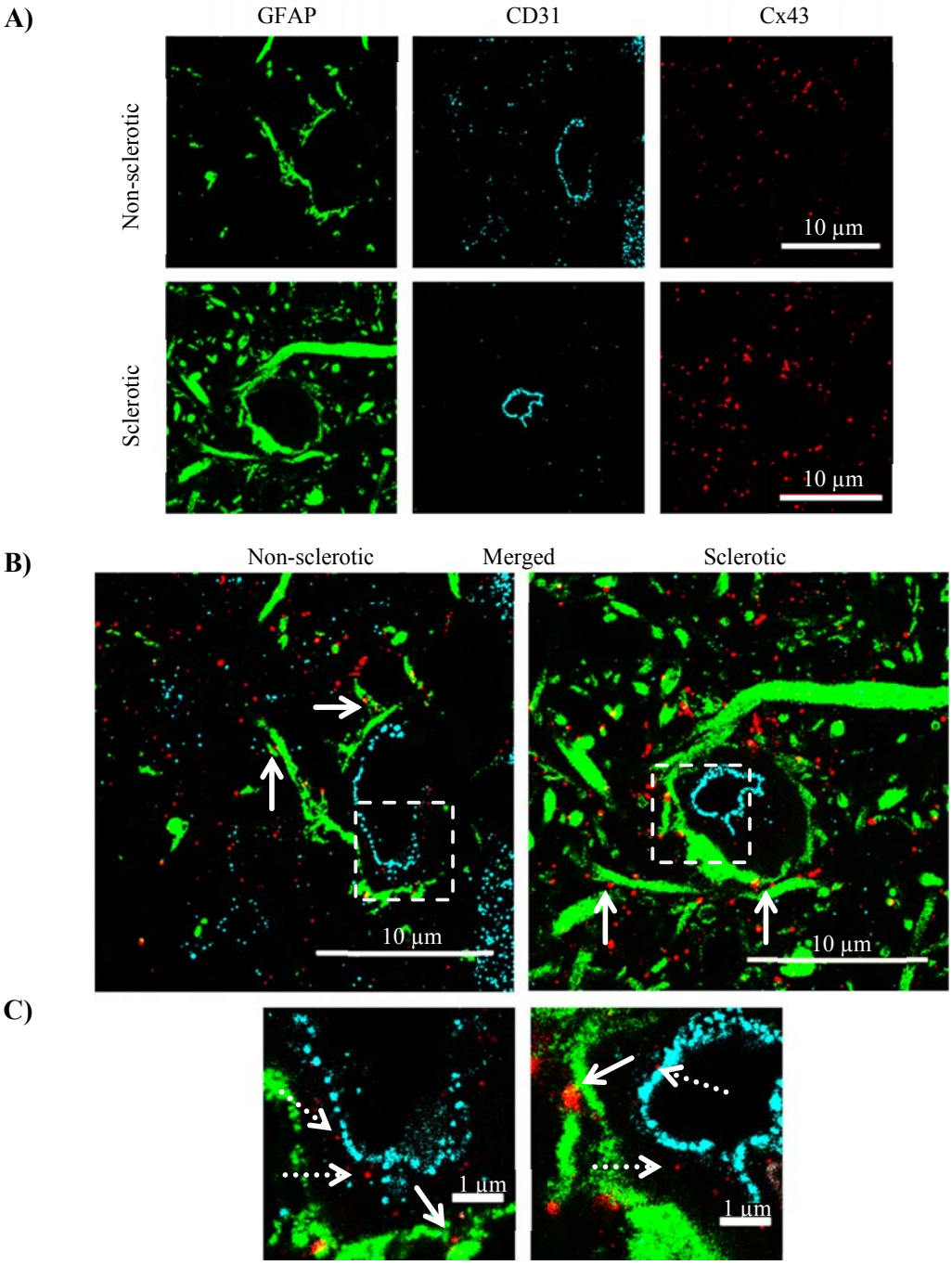

Figure 4.1.4.2: Expansion microscopy images displaying GFAP-CD31-Cx43 immunostaining in the CA1 region. Individual channels can be seen in panel A). Panel B) shows merged images while panel C) shows enlarged view of images indicated in the dashed boxes. CD31 positive endothelial cells can be seen surrounded by GFAP positive astrocytic endfeet. GFAP and Cx43 immunoreactivities were increased in the sclerotic specimens. Some of the Cx43 positive puncta were found to be present between astrocytic processes (solid arrows) in both groups. Although the majority of the Cx43 immunoreactivity was associated with GFAP, some relatively smaller Cx43 puncta were seen in the perivascular space, in close association with CD31 (dotted arrows). The scale bars show expansion adjusted distances in µm.

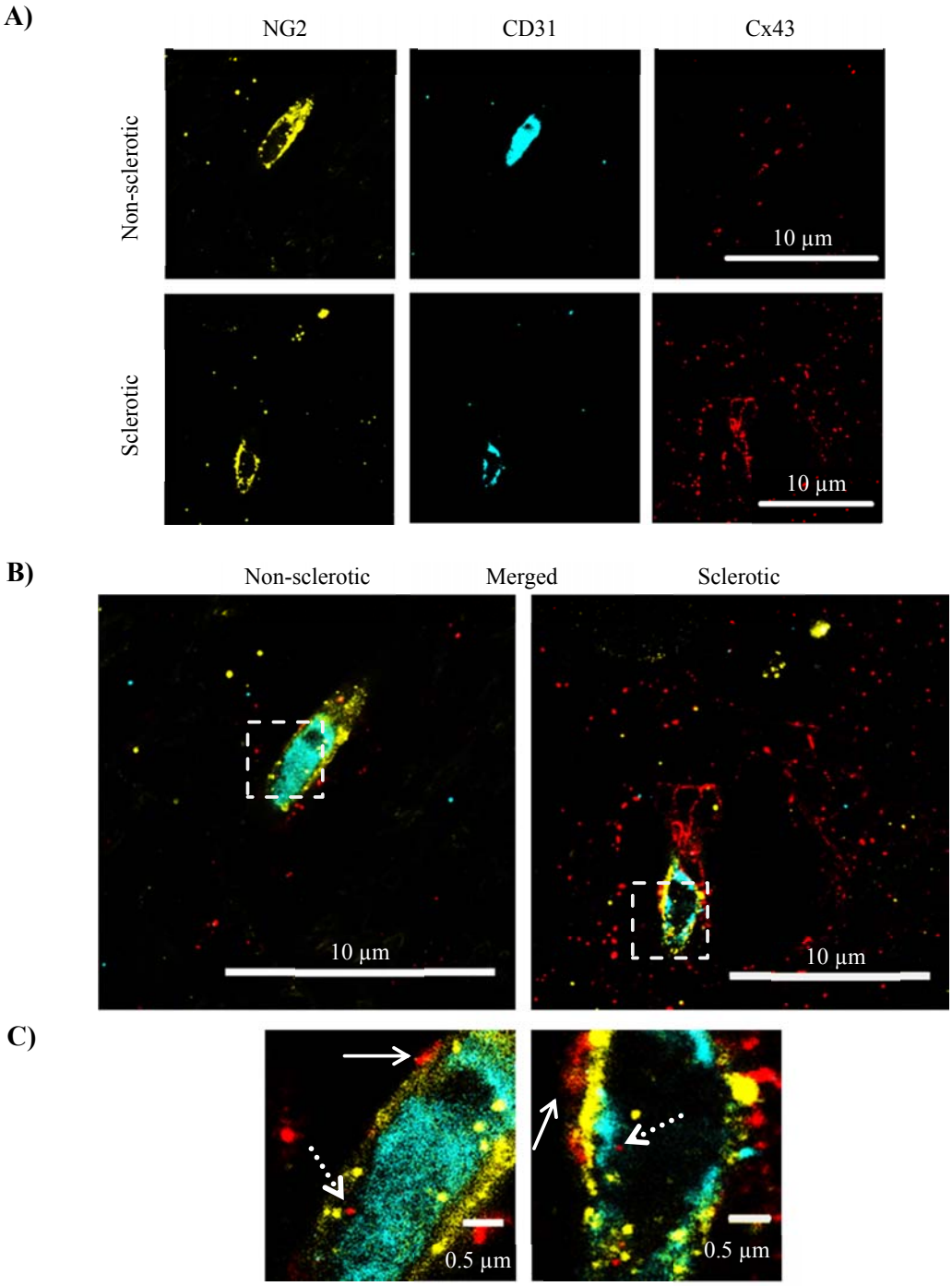

Figure 4.1.4.3: Expansion microscopy images displaying NG2-CD31-Cx43 immunostaining in the CA1 region. Individual channels can be seen in panel A). Panel B) shows merged images while panel C) shows enlarged view of images indicated in the dashed boxes. NG2 positive pericytes can be seen surrounding CD31 positive endothelial cells. The majority of the Cx43 immunoreactivity did not colocalize with NG2 or CD31. Some of the Cx43 plaques on the parenchymal side of the vessel were in close contact with pericytes (solid arrows) in both specimens. A minority of relatively smaller Cx43 puncta were seen in close association with CD31 (dotted arrows). The scale bars show expansion adjusted distances in µm.

4.1.5 Plasma membrane Cx43 levels are similar between sclerotic and non-sclerotic hippocampi

Dislocalization of connexin or its removal from the plasma membrane has been hypothesized as one of the mechanisms of loss of gap junction coupling (Malone et al., 2007). Tissue lysates from human specimens were enriched for the plasma membrane fractions (Chapter 3, section 3.3.9). These fractions were analyzed by Western blotting for expression of Cx43 and Cx30 (Figure 4.1.5 A). Cx43 immunoblot showed 3 distinct bands around 40 kDa representing different phosphorylation and conformational states while Cx30 showed a single band at 30 kDa. E-cadherin levels are indicative of total protein amounts which were loaded onto the gel. Plasma membrane Cx43 levels were similar in non-sclerotic and sclerotic hippocampi (Cx43/E-cadherin ratio 4.43 ± 2.22, N = 5 and 3.35 ± 0.90, N= 6, respectively), despite complete loss of functional coupling in sclerotic specimens (Bedner et al., 2015). The fractional contribution of the different phospho-bands of Cx43 (P0, P1 and P2) was also not different between sclerotic and non-sclerotic conditions, suggesting a similar phosphorylation status of the C-terminus. Similarly, the normalized expression levels of Cx30 were not different between sclerotic (Cx30/E-cadherin ratio 0.14 ± 0.04, N = 6) and non-sclerotic hippocampi (Cx30/E-cadherin ratio 0.16 ± 0.14, N = 5). In conclusion, the enhanced total Cx43 levels in human sclerotic specimens as seen in immunofluorescence analysis did not lead to increased assembly of Cx43 channels in the plasma membrane, indicating its impaired translocation.

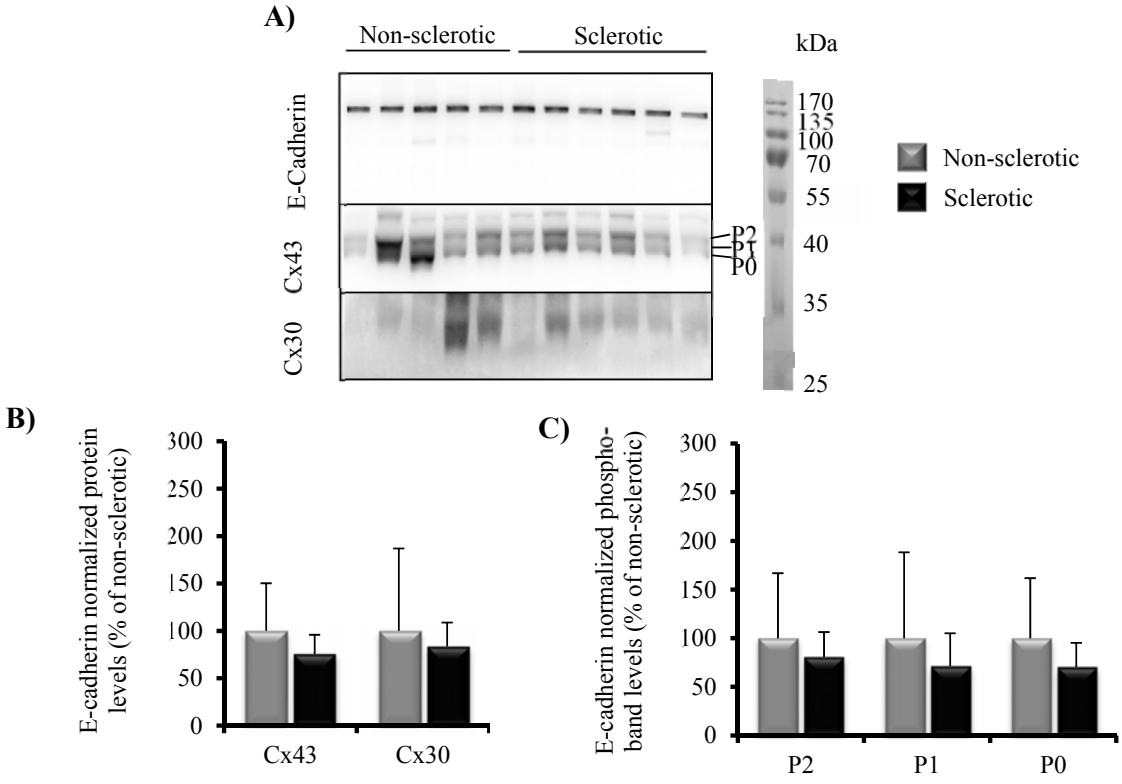

Figure 4.1.5: Plasma membrane associated connexins. A) Representative immunoblots showing Cx43, Cx30 and loading control E- cadherin. Plasma membrane associated proteins were selectively isolated from the human hippocampal specimens. Five µg of protein were loaded in each well. **B)** The bar graph shows the quantification of total Cx43 and Cx30 levels which were not significantly altered in the sclerotic hippocampus as compared with non-sclerotic hippocampus. **C)** Quantification of the phospho-bands. All phospho-bands (P2, P1 and P0) were similar between sclerotic and non-sclerotic hippocampi.

4.1.6 Total (whole-cell) Cx43 levels are increased in sclerosis

Stereological analysis performed on immuno-stained sections revealed increased Cx43 plaque size in sclerotic hippocampus when compared with the non-sclerotic hippocampus. There was also an increase in the intensity of the Cx43 immuno-labelling, indicating increase in the overall expression of Cx43 (Figure 4.1.2 B). However, Western blot analysis of plasma membrane proteins displayed no difference in the Cx43 levels (Figure 4.1.5 B). In order to assess the discrepancy, total (whole-cell) Cx43 protein levels were checked by Western blotting. Whole-cell protein lysates were obtained by homogenizing hippocampal specimens from epileptic patients. These lysates were subjected to SDS PAGE followed by Western blotting. The resultant blotted membranes were probed for Cx43, Cx30, E-cadherin and GAPDH (as a loading control) (Figure 4.1.6A). GAPDH was used as a loading control since its protein levels are proportional to the total protein present in the sample and are known to be unchanged in epilepsy (Becker et al., 2002). GAPDH normalized Cx43 protein levels were significantly higher ($N = 4$ per group, $p < 0.01$) in the sclerotic hippocampus as compared with the non-sclerotic hippocampus (7.89 ± 1.79 vs. 4.43 ± 0.94) (Figure 4.1.6 B). The increased Cx43 level in the sclerotic hippocampus was 178.12 % of the non-sclerotic hippocampus. There was no significant difference in phospho-band levels between the two groups. Similarly, Cx30 (sclerotic: 0.46 ± 0.22; non-sclerotic: 0.55 ± 0.20) and E-cadherin (sclerotic: 0.12 ± 0.027; non-sclerotic: 0.10 ± 0.013) levels were not significantly different between the two groups. Thus, total Cx43 expression is enhanced in the sclerotic hippocampus. On the other hand, the plasma membrane Cx43 levels were similar between sclerotic and non-sclerotic hippocampi. The data thus indicate that there was an inefficient or disproportional localization of Cx43 to the plasma membrane.

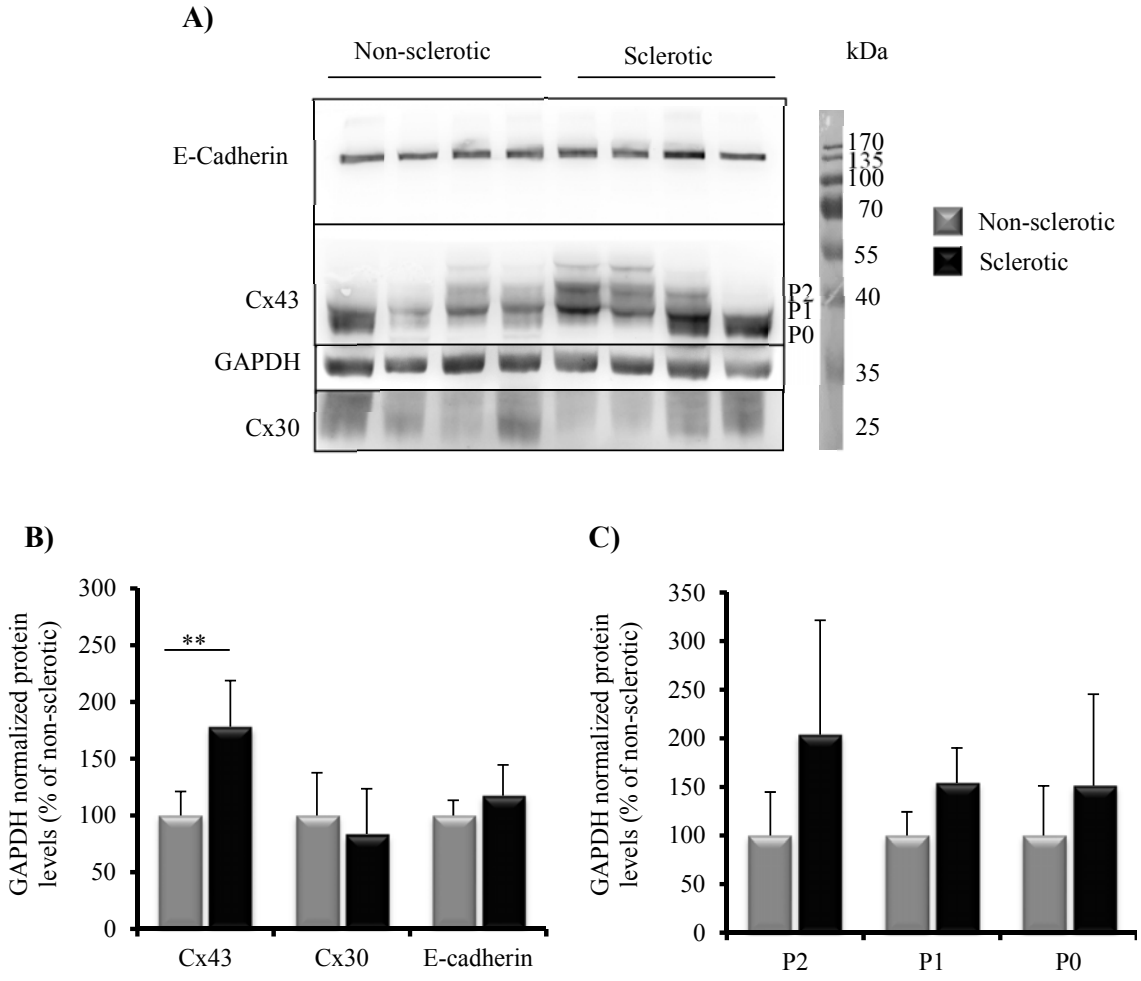

Figure 4.5.6: Western blot of total connexins, in sclerotic and non-sclerotic human hippocampus. **A)** Representative immunoblots showing E-cadherin, Cx43, GAPDH (loading control) and Cx30. Total (Whole-cell) protein lysates were obtained by homogenizing hippocampal specimens surgically resected from epileptic patients, in a lysis buffer containing detergents (section 3.3.8). Thirty µg of the proteins from each sample were subjected to SDS-PAGE followed by Western blotting. **B)** The bar graph shows that the total amount of Cx43 in the sclerotic hippocampus was significantly higher than that in the non-sclerotic hippocampus (178.12% ± 40.6 %, $p < 0.01$, N = 4 each group). No significant difference was found in E-cadherin and Cx30 protein levels in the two groups. **C)** The Cx43 blot was further analyzed for the phospho-isoforms which did not differ between the two groups.

4.1.7 Phosphorylation of the plasma membrane Cx43 is altered

The total gap junctional conductance between any two cells is influenced by the total number of gap junctions channles between them and unitary conductance and open probability of those channels (Moreno, 2005). The total Cx43 present at the plasma membrane as assessed by Western blotting and the plaque number as assessed by immunofluorescence are indicative of the possibility of gap junction formation. There was an increase in the Cx43 plaques (Figure 4.1.2 B) despite of lack of coupling in the sclerotic hippocampus (Bedner et al., 2015). Moreover, the plasma membrane connexin levels were similar between the two groups (Figure 4.4.3). Therefore, phosphorylation of Cx43 which is known to affect the gap junctional coupling was investigated. Phosphorylation of Cx43 by MAPKs on serine 255 is known to reduce the open probability of channels (Cottrell et al., 2003). On the other hand, when Cx43 is phosphorylated on serine 368, gap junctional conductance is reduced (Lampe et al., 2000). To evaluate the phosphorylation on these two sites, 5 µg of the plasma membrane lysates were subjected to SDS-PAGE followed by Western blotting and then probed with phospho-specific antibodies directed against P-Cx43 S255 and P-Cx43 S368. P-Cx43 S255 and P-Cx43 S368 antibodies identified 3 bands between 40 and 55 kDa, similar to the bands obtained by phosphorylation unspecific Cx43 antibody (Figure 4.1.7 A). Phospho-Cx43 band intensities were divided by total Cx43 band intensities to get the fraction of total Cx43 that is phosphorylated on the given serine residue. The P-Cx43 S255 fraction was significantly elevated in the sclerotic hippocampus (0.15 ± 0.043 ($N = 6$)) as compared with non-sclerotic hippocampus (0.09 ± 0.041 ($N = 5$), $p < 0.05$). There was no significant difference in P-Cx43 S368 fraction between the two groups (Figure 4.1.7 B). Thus, phosphorylation of Cx43 at serine 255 but not at serine 368 is increased in human hippocampal sclerosis. This change in the phosphorylation might contribute to the observed uncoupling possibly via a reduced open probability of the Cx43 channels.

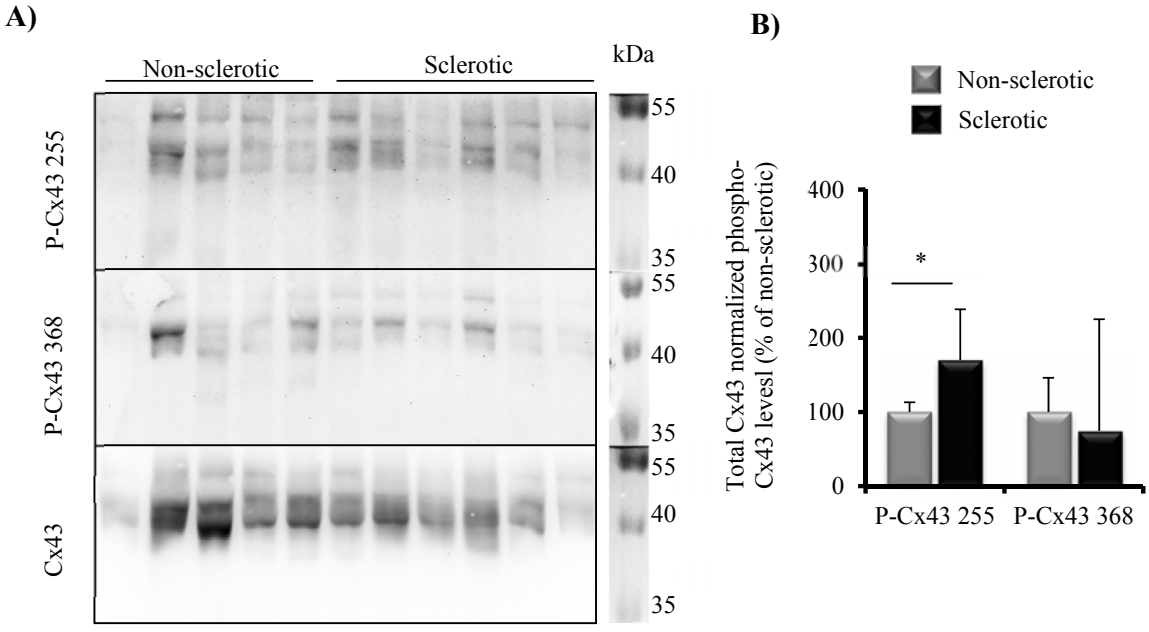

Figure 4.1.7: Western blot using phospho-specific antibodies. A) Plasma membrane protein lysates form human hippocampi were investigated for Cx43 phosphorylated on serine 255 and serine 368. The membrane used for detection with phospho-specific antibodies was further probed with phosphorylation unspecific Cx43 antibody. **B)** Quantification of Western blots performed using total Cx43 as a loading control. Phospho-Cx43 band intensities were divided by total Cx43 band intensities and expressed as a percentage of non-sclerotic mean values. The P-Cx43 S255 fraction was significantly elevated (169.72 ± 48.47 %) in sclerotic hippocampi. However, P-Cx43 S368 fractions were not significantly different between the two groups. (* $p < 0.05$, N = 5 for non-sclerotic and N = 6 for sclerotic group).

4.1.8 Cx43 distribution is associated with albumin extravasation in the sclerotic hippocampus

BBB breakdown characterized by albumin extravasation has been implicated in epileptogenesis (Vliet et al., 2007) (Ivens et al., 2007a). Therefore, albumin immunoreactivity in the vicinity of blood vessels was checked in human epileptic hippocampi. Albumin leakage around the vasculature was found to be a prominent feature of hippocampal sclerosis only. Extra-vascular immunoreactivity was almost absent in non-sclerotic hippocampi indicating intact BBB in contrast with the leaky vasculature of sclerotic hippocampi (Figure 4.1.8). Intraventricular albumin administration has been shown to disrupt astrocytic coupling (Braganza et al., 2012). It remains to be demonstrated whether the observed astrocytic uncoupling in the sclerotic hippocampus is due to albumin in the brain parenchyma.

Nevertheless, albumin immunoreactivity around the blood vessels followed a pattern similar to that of Cx43 distribution observed earlier (Figure 4.1.2).

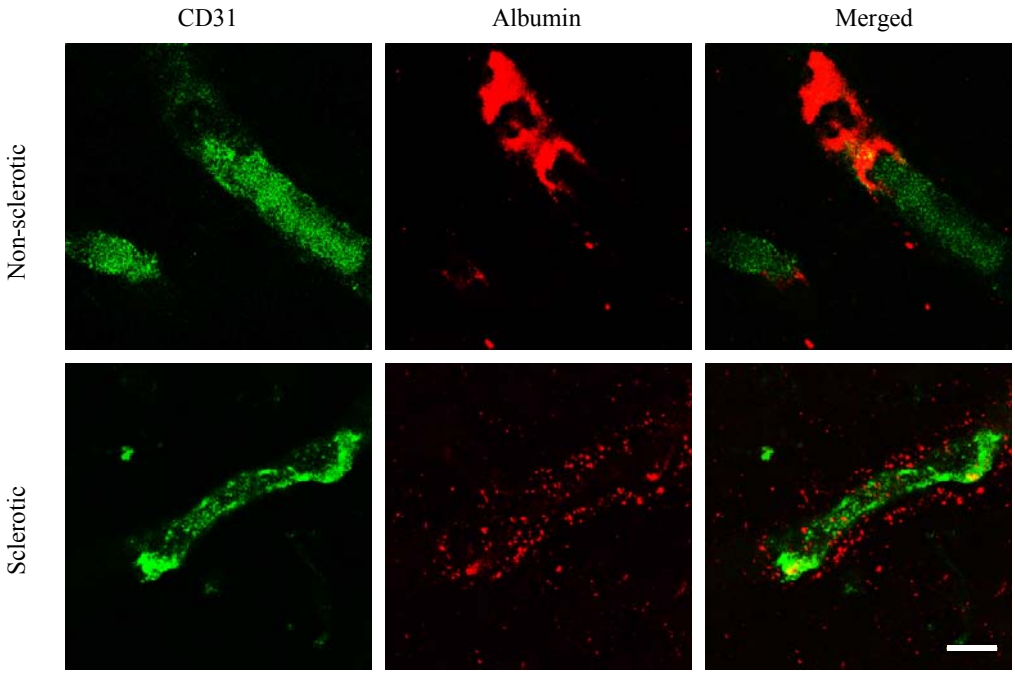

Figure 4.1.8: Albumin extravasation in human hippocampal specimens. CD31 and albumin immunostaining in the CA1 region of human hippocampi. Sclerotic hippocampi displayed prominent extra-luminal albumin immunoreactivity indicating BBB disruption. Scale bar, 10 μm.

4.2 Molecular alterations associated with astrocytic uncoupling, 3 months post kainate injection

Three months post kainate injection, the ipsilateral hippocampus recapitulates many features of human temporal lobe epilepsy with hippocampal sclerosis. These features include loss of CA1 pyramidal neurons, pronounced astrogliosis, granule cell dispersion and lack of inter-astrocytic coupling (Bedner et al., 2015). Possible mechanisms behind astrocytic uncoupling were investigated using immunohistochemistry and Western blotting. Since coupling is still present in the contralateral hippocampus, it was used as a pseudo-control. Data from human epileptic hippocampal specimens indicated possible roles of Cx43 phosphorylation and albumin extravasation, in disruption of astrocytic coupling (Section 4.1.7 and 4.1.8). Therefore, these two aspects were also investigated at the 3 months' time point.

4.2.1 Ipsilateral hippocampus 3 months post kainate injection has increased number of astrocytes

Astrocytic proliferation in epilepsy has been well documented (Niquet et al., 1994) (Hüttmann et al., 2003). The numbers of S100β positive cells were increased in the CA1 region of human sclerotic hippocampus (section 4.1.1). Therefore, for the 3 months' time point, the total number of astrocytes were counted in the CA1 region and compared between ipsilateral and contralateral hippocampi. Coronal sections of the brain were stained with either rabbit polyclonal anti-S100β (Figure 4.2.1 A) or rabbit polyclonal anti-GFAP antibodies (Figure 4.2.1 C). Confocal images from the CA1 region were used for cell counting. There was a significant increase in the total number of S100β-positive cells in the ipsilateral hippocampus (21.33 ± 3.78 in contralateral vs. 45.66 ± 6.65 in ipsilateral hippocampus, N = 3) (Figure 4.2.1 B). The morphology of S100β- and GFAP-positive cells was drastically altered in the ipsilateral hippocampus. The astrocytes in the ipsilateral hippocampus showed enlarged cell bodies and very few primary branches as compared with the astrocytes in the contralateral hippocampus (Figure 4.2.1 A and C).

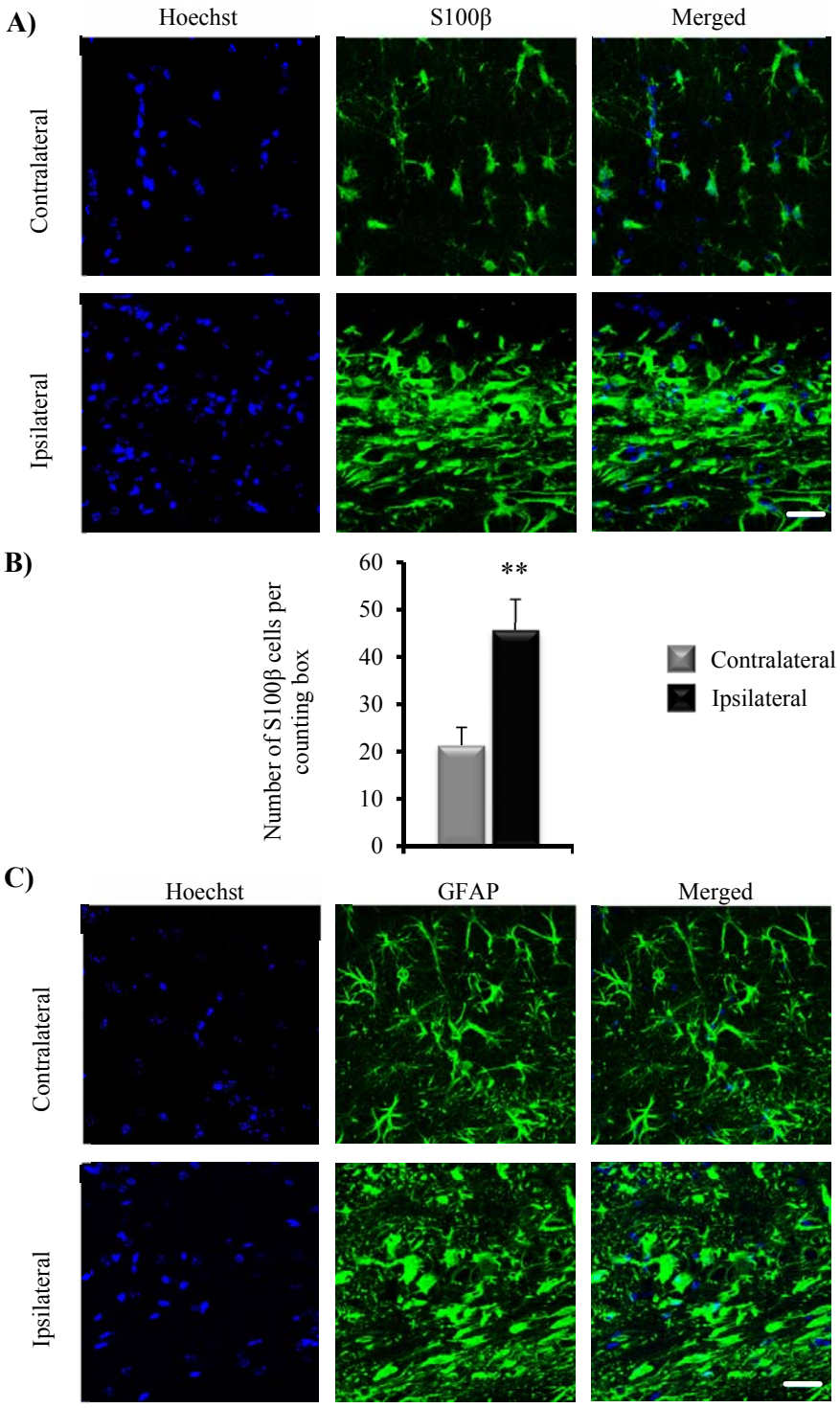

Figure 4.2.1: Astrocytic markers 3 months post kainate injection. A) S100β immunostaining with Hoechst as a nuclear marker. Representative images from the CA1 region, 3 months after kainate injection. Scale bar, 25 µm. **B)** The bar graph shows the number of astrocytes per counting box (184.52 x184.52 x30 μm^3). There was significant increase in the number of astrocytes in the ipsilateral hippocampus as compared with the contralateral hippocampus. (* $p < 0.01$, N = 3 per group). **C)** GFAP immunostaining with Hoechst as a nuclear marker. Note the hypertrophied astrocytes with few primary processes in the ipsilateral hippocampus. Scale bar, 25 µm.

4.2.2 Cx43 expression is augmented 3 months post kainate injection

Cx43 expression and stereology was assessed by immunolabeling with an antibody targeting amino acids 360 to 382 of the Cx43 C-terminal domain. Confocal images from the CA1 region revealed punctate staining patterns in the contralateral hippocampus while the ipsilateral hippocampus showed intense labelling with large aggregates (Figure 4.2.2 A). Indeed, quantification of fluorescence intensity and plaque size showed a significant increase in these two parameters in the ipsilateral hippocampus (203.94 ± 47.07 a.u. and 0.075 ± 0.018 μm^2 respectively) when compared with the contralateral hippocampus (112.41 ± 19.49 a.u. and 0.045 ± 0.002 μm^2 respectively). The increased plaque size was also reflected in the total area occupied by Cx43 and the number of Cx43 plaques (Contralateral: 132.78 ± 49.72 μm^2 and 2696.81 ± 928.18 vs. Ipsilateral: 1131 ± 456.02 μm^2 and 9287.39 ± 3489.04, respectively). Interestingly, Cx43 was found to be preferentially distributed around the blood vessels. This pattern of Cx43 expression was quantified by means of a distribution ratio (defined in section 3.3.7 and 4.1.2). The distribution ratio of Cx43 in the ipsilateral CA1 (1.49 ± 0.13) was significantly higher than that in the contralateral CA1 (1.09 ± 0.17) (Figure 4.2.2 B). The redistributed Cx43 was not co-localized with CD31, indicating its absence in the endothelial cells.

A)

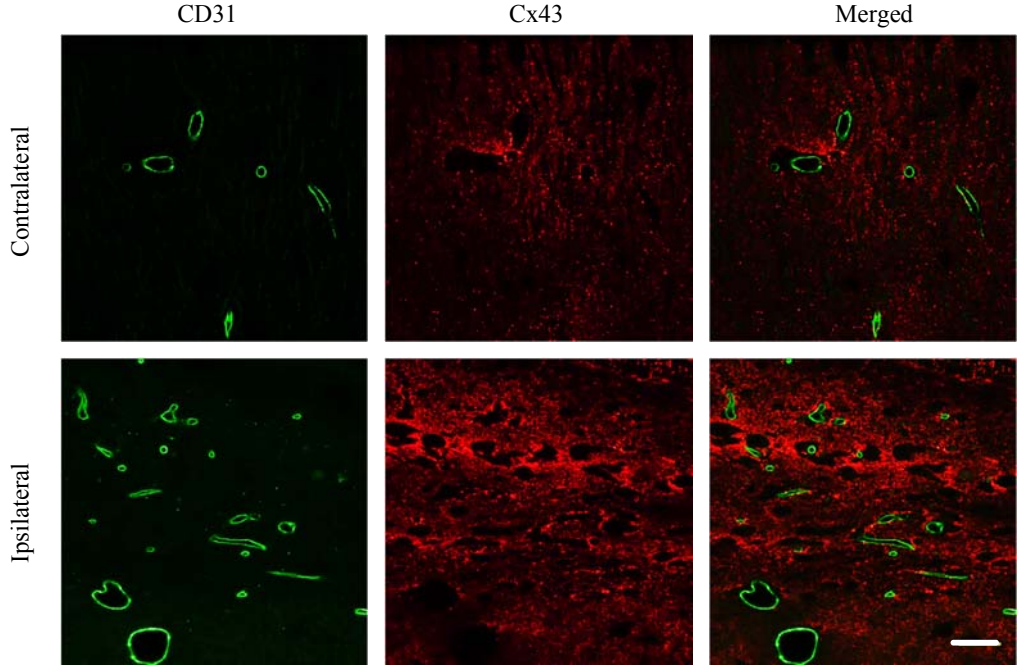

B)

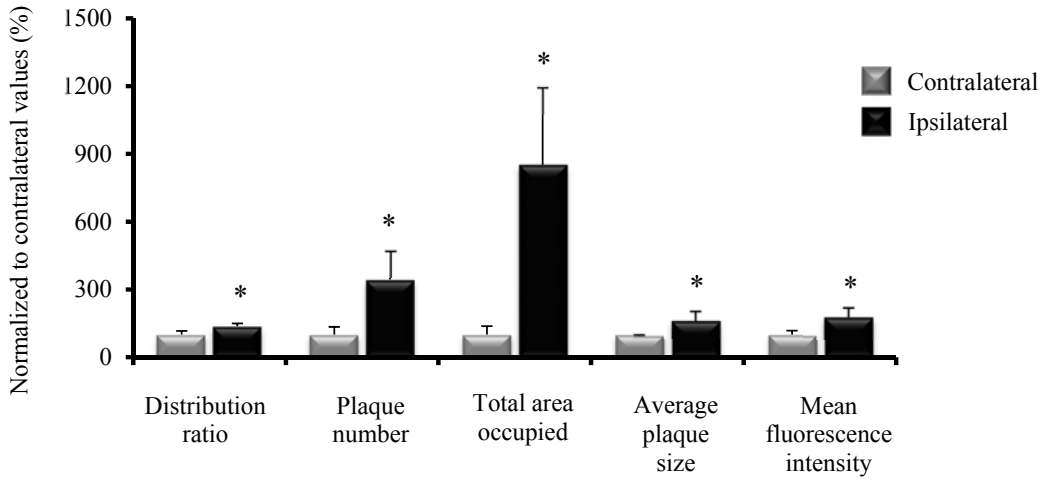

Figure 4.2.2: Cx43 expression and stereology 3 months post kainate injection. A) CD31 and Cx43 immunostaining in the CA1 region, 3 months post kainate injection. Cx43 signal in the contralateral hippocampus is punctate and evenly distributed around the blood vessels and in the rest of the tissue. The ipsilateral hippocampus displays intense, large aggregates of Cx43 preferentially around the blood vessels. **B)** The bar graph shows quantification of Cx43 plaques. There was a significant increase in the total number of plaques (344.38 ± 129.37%), area occupied by plaques (851.77 ± 343.44%), average plaque size (167.18 ± 41.43%) and average fluorescence intensity (181.42 ± 41.87%) in the ipsilateral hippocampus (all values normalized to contralateral). The distribution ratio in ipsilateral hippocampus was 136.97 ± 12.53% of the contralateral hippocampus, indicating altered Cx43 distribution. * $p < 0.05$, N = 3 per group. Scale bar, 25 µm.

4.2.3 Plasma membrane associated connexins, 3 months post kainate injection

Cx43 has a very short half-life of 1.5 to 5 h as compared with other membrane proteins (Laird et al., 1991)(Beardslee et al., 1998). It is continuously removed from the plasma membrane and replaced by newly synthesized Cx43. Increased total Cx43 levels in the human sclerotic hippocampus did not result in the increased assembly of these proteins at plasma membrane, indicating impaired translocation (Figure 4.1.5 and 4.1.6). Therefore, mouse hippocampi 3 months post kainate injection, were also assessed for plasma membrane associated connexins. The E-cadherin normalized intensities of total Cx43 and Cx30 did not differ between the contralateral and ipsilateral hippocampi (Figure 4.2.3 A and B). However, in the ipsilateral hippocampus, there was a significant increase in the P2 band levels (E-cadherin normalized protein levels, 0.12 ± 0.024 contralateral vs. 0.27 ± 0.053 ipsilateral, $p < 0.01$, N= 4 per group) (Figure 4.2.3 C). It is important to note here that this increase in the ipsilateral P2 band fraction was associated with increased P0 contribution on the contralateral side.

Taken together, the Western blotting data 3 months post kainate not only indicate similar plasma membrane connexin levels between the contralateral and ipsilateral hippocampi but also point out the altered phosphorylation of Cx43.

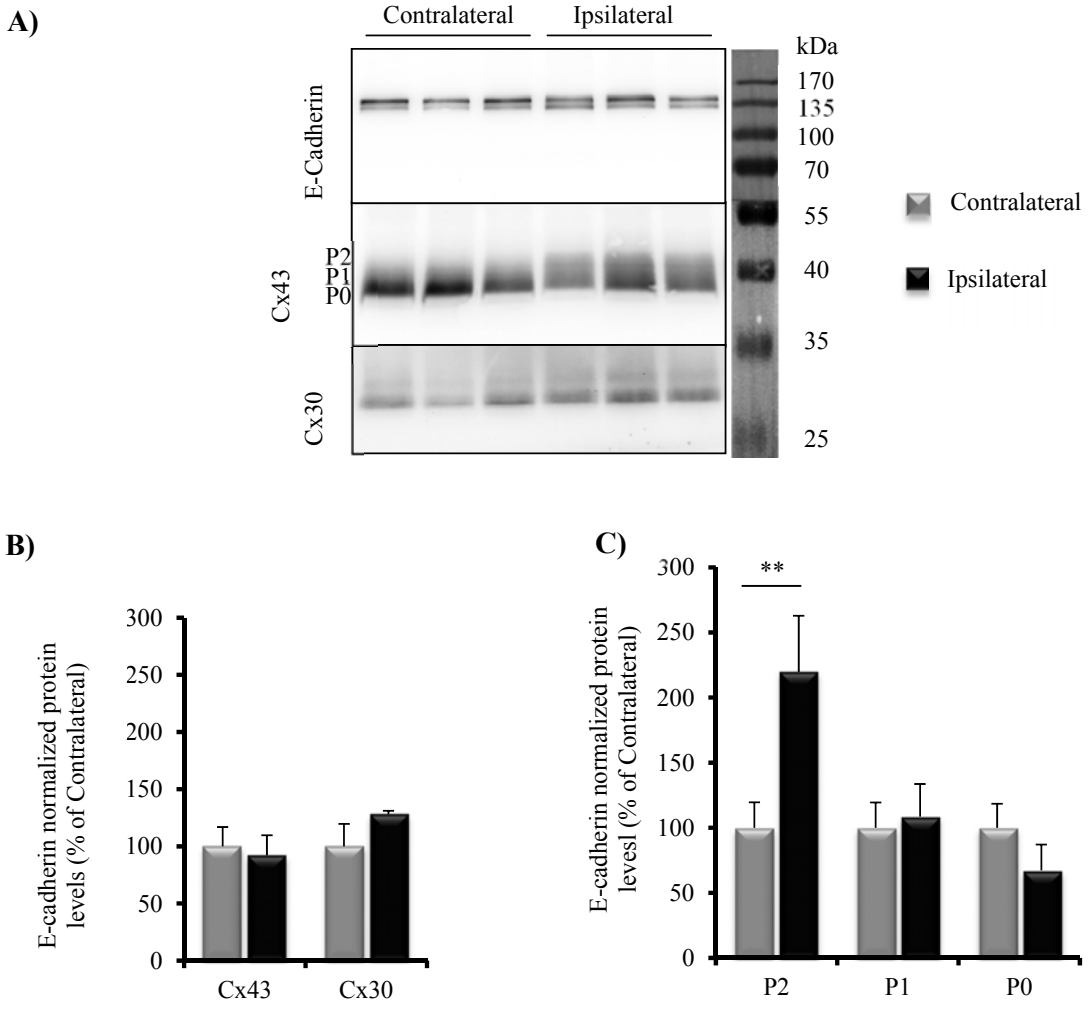

Figure 4.2.3: **Western blot of plasma membrane associated connexins, 3 months post kainate injection. A)** Plasma membrane associated proteins were isolated from dorsal hippocampi. Five µg of protein was loaded in each well. Immunoblots shows Cx43, Cx30 and E-cadherin (as a loading control). **B)** The bar graph shows E-cadherin- normalized protein levels expressed as a percentage of the E-cadherin normalized mean protein value of the contralateral group. Total Cx43 and Cx30 levels were not statistically different between contralateral and ipsilateral hippocampi. **C)** Phospho-bands P2, P1 and P0 were normalized to E-cadherin and then expressed as a percentage of the contralateral group. The P2 band in the ipsilateral hippocampus was 219.5 ± 43.35 % of the contralateral hippocampus ($p < 0.01$, N= 4 in each group). The other isoforms did not differ significantly between the two groups.

4.2.4 Total Cx43 is increased ipsilaterally, 3 months post kainate injection

Stereological analysis performed on immuno-stained sections revealed an increased Cx43 plaque size in the ipsilateral hippocampus, 3 months post kainate injection. There was also an increase in the intensity of the Cx43 immuno-labelling, indicating increase in the overall expression of Cx43 (Figure 4.2.2 B). However, Western blot analysis of plasma membrane proteins displayed no difference in the Cx43 levels (Figure 4.2.3 B). In order to assess the discrepancy between plasma membrane and global Cx43 expression, the total (whole-cell) Cx43 protein levels were checked by Western blotting. Dorsal hippocampi were harvested from mice, 3 months after kainate injection. Whole-cell protein lysates obtained by homogenizing the hippocampi were subjected to SDS PAGE followed by Western blotting. The resultant blotted membranes were probed for Cx43, Cx30, E-cadherin and GAPDH (as a loading control) (Figure 4.2.4 A). GAPDH-normalized Cx43 protein levels were significantly higher ($N = 4$ per group, $p < 0.01$) in the ipsilateral hippocampus (3.19 ± 0.50) as compared with contralateral hippocampus (2.18 ± 0.38) (Figure 4.2.4 B). The increased Cx43 levels in the ipsilateral hippocampus were $146.63 \pm 23.14\%$ of the contralateral hippocampus. This increase was primarily provided by significantly enhanced P2 band levels (0.21 ± 0.07 contralateral vs. 0.48 ± 0.16 ipsilateral, $N= 4$, $P < 0.05$) (Figure 4.4.4 C). In contrast, Cx30 (contralateral: 0.22 ± 0.04; ipsilateral: 0.31 ± 0.13) and E-cadherin (contralateral: 1.52 ± 0.73; ipsilateral: 1.44 ± 0.30) levels were not significantly different between the two groups. Thus, only the total Cx43 (and not the plasma membrane Cx43) expression is enhanced in the ipsilateral hippocampus. The data also indicate that there was an inefficient or disproportional localization of Cx43 to the plasma membrane, since the latter showed unchanged expression of Cx43 despite of enhanced total cellular Cx43 expression.

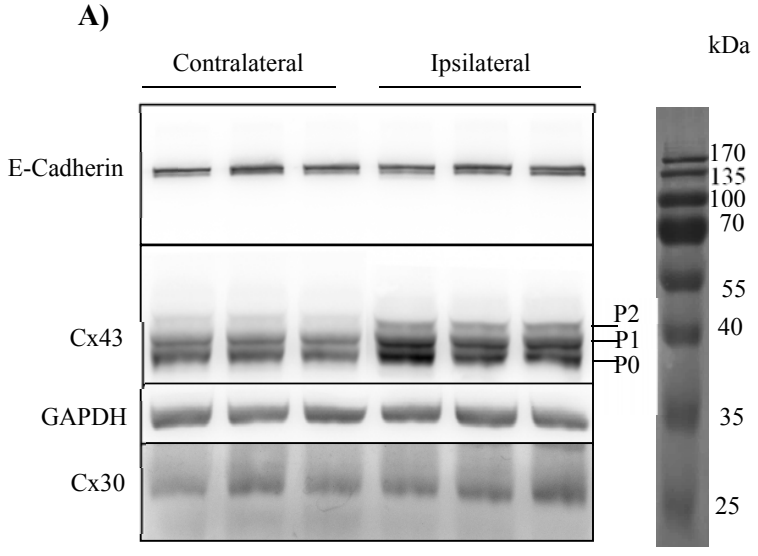

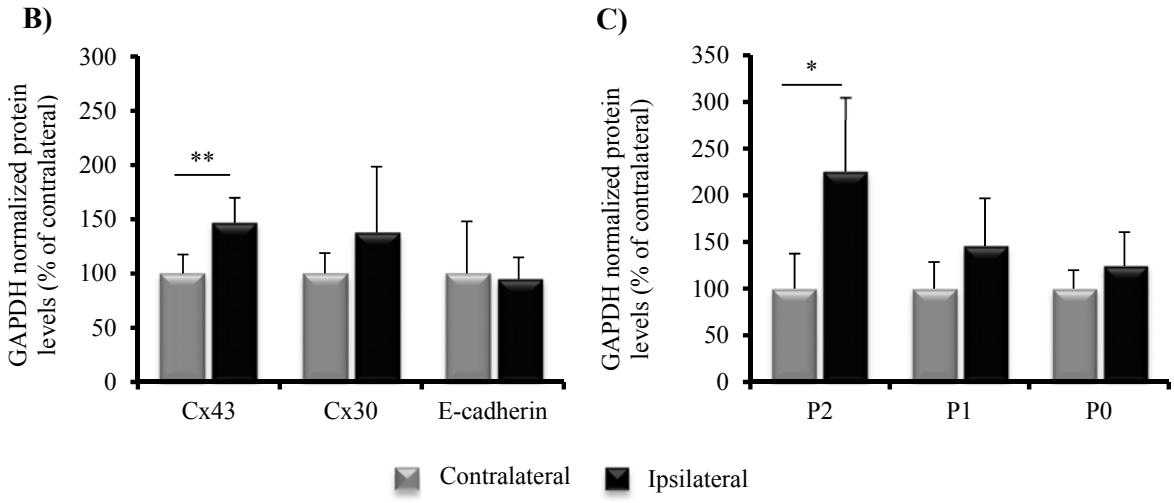

Figure 4.2.4: Western blot of total connexins, 3 months post kainate injection A) Total (Whole-cell) protein lysates were obtained by homogenizing dorsal hippocampi 3 months post kainate injection, in a lysis buffer containing detergents. Thirty µg of the proteins from each sample were subjected to SDS-PAGE followed by Western blotting. Representative immunoblots showing E-cadherin, Cx43, GAPDH (loading control) and Cx30. **B)** The bar graph shows that the total amount of Cx43 in the ipsilateral hippocampus was significantly higher than the contralateral hippocampus (146.6 ± 23.14% of the contralateral hippocampus, $p < 0.01$, N = 4 each group). No significant difference was found in E-cadherin and Cx30 protein levels between the two groups. **C)** Cx43 blot was further analyzed for phosphorylated bands. There was a significant increase in the P2 band of the ipsilateral hippocampus (225.03 ± 79.39 % of the contralateral hippocampus, $p < 0.05$, N= 4 in each group).

4.2.5 Ipsilateral Cx43 displays enhanced phosphorylation on serine 255 and 368, 3 months post kainate injection

There was an increase in Cx43 plaques despite of lack of coupling in the ipsilateral hippocampus; 3 months post kainate injection (Figure 4.2.2). The plasma membrane connexin levels were unaffected at this time point (Figure 4.2.3 B). However, Western blot indicated a change in the phosphorylation of Cx43 (Figure 4.2.3 C). Earlier analyses on human hippocampal samples had shown increased phosphorylation on S255 (but not on S368) of Cx43. Therefore, these sites were further investigated in the mouse model. 5 µg of plasma membrane lysates from mouse hippocampi, 3 months post kainate injection were subjected to SDS-PAGE followed by Western blotting and then probed with phospho-specific antibodies directed against P-Cx43 S255 and P-Cx43 S368. P-Cx43 S255 and P-Cx43 S368 antibodies identified one band between 40 and 55 kDa contrary to phosphorylation unspecific Cx43 antibody which identified 3 characteristic bands around 40 kDa (Figure 4.2.5 A).

Phospho-Cx43 band intensities were divided by total Cx43 band intensities to get the fraction of total Cx43 that is phosphorylated on the given serine residue. Both P-Cx43 S255 (0.067 ± 0.023 vs. 0.033 ± 0.004, N = 4 per group, $p < 0.05$) and P-Cx43 S368 (0.059 ± 0.018 vs. 0.012 ± 0.005, N = 4 per group, $p < 0.01$) fractions were significantly elevated in ipsilateral hippocampi (Figure 4.2.5 B). This altered phosphorylation profile of Cx43 might account for the observed uncoupling via reduced open probability and unitary conductance of the gap junction channels.

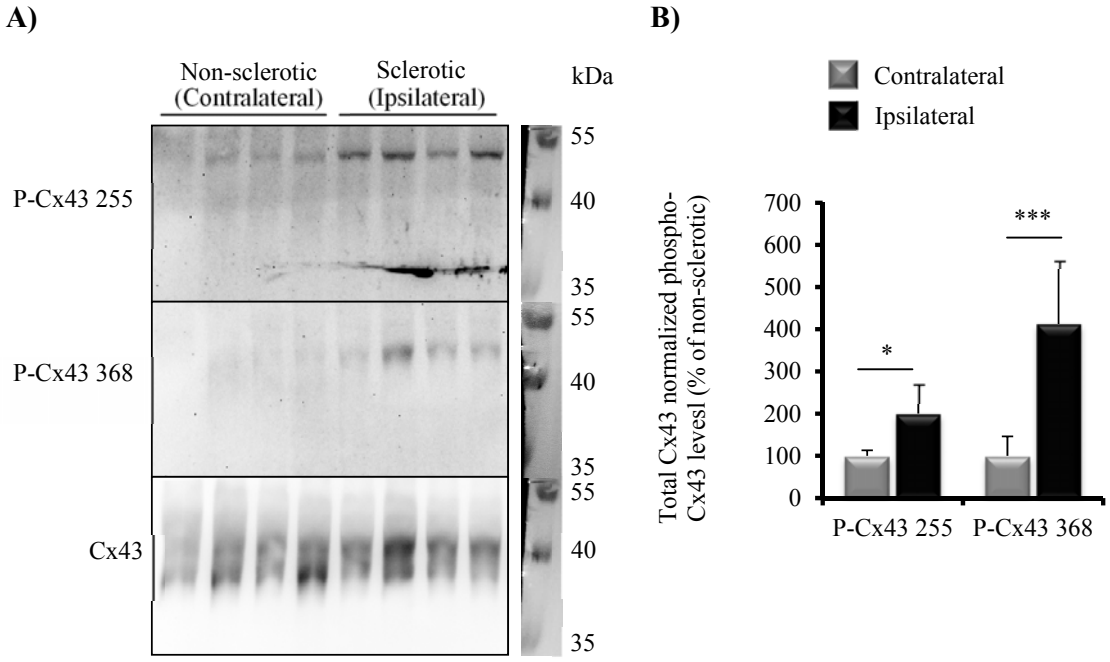

Figure 4.4.5: Western blot using phospho-specific antibodies. **A)** Three months after kainate injection, plasma membrane protein lysates form mouse hippocampi were investigated for Cx43 phosphorylated on serine 255 and serine 368. The membrane used for detection with phospho-specific antibodies was further probed with phosphorylation unspecific Cx43 antibody. P-Cx43 S255 and P-Cx43 S368 antibodies identified 1 band between 40 to 55 kDa contrary to phosphorylation unspecific Cx43 antibody which identified 3 bands around 40 kDa. **B)** Quantification of Western blots using total Cx43 as a loading control. Phospho-Cx43 band intensities were divided by total Cx43 band intensities and expressed as a percentage of contralateral mean values. Both P-Cx43 S255 and P-Cx43 S368 were significantly elevated in the ipsilateral hippocampus when compared with the corresponding contralateral hippocampus. Percentage of these two phospho-Cx43 proteins in the ipsilateral hippocampus over the contralateral group were 200.05 ± 68.83% and 412.4 ± 150.62% respectively (** $p < 0.01$, *** $p < 0.001$, N = 4 per group).

4.2.6 BBB disruption and albumin extravasation differs between ipsilateral and contralateral hippocampi

Even a single episode of epileptic seizure is sufficient to transiently open the BBB (Vliet et al., 2007). Serum proteins thus leak out of the vasculature and diffuse into the brain parenchyma. Local differences in inflammation might modulate the BBB permeability (Phares et al., 2006). Ipsilateral and contralateral hippocampi 3 months post kainate injection were shown to differ in the degree of astrogliosis (Figure 4.2.1). Therefore, it was evaluated whether these hippocampi also differ in BBB disruption and subsequent albumin extravasation. Coronal sections of the brain were stained with goat polyclonal anti-albumin antibody. Confocal images from the CA1 region revealed that the albumin immunoreactivity was present only in ipsilateral hippocampi of kainate injected mice while contralateral hippocampi in the same mice were devoid of any albumin signal (Figure 4.2.6). Interestingly, the blood vessels themselves lacked albumin immunoreactivity as the mice brains were perfused with PBS prior to fixation. Importantly, the albumin immunoreactivity was not restricted to perivascular space in the ipsilateral hippocampus. It was observed throughout the CA1 region indicating diffusion of albumin into the region away from the vasculature.

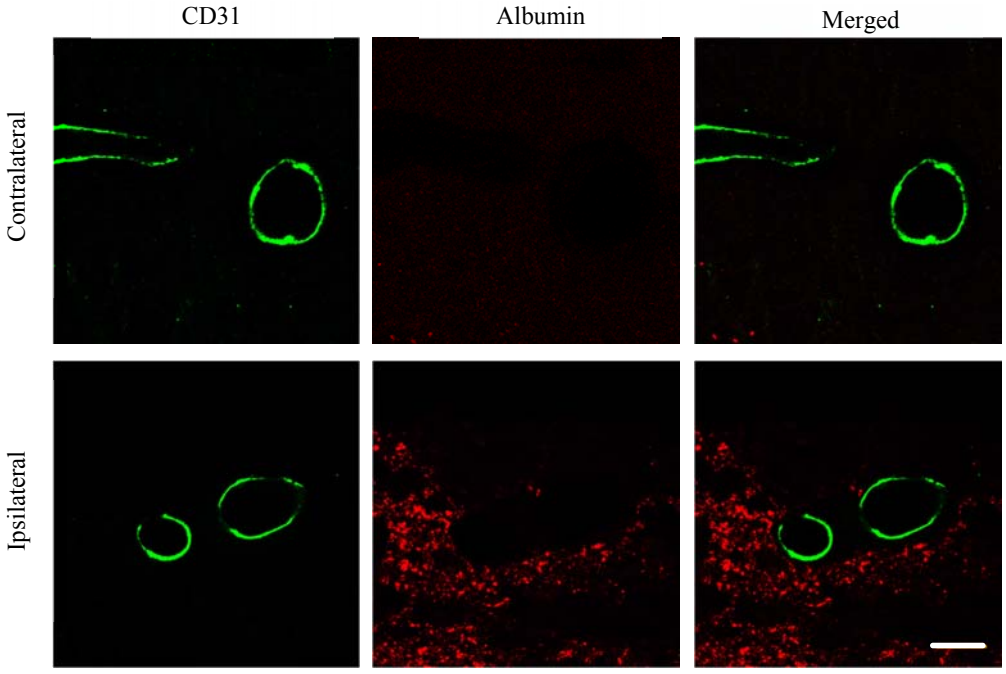

Figure 4.4.6: Albumin extravasation 3 months post kainate injection. CD31 and albumin immunostaining in the CA1 region. Ipsilateral hippocampi showed noticeable albumin immunoreactivity indicating BBB disruption. Scale bar, 10 µm.

4.2.7 Oligomerization of Cx43

Connexins as monomers do not form gap junctions. 6 connexins oligomerize to form a structure called connexon and two connexons from the neighbouring cells dock on each other to form a gap junction. There are various mechanisms that control the gating of a gap junctional channel. These mechanisms are functional only on a fully formed gap junction. Therefore, oligomerization of connexin was studied to check whether fully formed gap junctions exist in an epileptic hippocampus. For this purpose, a technique called 'blue native PAGE' (BN PAGE) was employed. Briefly, plasma membrane associated proteins from dorsal hippocampi were isolated and solubilised in a buffer that preserves protein interactions (Materials and methods, Section 3.3.11). Five µg of proteins were loaded on a native gradient gel. Proteins were given a uniform negative charge by the dye coomassie G250. As a result, the protein complexes got separated based on their molecular weights. After separation, proteins from the gel were electrophoretically transferred to a PVDF membrane and visualized with anti-Cx43 antibody. Line scans of the resultant blot revealed 4 peaks corresponding to 4 bands at different molecular weights (Figure 4.2.7 A and B). These bands represented different possible oligomerization states of Cx43. When molecular weights of 146, 240 and 516 kDa were plotted against the possible number of Cx43 molecules forming oligomers, 3, 6 and 12 respectively, it resulted in a straight line (Figure 4.2.7 C). Thus, band at 516 kDa represented a putative dodecameric configuration of Cx43. A horizontal line scan through this band showed a significant reduction in the ipsilateral hippocampus (Figure 4.2.7 D). The data indicated that the docking of connexon pairs might be impaired in the ipsilateral hippocampus.

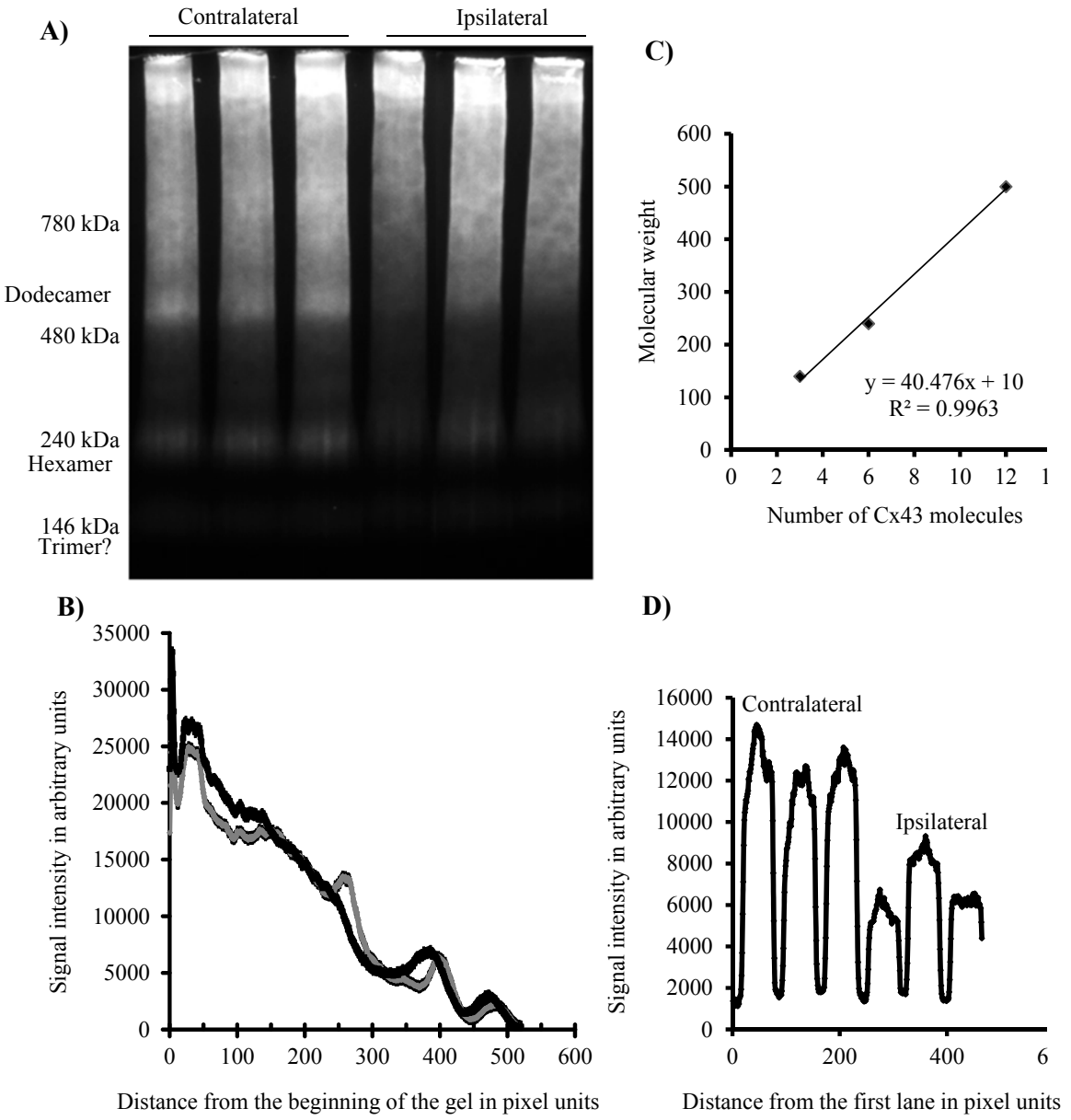

Figure 4.4.7: Blue Native PAGE followed by Western blot. A) Plasma membrane preparations of the dorsal hippocampi were obtained from mice 3 months after kainate injection. Cx43 immunoblots shows a spread across the lane with prominent bands at 240 and 500 kDa. **B)** Vertical line scans with Cx43 intensity on Y axis and distance in pixel units on the X axis. Note the peaks in the plot, representing putative oligomers. **C)** Plot of observed molecular weight of peaks and possible number of Cx43 molecules forming oligomer. **D)** Horizontal line scans through the 500 kDa (dodecamer) band, showing decreased intensity in the ipsilateral hippocampus.

4.3 Molecular alterations associated with astrocytic uncoupling 4 h post kainate injection

In the human sclerotic hippocampus and the mouse ipsilateral hippocampus 3 months post kainate injection, both of which represent chronic epilepsy, astrocytic coupling is completely absent (Bedner et al., 2015). In contrast, the coupling is only partially lost at 4 h post kainate injection. At this time point, astrocytic coupling is reduced by ~50 % (Bedner et al., 2015). However, apoptotic neurons are absent in ipsilateral and contralateral hippocampi. Thus, 4 h after kainate injection represents an early phase of epileptogenesis in which loss of astrocytic coupling might contribute to the neuronal death in subsequent phases. Possible mechanisms behind this observed uncoupling were investigated using immunohistochemistry and Western blotting. The underlying hypothesis was - seizure-induced alterations in astrocytic connexins lead to uncoupling. In addition to the effects on connexins, changes in astrocyte morphology were analyzed using stereological techniques.

4.3.1 Astrocytic markers at the onset of seizures

S100β and GFAP are two widely used markers for astrocytes (Sofroniew and Vinters, 2010). Two antibodies targeting distinct epitopes were used to label each of these proteins. One of these antibodies was monoclonal while the other one was polyclonal. The purpose of using two antibodies was to enhance the probability of detection of the target proteins, in case one of the antibodies failed to bind to its epitope.

4.3.1.1 S100β immunoreactivity is lost following kainate injection

Coronal sections of the brain 4 h post kainate injection were stained with mouse monoclonal and rabbit polyclonal anti-S100β antibodies. Confocal images revealed almost complete mutual co-localization of the signals from these two antibodies in the contralateral hippocampus (Figure 4.3.1.1 A). On the ipsilateral side, none of the antibodies labelled any cellular structures, especially in the SR region of the hippocampus (Figure 4.3.1.1 A). However, other regions of the brain, for example cortex and thalamus, showed normal S100β labelling (images not shown). Interestingly, the loss of immunoreactivity was specific to the ipsilateral hippocampus underneath the injection site (dorsal hippocampus). S100β signal was regained in the ipsilateral hippocampus distal from the injection site (Figure 4.3.1.1 B).

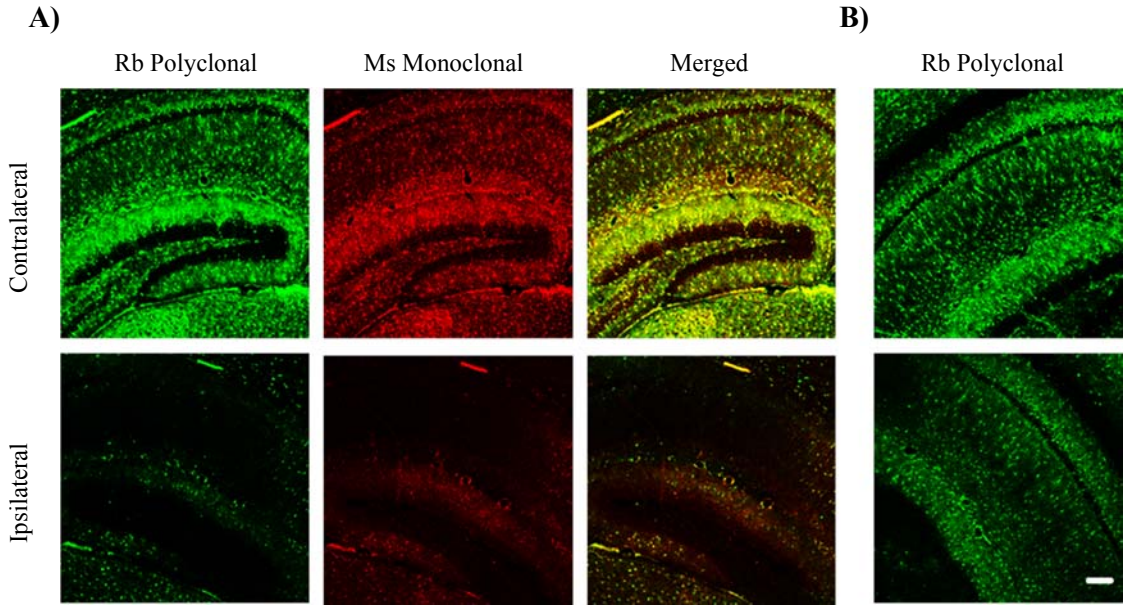

Figure 4.3.1.1: S100β immunostaining 4 h post kainate injection using antibodies targeting two different epitopes. A) S100 β immunostaining using monoclonal and polyclonal antibodies. In the contralateral hippocampus, there was an almost complete overlap of the signals from the two anti-S100 β antibodies. The signal was absent in the SR region of the ipsilateral hippocampus. **B)** S100β signal was regained in the ipsilateral hippocampus distal from the injection site. Scale bar, 100 µm.

4.3.1.2 Reduced number of astrocytes and altered astrocyte morphology, 4 h post kainate

In order to check if the absence of S100β immunoreactivity indicated loss of astrocytes, GFAP immunostaining was performed. As mentioned earlier, antibodies with two different epitopes were used to probe GFAP in the coronal sections. Signals from mouse monoclonal and rabbit polyclonal antibodies showed mutual co-localization (Figure 4.3.1.2 A) in both contralateral and ipsilateral hippocampi. Thus, astrocytes were indeed present in the ipsilateral hippocampus, contrary to the findings from S100β immunostaining (see Discussion, section 5.4). Further, GFAP positive structures co localizing with the nuclear marker Hoechst were counted in 184.52 x 184.52 x 30 μm^3 counting boxes in the SR region (Figure 4.3.1.2 B). There was a reduction of 27.9 % in the total number of astrocytes (15.1 ± 1.6 in contralateral hippocampus vs. 10.9 ± 1.4 in ipsilateral hippocampus, N = 6). This decline in the number of astrocytes paralleled a similar 24.4 % decrease in the number of nuclei in the same region (35.9 ± 3.9 in contralateral hippocampus vs. 27.1 ± 2.7 in ipsilateral hippocampus, N = 6). The number of primary branches per astrocyte was also significantly reduced on the ipsilateral side as compared with the contralateral side (7.2 ± 1.4 in contralateral hippocampus vs. 3.9 ± 1.1 in ipsilateral hippocampus, total 24 cells from 3 mice) (Figure 4.3.1.2 C). Thus, the overall morphology of astrocytes was drastically altered. However, the area occupied by GFAP signal,

was similar between the two groups (Figure 4.3.1.2 C), indicating reorganization of the cytoskeleton without reduction in GFAP protein levels. This was further confirmed with Western blot which revealed no significant difference in the GFAP protein levels (Figure 4.3.1.2 D, N =6).

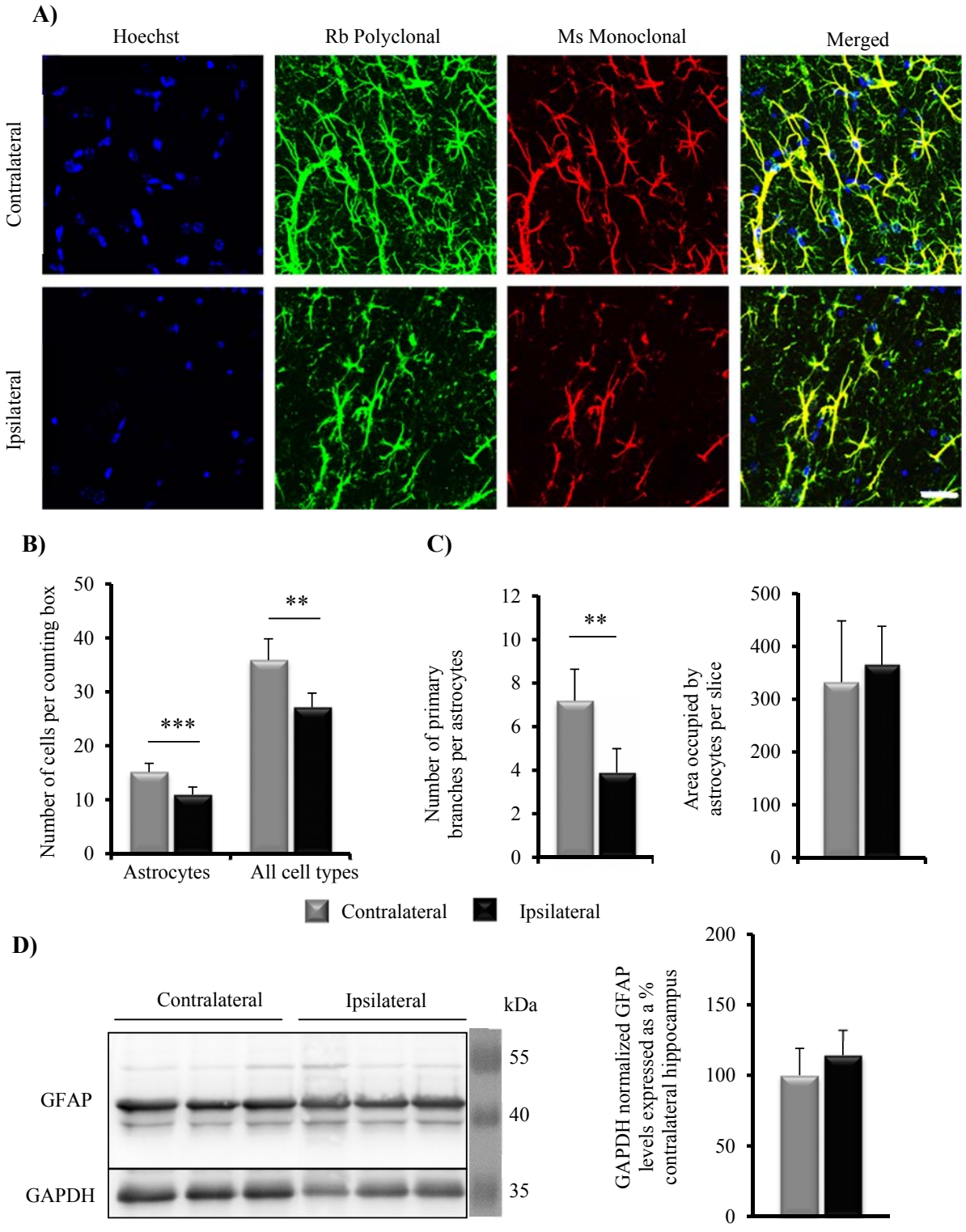

Figure 4.3.1.2: Astrocyte number and morphology 4 h post kainate. A) GFAP immunostaining using monoclonal and polyclonal antibodies in the SR region. In both hippocampi, there is a complete overlap of the signals from the two anti-GFAP antibodies with different clonalities. Scale bar, 100 μm. **B)** Number of GFAP positive astrocytes and total number of cells were significantly reduced in the ipsilateral hippocampus (*** $p < 0.001$, ** $p < 0.01$, N = 6). **C)** The number of primary branches per astrocyte were reduced in the ipsilateral hippocampus (** $p < 0.01$, 24 cells from 3 mice) even though the area occupied by GFAP signal remained unchanged. **D)** Western blot showing GFAP with GAPDH as a loading control. Total GFAP levels were similar in the two groups (N = 6). The graph shows the quantification of the Western blot.

4.3.2 Assessing astrocytic death by TUNEL assay

Apoptosis is a programmed cell death characterized by DNA fragmentation, cellular blebs and vesicular release (Elmore, 2007). Since GFAP immunostaining indicated reduced cell numbers, a TUNEL assay was performed to assess apoptosis in astrocytes. This assay is based on the incorporation of modified dUTPs by the enzyme terminal deoxynucleotidyl transferase (TdT) at the 3'-OH ends of fragmented DNA. A click reaction was employed to detect the incorporated dUTPs. DNAse treated sections were used as a positive control. Co-immunostaining with GFAP revealed that none of the astrocytes in the ipsilateral and contralateral hippocampi were TUNEL positive. In fact, no TUNEL positive signal was detected in either of these hippocampi (Figure 4.3.2 (A) and (B)), in contrast to a positive control which showed TUNEL positive astrocytes in addition to TUNEL positive pyramidal neurons (Figure 4.3.2 (C)). Thus lack of TUNEL signal ruled out the possibility of late stage apoptosis in astrocytes following kainate induced seizures.

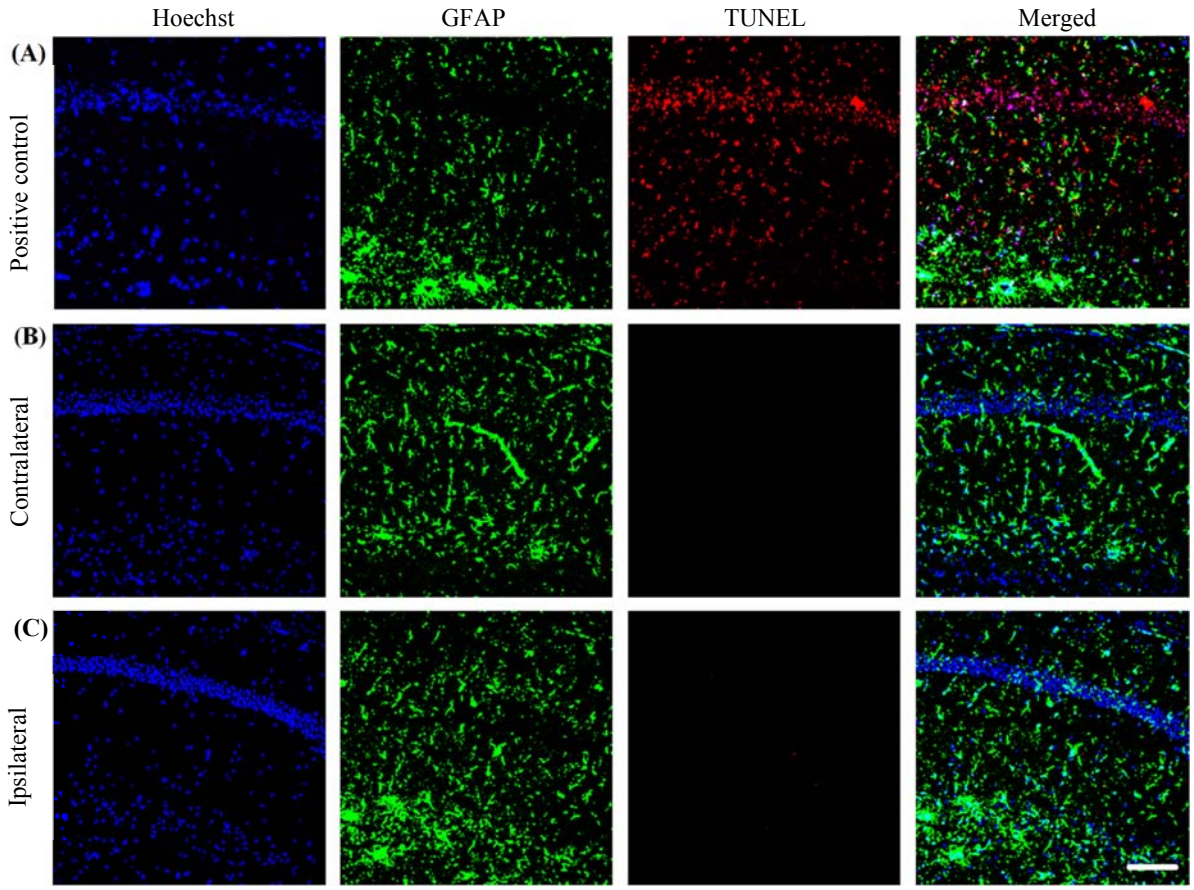

Figure 4.3.2: TUNEL assay to detect apoptotic cells, 4 h post kainate. TUNEL, GFAP and Hoechst co-staining to detect apoptotic astrocytes. DNAse treated brain section (A) was used as a positive control. Confocal images from the CA1 region revealed apoptotic cells in positive control. No TUNEL positive cells were detected in the contralateral (B) and ipsilateral (C) CA1 the regions, 4 h post kainate injection. Scale bar, 100 µm.

4.3.3 Cx43 expression and stereology

Cx43 is the most important gap junctional protein in hippocampal astrocytes. Its deletion resulted in 50% loss of astrocytic coupling despite a compensatory increase in Cx30 protein levels (Theis et al., 2003). Expression and distribution of Cx43 have been correlated with gap junctional coupling in many studies (Rouach et al., 2002)(Collignon et al., 2006)(Koulakoff et al., 2012). Cx43 expression and stereology was assessed by immunolabeling with an antibody targeting amino acids 360 to 382 of the Cx43 C-terminal domain. Cx43 showed a punctate staining pattern (Figure 4.3.3) in both, ipsilateral and contralateral hippocampi. Quantification of fluorescence intensity in the SR region revealed no significant difference in the mean intensity (91.25 ± 15.38 a.u. in contralateral vs. 91.07 ± 28.86 a.u. in ipsilateral, N = 3)

indicating similar expression levels between the two groups. Further analysis indicated similar size (0.04 ± 0.002 µm^2 in contralateral vs. 0.05 ± 0.007 µm^2 in ipsilateral, N = 3), number (89.1 ± 47.53 in contralateral vs. 80.09 ± 24.62 in ipsilateral, N = 3) and area occupied by Cx43 plaques (4.09 ± 2.17 µm^2 in contralateral vs. 4.01 ± 0.8 µm^2 in ipsilateral, N = 3). It can be concluded that Cx43 expression and plaque patterns are unaltered in the ipsilateral SR as compared with contralateral SR.

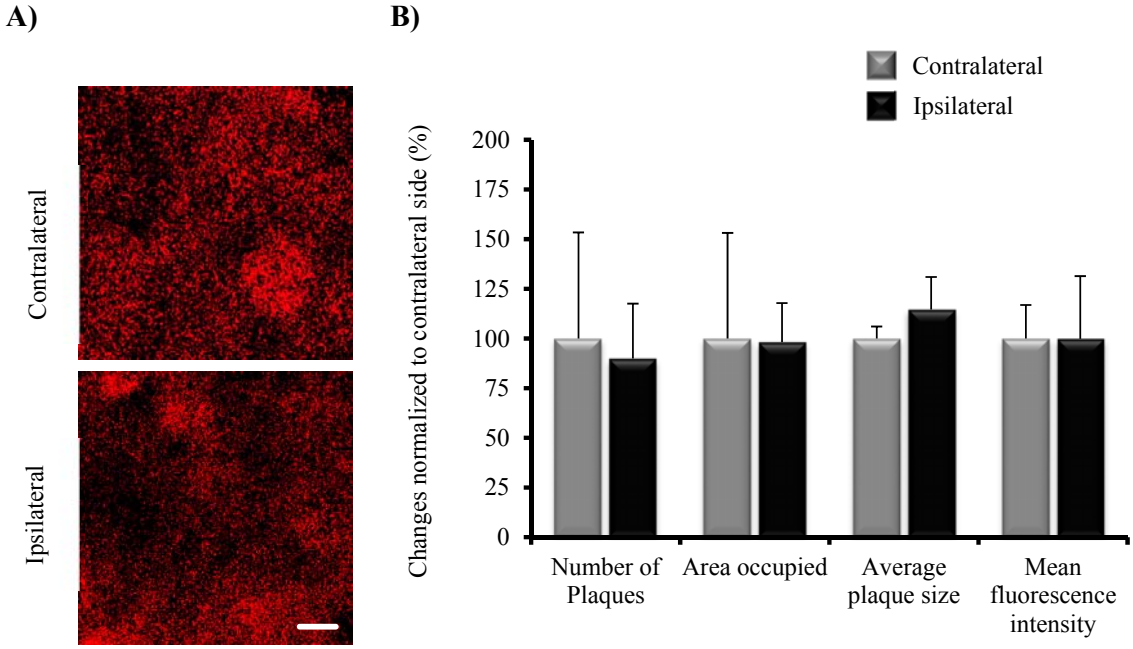

Figure 4.3.3: Cx43 immunostaining and stereology. A) Cx43 immunostaining in the stratum radiatum displaying punctate labelling. Scale bar, 25 µm. **B)** Bar graph shows the quantification of Cx43 plaques in 184.52 x 184.52 x 30 µm^3 boxes positioned in stratum radiatum. There was no significant difference in the total number of plaques, area occupied by plaques, average plaque size and average fluorescent intensity between contralateral and ipsilateral hippocampi. N = 3 per group.

4.3.4 Phosphorylation status of Cx43

Cx43 undergoes extensive post-translational modification, for example phosphorylation which is known to regulate its distribution, channel forming properties and gating (Axelsen et al., 2013). On SDS-PAGE, the protein is characterized by three bands namely the fast migrating P0 isoform and slows migrating P1 and P2 isoforms. The nomenclature P1 and P2 does not correlate with the extent of phosphorylation but it is rather the result of complex conformations arising from phosphorylation at different residues (Solan and Lampe, 2009). Changes in the relative levels of these isoforms indicate changes in the phosphorylation of the protein, which may affect gap junctional coupling.

In earlier experiments using immunofluorescence methods, Cx43 expression was found to be unaltered (Figure 4.3.3). Therefore, Cx43 phosphorylation was assessed by Western blotting. Total membrane preparations from the dorsal hippocampi of kainate and sham injected mice were subjected to SDS PAGE followed by blotting on to PVDF membranes. The membranes were probed with antibodies against Cx43 and the loading control E-cadherin (Figure 4.3.4 A, B). The normalized intensities revealed no difference in the total protein levels, as anticipated. However, in the kainate injected group, there was significant increase in the P2 band levels on the ipsilateral side as compared with contralateral side (increased to 165.02 ± 11.78 %) (Figure 4.3.4 C). In contrast, in sham injected mice all isoform levels were similar (Figure 4.3.4 D).

Cx30 is another gap junctional protein found in astrocytes in the hippocampus. Its contribution to astrocytic coupling is considered marginal, with 20% reduction in the network size when Cx30 is knocked out (Gosejacob et al., 2011). There has been no report of phosphorylation mediated regulation of Cx30. In order to check if the expression level of Cx30 was changed in epilepsy, Western blot was performed on total membrane preparations obtained from hippocampi of kainate injected mice. E-cadherin-normalized protein levels indicated no change in the expression of Cx30 in both, kainate and saline injected mice (Figure 4.3.4 C and D).

Altogether, these data demonstrate that, the phosphorylation status of Cx43 is altered 4 h after kainate injection. It is important to note that there are 21 potential phosphorylation sites on the cytoplasmic tail of Cx43. Phosphorylation at some of these sites has been postulated as a constitutive requirement for coupling while phosphorylation at other sites has been correlated with loss of coupling (Lampe and Lau, 2004)(Solan and Lampe, 2009). The bands seen on the Western blots are combined results of many possible combinations of these phosphorylation sites and they do not reveal exactly which amino residues were phosphorylated. These details can be identified with the help of mass spectrometry.

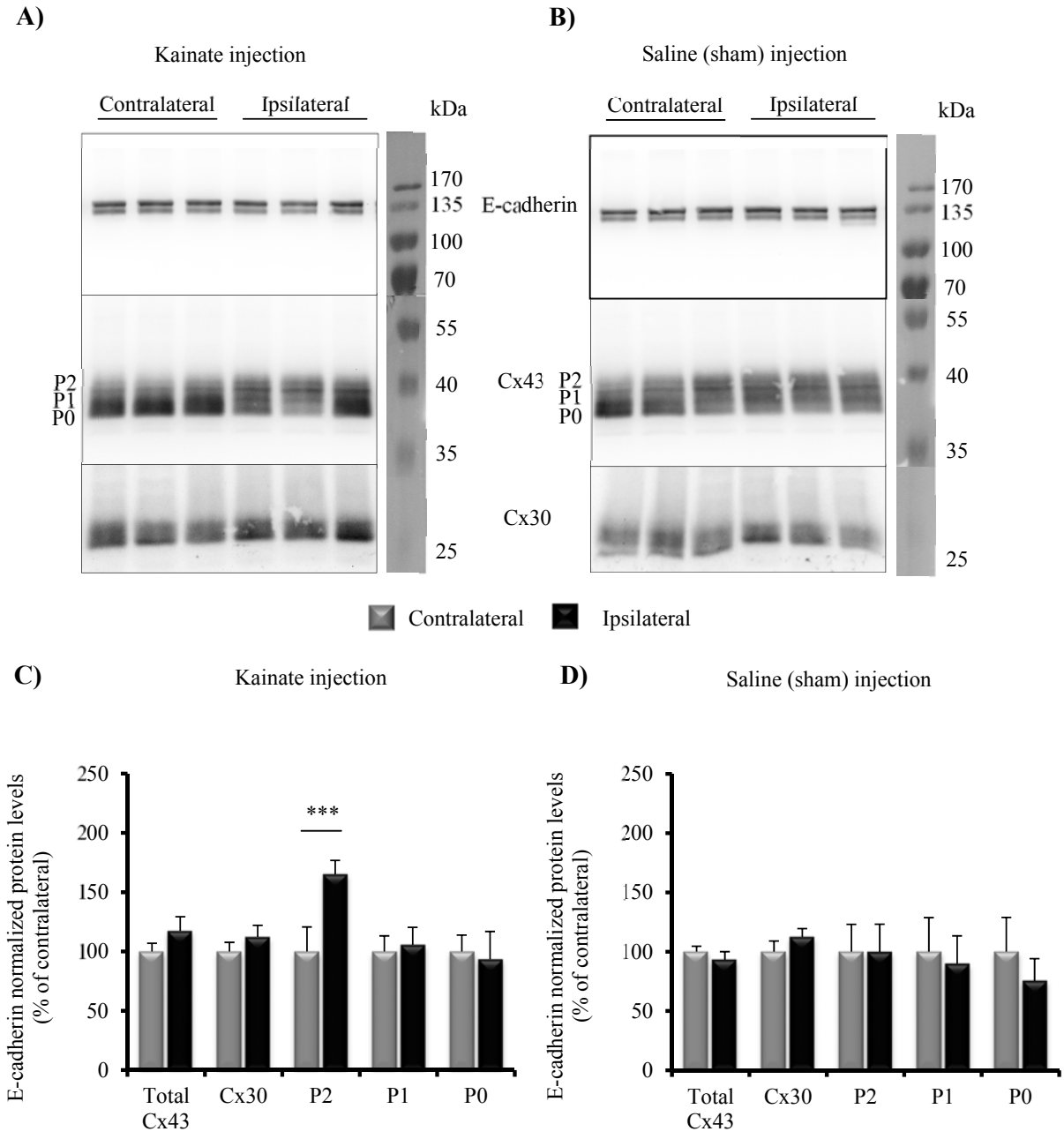

Figure 4.3.4: Immunoblot of Cx43 with E-cadherin as a loading control, 4 h after kainate (panel A) or saline injection (panel B). Total membrane preparations from the dorsal hippocampi were subjected to SDS PAGE followed by Western blotting. Cx43 antibody detected 3 bands that represent the different phosphorylation forms of Cx43 (P0, P1 and P2). **C) and D)** Bar graphs showing quantification of E-cadherin-normalized protein levels expressed as % of corresponding mean levels in the contralateral hippocampus. There was no difference in the total Cx43 and Cx30 levels across all the groups. However, the P2 bands was significantly elevated in the ipsilateral hippocampus of kainate injected mice (165.02 ± 11.78%) while the other bands were similar when compared with corresponding bands from the contralateral hippocampus. All isoforms were similar between contralateral and ipsilateral hippocampi in saline injected group. *** $p < 0.001$, N = 6 per group.

4.4 Mass spectrometry-based characterization of Cx43 phosphorylation

Mass spectrometry-based phosphoproteomics requires that the target protein is isolated in sufficient and pure amounts, posing an immense importance on sample preparation. Immunoprecipitation (IP) is the most widely used method to isolate a protein of interest from a complex mixture of tissue proteins. Successful immunoprecipitation requires a highly specific antibody coupled to a solid support (like protein A sepharose beads) and a buffer to solubilize the precipitated protein. Cx43, which is a membrane protein is not soluble in aqueous solutions without detergents. Therefore, a sample preparation protocol for the isolation of Cx43 from mouse hippocampi was systematically optimized. There were three main requirements:

To obtain an optimum ratio for bead and antibody coupling
To estimate the volume of antibody required for complete extraction of Cx43 from the lysate
Scaling up the optimized IP protocol and confirmation of the complete removal of Cx43

4.4.1 Optimization of the sample preparation protocol

4.4.1.1 Optimization of the bead antibody ratio

The concentration of custom made anti-Cx43 antibody as measured by UV spectrophotometer was found to be 0.82 µg/µl. 'Protein A' magnetic beads (30µg/µl) were used to non-covalently couple with this antibody. The minimum volume of beads required to adsorb 100 µl of the antibody was estimated as follows. 10 µl of the beads were sequentially added to 100 µl of the antibody. After each addition, the mixture was incubated for 30 minutes followed by magnetic separation. The concentration of the separated supernatant was measured and the supernatant was added back to the beads. Another 10 µl of the beads were added to the mixture and the process was repeated. After 6 such additions and subsequent measurements, 3 parameters were calculated and plotted for correlation analysis. The three parameters were i) cumulative amount of beads ii) cumulative amount of antibody adsorbed on to the beads and iii) adsorption efficiency. The last parameter is the ratio of the first two parameters and is defined as the µg of antibody adsorbed by per mg of beads. Plotting cumulative amounts of beads vs. cumulative amounts of antibody adsorbed on to the beads resulted into a zero intercept straight line according to the equation $y = 0.023x$ ($R^2 = 0.95$) (Figure 4.4.1.1 A). From this equation, the minimum volume of beads required to adsorb 100 µl of the antibody was estimated to be 93.5 µl.

Further, the adsorption efficiency was plotted against the cumulative amount of antibody adsorbed. It resulted into a non-linear relationship, with adsorption efficiency declining over the adsorbed antibody amount (Figure 4.4.1.1 B). This indicates that, adsorption efficiency is directly proportional to the availability of the free antibody.

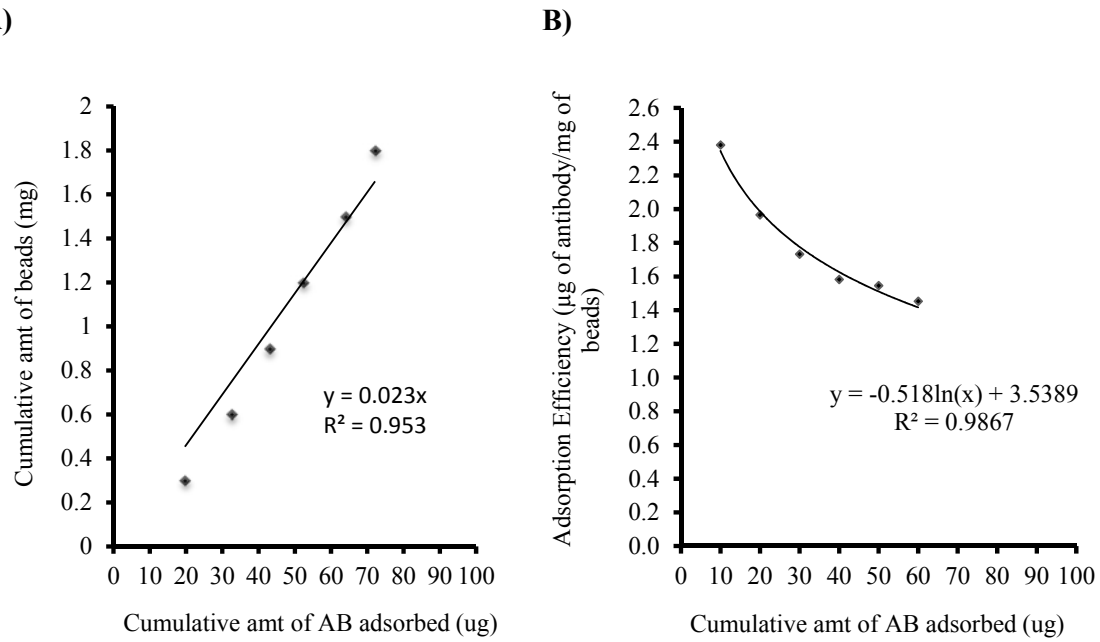

Figure 4.4.1.1: Optimization of the bead-antibody ratio. A) A linear plot of the antibody adsorbed to the beads against the cumulative amount of beads (in mg). Extrapolation yields a minimum required ratio of 0.023 between the beads and the antibody. **B)** Logarithmic plot of the cumulative amount of antibody adsorbed (µg) against the adsorption efficiency (µg of antibody/mg of beads). The latter decreases as the amount of free antibody depletes. AB = antibody, amt = amount

4.4.1.2 Estimation of the volume of antibody required for complete extraction of Cx43

Complete extraction of Cx43 from the tissue is necessary to obtain sufficient amount for phospho-site detection. 2.5, 5 and 10 µl of antibody was used to immunoprecipitate Cx43 from 50 µg of the protein lysate of mouse hippocampus. After overnight incubation, the eluates and the respective supernatants were subjected to SDS PAGE and subsequent Western blotting. Direct probing of the membrane with the secondary antibody alone revealed bands at 55 kDa representing the heavy chain of the antibody used for immunoprecipitation (Figure 4.4.1.2, upper panel). The same membrane was later probed with anti-Cx43 antibody to visualize the Cx43 band at 40 kDa. 2.5 µl of antibody gave partial extraction of Cx43 while 5 and 10 µl of antibody resulted in complete extraction from the 50 µg of lysate (Figure 4.4.1.2, lower panel).

Thus, a minimum 5 µl of the antibody is required to extract the entire pool of Cx43 from 50 ug of the lysate. This can be extrapolated to a 100 µl of antibody for complete extraction of Cx43 from 1000 µg of protein lysate, which is an average amount of protein obtained from one mouse hippocampus.

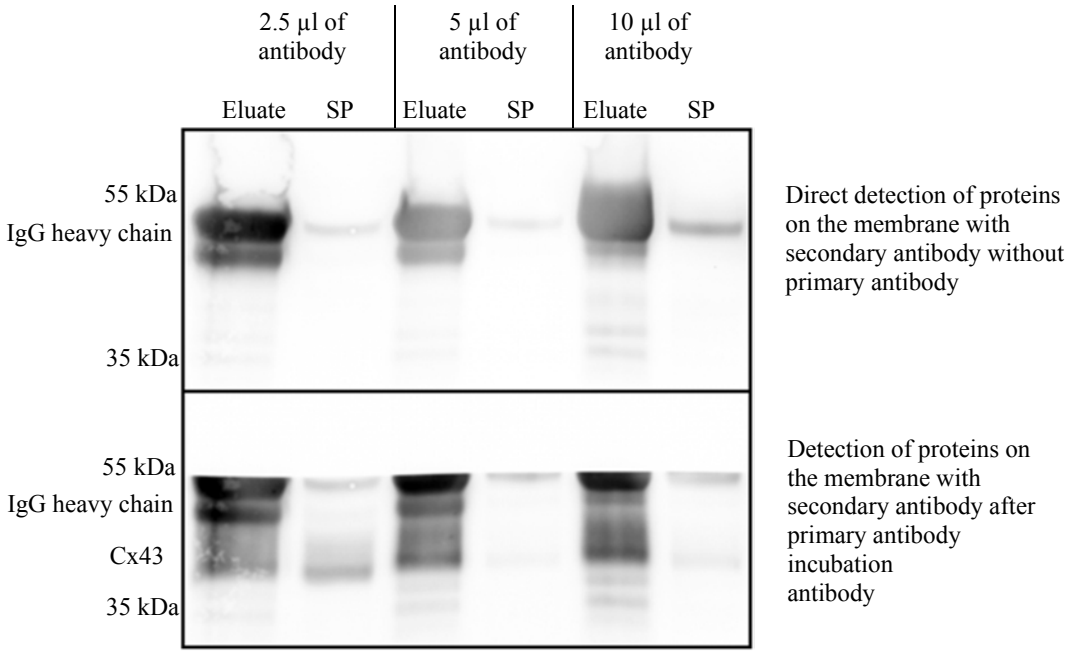

Figure 4.4.1.2: Optimization of the lysate-antibody ratio. Western blot showing immunoprecipitation efficiency of various volumes of the antibody in 50 µg of the protein lysate. The upper panel represents signal from direct incubation of secondary antibody. The band representing the heavy chain of IgG is visible at around 55 kDa. After primary antibody incubation and subsequent detection with secondary antibody, all Cx43 related bands were visible (lower panel). 2.5 µl of antibody resulted in partial extraction of Cx43 while 5 and 10 µl resulted in complete extraction as indicated by absence of Cx43 signal in the supernatant lane. SP = Supernatant.

4.4.1.3 Scaling up the optimized IP protocol and confirmation of the complete removal of Cx43

Based on the optimized bead-antibody and antibody-lysate ratio (4.4.1.1 and 4.4.1.2), a scaled up IP reaction was undertaken. 100 µl of the antibody was coupled with 100 µl of the magnetic protein A beads. The bead-antibody conjugate was then incubated with either 1000 µg of total cellular lysate or 1000 µg of the total membrane lysate overnight at 4 ^{0}C with shaking. The next day, the immunoprecipitated Cx43 was eluted with glycine buffer (pH 2.8). Eluates and the corresponding supernatants were subjected to SDS PAGE followed by Western blotting. The resultant blots were probed with mouse anti Cx43 antibody directed against the N-terminal

domain of Cx43 (NT-1 antibody). It is important to note here, that the antibody used for probing the blot recognized a different epitope than the antibody that used for immunoprecipitation, which targets the last 23 amino acids of the C terminal region of Cx43. The entire C terminal tail of Cx43 has many Serine, Tyrosine and Threonine residues with potential for undergoing phosphorylation. On the other hand the NT-1 antibody used for detection targets the N-terminal region of Cx43 which is not phosphorylated. The use of two different antibodies for immunoprecipitation and detection helped in the unbiased evaluation of immunoprecipitation efficiency. Indeed, no left over Cx43 was detected in the supernatant lane (Figure 4.4.1.3) while the eluate was enriched in Cx43. Interestingly, total membrane preparations gave better yield of Cx43 phospho-isoforms as compared with total cellular preparations.

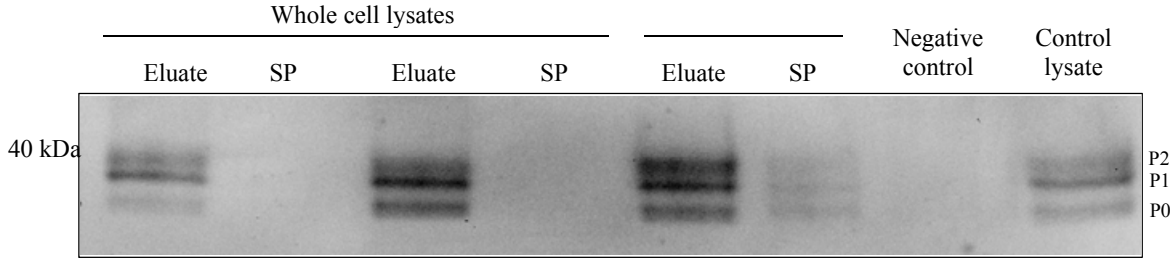

Figure 4.4.1.3: Western blot using antibody targetting the N-terminal of Cx43. The blot shows the immunoprecipitation efficiency of a scaled up reaction on the entire hippocampal lysate (equivalent to 1000 µg of protein). The antibody used for immunoprecipitation was raised against amino acids 360 to 380 of Cx43. The antibody used for detection recognized amino acids 1 to 20 of Cx43. There was complete extraction of Cx43 as indicated by the absence of Cx43 signal in the SP lane. Total membrane preparation gave better yield of phosphorylated Cx43 as indicated by the P2 band. Lysate from the hippocampus of the Cx43 knock out mouse was used as a negative control. Control lysate was not subjected to immunoprecipitation. SP = Supernatant.

4.4.2 Identification of the phosphorylation sites

(In collaboration with Dr. M. Sylvester, Institute of Biochemistry and Molecular Biology, Bonn)

The eluate obtained after IP reaction is a mixture of the target protein and the antibody. It is essential to separate them before mass spectrometric analysis. Therefore, eluate from the scaled up IP reaction was subjected to SDS PAGE. The gel was stained with colloidal coomassie (G 250). The band corresponding to 40 kDa was excised and subjected tryptic digestion. The peptides thus obtained were spin dried and analyzed with LC MS. The resultant spectra were then examined for the presence of phosphorylated residues with the help of a computer program. An example of such an analysis is presented in Figure 4.4.2 B. The sequence coverage

shown in the figure is the fraction of total sequence of Cx43 protein detected by the mass analyzer (corresponding sequences highlighted in green). The phosphorylated residues are designated with the letter P. As shown in this figure, there were 8 phospho-sites detected with 99 to 100% confidence. Some of these sites are considered to be constitutively phosphorylated and essential for gap junctional coupling (see discussion).

A)

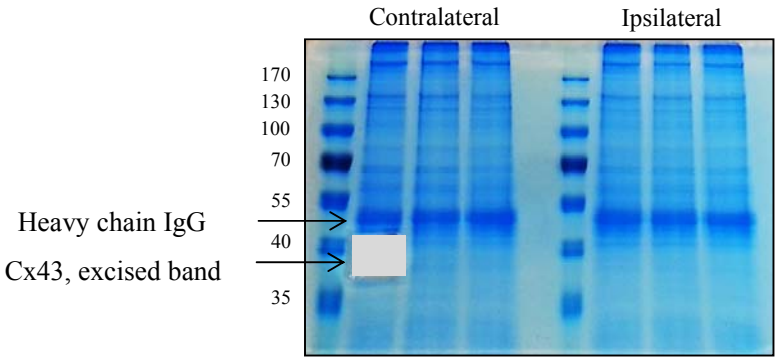

B)

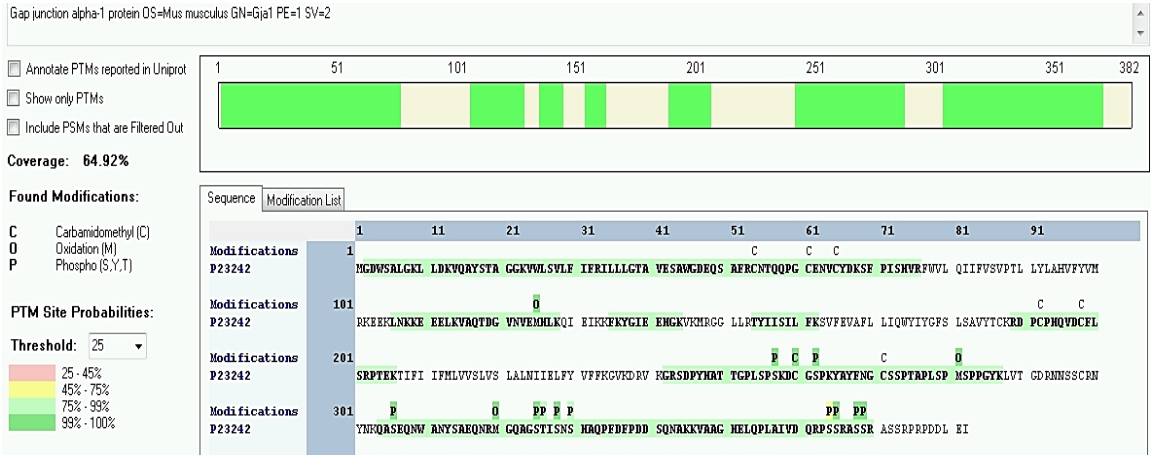

Figure 4.4.2: Identification of the phosphorylation sites. A) Representative image of a coomassie stained gel**.** The eluates obtained from immunoprecipitation reaction were subjected to SDS PAGE. The strong band between 40 and 55 kDa represents the heavy chain of the IgG antibody that was used for immunoprecipitation. Bands at 40 kDa were carved out and subjected to tryptic digestion. **B)** Sequence coverage obtained after a typical mass-spectrometric analysis. Percentage coverage indicates the percentage of total protein sequence identified by a mass analyzer in the form of peptide fragments (highlighted in green). Colour code on the left corner represents the confidence in predicting the phosphorylation sites. P = phosphorylated residue.

4.4.3 Phosphorylation profile of Cx43 4 h after kainate induced seizures

(In collaboration with Dr. M. Sylvester, Institute of Biochemistry and Molecular Biology, Bonn).

Dorsal ipsilateral and contralateral hippocampi were resected from mice subjected to unilateral kainate injections. Ipsi- and contralateral hippocampi from 2 mice were pooled. In total, hippocampi from 30 mice were pooled to obtain 9 samples for kainate injected contralateral group (Kainate C), 9 samples for kainate injected ipsilateral group (Kainate I), 6 samples for saline injected contralateral group (Sham C) and 6 samples for saline injected ipsilateral group (Sham I). The IP reaction was performed as described in section 4.4.2.3, except for the elution procedure. Immunoprecipitated Cx43 was eluted by heating the beads in Laemli buffer at 65 ^{0}C for 10 min. Separation of antigen and antibody, protein digestion and detection of phosphorylated residues on the resultant peptides were carried out illustrated in section 4.4.2. In total, 14 phosphorylation sites were detected with a post translational modification (PTM) score of more than 95% (Table 4.4.3.1). On 2 of these 14 positions, threonine was present. 11 residues were serines while only one phosphorylated tyrosine was detected.

In order to quantify the extent of phosphorylation on each of these sites, chromatographic peak areas of their corresponding peptides were measured. These areas were normalized with chromatographic peak areas of the non-phosphorylated peptides. These area ratios were calculated for each site and then used for statistical analyses. There was no significant difference in the area ratios for any of the phosphorylation sites between Sham I (i.e. ipsilateral) and Sham C (i.e. contralateral) (Mann-Whitney test, N = 6 per group). Thus, there was no effect of saline injection on the phosphorylation profile of Cx43. Therefore, the area ratios from these two groups were pooled together for further comparison with Kainate I (i.e. ipsilateral) and Kainate C (i.e. contralateral) groups.

Table 4.4.3.1: Phosphorylated amino acid residues detected with a PTM score of more than 95%. Small letters in the sequence motif represent the phosphorylated residues. In total, 14 phosphorylation sites were detected. On 2 of these 14 positions, threonine was present. 11 residues were serines while one phosphorylated tyrosine was detected.

Position	Target	PTM Localization probability	Sequence Motif
244	Serine	98.71	DRVKGRsDPYHAT
257	Serine	99.97	TGPLSPsKDCGSP
262	Serine	100	PSKDCGsPKYAYF
290	Threonine	99.3	PGYKLVtGDRNNS
296	Serine	99.07	TGDRNNsSCRNYN
297	Serine	99.75	GDRNNSsCRNYNK
301	Tyrosine	97.19	NSSCRNyNKQASE
306	Serine	100	NYNKQAsEQNWAN
325	Serine	99.37	RMGQAGsTISNSH
326	Threonine	97.54	MGQAGStISNSHA
328	Serine	99.98	QAGSTIsNSHAQP
330	Serine	99.99	GSTISNsHAQPFD
364	Serine	95.8	IVDQRPsSRASSR
365	Serine	98.75	VDQRPSsRASSRA

Kruskal-Wallis followed by post hoc Dunn's test revealed differential phosphorylation on 4 sites, namely S328, S330, S257 and S262 (Table 4.4.3.2). Representative spectra for these sites are displayed in Figure 4.4.3.1 (below).

(A) S328

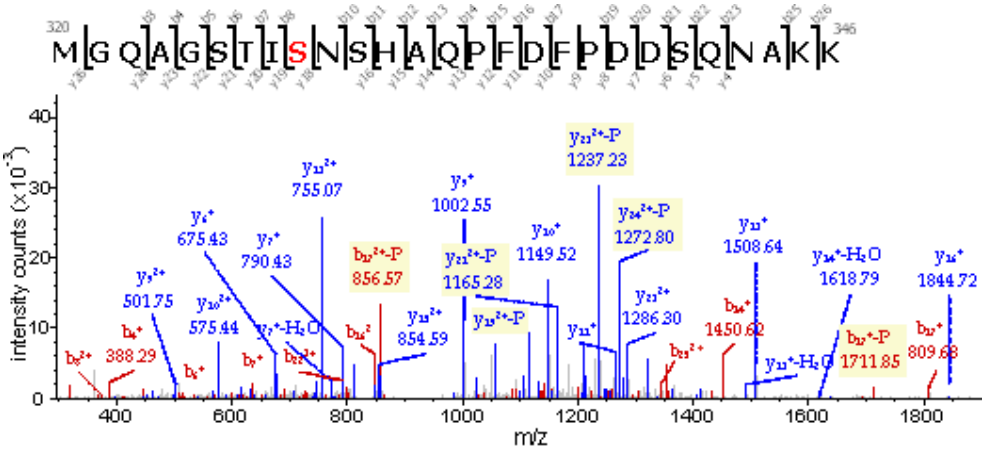

Fragment ion spectrum demonstrating evidence for pS328 from ipsilateral tissue of kainate-injected mice. RT: 53.61 min, precursor m/z= 986.75934 Da, (z=3, MH+= 2958.26346 Da), match tolerance =0.5 Da. Mascot ion score = 68, Percolator PEP = 1.1E-07

(B) S330

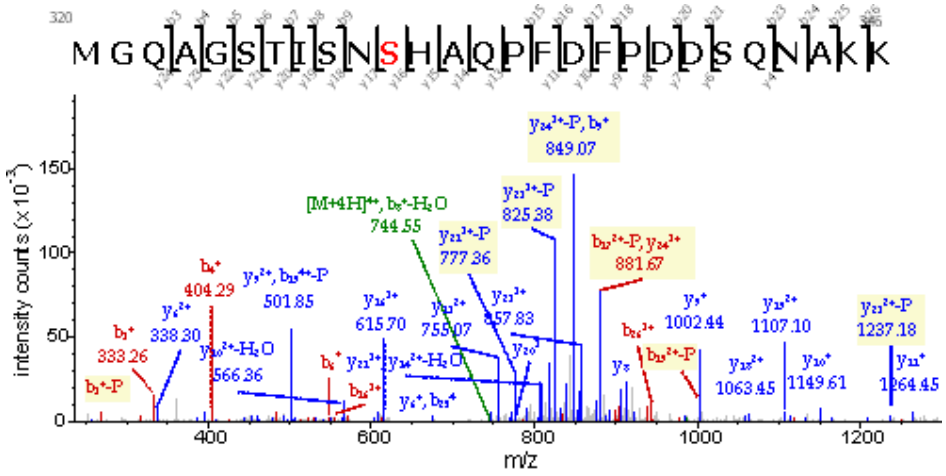

Fragment ion spectrum demonstrating evidence for pS330 from ipsilateral tissue of sham-injected mice. RT: 51.90 min, precursor m/z= 744.32166 Da, (z=4, MH+= 2974.26479 Da), match tolerance =0.5 Da. Mascot ion score = 38, Percolator PEP = 1.1E-04

(C) S257

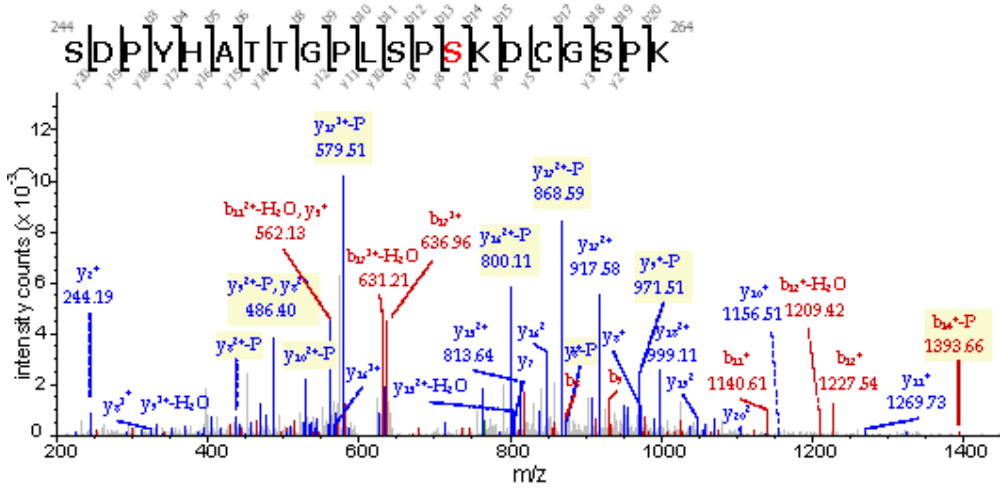

Example of a fragment ion spectrum demonstrating evidence for pS257 from ipsilateral tissue of kinate-injected mice. RT: 39.90 min, precursor m/z=766.00299 Da, (z=3, MH+=2295.99442 Da), match tolerance =0.5 Da. Mascot ion score = 42, Percolator PEP = 5.3E-04. Not all matching fragment ions are annotated due to space restraints. Fragmentation pattern of the peptide sequence generated with GPMAW10 (Lighthouse Data, Odense, Denmark).

(D) S262

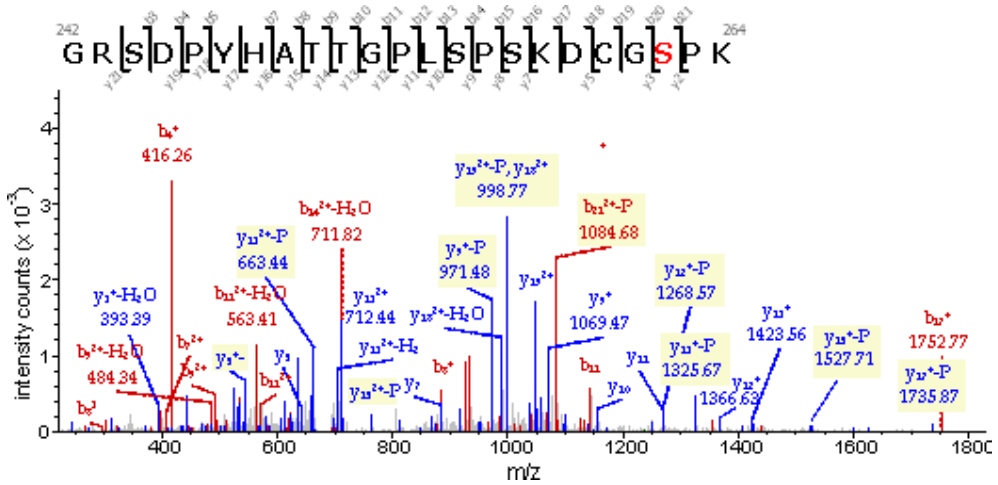

Fragment ion spectrum demonstrating evidence for pS262 from contralateral tissue of sham-injected mice. RT: 35.48 min, precursor m/z= 837.04230 Da, (z=3, MH+= 2509.11234 Da), match tolerance =0.5 Da. Mascot ion score = 56, Percolator PEP = 4.5E-07

Figure 4.4.3.1: Representative spectra of the distinctly phosphorylated serines, 4 h post kainate injection. Phosphorylations at S328 (A), S330 (B), S257 (C) and S262 (D) of Cx43 were altered in hippocampus following kainate induced seizures.

S328 and S330 are the targets of Caseine kinase 1 and are considered to be constitutively phosphorylated. Their phosphorylation is required for gap junctional assembly (Lampe et al., 2006). Indeed, in all samples of the saline injected group, S328 and S330 were phosphorylated. Interestingly, in the Kainate group (both C and I) S330 phosphorylation is reduced when compared with the Sham group (Figure 4.4.3.2 B). On the other hand S328 phosphorylation is reduced only in the Kainate C group when compared with the Sham group (Figure 4.4.3.2 A). S257 can be phosphorylated by protein kinase G (PKG) (Kwak et al., 1995) or CamK II (Huang et al., 2011). Phosphorylation of S257 has been associated with reduced gap junctional conductance (Kwak et al., 1995). Phosphorylation at this site was increased the in Kainate I group when compared with the Sham group. Surprisingly, there was no significant difference between I and C subgroups of the Kainate group (Figure 4.4.3.2 C).

S262 can be phosphorylated by MAPK or CDK-2 and this phosphorylation is known to reduce the open probability of the gap junction channels (Thévenin et al., 2013). Phosphorylation of S262 was increased in Kainate I group when compared with Kainate C and Sham groups (Figure 4.4.3.2 D). It is worth noting here that S262 was the only phospho-site that was differentially regulated in the ipsilateral (kainate I) hippocampus when compared with the contralateral hippocampus (kainate C). Qualitative analysis also revealed increased occurrence of S262 phosphorylation in the ipsilateral hippocampus of the kainate group (found in 8 out of

9 samples) when compared with ipsilateral and contralateral hippocampi of the sham group (found in 2 out of 6 samples per group) (Table 4.4.3.2).

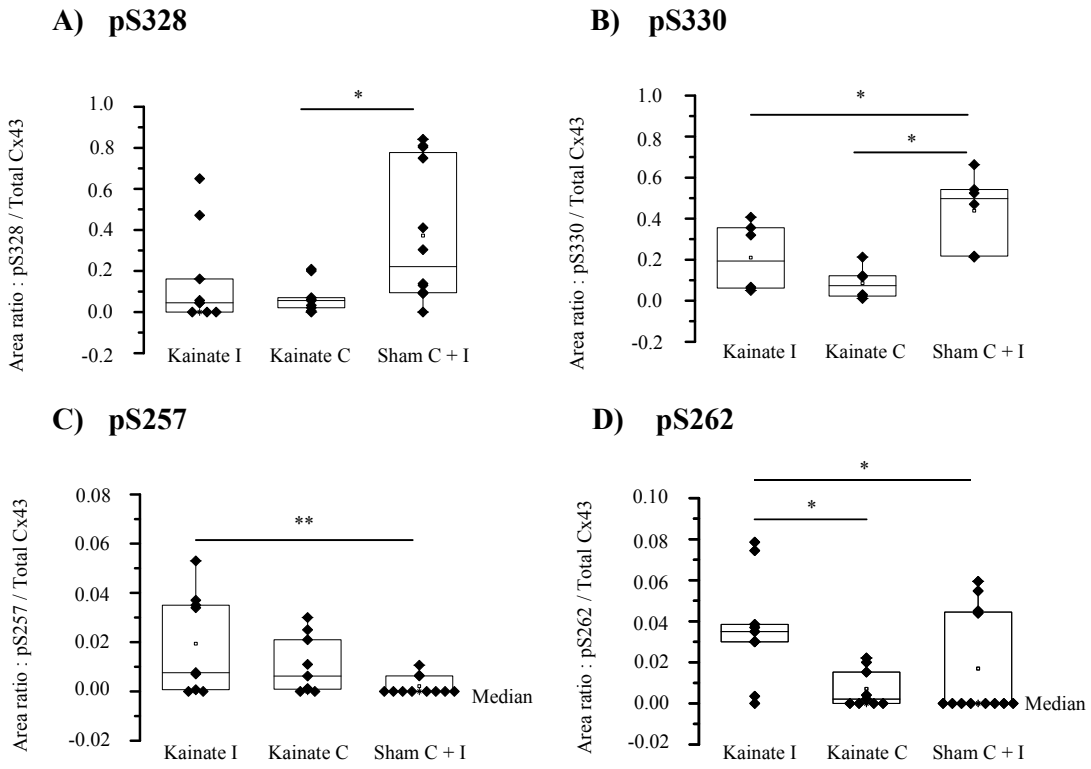

Figure 4.4.3.2: Box-whisker plots showing normalized chromatographic peak areas of the phospho-peptides, 4 h after kainate or saline injection. Chromatographic peak areas of the phospho-peptides were normalized with the chromatographic peak areas of complete Cx43 in the same sample to obtain 'area ratios'. Peptide forms that contained the same phospho-site but different peptide boundaries, oxidation states or charge states were summed up. The area ratios were calculated for each site and then used for statistical analyses. There was no significant difference in the area ratios for any of the phosphorylation sites between Sham I (i.e. Ipsilateral Sham) and Sham C (i.e. Contralateral Sham) (Mann-Whitney test, N = 6 per group). Thus, there was no effect of the saline injection on the phosphorylation profile of Cx43. Therefore, the area ratios from these two groups were pooled together for further comparison with Kainate I (i.e. Ipsilateral Kainate) and Kainate C (i.e. Contralateral Kainate) groups. The boundaries of the boxes encompass the lower (25 %) and the upper (75%) quartiles of the samples. The horizontal line inside the box represents the median. Each dot denotes a sample.** $p < 0.01$, * $p < 0.05$, Kruskal-Walis followed by Dunn's test for pairwise comparison. N = 9 each for Kainate I and Kainate C group. N = 12 for sham C + I group. **A)** pS328 The area ratio of the sham group was significantly higher than that of the Kainate C and Kainate I groups. There was no difference between Kainate I and Kainate C group. **B)** pS330 Phosphorylation on S328 was significantly decreased in the Kainate groups when compared with the Sham group. There was no difference between kainate I and C groups. **C)** pS257 The area ratio for pS257 was significantly higher in the Kainate I group when compared with Sham group. There was no significant difference between Kainate I and Kainate C groups. The median for the sham group was 0. **D)** pS262 This was the only phospho-site which differed significantly between Kainate I and Kainate C groups. The area ratio for pS262 was significantly higher in the Kainate I group when compared with Kainate C and Sham C + I groups. The median for the sham group was 0.

In conclusion, phosphorylation at S262 and 257 was increased after kainate injection. This increase was more pronounced in the ipsilateral hippocampus of the kainate group when compared with the sham group. Out of these two sites, S262 was more phosphorylated in ipsilateral hippocampus of the kainate group when compared with the contralateral hippocampus of the same group ($p < 0.05$, $N = 9$ per group). Therefore, S262 phosphorylation was investigated further.

Table 4.4.3.2: Occurrences of the distinctly phosphorylated serines, 4 h after kainate or saline injection. The numbers represent the number of samples in which the respective site was found to be phosphorylated. Each sample was obtained by pooling the cognate hippocampi from two mice. S262 phosphorylation was more frequently observed in the kainate I group when compared with other groups.

		Groups			
Site	Putative kinase	Kainate R	Kainate L	Sham R	Sham L
S328	Caseine kainase I	6 out of 9	8 out of 9	6 out of 6	5 out of 6
S330	Caseine kainase I	6 out of 6	6 out of 6	3 out of 3	3 out of 3
S257	PKG	7 out of 9	7 out of 9	3 out of 6	1 out of 6
S262	MAPK/CDK-2	8 out of 9	6 out of 9	2 out of 6	2 out of 6

4.4.4 Western blot using antibody against phospho-S262

Mass-spectrometric analysis of Cx43 revealed increased kainate-induced phosphorylation of S262. In order to confirm this finding, phospho-specific antibody against a peptide targetting phosphorylated S262 of mouse Cx43 was used for Western blotting. Hippocampi were harvested from mice 4 h after kainate or saline (Sham group) injection. Total membrane preparations from the dorsal hippocampi were subjected to SDS PAGE followed by Western blotting. The blotted membranes were probed with anti-pS262 Cx43 followed by phosphorylation-unspecific Cx43 antibody. Cadherin was used as a loading control (Figure 4.4.4 B). The phosphorylation-unspecific antibody recognized 3 characteristics bands namely P2, P1 and P0 with an additional lower molecular weight band. The phospho-specific anti-S262 antibody identified many bands between 35 to 40 kDa. Bands co-localizing with those identified by phosphorylation-unspecific antibody were considered as specific signals (Figure 4.4.4 A). Phospho-S262 intensities were normalized by two methods: 1) with cadherin protein intensity which is indicative of the total protein present in the membrane fractions. This method gave a ratio of S262 phosphorylation to the total protein loaded on to the gel. 2) With total Cx43 intensity obtained by probing with phosphorylation-unspecific Cx43 antibody. This method gave a fraction of total Cx43 that is phosphorylated on S262. Both of these methods revealed an increased proportion of phosho-S262 in the ipsilateral hippocampus of the kainate group when compared with the contralateral hippocampus of the same group and both hippocampi of the sham group (Figure 4.4.4 C and D). Further, phospho-isoforms obtained by probing the membranes with phosphorylation-unspecific Cx43 antibody indicated increased P2 isoform levels in the ipsilateral hippocampus of the kainate group when compared with all other three groups (Figure 4.4.4 E). However, there was no significant difference in the total Cx43 levels (i.e. P2 + P1 + P0) between any of the groups. Thus, there was a shift in bands towards P2, without any significant change in the total protein levels. The data indicate that this shift towards P2 band was caused by kainate injection and was not merely an injection artefact. Moreover, the data confirm the increased phosphorylation of S262 previously suggested by mass-spectrometric analysis.

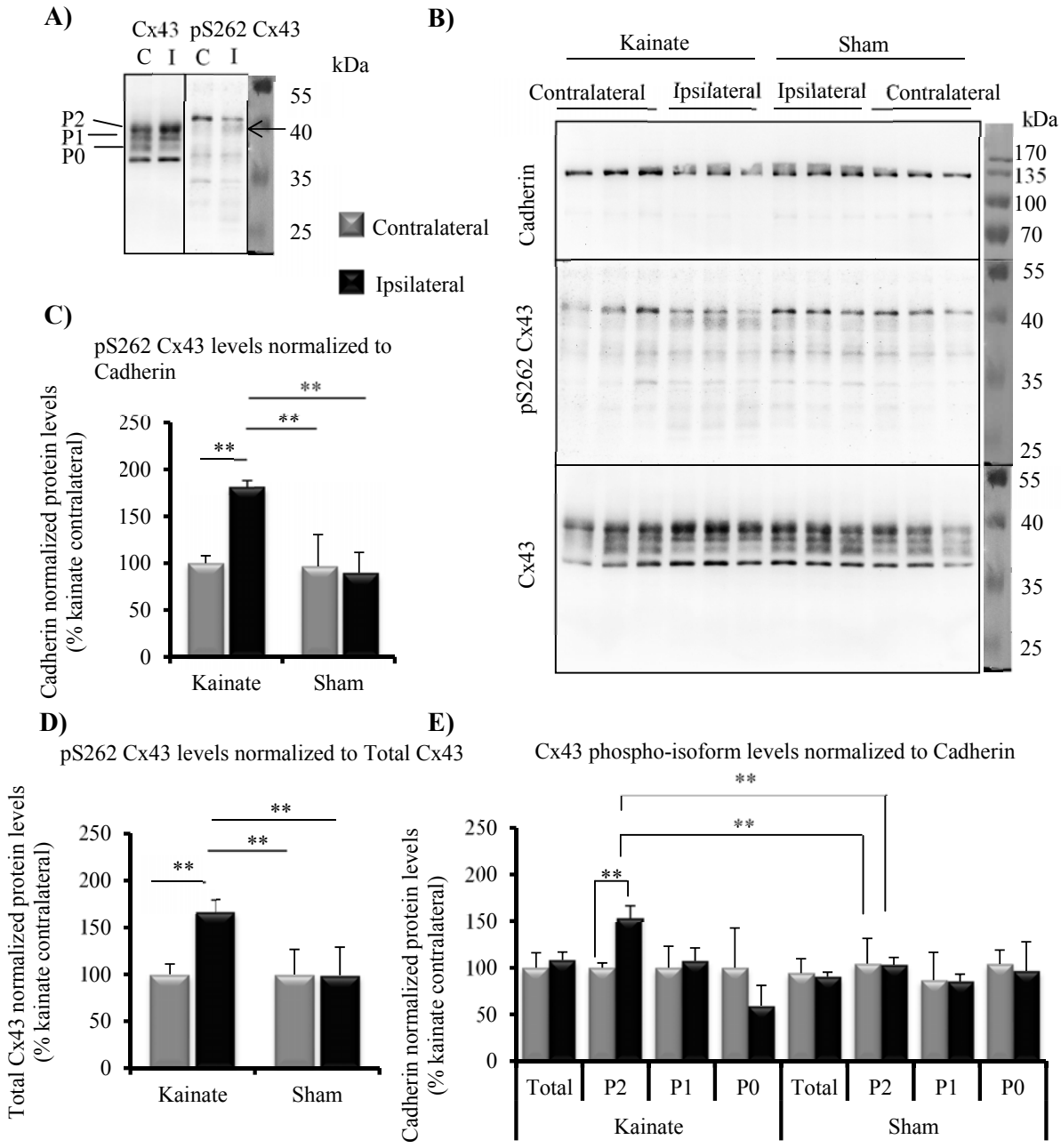

Figure 4.4.4: Phosphorylation at S262 of Cx43, 4 h post kainate. **A)** Immunoblot with phosphorylation-unspecific and phospho-specific (pS262 Cx43) Cx43 antibody. The phosphorylation-unspecific antibody (also used for all previous Western blots and immunoprecipitations) recognized 3 characteristics bands namely P2, P1 and P0 with an additional lower molecular weight band. The phospho-specific anti-S262 antibody identified many bands between 35 to 40 kDa. Bands co-localizing with those identified by phosphorylation-unspecific antibody were considered as specific signals. **B)** Hippocampi were harvested from mice, 4 hr after kainate or saline (Sham group) injection. Total membrane preparations from the dorsal hippocampi were subjected to SDS PAGE followed by Western blotting. The blotted membranes were probed with anti- pS262 Cx43 followed by phosphorylation-unspecific Cx43 antibody. Cadherin was used as a loading control. **C)** Histogram showing pS262 levels normalized with cadherin and then expressed as a percentage of contralateral hippocampus of the kainate group. Phosphorylation of S262 was increased in ipsilateral hippocampus (181.72 ± 6.9) of the

kainate group when compared with other three groups (Contralateral hippocampus of the kainate group: 100 ± 7.87, Contralateral hippocampus of the sham group: 96.56 ± 33.92, Ipsilateral hippocampus of the sham group: 89.35 ± 22.14). These three groups did not differ with each other in pS262 phosphorylation. **D)** Histogram showing pS262 levels normalized with total Cx43 (identified by phosphorylation-unspecific Cx43 antibody) and then expressed as a percentage of contralateral hippocampus of the kainate group. Phosphorylation of S262 was increased in ipsilateral hippocampus (166.74 ± 13.13) of the kainate group when compared with other three groups (Contralateral hippocampus of the kainate group: 100 ± 11.09, Contralateral hippocampus of the sham group: 99.80 ± 26.75, Ipsilateral hippocampus of the sham group: 99.02 ± 29.99). These three groups did not differ with each other in pS262 phosphorylation. **E)** Quantification of total Cx43 and Cx43 phospho-isoforms (identified by phosphorylation-unspecific Cx43 antibody) normalized with pan-cadherin and then expressed as a percentage of contralateral hippocampus of the kainate group. Total Cx43 did not differ between any of the groups. Among phospho-isoforms, only P2 isoform was significantly elevated in ipsilateral hippocampus (154.11 ± 13.39) of the kainate group when compared with the other three groups (Contralateral hippocampus of the kainate group: 100 ± 5.16, Contralateral hippocampus of the sham group: 104.46 ± 26.93, Ipsilateral hippocampus of the sham group: 103.1 ± 8.05). These remaining three groups did not differ with each other in any of the phospho-isoform levels. ** $p < 0.01$, * $p < 0.05$, N = 3 per group.

4.4.5 Cytokines mediated phosphorylation of Cx43 at S262

Incubation of mouse hippocampal slices in cytokines namely TNFα and IL-1β has been shown to reduce the astrocytic gap junctional coupling (Bedner et al., 2015). The phosphorylation of Cx43 was assessed in hippocampal slices incubated under following conditions: ACSF (as a control), TNFα + IL-1β (10 ng/ml) or TNFα + IL-1β (10 ng/ml) with XPRO 1595 (10 μg/ml) for 3.5 hr. XPRO 1595 is a dominant negative inhibitor of the soluble TNFα (Fischer et al., 2015). Total membrane preparations from the slices incubated in above-mentioned conditions were subjected to SDS PAGE followed by Western blotting. The blotted PVDF membranes were probed with anti- pS262 Cx43 followed by phosphorylation-unspecific Cx43 antibody. The phosphorylation-unspecific antibody recognized three characteristics bands namely P2, P1 and P0 with an additional faint lower molecular weight band. The phospho-specific anti-S262 antibody identified strong bands at 40 kDa (Figure 4.4.5 A). Bands co-localizing with those identified by phosphorylation-unspecific antibody were considered as specific signals. Densitometry was performed as described in 4.4.4. Cytokine treatment increased the extent of S262 phosphorylation on Cx43. This increase was attenuated by co-treatment with XPRO 1595 (Figure 4.4.5 B, C). Remarkably, phospho-bands seen after probing the membranes with phosphorylation-unspecific Cx43 antibody indicated increased P2 band levels in the cytokine-treated group when compared with control and XPRO 1595 treated groups (Figure 4.4.5 D).

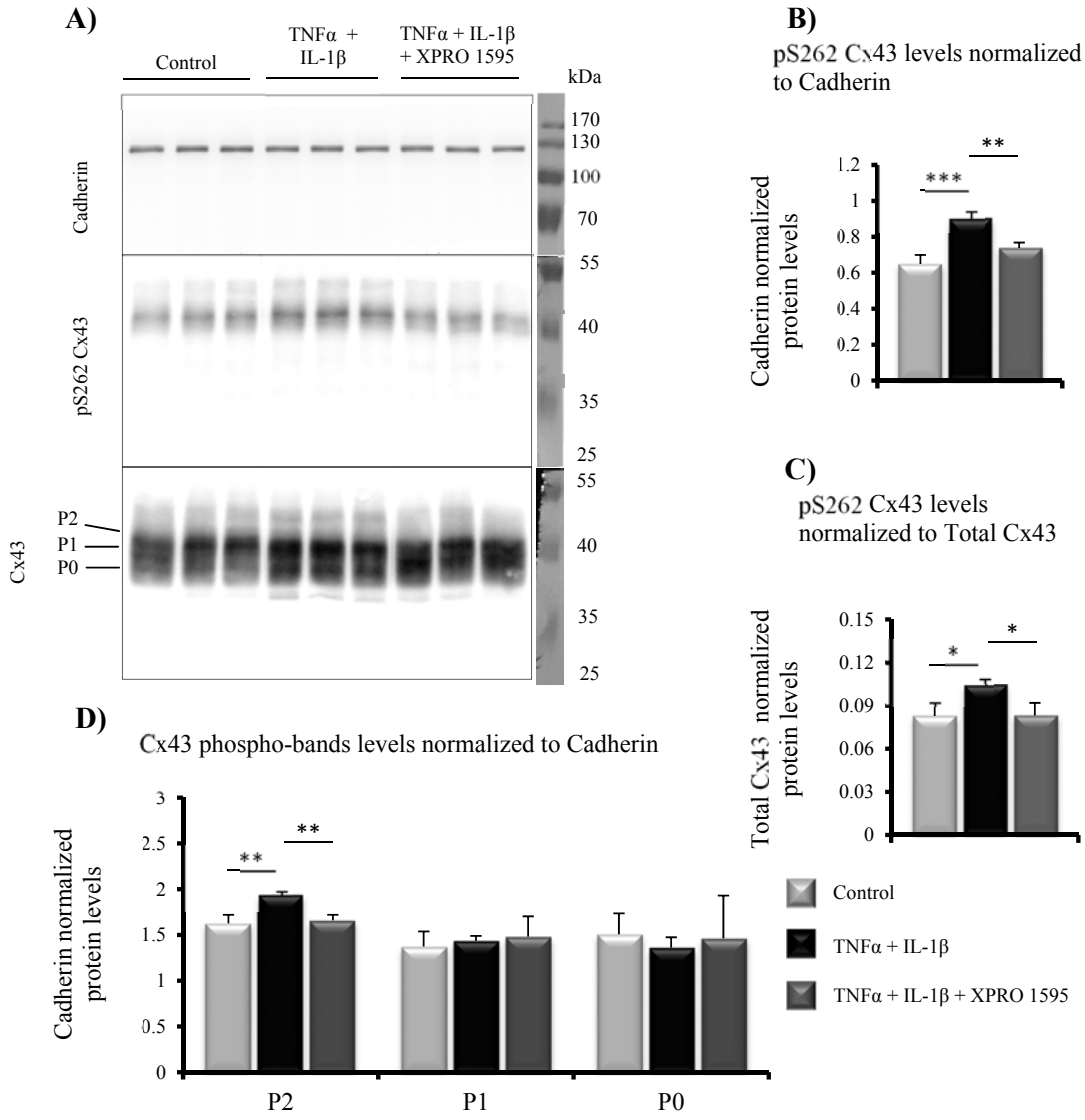

Figure 4.4.5: Cytokines mediated phosphorylation of Cx43 at S262. A) Immunoblot with phosphorylation-unspecific and phospho-specific (pS262 Cx43) Cx43 antibody. Hippocampal slices incubated in ACSF (as a control), TNFα + IL-1β (10 ng/ml) or TNFα + IL-1β (10 ng/ml) with XPRO 1595 (10 µg/ml) for 3.5 h, were homogenized in a lysis buffer to obtain total membrane preparations. Five µg of proteins from each sample were subjected to SDS PAGE followed by Western blotting. The blotted membranes were probed with anti- pS262 Cx43 followed by phosphorylation-unspecific Cx43 antibody. The phosphorylation-unspecific antibody recognized 3 characteristics bands namely P2, P1 and P0. The phospho-specific anti-S262 antibody identified strong bands at 40 kDa. **B)** Bar graphs showing pS262 levels normalized with pan-cadherin. pS262/cadherin ratio was increased in cytokine treated slices (0.9 ± 0.03) when compared with control slices (0.64 ± 0.05) or XPRO 1595 treated slices (0.73 ± 0.03). **C)** Bar graphs showing pS262 levels normalized with total Cx43. The pS262/total Cx43 ratio was increased in cytokine treated slices (0.104 ± 0.003) when compared with control slices (0.082 ± 0.009) or with XPRO 1595 treated slices (0.083 ± 0.008). **D)** Quantification of Cx43 phospho-isoforms (identified by phosphorylation-unspecific Cx43 antibody) normalized with pan-cadherin. Only P2 isoform is significantly elevated in cytokine treated slices (1.93 ± 0.03) when compared with the other two groups (Control group: 1.62 ± 0.09, XPRO 1595 group: 1.65 ± 0.06). *** $p < 0.001$, ** $p < 0.01$, * $p < 0.05$, N = 3 per group.

4.5 Molecular alterations in astrocytes 5 days post kainate injection

Status epilepticus is typically followed by a latent phase in which the brain is virtually seizure free but is undergoing molecular changes that increase its propensity to have seizures (Wong, 2009). This enduring predisposition to generate seizures is the characteristic feature of chronic epilepsy. In our animal model of temporal lobe epilepsy, the latent phase typically lasts for about 5 days after kainate injection. At this time, astrocytic coupling in the ipsilateral hippocampus continues to be at 50% of the level in the contralateral hippocampus (Bedner et al., 2015). Possible mechanisms behind this observed uncoupling were investigated using immunohistochemistry and Western blotting. Astrocyte number, proliferation and connexin expression were examined for their association with uncoupling. Further, changes in the blood brain barrier permeability were studied with the help of albumin immunohistochemistry.

4.5.1 Astrocytic markers 5 days post kainate injection

Immunohistochemistry and stereology had indicated reduced number of astrocytes in the stratum radiatum of the ipsilateral hippocampus 4 h after kainate injection. However, no apoptotic astrocytes could be detected (section 4.3). Therefore, astrocytic markers were assessed 5 days after kainate injection. Coronal sections of the brain were stained with mouse monoclonal anti-S100β and rabbit polyclonal anti-GFAP antibodies. Confocal images revealed almost complete mutual co-localization of the signals from these two antibodies (Figure 4.5.1 A). Numbers of astrocytes were not statistically different in contralateral (17.91 ± 0.62) and ipsilateral (18.08 ± 1.75) hippocampi (N = 3 per group) (Figure 4.5.1 B).

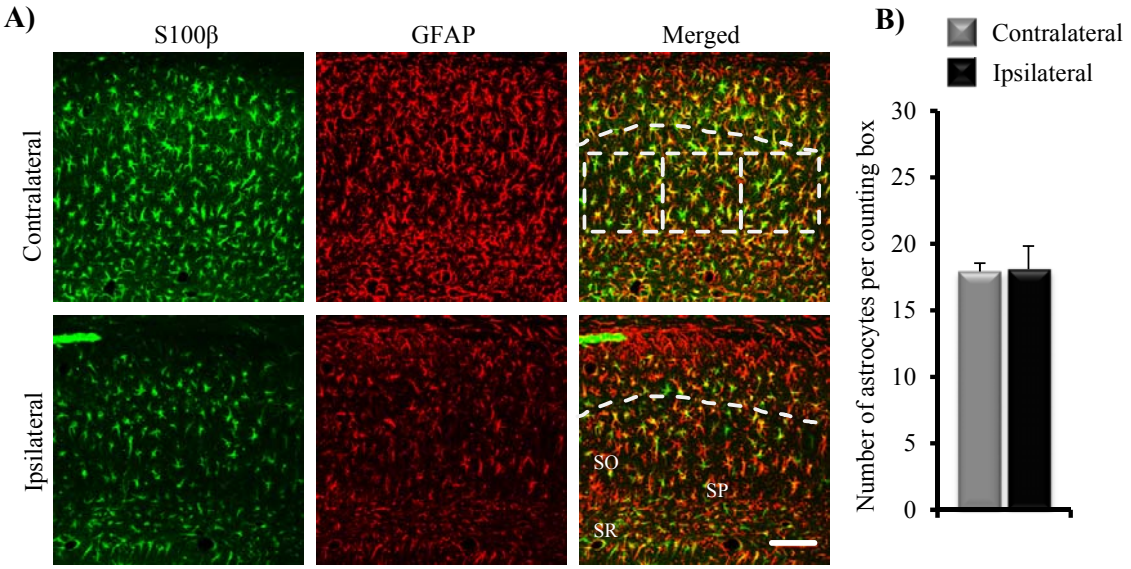

Figure 4.5.1: Astrocytic markers, 5 days after kainate injection. A) S100β and GFAP co-immunostaining. Representative images from the CA1 region 5 days after kainate injection. All GFAP-positive cells were also S100β-positive. Dashed curved line represents lower border of the pyramidal cell layer. Three counting boxes (184.52 x184.52 x30 μm^3) were positioned in the SR region. SO = stratum oriens, SR = stratum radiatum, SP = stratum pyramidale. Scale bar, 100 µm. **B)** The bar graph shows the number of astrocytes per counting box. There was no significant difference in the number of astrocytes in the two groups. N = 3 per group.

4.5.2 Astrocyte proliferation 5 days post kainate injection

Since the difference in astrocyte numbers at 4 h (4.1.1.2) was abolished on day 5 post kainate (4.5.1), astrocytes were assessed for proliferative activity. BrdU was administered through drinking water from day 2 till day 5 after kainate injection. Coronal sections of the brain were stained with anti S100β and anti BrdU antibodies. Confocal images from the CA1 region revealed newly (post kainate injection) generated or dividing nuclei with BrdU signal (Figure 4.5.2 A, red channel). Newly generated or dividing astrocytes were identified by co-localization of S100β with BrdU. The number of such cells was significantly higher in the contralateral hippocampus as compared the ipsilateral hippocampus (6.85 ± 1.98 in contralateral vs. 3.52 ± 0.96 in the ipsilateral hippocampus, N = 3 per group). However, the total number of S100β cells in the two groups was not statistically different (19.69 ± 1.24 in contralateral vs. 15.97 ± 3.37) (Figure 4.5.2 B).

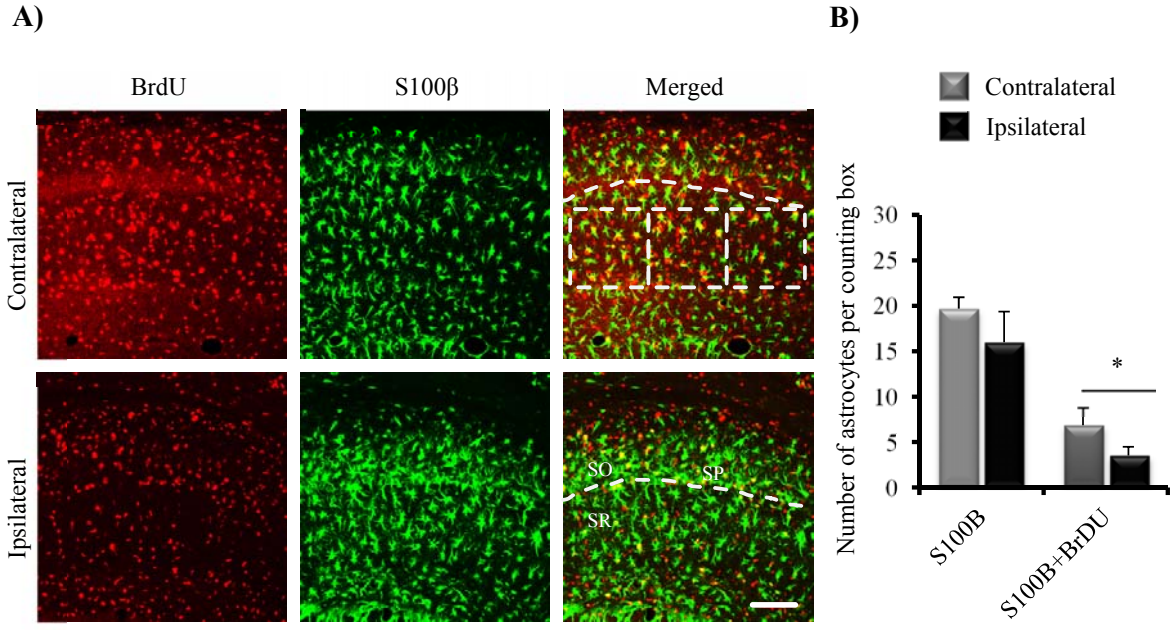

Figure 4.5.2: Astrocytic proliferation 5 days post kainate injection. A) BrdU and S100β co-immunostaining. Representative images from the CA1 region 5 days after kainate injection. S100β cells co-labelled with BrdU indicate newly generated or proliferating astrocytes. Dashed curved line represents lower border of the pyramidal cell layer. 3 counting boxes of the dimension

184.52x184.52x30 μm^3 were positioned in the SR region. SO = stratum oriens, SR = stratum radiatum, SP = stratum pyramidale. Scale bar, 100 µm. **B)** Bar graph shows total number of S100β -positive cells and the number of S100β-positive BrdU cells per counting box. There was no significant difference in the total number of astrocytes in the two groups. The number of newly generated or proliferating astrocytes was significantly higher in the contralateral hippocampus. (* $p < 0.05$, N = 3 per group).

4.5.3 Cx43 expression and stereology 5 days post kainate injection

Cx43 expression was assessed by immunolabeling with an antibody targeting amino acids 360 to 382 of the Cx43 C-terminal (360-382 antibody). Cx43 showed punctate staining pattern in the SR of the ipsilateral hippocampus. Surprisingly, Cx43 immunoreactivity was drastically reduced in the same region of the contralateral hippocampus (Figure 4.5.3 A). It is noteworthy here that any modification in the epitope of the antibody might result the loss of signal. Therefore, another antibody targeting a totally different epitope (250-270) was used to verify the staining pattern observed with 360-382 antibody. The 250-270 antibody detected Cx43 in both contralateral and ipsilateral hippocampi, indicating epitope masking of 360-382 antibody in the contralateral hippocampus. Therefore, the 250-270 antibody was used for stereological analysis. Quantification of the fluorescence intensity in the SR revealed no significant difference in the mean intensity indicating similar expression levels between the two groups (Contralateral: 69.73 ± 8.49 a.u. vs. Ipsilateral: 66.01 ± 5.31 a.u.). Further, plaque analysis indicated similar size (Contralateral: 0.046 ± 0.002 μm^2 vs. Ipsilateral: 0.048 ± 0.001 μm^2), number (Contralateral: 371.1 ± 176 vs. Ipsilateral: 371.3 ± 106.8) and area occupied by Cx43 plaques (Contralateral: 17.78 ± 8.89 μm^2 vs. Ipsilateral: 18.73 ± 5.77 μm^2) (Figure 4.5.3 B). The data indicated that 5 days post kainate injection, Cx43 expression and plaque stereology was unaltered in ipsilateral SR as compared with contralateral SR, although epitope masking for the region 360 to 382 of Cx43 was observed in the contralateral hippocampus.

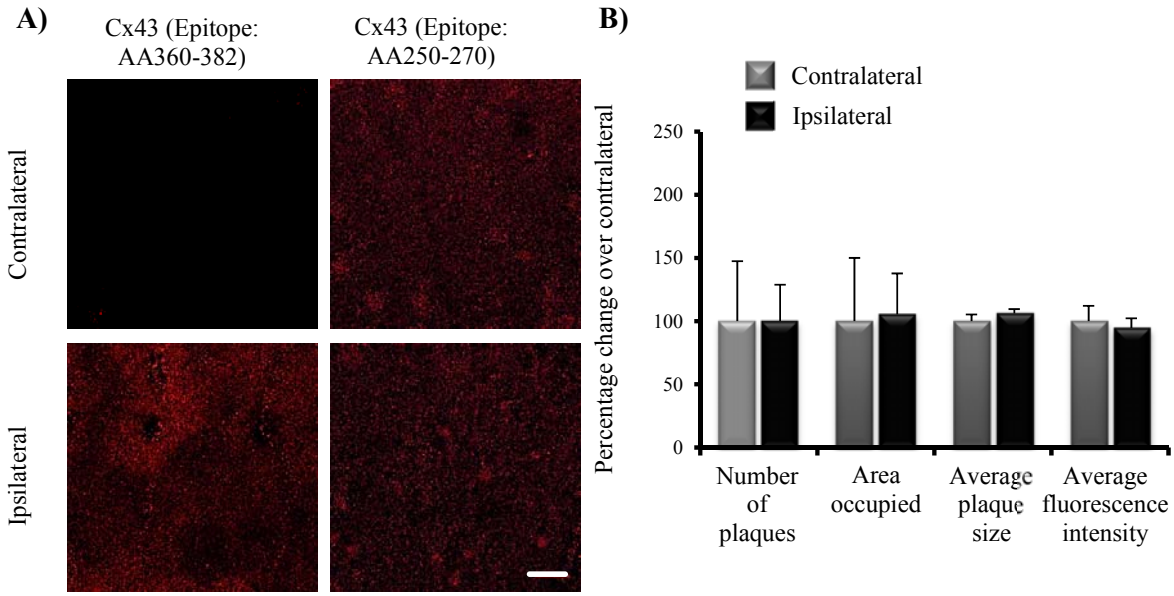

Figure 4.5.3: Cx43 expression and stereology, 5 days post kainate injection. A) Cx43 immunostaining 5 days post kainate injection, in the SR region using two antibodies recognizing different epitopes. The signal from Cx43 (360-382) antibody was lost in the contralateral SR. Scale bar, 25 µm. **B)** Bar graphs showing the quantification of Cx43 plaques immunostained with Cx43 (250-270) antibody. There was no significant difference in the total number of plaques, area occupied by plaques, average plaque size and average fluorescent intensity between contralateral and ipsilateral hippocampi. N = 3 per group.

4.5.4 Phosphorylation status of Cx43 5 days post kainate injection

As discussed in section 4.3.5, Cx43 is extensively phosphorylated and its phosphorylation profile is altered, 4 h after kainate injection. In case of 5 day time point, Cx43 expression was found to be unchanged using immunofluorescence methods (Figure 4.5.3). Therefore, phosphorylation of Cx43 was assessed with Western blotting. Plasma membrane associated proteins were isolated from ipsilateral and contralateral hippocampi of mice, 5 days post kainate injection. SDS PAGE and Western blotting were performed to detect Cx43 and Cx30 (Figure 4.5.4 A). Using E-cadherin as a loading control, total Cx43 protein levels and protein levels of phospho-bands were found to be unaltered (Figure 4.5.4 B & C). In contrast to the data from 4 h time point, the absolute levels of the P2 bands between the two hippocampi are not changed at 5 day time point. It is likely that the elevated ipsilateral P2 bands levels at 4 h decline to normal till day 5 by dephosphorylation. Similar to the total Cx43 protein levels, Cx30 protein levels were also found to be similar between ipsilateral and contralateral hippocampi. Thus, neither the phosphorylation status of Cx43 nor the connexin availability at the plasma membrane correlates with the astrocytic uncoupling prevalent at the end of the latent phase as reported by Bedner et al., 2015.

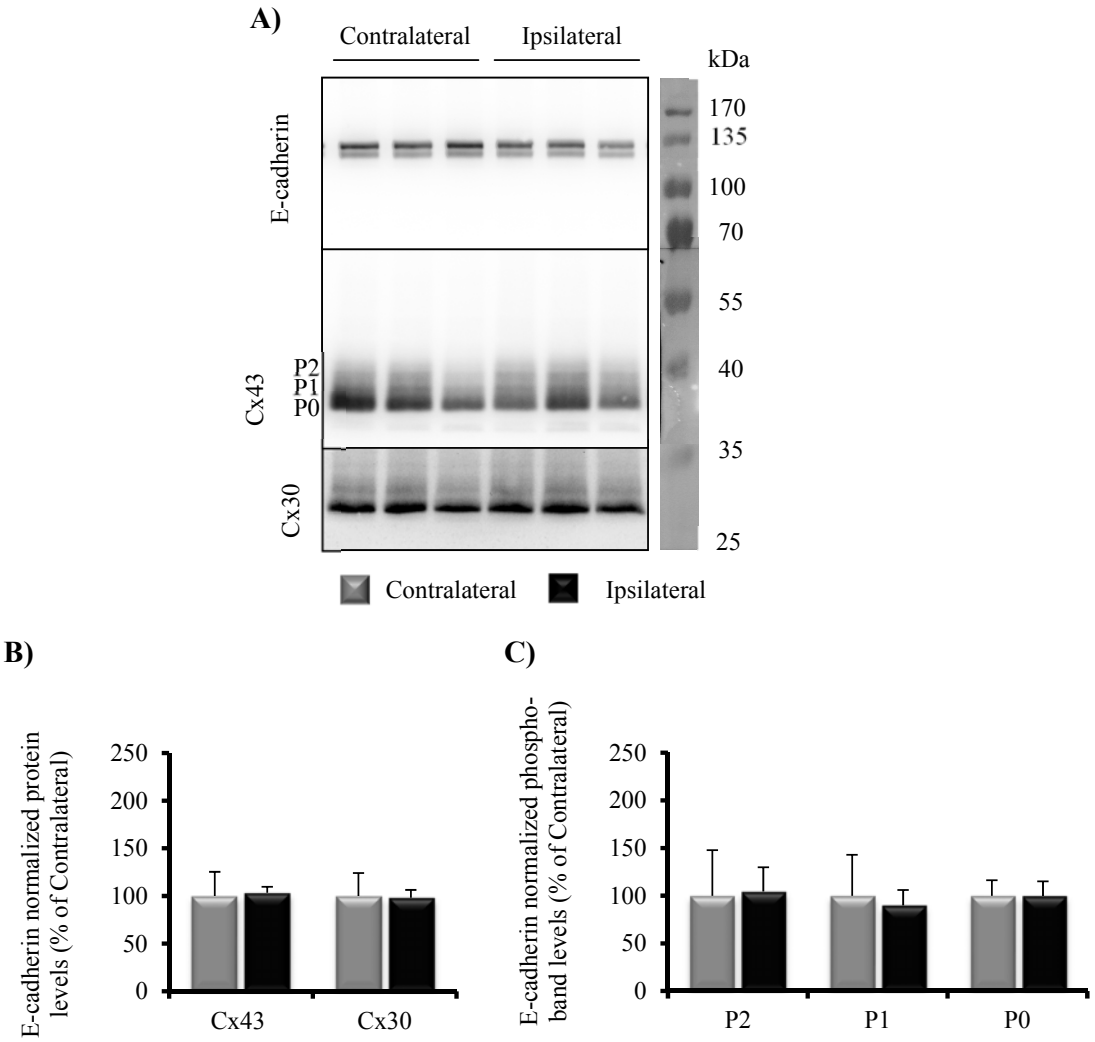

Figure 4.5.4: **Western blot of plasma membrane associated connexins, 5 days post kainate injection. A)** Plasma membrane associated proteins were selectively isolated from the dorsal hippocampi. 5 µg of protein was loaded in each well. Immunoblot displays Cx43, Cx30 and E-cadherin (as a loading control). **B)** The histogram shows E-cadherin-normalized protein levels expressed as a percentage of the contralateral group. Total Cx43 and Cx30 levels were not statistically different between the contralateral and the ipsilateral hippocampi. **C)** Phospho-bands P2, P1 and P0 were normalized to E-cadherin and then expressed as a percentage of the contralateral group. There was no significant change in any of the phospho-bands between the two groups.

4.5.5 BBB disruption and albumin extravasation 5 days post kainate injection

BBB breakdown characterized by albumin extravasation has been implicated in epileptogenesis (Vliet et al., 2007)(Ivens et al., 2007). However, was not clear whether this aspect was different between ipsilateral and contralateral hippocampi in the mouse model of epilepsy. Intraventricular albumin administration has already been shown to cause uncoupling in astrocytes (Braganza et al., 2012). Therefore, albumin extravasation was investigated in

connection with reduced coupling in the ipsilateral hippocampus. Five days after kainate injection, coronal sections of the brain were stained with goat polyclonal anti-albumin antibody. Saline injected animals were used as a control. Confocal images from the CA1 region revealed that the albumin immunoreactivity was present only in ipsilateral hippocampi of the kainate injected mice while contralateral hippocampi in the same mice were devoid of any albumin signal. Importantly, albumin immunoreactivity was completely absent in sham injected mice indicating that the BBB breakdown was the result of kainate injection (Figure 4.5.5). Thus, albumin extravasation is a distinct feature of the ipsilateral hippocampus that can be associated with reduced coupling.

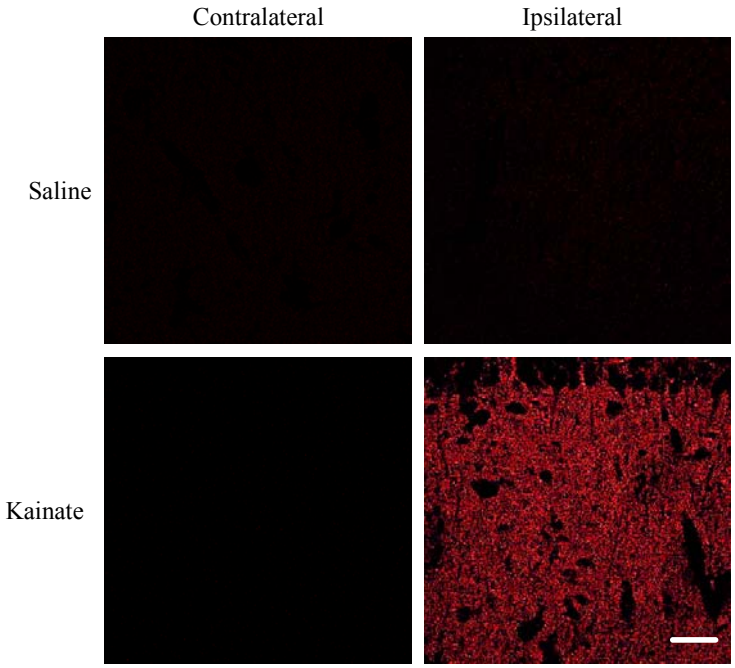

Figure 4.5.5: Albumin extravasation 5 days post kainate injection. Albumin immunostaining 5 days post kainate injection, in the SR region. Only ipsilateral hippocampi of kainate injected mice showed albumin immunoreactivity indicating BBB disruption. Scale bar, 25 µm.

4.6 Seizure-induced hippocampal changes in mice with astrocytic deletion of connexins

Hippocampal sclerosis in epilepsy is characterized by the loss of CA1 pyramidal neurons, pronounced astrogliosis and granule cell pathologies (Thom, 2014). The granule cell pathologies have been correlated with memory disturbances and cognitive dysfunction in epilepsy patients (Hester and Danzer, 2014). They include axonal connections with inappropriate targets, abnormal dendrite growth, and migration of granule cells to ectopic locations resulting in granule cell dispersion (GCD). The latter process was shown to be independent of the seizure induced adult neurogenesis (Fahrner et al., 2007). Astrocytic connexins (Cx43 and Cx30) are known to regulate neurogenesis in the adult dentate gyrus (Kunze et al., 2009a). Interestingly, knock out of these connexins resulted in reduced seizure-induced GCD (Pavel Dublin, PhD thesis 2012). To investigate this finding further, GCD and neuronal proliferation were investigated in mice lacking astrocytic connexins (DKO mice).

4.6.1 Seizure-induced GCD is attenuated in DKO mice

GCD is a remarkable feature observed in 40-50% of MTLE-HS patients (Thom, 2014). Granule cells have closely packed architecture in the dentate gyrus of control mice. Seizure induced dispersion of granule cells in the mouse model 1 month post injection was quantified by measuring the thickness of the blades of dentate gyrus. In the ipsilateral hippocampi, the granule cells were dispersed in contrast to the compact cellular architecture in contralateral hippocampi. The average thickness of the granule cell layer (average of T1, T2, T3 and T4, Figure. 4.6.1) was significantly increased in the ipsilateral hippocampus when compared with the corresponding contralateral hippocampus. The average thickness of the ipsilateral granule cell layer (GCL) was shorter in the DKO mice as compared with wild type (WT) mice (157.90 ± 29.63 vs. 219.47 ± 7.66 µm, N = 3 per group, respectively). These data show that astrocytic connexins influence the seizure-induced GCD.

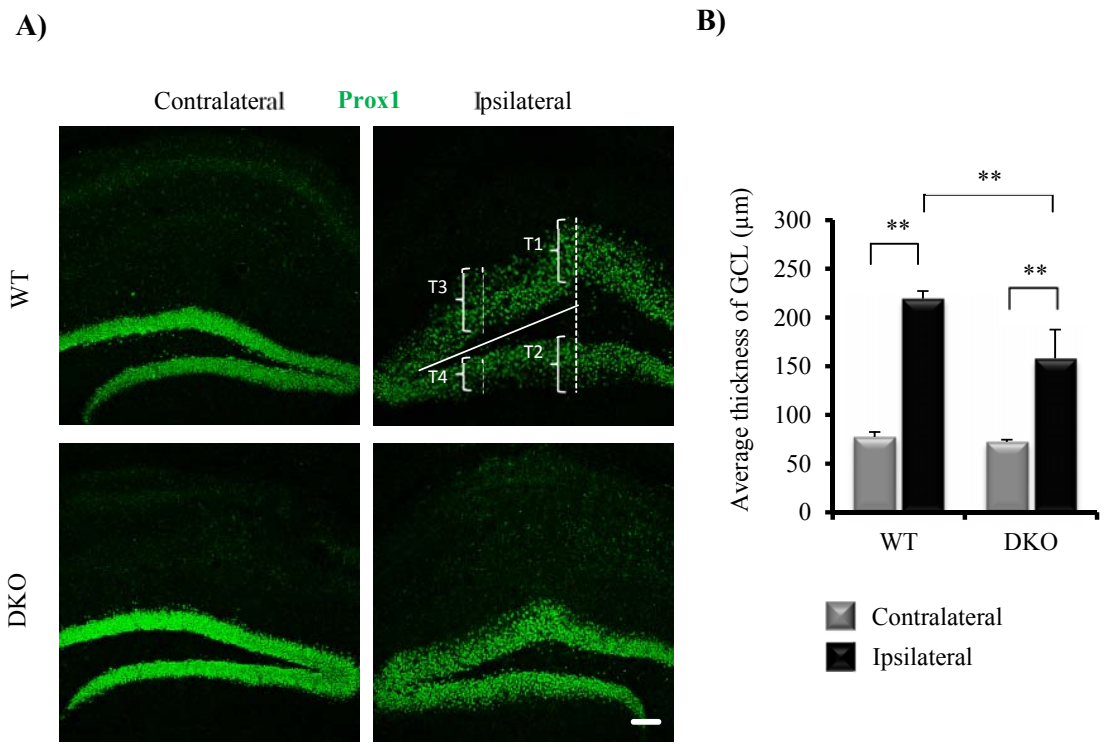

Figure 4.6.1: Seizure-induced GCD is attenuated in DKO mice. A) Prox1 immunostaining 1 month after kainate injection. Prox1 is a marker for mature granule cells. In ipsilateral hippocampi, the granule cells are dispersed in contrast to the compact cellular architecture in contralateral hippocampi. T1, T2, T3 and T4 are the thicknesses of the GCL averaged to obtain a single parameter indicative of GCD. T1 and T2 are measured along the line D. T3 and T4 are measured at a distance half-way between line D and the tip of the hilus. Scale bar, 100 µm. **B)** Quantification of GCD using the average thickness of the GCL (µm). The average thickness of the GCL was significantly higher on the ipsilateral side when compared with the corresponding thickness on the contralateral side. Interestingly, the ipsilateral dentate gyrus of DKO mouse displayed a lesser GCD as compared with the ipsilateral dentate gyrus of the WT mouse. ANOVA followed by post hoc Tukey´s test. N = 3 per group, ** $p < 0.01$

4.6.2 Seizure-induced cellular proliferation in the hippocampus

Seizure-induced cellular proliferation in hippocampus has been documented using BrdU labelling (Parent et al., 1997) (Bengzon et al., 1997) (Zhu et al., 2005). All of these studies involved intraperitoneal injections of BrdU over short intervals. Since BrdU has a very short half-life (2 h), only a small population of proliferating cells could be labelled in these studies. In order to circumvent this limitation, in the present study the BrdU was administered through drinking water. 15 days after kainate injection, the BrdU containing drinking water was replaced by normal water for the remaining 15 days. This enabled to assess the survival of the cells born during the first 15 days. Kunze et al. with the help of pulse chase BrdU labelling showed that neurogenesis was impaired in DKO mice (Kunze et al., 2009a). Therefore, post kainate-injection cellular proliferation in DKO mice was compared with that in post kainate

WT mice. 30 days after the kainate injection and 15 days after the last dose of BrdU, many BrdU-positive cells were seen in the entire hippocampus. These cells were counted in counting boxes (290 x 290 x 8 μm^3) positioned in the DG and CA1 regions. In the DG, the numbers of BrdU-positive cells were similar between ipsilateral and contralateral sides and also between the genotypes (Table 4.6.2). In the CA1 region, the ipsilateral side showed more cellular proliferation than the contralateral side irrespective of the genotypes (ANOVA followed by post hoc Tukey's test, $p < 0.01$, $N = 3$ each group). Here again, the two genotypes did not differ in the number of BrdU-positive cells (Table 4.6.1).

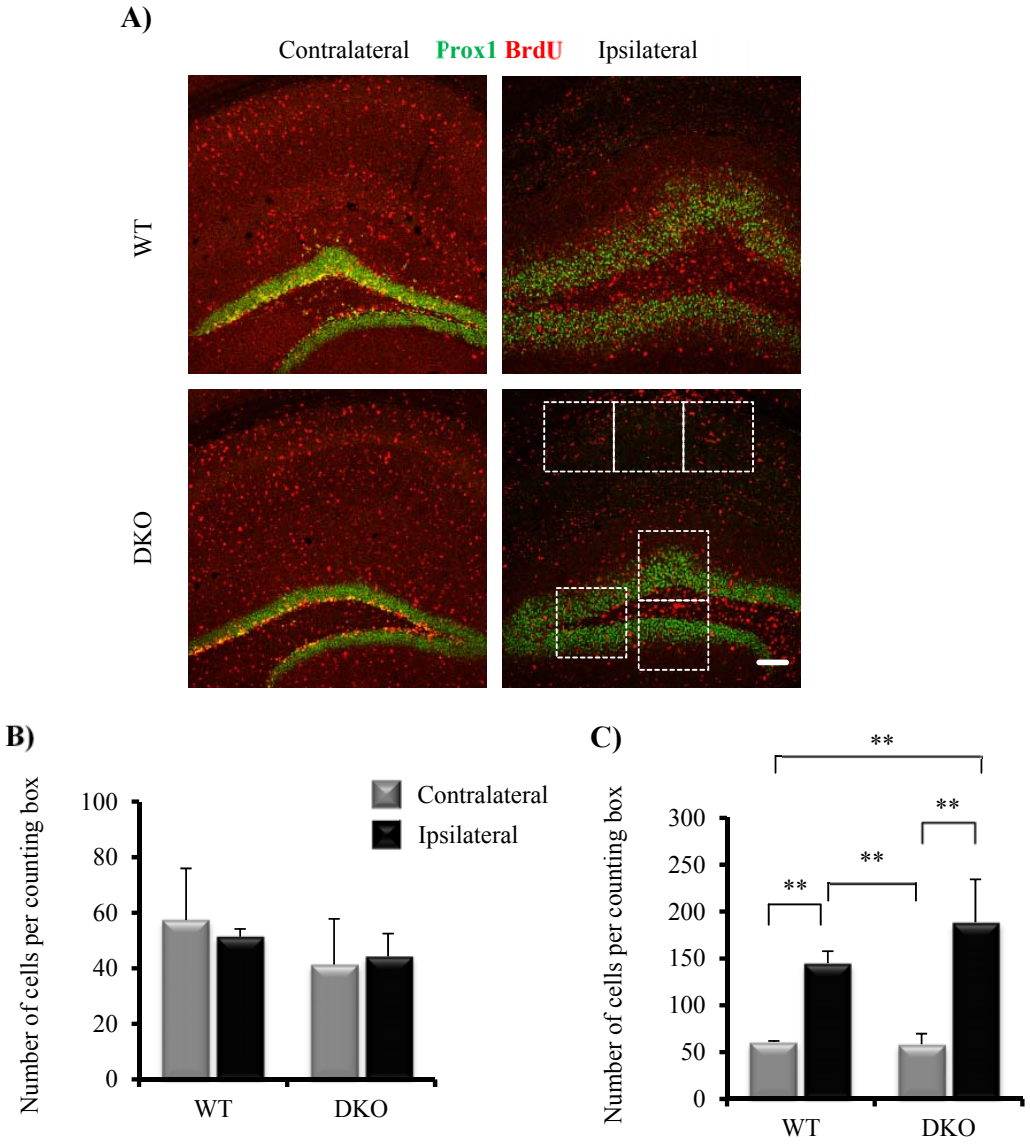

Figure 4.6.2: Seizure-induced cellular proliferation in the hippocampus. A) Prox1 (green) and BrdU (red) immunostaining in WT and DKO mice, 1 month after kainate injection. BrdU was administered through drinking water for the first 15 days. Presence of BrdU signal in the cell nucleus indicates a newly generated or a proliferating cell. Counting boxes (290 x 290 x 8 μm^3) were positioned in CA1 and DG regions.

Averages of 3 counting boxes were considered per region and per section. Scale bar, 100 µm**. B) and C)** Number of BrdU-positive cells per counting box in DG and CA1 respectively. In DG (B), there was no significant difference between ipsilateral and contralateral side. However, in the CA1 region (C), the number of BrdU-positive cells was significantly higher on the ipsilateral side. In both regions, there was no difference between the genotypes. ANOVA followed by post hoc Tukey´s test. N = 3 per group, ** $p < 0.01$.

Table 4.6.2: Number of BrdU-positive cells per counting box (290 x 290 x 8 μm^3) per mouse in the DG and CA1. All values are expressed as mean ± SD. N = 3.

Genotype	DG		CA1	
	Contralateral	Ipsilateral	Contralateral	Ipsilateral
WT	57.38 ± 18.59	51.36 ± 2.82	60.77 ± 1.17	145 ± 12.66
DKO	41.33 ± 16.46	44.27 ± 8.21	58.44 ± 11.2	188.55 ± 45.81

4.6.3 Reduced GCD in DKO mice is not caused by impaired neurogenesis

Post-seizure GCD was reduced in DKO mice as shown by the thickness of granule cells (Figure 4.6.1). These mice have reduced adult neurogenesis in the DG (Kunze et al., 2009a). Therefore, one month post kainate injection; neurogenesis was assessed in the ipsilateral DGs of WT and DKO mice for its association with the observed differences in the GCD. Prox1 was used as a marker for mature granule cells while Doublecortin (DCX) was used to detect immature or newborn neurons. Surprisingly, no DCX-positive cells were detected in the ipsilateral hippocampus despite of large proliferative activity. Moreover, no Prox1-BrdU colabelling was found, indicating absence of newly generated granule cells. Thus, neurogenesis was completely lacking in the ipsilateral DG irrespective of the genotypes. Therefore, the reduced GCD in DKO mice cannot be ascribed to the post-kainate neurogenesis.

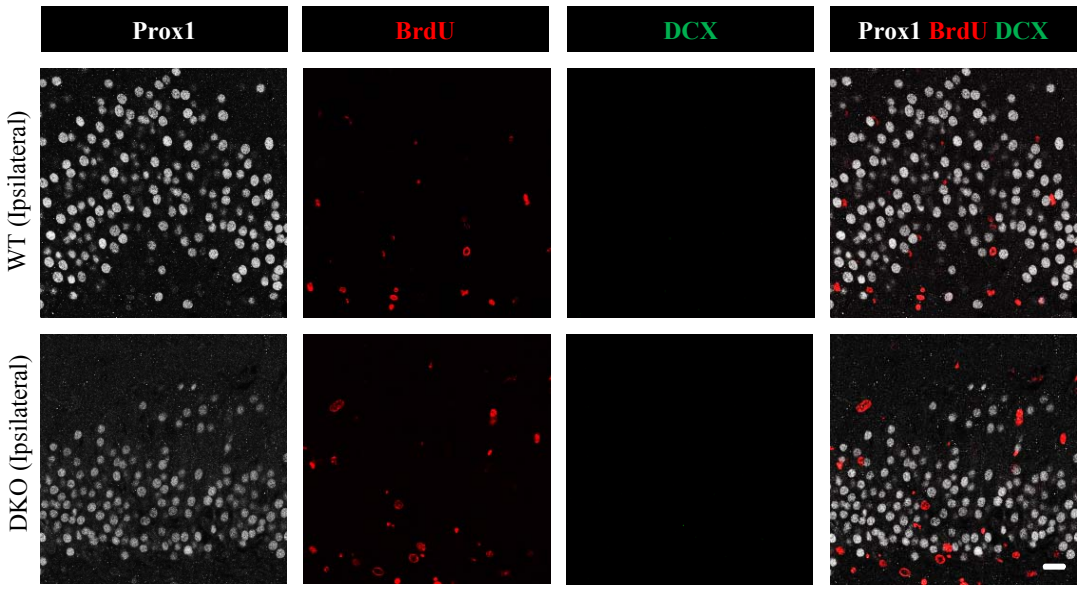

Figure 4.6.3: Reduced GCD in DKO mice is not caused by impaired neurogenesis. Prox1 (white), BrdU (red) and DCX (green) immunostaining in WT and DKO mice, 1 month after kainate injection. Coronal sections underneath the injection site were used for immunostaining. All images are from the ipsilateral DG. No DCX-positive cells were detected in the ipsilateral dentate gyrus, irrespective of the genotype. There was no colocalization between Prox1 and BrdU, indicating absence of newly born granule cells. Scale bar, 25 µm.

4.6.4 Seizure-induced neurogenesis in the contralateral hippocampus is dampened in DKO mice

Seizure is a strong stimulus for neurogenesis in the dentate gyrus (Marta et al., 2011). Absence of Cx43 and Cx30 is known to pose a limitation on the extent of adult neurogenesis in the DG. Therefore, by inspecting the post-kainate neurogenesis on the contralateral side, it was evaluated whether seizures are able to overcome this limitation. Prox1 was used as a marker for mature granule cells while DCXwas used to detect immature or newborn neurons. Cells co-labelled with Prox1 and BrdU represented newly (post BrdU administration) generated mature granule cells while cells co-labelled with DCX and BrdU represented newly generated immature neurons. The triple positive cells (not quantified) denoted immature granule cells. Both, the Prox1- BrdU colocalized cells and DCX- BrdU colocalized cells were significantly reduced in the contralateral dentate gyri of DKO mice (N = 3 per group, t test, * $p < 0.05$).

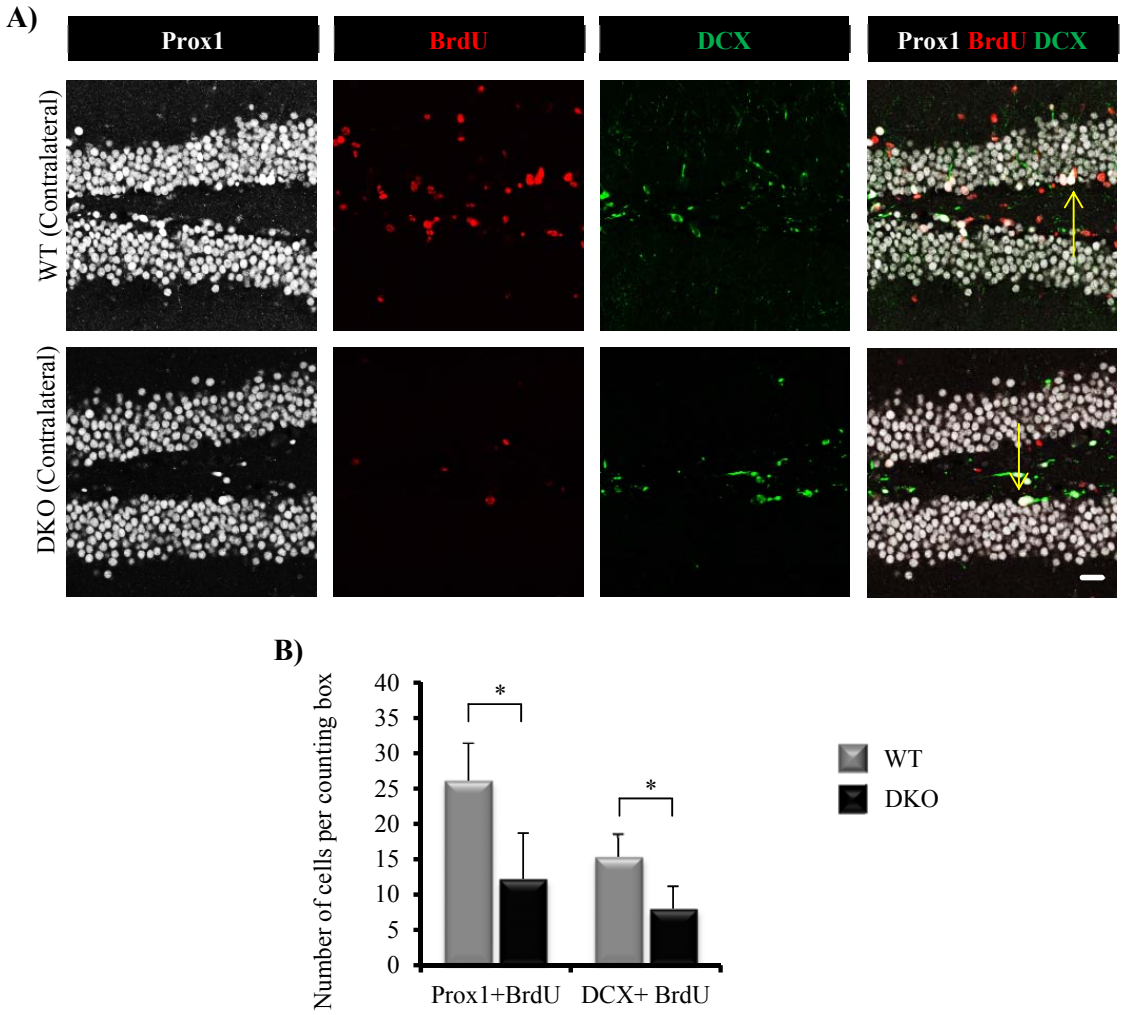

Figure 4.6.4: Seizure-induced neurogenesis in the contralateral hippocampus. A) Prox1 (white), BrdU (red) and DCX (green) immunostaining in WT and DKO mice, 1 month after kainate injection. Coronal sections underneath the injection site were used for immunostaining. All images are from the contralateral dentate gyrus. Merged images show colocalization of Prox1, BrdU and DCX (arrows). Scale bar, 25 µm. **B)** Quantification of Prox1- BrdU and DCX- BrdU colocalization. Counting boxes (290 x290 x 4 μm^3) were positioned 250 µm away from the outermost margin of the GCL flexure and perpendicularly oriented to the longitudinal axis of the GCL. Number of Prox1 and DCX cells colocalizing with BrdU-positive cells per counting box were counted. Prox1- BrdU positive cells represent newly (post BrdU administration) generated mature granule cells while DCX- BrdU cells represent newly generated immature neurons. The triple positive cells (not quantified) denote immature granule cells. There was a significant decline in Prox1- BrdU positive and DCX- BrdU types of cells in DKO mice. Thus, post-kainate neurogenesis was significantly reduced in DKO mice. N = 3 per group, * $p < 0.05$.

Table 4.6.4: Number of Prox1+ BrdU and DCX+ BrdU positive cells per counting box (290 x290 x 4 μm^3) per mouse in contralateral DG. All values are expressed in mean ± SD. N = 3.

Prox1+ BrdU		DCX+BrdU	
WT	DKO	WT	DKO
26.11 ± 5.33	12.22 ± 6.46	15.33 ± 3.28	8 ± 3.17

4.6.5 DKO mice have thinner GCL and lower basal neurogenesis

Kunze at al. reported that DKO mice have less Prox1-positive cells as compared with WT mice (Kunze et al., 2009b). Therefore, it was hypothesized that the GCL in DKO mice has lower thickness. This hypothesis was evaluated by measuring the GCL thickness in DKO and WT mice, which were not subjected to kainate injection. These mice were also assessed for the basal neurogenesis using BrdU administration through drinking water (as described in section 4.6.2, but without kainate injection). GCL thickness was measured at four locations on the blades of GCL and then averaged (Figure 4.6.5 A). As expected, the average thickness of the GCL in DKO mice was less than that in WT mice (54.5 ± 5.45 μm vs. 69.41 ± 2.92 μm respectively, N =3, $p < 0.01$) (Figure 4.6.5 B). Almost all of the BrdU- or DCX-positive cells were also labelled with Prox1 (Figure 4.6.5 C) indicating that most of the proliferative activity in the DG under basal conditions is neurogenic. The basal level of neurogenesis indicated by the numbers of BrdU, DCX and BrdU-DCX colocalizing cells was drastically reduced in DKO mice (Figure 4.6.5 B, Table 4.6.5). It is important to note here that the counting boxes used in this experiment (290 x290 x 24 μm^3) were 6 times larger than those used in section 4.6.4 (290 x290 x 4 μm^3). By comparing the BrdU-DCX positive cells (after adjusting for the counting boxes) between mice with and without seizures (Table 4.6.4 and 4.6.5), it can be concluded that the neurogenesis in epileptic DKO mice (kainate injected DKO mice) was 6 times higher than the neurogenesis in non-epileptic DKO mice (non-injected DKO mice) and 3 times higher than the neurogenesis in healthy-WT mice (non-injected WT mice).

Table 4.6.5: Number of DCX, BrdU and DCX+BrdU positive cells per counting box (290 x290 x 24 μm^3) per mouse in contralateral DG. All values are expressed in mean ± SD. N =3.

DCX		BrdU		DCX +BrdU	
WT	DKO	WT	DKO	WT	DKO
26.49 ± 4.17	12.55 ± 4.5	22.87 ± 2.17	11.55 ± 2.27	15.78 ± 2.08	7.83 ± 1.92

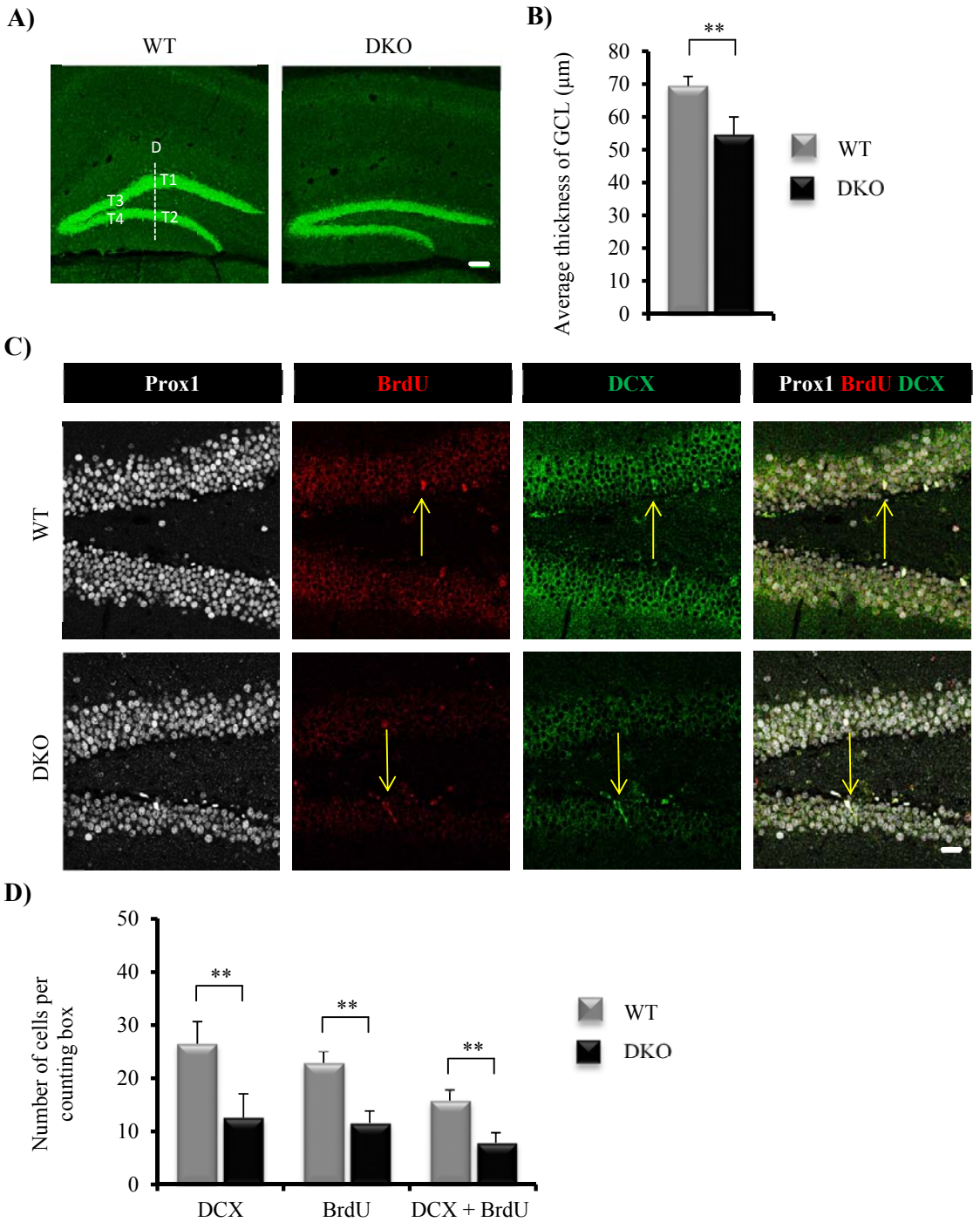

Figure 4.6.5: GCL thickness and basal neurogenesis in WT and DKO mice. A) Prox1 immunostaining labelling granule cells in hippocampi from WT and DKO mice. T1, T2, T3 and T4 are the thicknesses of GCL averaged to obtain a single parameter that was compared between WT and DKO mice. T1 and T2 were measured along the line D passing through the major curvature of the upper blade. T3 and T4 were measured at a distance half-way between line D and the tip of the hilus. Scale bar, 100 µm. **B)** The bar graph shows that the average thickness of the GCL was significantly lower in DKO mice. ** $p < 0.01$, N =3. **C)** Prox1 (white), BrdU (red) and DCX (green) immunostaining in DG of WT and DKO mice. Arrows indicate cells colocalizing BrdU and DCX. Almost all of the BrdU or DCX cells were also Prox1-positive. **D)** Quantification of basal neurogenesis. Counting boxes (290

x290 x 24 µm^3) were positioned 250 µm away from the outermost margin of the GCL flexure and perpendicularly oriented to the longitudinal axis of the GCL. Numbers of DCX, BrdU and DCX +BrdU colabelled cells were counted. Numbers of all of these cell types were reduced in DKO mice indicating reduced basal neurogenesis. N = 3, ** $p < 0.01$.

4.6.6 DKO mice have reduced post-seizure endothelial proliferation

Angiogenesis is enhanced in epilepsy and it takes place before the onset of spontaneous seizures (Rigau et al., 2007) (Newton et al., 2006). Endothelial cell proliferation is the hallmark of angiogenesis (Hellsten et al., 2004). Newly generated endothelial cells were visualized by co-immunostaining with the endothelial cell marker CD31 and BrdU (Figure 4.6.6 A and B). The ipsilateral hippocampus showed enhanced endothelial proliferation when compared with the corresponding contralateral hippocampus. This was evident in both, the DG and the CA1 region (Figure 4.6.6 C and D). However, the ipsilateral hippocampus of DKO mice showed statistically significant lower CD31+ BrdU positive cells when compared with the ipsilateral hippocampus of the WT mice (Table 4.6.3). These data indicate that post-seizure angiogenesis is modulated by astrocytic connexins.

Table 4.6.6: Number of CD31+BrdU positive cells per counting box (290 x 290 x 8 µm^3) per mouse in DG and CA1, 1 month after kainate injection. All values are expressed as mean ± SD. N = 3.

Genotype	DG		CA1	
	Contralateral	Ipsilateral	Contralateral	Ipsilateral
WT	4.56 ± 2.69	14.67 ± 0.58	5.33 ± 2	19.07 ± 1.74
DKO	3.11 ± 0.77	8.33 ± 2.65	5.33 ± 3.18	12.67 ± 2.6

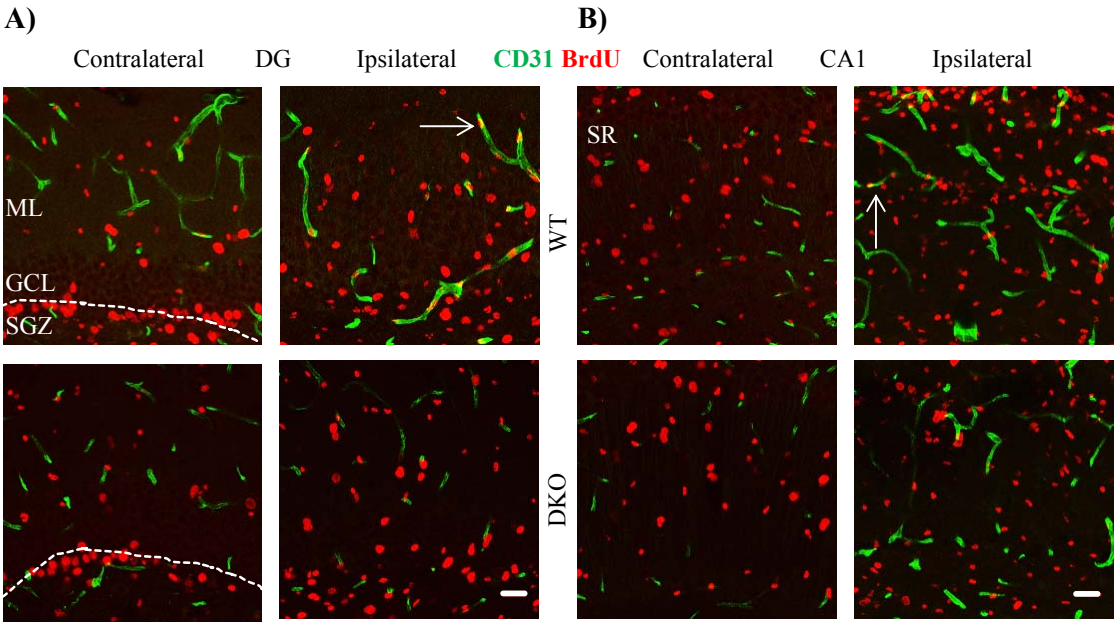

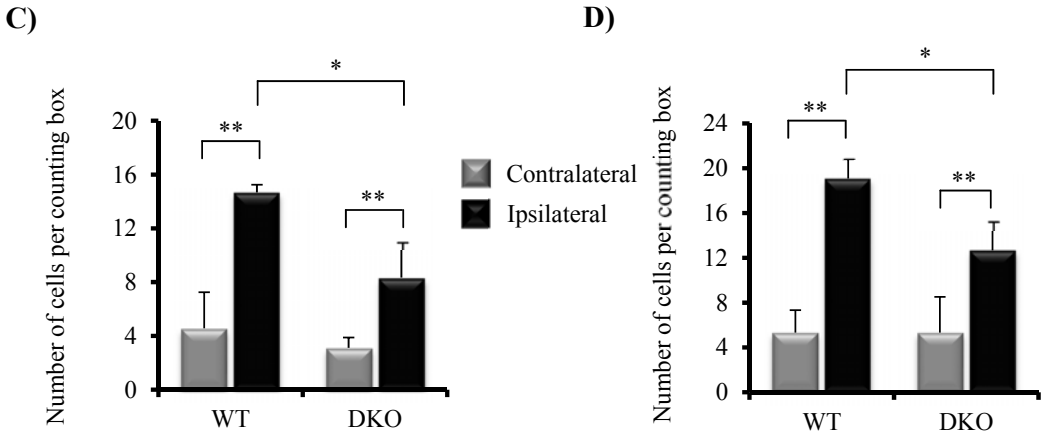

Figure 4.6.6: Endothelial proliferation 1 month after kainate injection. A-B) Endothelial cell marker CD31 (green) and BrdU (red) immunostaining in WT and DKO mice, in the DG (A) and CA1 (B). Co-localization of BrdU with CD31 indicates newly generated or a proliferating endothelial cell (examples indicated by arrows). Dotted line demarcates the subgranular zone (SGZ) of the GCL. ML: molecular layer, SR: stratum radiatum. Scale bar, 25 µm. **C-D)** Number of BrdU-positive CD31 cells per counting box (290 x 290 x 8 μm^3) in the DG (C) and CA1 (D). In both regions, the ipsilateral side showed more endothelial cell proliferation than the corresponding contralateral side. However, the ipsilateral side of DKO mice showed a lower proliferation when compared with the ipsilateral side of WT mice, indicating a modulatory role of astrocytic connexins on angiogenesis. ANOVA followed by post hoc Tukey´s test. N = 3 per group, ** $p < 0.01$.

4.6.7 Connexin-mediated modulation of angiogenesis in epilepsy

Increased angiogenesis in epileptic tissue was described more than 100 years ago (Sommer, 1880). Since endothelial proliferation was found to be altered in epileptic DKO mice, the vascular density was assessed using CD31 immunostaining. Images for the determination of vascular density were obtained from epileptic patients and the mouse model of epilepsy (1 and 3 months post kainate injection) (Figure 4.6.7 A). A point counting method was employed as reported previously (Rigau et al., 2007). A higher density of CD31-positive structures (N = 8, $p < 0.01$) was found in huamn hippocampal specimens with sclerosis (51.94 ± 12.58) as compared to those without sclerosis (32.53 ± 11.34) (Figure 4.6.7 B). Interestingly, similar differences were observed when comparing the ipsilateral and contralateral hippocampus in our mouse model at 3 month (51.16 ± 7.52 in contralateral vs. 69.16 ± 8.28 in ipsilateral, N = 3, $p < 0.05$) and 1 month post kainate injection (57.55 ± 6.40 in contralateral vs. 81.55 ± 8.94 in ipsilateral, N = 3, $p < 0.05$) (Figure 4.6.7 B). However, deletion of the astrocytic connexins abolished the differences in angiogenesis between the ipsilateral and contralateral hippocampi (50.55 ± 14.41 in contralateral vs. 60.33 ± 1.76 in ipsilateral, N = 3). This data indicate the association of connexins with seizure-induced angiogenesis.

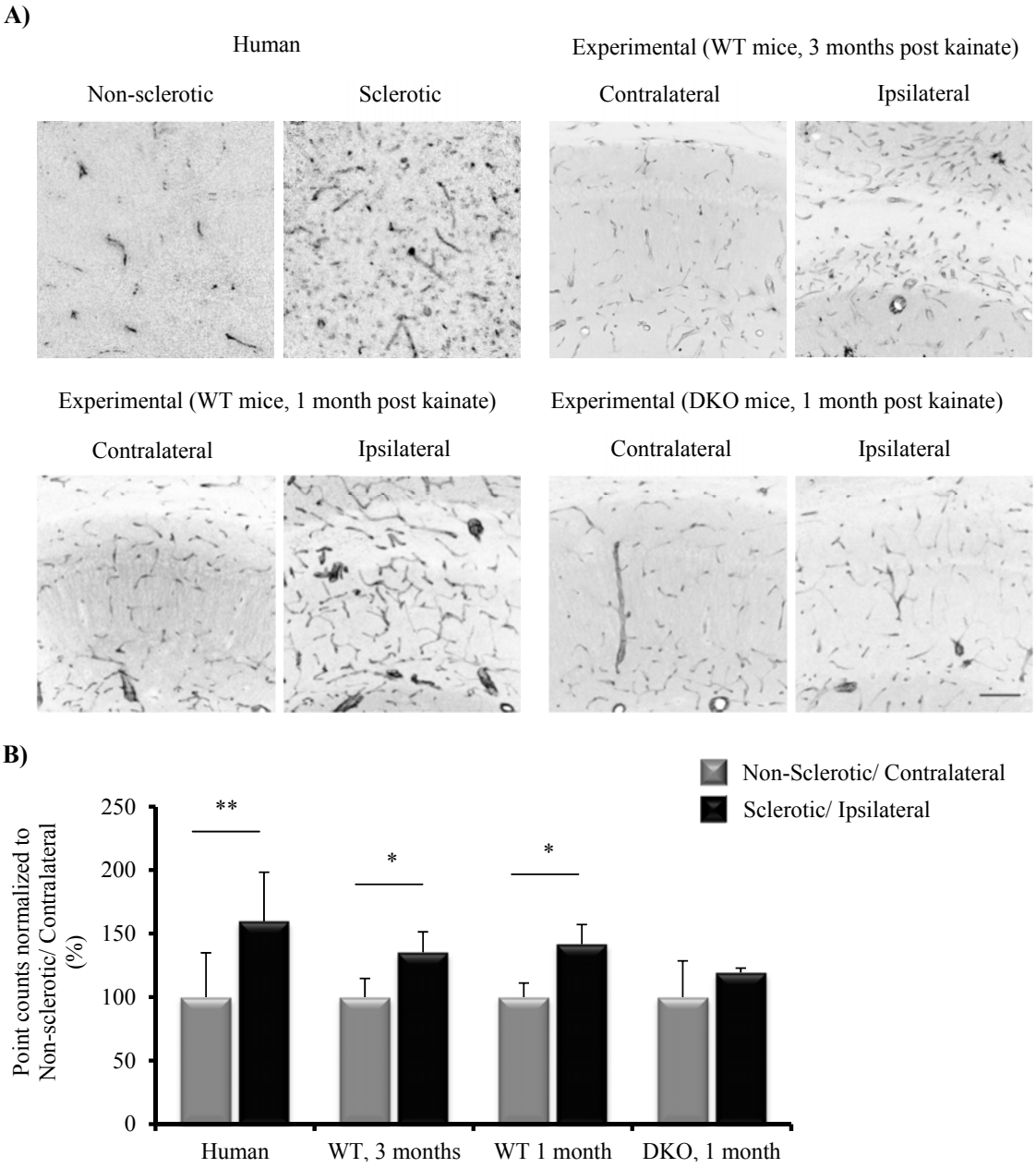

Figure 4.6.7: Connexin mediated modulation of angiogenesis in epilepsy. A) CD31 immunostaining in human and experimental epileptic specimens. CD31 delineates blood vessels. Note the increased vascular density in all sclerotic hippocampi (except DKO mice) when compared with corresponding non-sclerotic hippocampi. Scale bar, 100 μm **B)** The 'Point counting method' was applied to the confocal images from the CA1 region. The bar graph shows normalized to Non-sclerotic/ Contralateral point count values. The vascular density in sclerotic human specimens was 159.7% of non-sclerotic specimens ($p < 0.01$, $N = 8$ in each group). In the animal model, the vascular density in the ipsilateral hippocampus was 135.2% ($p < 0.05$, $N= 3$ in each group) and 141.7% ($P < 0.05$, $N= 3$ in each group) of the contralateral hippocampus at 3 and 1 month post kainate injection, respectively. In DKO mice, astrocytic deletion of connexins abolished the vascular density differences between ipsilateral and contralateral hippocampi.

4.6.8 Altered microglial activation in DKO mice after kainate injection

Activation of microglia is a primary inflammatory response to seizures (Eyo et al., 2016). This involves hypertrophy and process elongation of microglia and their proliferation (Avignone et al., 2015) (Avignone et al., 2008). Connexin hemichannels have been shown to regulate chemoptaxis and process elongation of microglia via release of ATP (Davalos et al., 2005). Therefore, with the help of Iba1-BrdU immunostaining, it was assessed whether the post-seizure microglial activation differs in DKO mice. The area occupied by microglia, 1 month after kainate injection was increased on the ipsilateral side when compared with the corresponding contralateral side in both, the CA1 and the DG (Figure 4.6.8 E and F, respectively). In the CA1 region, this increase was associated with an increase in the number of BrdU-positive Iba1 cells (Figure 4.6.8 D). In the DG, there was no difference in Iba1 proliferation across all the groups (Figure 4.6.8 C). Interstingly, 1 month post kainate injection in the CA1 region, DKO mice showed significantly reduced microglial activation on the ipsilateral side when compared with the ipsilateral side of WT mice (Table 4.6.8 A and B). Thus, the absence of astrocytic connexins modulated post seizure microglial activation and this effect was seen in the CA1 region and not in the DG.

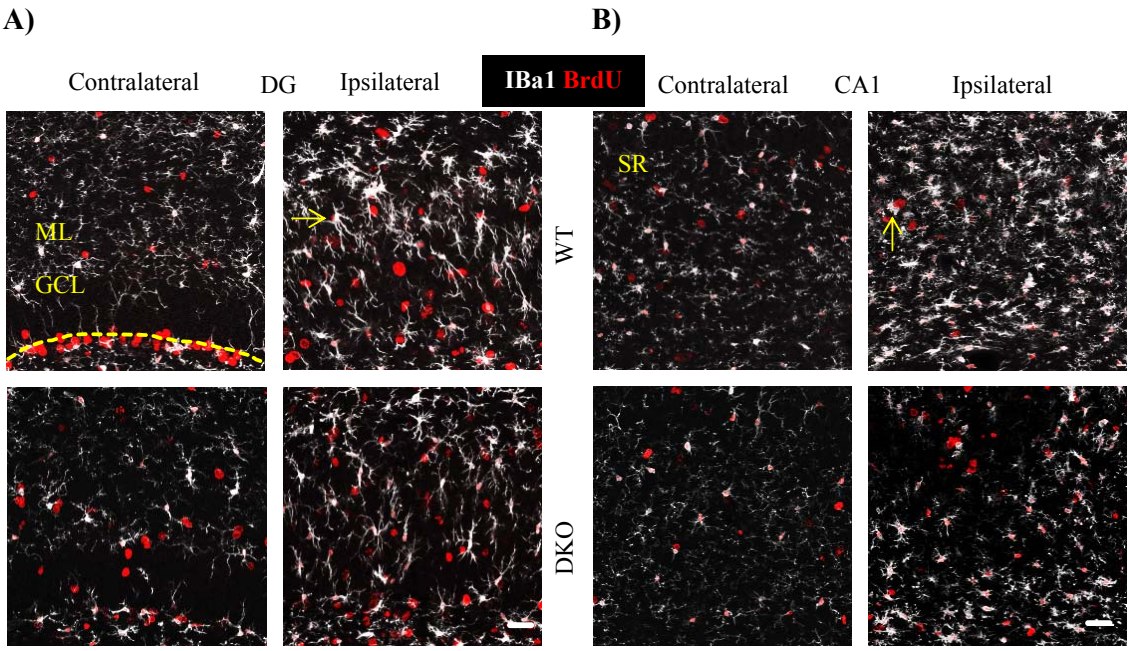

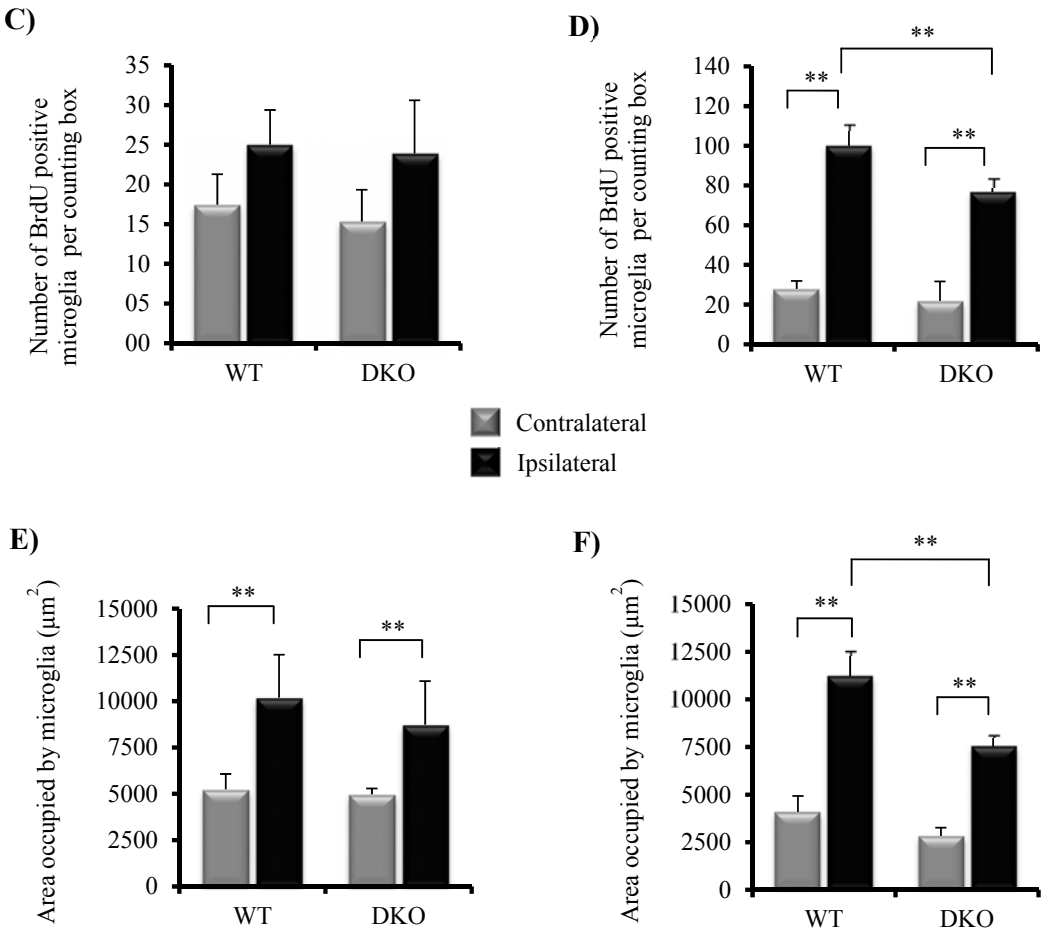

Figure 4.6.8: Altered seizure-induced microglial activation in DKO mice. A-B) Microglial marker Iba1 (white) and BrdU (red) immunostaining in WT and DKO mice, in DG (A) and CA1 (B), 1 month after kainate injection. Co-localization of BrdU with Iba1 indicates newly generated or a proliferating microglial cell (examples indicated by arrows). Dashed-line demarcates the sub-granular zone (SGZ) from granule cell layer (GCL). ML: molecular layer, SR: stratum radiatum. Scale bar, 25 µm. **C-F)** Quantification of microglial activation by counting newly generated microglia (C and D) and estimating area occupied by Iba1 signal (E and F) in counting boxes (290 x 290 x 8 μm^3). In the DG, microglia from the ipsilateral side occupied a higher area (E). The proliferation (C) however did not differ between the two sides. Microglial proliferation and area occupied by microglia were similar between kainate-injected WT and DKO mice. In the CA1 region, both the number of newly generated microglia and the area occupied by the Iba1 signal were higher on the ipsilateral side. Further, in contrast with the DG, in the CA1 region, these two parameters were significantly lower on the ipsilateral side of DKO mice when compared with the ipsilateral side of WT mice. ANOVA followed by post hoc Tukey´s test. N = 3 per group, ** $p < 0.01$.

Table 4.6.8.1: Number of Iba1- BrdU positive cells per counting box (290 x 290 x 8 μm^3) per mouse in DG and CA1, 1 month post kainate injection. All values are expressed as mean ± SD. N = 3.

Genotype	DG		CA1	
	Contralateral	Ipsilateral	Contralateral	Ipsilateral
WT	17.44 ± 3.83	25 ± 4.37	27.88 ± 3.97	100 ± 11.13
DKO	15.33 ± 4	23.89 ± 6.7	21.88 ± 9.75	76.77 ± 6.76

Table 4.6.8.2: Area occupied (μm^2) by Iba1-positive cells per counting box (290 x 290 x 8 μm^3) in DG and CA1, 1 month post kainate injection. All values are expressed as mean ± SD. N = 3.

Genotype	DG		CA1	
	Contralateral	Ipsilateral	Contralateral	Ipsilateral
WT	5242.9 ± 829.1	10191.9 ± 2319.1	4095.1 ± 834.6	11201.5 ± 1348
DKO	4971.7 ± 317.3	8729.3 ± 2359.7	2826.6 ± 439.1	7521.7 ± 650.6

5 Discussion

5.1 Connexin expression, distribution and phosphorylation in hippocampal specimens from epilepsy patients

Astrocytes in the sclerotic human hippocampus display an altered phenotype with atypical electrophysiological, morphological and molecular properties (Steinhäuser et al., 2016) (Coulter and Steinhäuser, 2015). They are completely devoid of dye coupling in contrast to the astrocytes in the non-sclerotic hippocampus (Bedner et al., 2015). The contribution of Cx43 to hippocampal astrocytic coupling in mouse exceeds that of Cx30 (Gosejacob et al., 2011). It is not known whether this holds true for human hippocampal astrocytes as well. Unlike Cx30, Cx43 protein has a very short half-life (1.5 to 5 h) (Kelly et al., 2015) and undergoes extensive post-translational modification, for example phosphorylation (Solan and Lampe, 2014). The distribution of Cx43 (plasma membrane vs. intracellular membranes) and its phosphorylation status can influence the level of gap junctional coupling. Expression studies of connexins (Cx43 and Cx30) in human epileptic specimens have been inconsistent (Mylvaganam et al., 2014)(Steinhäuser et al., 2016) . Moreover, the cellular distribution and phosphorylation of Cx43 in human specimens has not been addressed so far. In order to address these issues and explore the Cx43-related mechanisms leading to astrocytic uncoupling, expression, distribution and phosphorylation of Cx43 in hippocampal specimens from epilepsy patients were investigated in the present study.

The total Cx43 expression in a specimen is affected by the number of astrocytes present in that specimen, provided that Cx43 expression per astrocytes stays constant. As shown in figure 4.1.1, the number of S100β positive cells (most of which were GFAP positive) is 2.2 times higher in sclerotic CA1 region than that in the non-sclerotic one. There was also 1.8 fold increase in the average fluorescence intensity of Cx43. Thus, the overall increase in Cx43 expression paralleled the increase in the number of astrocyte like cells. The increased Cx43 puncta formed large plaques and occupied overall a larger surface area (Figure 4.1.2). Interestingly, there was a non-uniform distribution of Cx43 with preferential localization around blood vessels, as denoted by the distribution ratio. Cx43 is known to form larger plaques in endfeet as compared with Cx43 away from the blood vessels (Rouach et al., 2008). In fact, in the study by Rouach et al. (2008), Cx43 was found to be enriched in perivascular

endfeet of astrocytes and it was found to delineate the blood vessel walls. This study, however, did not give a quantitative measure of Cx43-enrichment. The distribution ratio, defined in section 3.3.7, measures the relative distribution of Cx43 with respect to the blood vessels. In non-sclerotic CA1, the distribution ratio was close to 1 while in sclerotic CA1 the ratio was 1.8, suggesting enhanced accumulation of Cx43 in the perivascular space (Figure 4.1.2 B). The perivascular space comprises of the basement membranes that enclose endothelial cells and pericytes. In larger vessels, pericytes are replaced by smooth muscle cells (Abbott et al., 2006). Astrocytic endfeet are closely adjacent to the basement membrane encircling the vessel (Serlin et al., 2015). In the CNS, Cx43 has been described to be present mainly in astrocytes and to some extent in ependymal cells (Rash et al., 2001). However, there have been reports of extra-astrocytic presence of Cx43 for example in pericytes (Li et al., 2003). Therefore, in the present study it was important to ascertain the exact cellular localization of perivascular Cx43.

Cx43 did not colocalize with the endothelial cell markers lectin and CD31. Its absence in pericytes was also confirmed by checking its colabelling with PDGFRβ and NG2 (Figure 4.1.3 A and B). Thus, the only plausible cellular component of the neurovascular unit that could harbor the observed perivascular Cx43 was the astrocytic endfoot. Indeed, Cx43 was closely associated with the astrocytic markers, S100β and GFAP (Figure 4.1.4.1). Being a membrane protein, its colocalization with any of these astrocytic markers (which are essentially cytoplasmic), could not be shown. Moreover, the diffuse GFAP staining in the sclerotic CA1 and the limited optical resolution obtained by the confocal microscope, made it difficult to assign the exact location of Cx43 with respect to the blood vessel-astrocyte interface. These limitations were overcome by employing a recently developed expansion microscopy technique (Chozinski et al., 2016). In expanded images, most of the Cx43 in the perivascular space was found to be present on the parenchymal side of the astrocytic endfoot as GFAP or S100β separated the Cx43 signal from the vessel wall (Figure 4.1.4.1). Hence, most of the Cx43 proteins obviously do not face vessel walls. Expansion microscopy also made it possible to resolve the fine GFAP positive structures. Interestingly, Cx43 was also observed to be hemmed between GFAP branches (Figure 4.1.4.2). It could not be resolved whether these puncta represented fully formed gap junctions, hemichannels or Cx43 monomers. Even though the majority of perivascular Cx43 immunoreactivity was astrocytic, a minor endothelial and pericytic expression of Cx43 could not be ruled out.

After confirming the presence of Cx43 in astrocytes, its distribution in cellular compartments was studied by Western blotting. Cx43 is a membrane protein synthesized in the rough

endoplasmic reticulum, oligomerized in the trans-golgi network and it reaches the plasma membrane in a hexameric and phosphorylated form (Laird, 2006). Only Cx43 in the plasma membrane can contribute to gap-junctional coupling. Therefore, the plasma membrane associated Cx43 was analyzed by Western blotting. Surprisingly, the levels of plasma membrane Cx43 did not differ between sclerotic and non-sclerotic hippocampi (Figure 4.1.5). This data contradicted the immunostaining data which showed not only an increase in the fluorescence intensity of Cx43 but also increased plaque size and area occupied by Cx43. It is important to note here that the immunostaining did not distinguish between Cx43 at the plasma membrane and intracellular membrane. It rather represented total Cx43 expression. In order to address this discrepancy between plasma membrane Cx43 levels and immunostaining data, total (whole-cell) Cx43 protein levels were assessed. Western blot of total Cx43 showed a marked increase in the sclerotic hippocampus (Figure 4.1.6). This implied that despite of augmented total Cx43 expression, plasma membrane Cx43 did not increase proportionally to its synthesis. Thus, the enhanced total Cx43 levels in human sclerotc specimens did not lead to increased assembly of Cx43 channels in the plasma membrane, possibly indicating its impaired plasma membrane translocation.

Dye coupling was completely absent in sclerotic specimens (Bedner et al., 2015) despite of the presence of Cx43 at the plasma membrane and increased plaque size (Figure 4.1.5 and 4.1.2). There could be two reasons behind this contradiction: 1) assembly of gap junctions (i.e. docking of two connexons from neighboring astrocytes) was impaired because of altered morphology of astrocytes which resulted in the loss of contact between two apposing membranes. 2) The gap junctions were closed, for example, due to post-translational modifications of Cx43. Assembled gap junctions tend to aggregate across plasma membranes of the two cells forming large plaques (Laird, 2006). Thus, the size of assembled gap junctions is more than the non-docked connexons. Indeed, plaques were larger in the sclerotic tissue (Figure 4.1.2). Moreover, many Cx43 puncta could be seen hemmed between astrocytic processes (Figure 4.1.4.2). It could not be concluded from the images whether these puncta represented fully formed gap junctions between astrocytic processes. However, it was clear from the previous report that there was no functional gap junction coupling between astrocytes in sclerosis (Bedner et al., 2015). Thus, if fully formed gap junctions between astrocytes existed in the sclerotic tissue, these channels were non-functional. Existence of a fully formed but non-functional gap junction implies channel closure.

Gap junction closure is influenced by both, the open probability and the unitary conductance of the channel. Phosphorylation is known to influence both of these channel properties (Moreno and Lau, 2007). Among 21 putative sites, phosphorylation on S279/282, S255 and S262 has been shown to reduce the open probability of Cx43 channels (Thévenin et al., 2013). All of these sites are targets of MAPKs. However, S262 can be phosphorylated by CDK-2 as well. While phosphorylation of S279 and S282 cannot be differentiated from each other with currently available techniques, phosphorylation of S255 can be distinguished from that of the neighboring sites. Therefore, phosphorylation of S255 was investigated with the help of a phospho-specific antibody. The fraction of plasma membrane Cx43 phosphorylated at S255 was increased in sclerotic specimens, indicating potential drop in the open channel probability (Figure 4.1.7). Phosphorylation at S257 or S368 has been suggested to shift the conductance of channels to a lower state. S257 can be phosphorylated by PKG (Kwak et al., 1995) while S368 is one of the targets of PKC (Ek-Vitorin et al., 2006). However, the residue 257 in human Cx43 is an alanine and not a serine in contrast with mouse or rat Cx43. As a result, phosphorylation at position 257 cannot take place in human Cx43. Therefore, only phospho-S368 was investigated by Western blotting. The fraction of Cx43 phosphorylated on 368 did not differ between sclerotic and non-sclerotic hippocampi (Figure 4.1.7). Taken together, phospho-specific Western blots revealed altered phosphorylation at least on Serine 255 which might have contributed to uncoupling.

Seizures are known to open the BBB and cause albumin leakage into the brain parenchyma (Vliet et al., 2007). Extravascular albumin decreases the gap junctional coupling in astrocytes (Braganza et al., 2012). Therefore, albumin extravasation was assessed in human epileptic specimens. In both, sclerotic and non-sclerotic specimens albumin was found to be present inside the blood vessels. However, perivascular albumin immunoreactivity was seen only in sclerotic specimens (Figure 4.1.8) consistent with findings from Ravizza et al., 2008. Extravascated albumin is taken up by astrocytes by a TGFβ receptor mediated process (Ivens et al., 2007). The process can trigger inflammatory reactions in the brain parenchyma. Albumin is known to activate microglia and astrocytes by inducing inflammatory cytokines (Ralay Ranaivo and Wainwright, 2010). Remarkably, these effects are mediated by activation of MAPKs in astrocytes. Activated MAPKs may in turn phosphorylate Cx43 on the sites discussed above and thereby cause uncoupling. In summary, impaired translocation of Cx43 to the plasma membrane, its preferential distribution around blood vessels and phosphorylation at serine 255 possibly as a result of albumin extravasation were associated with astrocytic uncoupling in human hippocampal sclerosis.

5.2 Three months after kainate injection the mouse model recapitulates key features of human epilepsy

In the unilateral kainate injection model, at 3 months after injection, the ipsilateral hippocampus showed pronounced loss of pyramidal neurons in all subfields, astrogliosis and granule cell dispersion. Astrocytic coupling was also lacking in SR of the CA1 region. At this time point the mice consistently showed spontaneous generalized seizures (Bedner et al., 2015). These morphological and functional features resemble those in human MTLE-HS. The contralateral hippocampus in the mouse model appeared morphologically unaffected and served thus as a pseudo control. Since, the human MTLE-HS displayed altered distribution and phosphorylation of Cx43 (section 5.1); I investigated whether these features were also observed in the mouse model.

As discussed in section 5.1, increase in the number of astrocytes accompanied enhanced total Cx43 expression in the sclerotic human hippocampus. In the mouse model, the ipsilateral hippocampus also showed a ~ 2 times increase in the number of astrocytes (Figure 4.2.1 B) which was associated with a 1.8 fold increase in average Cx43 fluorescence intensity (Figure 4.2.2 B). It is likely that in both cases the amount of Cx43 per astrocyte did not change. Nevertheless, enhanced Cx43 expression was observed in the form of larger plaques in the ipsilateral hippocampus. These plaques were preferentially distributed around blood vessels as indicated by the distribution ratio. Cx43-mediated astrocytic coupling around blood vessels performs many functions including transport of metabolites and nutrients through gap junctions (Rouach et al., 2008) and regulating the vascular tone (Filosa et al., 2016). Neuronal activity requires continuous supply of glucose, which is converted to lactate and then released into the extracellular space by astrocytes. Astrocytic gap junctions play an important role in the distribution of glucose and its metabolites from blood vessels to regions of neuronal activity distal from the vasculature. Demand for energy is enhanced during seizure activity (Wu et al., 2015) posing immense importance on gap junction mediated supply of glucose. Although, Cx43 immunoreactivity around blood vessels was enhanced in the ipsilateral hippocampus 3 months post kainate, there was no astrocytic coupling. Thus, increased Cx43 in the ipsilateral hippocampus may not result in increased energy supply to the firing neurons.

Astrocytes are known to regulate the vascular tone by Ca^{2+} mediated release of vasoactive molecules (Filosa et al., 2016). Cx43 hemichannels, which open up in response to the reduced extracellular Ca^{2+}, regulate intercellular Ca^{2+} waves and ATP release in astrocytes (Stout et al., 2002).

Interestingly, during epileptic discharges, extracellular Ca^{2+} is markedly reduced creating a favourable environment for hemichanel opening (Torres et al., 2012). Thus, directly or indirectly astrocytic Cx43 hemichannels might cause the release of vasoactive molecules for example ATP, phospholipase A2 and thereby control the vascular tone. These molecules have also been implicated in BBB disruption (Abbott et al., 2006). Indeed, albumin immunoreactivity indicative of BBB disruption was seen around blood vessels in the ipsilateral hippocampus (Figure 4.2.6). Notably, Cx43 upregulation was also seen in the same region (Figure 4.2.2 A). However it was not clear from the immunofluorescence images whether the perivascular Cx43 was in a hemichanel or gap junction configuration. In order to investigate this, BN PAGE, a method that allows separating proteins according to their native conformation, was used. Cx43 showed three bands at around 146, 240 and 480 kDa, indicating configurations as trimer, hexamer and dodecamer (Figure 4.2.7). Remarkably, the band representing a putative dodecamer configuration had less intensity in the ipsilateral hippocampus. There was no difference in the hexamer bands. Thus, most of the perivascular Cx43 in ipsilateral hippocampus is seemed to be in a hemichanel configuration.

Owing to its short half-life, Cx43 is continuously removed from the plasma membrane and new channels are recruited in the plaques (Laird, 2006). The rate of Cx43 synthesis has to match the rate of channel removal in order to maintain the pool of connexons at the plasma membrane. When the rate of Cx43 synthesis far exceeds the rate of channel recruitment at the plasma membrane, most of the Cx43 is seen in intracellular stores, for example, Golgi apparatus and endoplasmic reticulum. This intracellular Cx43 is not available for coupling. Indeed, a disparity between plasma membrane Cx43 levels and Cx43 immunostaining data was observed in the ipsilateral hippocampus, implying that most of the Cx43 resided in intracellular stores (Figure 4.2.2 and 4.2.3). Moreover, although total Cx43 levels were increased (Figure 4.2.4), Cx43 levels at the plasma membrane were not, indicating impaired translocation of Cx43 to the plasma membrane, an observation similar to that made in human sclerotic hippocampus. Interestingly, there was a shift towards the P2 band on the Western blot (Figure 4.2.3), signifying an altered phosphorylation of Cx43. Our data from human specimens revealed augmented phosphorylation at serine 255 but unchanged phosphorylation at serine 368. Therefore, phosphorylation on these sites was also investigated in the mouse model. The fraction of Cx43 phosphorylated at serine 255 was two times higher in the ipsilateral hippocampus compared with the contralateral hippocampus. On the other hand, there was a fourfold upsurge in serine 368 phosphorylation (Figure 4.2.5). As discussed earlier, phosphorylation at both of these sites results in reduced coupling albeit by different

mechanisms. Serine 255 phosphorylation causes reduced open probability (Thévenin et al., 2013) while serine 368 phosphorylation results in lower channel conductance (Ek-Vitorin et al., 2006). Phosphorylations at these two sites are expected to have a synergistic effect manifesting in uncoupling. Taken together, 3 months after kainate injection, the mouse model recapitulated many features of Cx43 expression, distribution and phosphorylation observed in human sclerotic hippocampus. In order to see if these changes take place during early uncoupling potentially causing epileptogenesis, 4 h time point after kainate injection was investigated.

5.3 Altered phosphorylation of Cx43 is an early event in epileptogenesis

MTLE-HS involves, among other features, loss of pyramidal neurons in the hippocampus. This loss is a result of a progressive process with its beginning in the status epilepticus (Thom, 2014). Intracortical injection of kainate above the hippocampus induces status epilepticus in mice. This phase is characterized by synchronous rapid firing of principal hippocampal neurons for 6 to 12 h. As early as 4 h after kainate injection, astrocytic coupling is reduced approximately by 50%. However, no TUNEL positive apoptotic neurons were seen in the hippocampus (Bedner et al., 2015). Therefore, changes in astrocytes may be associated with the mechanisms of subsequent neuronal death. Reduction in coupling is an important astrocytic change potentially causative to epileptogenesis. In order to investigate mechanisms causing uncoupling in the early phase of epileptogenesis, modifications of Cx43 were investigated.

Cx43 showed a punctate staining pattern in both contralateral and ipsilateral CA1 regions 4 h after kainate injection (Figure 4.3.3 A). Plaque size and number as well as the area occupied by Cx43 were not modified by kainate injection (Figure 4.3.3 B). However, in the Western blot ipsilateral Cx43 displayed a shift towards the P2 band (Figure 4.3.4), similar to that seen at 3 months post kainate (Figure 4.2.3). The total Cx43 levels, however, were unchanged at 4 h post kainate. This shift in the P2 band was the result of kainate and not mere an injection artifact as demonstrated by Western blot performed with lysates from sham injected mice (Figure 4.3.4 B and D). The P2 band is the slowest migrating band of Cx43 resulting from complex conformational changes in the phosphorylated Cx43 protein (Solan and Lampe, 2009). Phosphorylation at S325, S328 and S330 is believed to mediate the shift to the P2 band conformation (Lampe et al., 2006). Phosphorylation at these sites is a signal for the assembly of gap junctions (Cooper and Lampe, 2002). However, phosphorylation at S262 also results in slower migrating Cx43 bands (Solan and Lampe, 2008). There are 21 putative phosphorylation sites described for Cx43 (Pogoda et al., 2016). Bands in the Western blot do not reveal exactly which of these sites have been phosphorylated. Moreover, not all phosphorylations result in changes of mobility in SDS PAGE. Therefore a method dissecting the phosphorylation profile of Cx43 was sought. Mass spectrometry based phosphoproteomics has been proposed to resolve the phosphorylation profile of Cx43 (Chen et al., 2013).

Sample preparation is the critical step in the mass spectrometry workflow. Its efficiency is determined by purity and quantity of the isolated protein of interest. Proteins in the lysate tend to bind non-specifically to magnetic beads used for immunoprecipitation. Hence, it was important to keep the quantity of the beads as low as possible. Optimization of the bead-antibody proportion revealed that a minimum ratio of 0.023 between beads and antibody was sufficient to cause the complete adsorption of the antibody on to the beads (Figure 4.4.1.1). Similarly, the minimum volume of the antibody required to extract all of the Cx43 from 1 mg of the lysate was estimated to be ~100 µl (Figure 4.4.1.2). By means of these two estimates, the immunoprecipitation reaction was scaled up and efficiency of the immunoprecipitation was confirmed using antibody targetting the N-terminus of Cx43. Interestingly, total membrane preparations gave better yield of phospho-Cx43 and hence were used in the subsequent experiments (Figure 4.4.1.3). The optimized protocol for sample preparation was applied to lysates from mice 4 h post kainate.

In total, 14 sites (1 tyrosine, 2 threonines and 11 serines) with phosphorylation were detected (Table 4.4.3.1). Of these sites, phosphorylation at T290 and Y301 has been described for the first time. Statistical analysis of the normalized chromatographic peak areas of the phospho-peptides revealed differential phosphorylation at 4 sites namely S328, S330, S257 and S262 (Table 4.4.3.2). The fact that there was no difference between ipsilateral and contralateral hippocampi of saline-injected mice proved that the changes in the phosphorylation in kainate injected mice were caused by kainate and were not mere an injection artifact.

Among the differentially phosphorylated sites, phosphorylation at S328 and S330 (and also at S325) by casein kinase 1 has been shown to enhance assembly of gap junctions (Cooper and Lampe, 2002). These phospho-sites therefore can be viewed as promoters of gap junction formation. Indeed, in ischemic hearts, which show decreased gap junctions in the intercalated discs, S328, S330 (and S325) phosphorylation was reduced 8 fold (Lampe et al., 2006). Replacing serines at these sites by glutamate (mimicking phosphorylation, S3E mice) resulted in slower migrating Cx43 bands, which were abolished after substitution by alanine (resembling dephosphorylation, S3A mice) (Remo et al., 2011). Consequently, S3E mice were resistant to ischemia-induced gap junction remodeling and arrhythmias (Remo et al., 2011). Interestingly, S3A constructs in cell culture showed decreased dye coupling and channel conductance (Lampe et al., 2006). All these findings highlight the importance of phosphorylation at S328 and S330 for coupling. In the present study, phosphorylation at these sites was reduced in kainate-injected mice as compared with saline-injected mice (Figure

4.4.3.2 A and B). However, there was no difference between ipsilateral and contralateral hippocampus of kainate-injected mice. It is worth noting here that the ipsilateral hippocampus showed reduced coupling not only in comparison with the contralateral hippocampus but also in comparison with both hippocampi of saline injected mice (Bedner et al., 2015). Therefore, it is unlikely that dephosphorylation at S328 andS330 alone might have caused the observed uncoupling.

S257 can be phosphorylated by CamKII and PKG. Phosphorylation by CamKII has been shown only in an *in vitro* assay (Huang et al., 2011) while PKG-mediated *in vivo* phosphorylation of S257 has been induced by cGMP (Kwak et al., 1995). In the latter study, 8-bromoguanosine 3': Y-cyclic monophosphate (a membrane-permeant activator of PKG), shifted the conductance of wild-type Cx43 channels to a lower state. The effect was abolished when serine at 257 was replaced by alanine (Kwak et al., 1995). Our mass spectrometric analysis revealed increased phosphorylation at S257 in the ipsilateral hippocampus of the kainate injected mice as compared with sham injected mice (Figure 4.4.3.2 C). This indicated a possible activation of the nitric oxide- cGMP-PKG pathway in ipsilateral astrocytes. S100β, which is released by astrocytes upon kainate injection (Figure 4.3.1.1 A, discussed in section 5.4), is known to increase nitrite production in astrocytes (Hu et al., 1996). Thus, S100β could be a mediator of kainate-induced phosphorylation of Cx43 at S257. Alternatively, activation of CamKII in ipsilateral astrocytes might have resulted in increased S257 phosphorylation.

S262 was the only phospho-site which in the kainate-injected mice showed increased phosphorylation ipsilaterally (Figure 4.4.3.2 D). Increased S262 phosphorylation was further confirmed by Western blot using a specific antibody against Cx43 phosphorylated at S262 (Figure 4.4.4). S262 is the target of CDK-2 and MAPKs (Pogoda et al., 2016). CDK-2 is believed to be active during mitosis and causes gap junction internalization by S262 and S255 phosphorylation (Lampe et al., 1998)(Doble et al., 2004). MAPKs, on the other hand, have been shown to be upregulated in astrocytes following kainate-induced seizures (Choi et al., 2003). They can phosphorylate Cx43 at S255, S262 and S279/282 (Thévenin et al., 2013). In general, phosphorylation of Cx43 by MAPKs decreases the open probability of gap junctions and thereby attenuates coupling (Thévenin et al., 2013). In endothelial cells, MAPK-mediated phosphorylation of Cx43 upon VEGF stimulation has been shown to result in gap junction internalization (Nimlamool et al., 2015). Both of these mechanisms (reduction in open probability and internalization of the gap junctions) can lead to uncoupling.

MAPKs are known to be downstream effectors in inflammatory cascades (Kaminska et al., 2009)(Kyriakis and Avruch, 2012). Stimulation of astrocytic TLR-4 resulted in a proinflammatory environment involving MAPK activation (Gorina et al., 2011). MAPKs are also activated by cytokines, for example TNFα (Takada and Aggarwal, 2004). Indeed, cytokine mediated uncoupling in cultured astrocytes was prevented by a MAPK inhibitor (Retamal et al., 2007). Incubation of acute slices with cytokines also resulted in astrocytic uncoupling (Bedner et al., 2015). Interestingly, this cytokine mediated uncoupling was rescued by co-treatment with the soluble TNFα blocker, XPRO 1595 (Dupper, 2014). Expression of cytokines is known to be upregulated following seizures (Vezzani and Granata, 2005). For example, 6 h after electrically induced limbic seizures, TNFα and IL-1β transcripts reached their peak levels (De Simoni et al., 2000). Another study has reported the activation of MAPK at 6 h after kainate injection (Choi et al., 2003). With this background information, S262 phosphorylation was investigated in acute hippocampal slices incubated with the cytokines TNFα and IL-1β. The increased S262 phosphorylation upon cytokine incubation was attenuated by co-treatment with XPRO 1595 (Figure 4.4.5 A, B and C). Intriguingly, cytokine treatment also resulted in a Cx43 band shift similar to that seen after kainate injection. This shift towards the P2 band was prevented by XPRO 1595 (Figure 4.4.5 D). This data and the supporting literature propose a mechanistic link between cytokine mediated Cx43 phosphorylation at S262 and astrocytic uncoupling following kainate injection. Importantly, this alteration in Cx43 phosphorylation takes place quite early after kainate injection (4 h post injection), highlighting its potential causative role in epileptogenesis.

5.4 Changes in astrocytic immuno-labelling 4 h post kainate injection

GFAP and S100β are the most commonly used markers to identify astrocytes. S100β is a member of cytosolic EF hand calcium binding proteins (Rothermundt et al., 2003) and plays a crucial role in intracellular Ca^{2+} homeostasis, cell morphology and motility (Donato et al., 2013). GFAP is a type III intermediate filament protein mainly responsible for the cyto-architecture of astrocytes (Hol and Pekny, 2015).

There was a drastic reduction in S100β immunoreactivity in the ipsilateral CA1 region 4 h after kainate injection (Figure 4.3.1.1). In order to assess whether this was caused by any modification in the epitope targeted by the antibody, another antibody with different clonality was employed. Both of these antibodies failed to show S100β signal in the ipsilateral CA1 area, while the signal was persistent in the corresponding contralateral area and ipsilaterally distant from the injection site. This implied that the reduction in immunoreactivity was confined to the ipsilateral CA1 area underneath the injection site (dorsal hippocampus). S100β is known to be released by astrocytes by various stimuli. Upon activation, astrocytes release S100β to regulate extracellular Ca^{2+} which in turn influences neuronal rhythmic firing (Morquette et al., 2015). S100β is also one of the 'damage associated molecules' whose presence in the CSF indicates substantial CNS damage (Sorci et al., 2010). Presence of S100β in the CSF has also been associated with the degree of cerebral infarction in stroke patients (Brouns et al., 2010). In general, the basal level of extracellular S100β is low in the hippocampus. Interestingly, in acute hippocampal slices, kainate potentiated the release of S100β in a neural-activity-dependent way (Sakatani et al., 2008). Further, it was shown that kainate-induced astrocytic S100β release was dependent on presynaptic glutamate discharge. This glutamate then activated metabotropic glutamate receptors (mGluR 3) on astrocytes which prompted S100β release by a mechanism independent of Cx43 hemichannels. The concentration and the volume of kainate used were 400 nM and 500 µl respectively. As described in section 3.1.2, intracortical injection of 70 nl of 20 mM kainate was used to induce status epilepticus in our mouse model. Thus, the amount of kainate used in our animal model was 7 times higher than that used in the study by Sakatani et al., 2008. This amount of kainate is expected to cause a massive release of S100β into the extracellular space, virtually emptying cellular S100β. This could be the reason why S100β immunoreactivity was almost negligible in the ipsilateral CA1 as compared with the contralateral CA1, when imaged under same microscope settings. GFAP immunostaining however was retained (Figure 4.3.1.2 A). In summary, the apparent disappearance of S100β

immunoreactivity did not indicate the absence of astrocytes. Release of S100β could be a plausible explanation behind the loss of signal.

In the absence of ipsilateral S100β labelling, counting of astrocytes was based on GFAP positive cells co-labelled with the nuclear marker Hoechst. The total number of GFAP positive cells was reduced by 27.9% in the ipsilateral SR as compared with contralateral SR (Figure 4.3.1.2 B). The result was confirmed by employing two antibodies targetting different epitopes. There was also a 24.4% reduction in the number of nuclei corroborating the decline in the number of astrocytes (Figure 4.3.1.2 B). This reduction might indicate astrocytic death. The known pathways for cell death comprise of apoptosis, necrosis, autophagy, oncosis and pyroptosis (Fink and Cookson, 2005). Apoptosis is a programmed cell death that involves initiator caspases stimulating effector caspases to cleave cellular structures (Elmore, 2007). Apoptotic cells display cytoplasmic and nuclear condensation, DNA fragmentation, and formation of apoptotic bodies. However, the plasma membrane usually remains intact displaying surface molecules targetting for phagocytosis. In the absence of phagocytosis, apoptotic bodies may proceed to lysis and secondary or apoptotic necrosis (necroptosis) (Fink and Cookson, 2005). Signals like intracellular Ca^{2+}, oxidative stress, nitric oxide (NO), mitochondrial dysfunction and endoplasmic reticulum stress can initiate apoptosis in astrocytes (Takuma et al., 2004). Of these, rise in the intracellular Ca^{2+} and activation of NO (by the action of S100β) pathway are expected to take place in kainate-exposed astrocytes. During epileptiform activity, an increase in the frequency of Ca^{2+} oscillations in astrocytes has been reported (Tian et al., 2005). S100β release (for example induced by kainate) from astrocytes can activate a NO pathway in a paracrine manner (Hu et al., 1996). Both of the above-mentioned events (Ca^{2+} increase and activation of NO pathway) are inducers of apoptosis (Takuma et al., 2004). Indeed, kainate-induced emptying of astrocytic S100β stores was observed during this study (Figure 4.3.1.1 A). Moreover, S100β has been found to induce apoptotic cell death in cultured astrocytes via a nitric oxide-dependent pathway (Hu and Van Eldik, 1996). Therefore, the possibility of astrocyte death via apoptosis was checked with A TUNEL assay. This assay detects DNA breaks caused by apoptosis. Surprisingly, there were no TUNEL positive nuclei in the CA1 region, 4 h after kainate injection (Figure 4.3.2). This implied that any cell death via apoptotic pathway could be ruled out. It is important to note here that DNA breaks (detected by TUNEL) are features of late stage apoptosis. Any cell in the early phases of apoptosis cannot be detected by TUNEL. Further, apoptosis is followed by phagocytosis by innate or adaptive immune cells. If this takes place for instance before the 4 h time point post kainate, then it is not possible to detect apoptosis at this time point. In this case,

it is desirable to perform the TUNEL assay at an earlier time point, for example 2 h after kainate injection.

There are other pathways of cell death, mainly necrosis, autophagy, oncosis and pyroptosis (Fink and Cookson, 2005). Necrosis is defined as a passive, non-programmed (non-apoptotic) cell death. It refers to the morphological remains seen after a cell has already died and reached equilibrium with its surroundings. Thus, necrotic features are indicative of an end-stage death rather than any mechanism leading to the death. Further, any programmed cell death pathway can secondarily lead to necrosis. Autophagy is characterized by the degradation of cellular components within the intact dying cell in autophagic vacuoles. The morphological appearances of autophagy comprise vacuolization, degradation of cytoplasmic contents, and chromatin condensation. Oncosis involves cellular and organelle swelling in addition to membrane breakdown, with the eventual release of inflammatory cellular contents. Pyroptosis is mediated by the activation of caspase-1 leading to cell lysis and release of inflammatory cellular contents. This pathway is therefore inherently pro-inflammatory. All of these pathways might present indistinguishable morphological features. Therefore, it is important to have specific markers for these pathways. Moreover, as discussed in the earlier paragraph, any mechanistic investigation of astrocytic death 4 h post kainate should be performed at an earlier time point, for instance 2 h after kainate injection.

GFAP immunostaining showed altered morphology of astrocytes in the ipsilateral CA1 as suggested by the reduced number of primary branches (Figure 4.3.1.2. C). The thickness of the branches also appeared to be increased ipsilaterally (not quantified). However, there was no change in the area occupied by GFAP, indicating unaltered GFAP expression (Figure 4.3.1.2 C). This was further confirmed by Western blotting (Figure 4.3.1.2 D). As the number of astrocytes was also reduced, the data indicated that there was an increase in the GFAP-content per astrocyte. In summary, ipsilateral astrocytes 4 h after kainate injection displayed depletion of S100β, altered morphology, reduced number but no evidence of late stage apoptosis (i.e. TUNEL labelling). It could not be resolved whether these changes were directly linked with uncoupling.

5.5 Astrocytic proliferation and Cx43, 5 d post kainate injection

Status epilepticus in the mouse model is followed by a latent phase that lasts approximately 5 days (Bedner et al., 2015). Four h post kainate, the number of astrocytes was found to be reduced ipsilaterally (Figure 4.3.2). However, 5 d post kainate the number of astrocytes were similar between ipsilateral and contralateral hippocampi (Figure 4.5.1). This recovery of astrocytic number indicated possible proliferation. Indeed, newly generated astrocytes, as indicated by BrdU labelling, were observed in both hippocampi (Figure 4.5.2 A). Surprisingly, the number of BrdU positive S100β cells was ~2 times higher in the contralateral SR region although the total number of astrocytes was not different from the ipsilateral SR region (Figure 4.5.2 B). It is important to note here that BrdU not only labels newly generated cells but also cells which are currently having DNA synthesis implying that some of the BrdU positive cells might represent cells in the state of division or DNA repair (Taupin, 2007). Moreover, a small proportion (~ 13% in the SR region of adult mice) of NG2 cells also express S100β (Moshrefi-Ravasdjani et al., 2016). NG2 cells, whether S100β positive or negative, have potential to proliferate (Moshrefi-Ravasdjani et al., 2016). Remarkably, seizures have been shown to induce proliferation in NG2 cells (Wennström et al., 2003). Nevertheless, BrdU labelling confirmed the proliferation of S100β cells most of which were astrocytes as indicated by colabelling with GFAP (Figure 4.5.1).

Cx43 immunostaining using an antibody targeting aa 360 to 382 of Cx43 revealed apparent loss of signal in the contralateral SR relative to the ipsilateral SR 5 d post kainate (Figure 4.5.3 A). This apparent loss, however, did not indicate the absence of Cx43 as another antibody targeting aa 250-270 of Cx43 showed Cx43 positive puncta. Such a change in antibody binding efficiency has been reported in kainate-induced seizures (Hossain et al., 1994)(Ochalski et al., 1995). The authors termed this phenomenon epitope masking and proposed that kainate-induced change in the conformation of the antibody epitope was responsible for loss of antibody binding to it. In these studies, various sequence specific antibodies were used for immunostaining and Western blotting after intracortical kainate injection. Immunohistochemical signal from the antibody targeting aa 346-363 was lost as early as 2 days after kainate injection while immunohistochemical signal from the antibody targeting aa 241-260 was still present. Surprisingly, both antibodies showed similar reactivity in Western blot, indicating that epitope masking was present only in immunostaining (Hossain et al., 1994). Immunolabelling shown by the antibody targeting aa 250-270 was quantified in the present

study. Plaque size, number of plaques, area occupied by Cx43 and Cx43 fluorescence intensity did not differ between ipsilateral and contralateral SR regions indicating similar expression pattern of Cx43 (Figure 4.5.3 B).

Western blots of Cx43 showed an increase in P2 band at 3 months' and 4 h time points. At the 5 d time point, however, there was no change in the phospho-bands (Figure 4.5.4). This indicated that the increased phospho band levels 4 h after kainate returned to baseline after 5 d, possibly by the action of phosphatases. Phosphatase-mediated dephosphorylation of Cx43 has been shown in heart tissue (Remo et al., 2011). These phosphatases colocalized with Cx43 in the intercalated discs in heart failure (Ai and Pogwizd, 2005). Mice expressing glutamate at S325, S328 and S330 of Cx43 were resistant to ischemia-induced Cx43 dephosphorylation and subsequent arrhythmia (Remo et al., 2011). Dephosphorylation of Cx43 has also been shown in the acute phase of seizures induced by intraperitoneal 4-aminopyridine (Zádor et al., 2008). This dephosphorylation was proposed to be regulated by neuronal and/or glial NMDA receptors.

At the 5 d time point, there was no difference in astrocytic coupling between ipsilateral and contralateral hippocampi (Julia Mueller, unpublished data). This result is in apparent contradiction with that reported in Bedner et al. (2015), because of the selection criterion used for the inclusion of animals in the study (Bedner et al., 2015). In Bedner et al., (2015), one of the objectives was to investigate astrocytic coupling in the latent phase. Therefore, those mice showing spontaneous seizure activity in EEG (and hence chronic seizure onset) were excluded from the analysis. However, in the study by Julia Mueller (and also in the present study), no such exclusion criterion was employed. All the kainate injected mice at the end of 5 days were considered for coupling or Cx43 phosphorylation analysis. It is likely that some of the mice included for coupling or Cx43 phosphorylation analysis might not have been in the latent phase. Consequently, the contralateral and ipsilateral hippocampi did not differ in astrocytic coupling and also in Cx43 phospho bands. Considering the Western blot and coupling data from 3 months, 4 h and 5 d time points, changes in the phospho bands of Cx43 can be associated with changes in astrocytic coupling.

5.6 Seizure-induced granule cell dispersion and neurogenesis in connexin-DKO mice

About 60% of the human MTLE HS cases show GCD in the DG while ~ 40% show substantial granule cell loss (Blümcke et al., 2009). Granule cell pathologies in epilepsy have been found to correlate with the duration of epilepsy but not with the extent of pyramidal cell loss in the CA1 region (Blümcke et al., 2009). The animal model of epilepsy used in the present study also showed noticeable GCD in the ipsilateral hippocampus 1 and 3 months post kainate injection. Granule cells in the contralateral DG on the other hand showed a compact cellular architecture with distinct borders between the granule cell and the molecular layer, similar to what is observed in non-injected control mice. A reduced GCD in kainate-injected DKO mice was first reported in the PhD thesis by Pavel Dublin (Pavel Dublin, 2012). In the present study this finding was investigated further.

Quantification of GCD has been based on the width of the blades of the granule cell layer (Schmeiser et al., 2016). The seizure-induced increase in this width was lower in DKO mice as compared with WT mice (Figure 4.6.1). Granule cells labelled with Prox1 also occupied smaller area in DKO mice. Since DKO mice were earlier shown to have reduced adult neurogenesis (Kunze et al., 2009), the contribution of this process to seizure-induced GCD was explored. Seizure-induced neurogenesis in DKO mice has not been investigated before. Fate mapping of the new born cells was enabled by BrdU which was administered through drinking water for the first 15 days post kainate injection. Neurogenesis was assessed 15 days after the last BrdU administration (Figure 3.3.5). Therefore, any BrdU positive neuron that was detected at this time point had survived at least 15 days after its generation. Surprisingly, no BrdU-positive Prox1 cells could be observed in the ipsilateral DG underneath the injection site. BrdU-positive DCX cells were also absent (Figure 4.6.3). On the other hand many BrdU-positive DCX cells could be detected in contralateral hippocampi of both WT and DKO mice, albeit to a lesser extent in the latter (Figure 4.6.4). Nevertheless, these results ruled out the hypothesis that the reduced GCD in DKO mice was caused by reduced seizure-induced neurogenesis.

Lack of newborn granule neurons in the ipsilateral DG underneath the injection site has been reported earlier in the intrahippocampal model of epilepsy (Häussler et al., 2012). The authors found no BrdU-positive DCX or Prox1 neurons in the ipsilateral DG below the injection site. However, seizure induced neurogenesis could be detected in the contralateral DG and also in the ipsilateral DG distal to the injection site. This study differed from the present study in two aspects: 1) The animal model involved intrahippocampal injection that causes mechanical

damage to the CA1 as compared with intracortical injection used in the present study that spares mechanical injury to the CA1 region 2) BrdU was administered intraperitoneally only on the 6th day post injection while in the present study BrdU was administered through drinking water continuously for first 15 days. The different design of the present study was intended to detect the maximum of post seizure neurogenesis which is known to take place mostly in the first 15 days after status epilepticus and declines severely in the chronic phase (Hattiangady et al., 2004). Despite of the differences in the design, the present study confirmed the findings of Häussler et al., 2012.

One possible reason behind the attenuated GCD in DKO mice could be the already lower number of granule cells in DKO mice as reported earlier (Kunze et al., 2009b). In the study by Kunze at al., DKO mice were found to have less Prox1 positive cells as compared with WT mice. Thus, upon seizure induction spread of granule cells owing to their small number appeared to a lower extent in DKO mice. Indeed, the non-injected DKO mice had thinner granule cell layers as compared with those of the non-injected WT mice (Figure 4.6.5 A and B). DKO mice also have a lower basal level of neurogenesis. However, Nitta et al., showed that the extent of GCD does not depend on the basal level of neurogenesis (Nitta et al., 2008). The authors found that seizure-induced GCD in aged and irradiated mice, which are known to have reduced neurogenesis, does not differ from GCD in those mice which have normal adult neurogenesis.

Connexins are essential for the proliferation of RG-like cells in the DG (Kunze et al., 2009b). As a result, seizure induced neurogenesis in the contralateral DG of DKO mice was lower than in the contralateral DG of the WT mice. However, neurogenesis in kainate-injected DKO mice was still higher than the non-injected DKO and the non-injected WT mice (Table 4.6.4 and 4.6.5). This implies that the seizures overcome the limitations on neurogenesis posed by the absence of connexins. Thus, seizure-induced neurogenesis is actually independent of astrocytic connexins. The differences in seizure-induced neurogenesis observed between DKO and WT mice can be attributed to the lower level of basal neurogenesis in the former.

Kainate injection caused increased proliferation of endothelial cells in the ipsilateral hippocampi 1 month post kainate (Figure 4.6.6). This was further reflected in vascular density that showed higher values in ipsilateral hippocampi when compared with the corresponding contralateral hippocampi at 1 month and 3 month post injection in WT mice (Figure 4.6.7 A and B). The sclerotic human hippocampus also showed an increased vascular density, in contrast with the non-sclerotic one. This difference in vascular densities was not observed in

DKO mice 1 month post injection (Figure 4.6.6 B). Interestingly, DKO mice presented reduced ipsilateral seizure-induced proliferation of endothelial cells when compared with WT mice (Figure 4.6.7 C and D). This pattern of reduced endothelial cell proliferation was similar in both DG and the CA1 region. The pattern of microglial proliferation, however, was different in these two regions. While the ipsilateral CA1 region of DKO mice showed reduced microglial area and proliferation as compared with WT mice, the DG of these mice did not differ (Figure 4.6.8). Both, microglial proliferation (Vezzani and Granata, 2005) and enhanced angiogenesis (Rigau et al., 2007) have been proposed to contribute to epileptogenesis. The differential modulation of these processes in DKO mice indicates that astrocytic connexins influence seizure-induced proliferation of non-neuronal cells.

6 Summary

The dynamic regulation of connexins throughout its life cycle has profound impact on the level of gap junctional coupling in astrocytes. Astrocytic uncoupling in epilepsy can be viewed in the context of modifications in their connexins. The present work sheds a light on seizure-induced alterations in connexins associated with uncoupling in astrocytes.

This study unequivocally proves that post seizure uncoupling in astrocytes is not caused by the scarcity of connexins. In fact, in hippocampal specimens from epilepsy patients and in the mouse model of epilepsy 3 months post injection, an increase in the total Cx43 protein levels was found. This increase in the total Cx43 levels, however did not result in the increase in plasma membrane Cx43 levels indicating impaired translocation of this protein. Nevertheless, plasma membrane Cx43 levels in the human sclerotic hippocampus were comparable to those in non-sclerotic hippocampus. Expansion microscopy utilized for the first time to resolve the gap junction-blood vessel interface in human hippocampal specimens, further enabled to localize Cx43 with respect to blood vessels. Interestingly, in the sclerotic hippocampus, a preferential distribution of Cx43 around blood vessels was observed, which coincided with albumin extravasation.

All these features of Cx43 expression and distribution were also observed in the mouse model of epilepsy at the 3 months' time point highlighting its clinical relevance. At this time point, a significant change in the phosphorylation of Cx43 was detected. Remarkably, as early as 4 h after kainate injection, altered Cx43 phosphorylation, indicated by a shift of Cx43 bands towards P2, was noticed. This phosphorylation of Cx34 was further characterized in detail with the help of mass-spectrometry reported for the first time in an epilepsy model. In total, 14 Cx43 phosphorylated sites were detected of which, phosphorylated T290 and Y301 have not been described before. Phosphorylation at S257, S262, S328 and S330 was found to be differentially regulated after kainate-induced seizures. Phosphorylation at S262 could be associated with astrocytic uncoupling in the ipsilateral hippocampus. Interestingly, this phosphorylation could also be induced by TNFα and IL-1β and could be blocked by XPRO1595, a blocker of the soluble form of TNFα. It is noteworthy that both of these cytokines have been reported to be upregulated after kainate-induced seizures (Vezzani and Granata, 2005).

The 4 h time point also showed dramatic changes in the morphology and markers of astrocytes. S100β immunoreactivity in the ipsilateral hippocampus was drastically reduced while GFAP immunoreactivity showed reduced astrocytic branching. Although the total number of GFAP positive astrocytes was reduced ipsilaterally, there was no evidence of apoptotic cell death. The possibility of other mechanisms of cell death, however cannot be ruled out. Furthermore, 5 d post kainate injection the numbers of astrocytes in the ipsilateral and contralateral hippocampi were similar. These numbers were still higher than those at the 4 h time point, indicating astrocytic proliferation. Indeed, BrdU labelling 5 d post injection revealed newly generating and/or proliferating astrocytes in both hippocampi. The higher molecular weight shift in Cx43 bands observed at 4 h post kainate was absent at the 5 days' time point agreeing with the state of astrocytic coupling at these time points.

All these results exemplified how seizures affected astrocytic connexins and thereby the gap junctional coupling. In the second part of my thesis, I checked how the deletion of astrocytic connexins influenced seizure-induced granule cell dispersion and neurogenesis. I found that the attenuated granule cell dispersion in connexin DKO mice could not be ascribed to the newborn neurons. It could however be attributed to the lower number of granule cells (Prox1 positive cells) resulting into thinner granule cell layers under basal conditions. The ipsilateral dentate gyri of both WT and connexin DKO mice were devoid of seizure-induced neurogenesis 1 month post injection. On the other hand, neurogenesis was present in the contralateral dentate gyri although lower in the connexin DKO mice than WT mice. Interestingly, neurogenesis in connexin DKO mice with seizures (kainate-injected connexin DKO mice) was 6 times higher than the neurogenesis in connexin DKO mice without seizures (non-injected connexin DKO mice) and 3 times higher than the neurogenesis in WT mice without seizures (non-injected WT mice). It can be concluded that seizure-induced neurogenesis is independent of astrocytic connexins.

In summary, the present study provides vital insights into the mechanisms of astrocytic uncoupling in epilepsy. These can be utilized to devise strategies to prevent astrocytic uncoupling in experimental and clinical epilepsies.

7 Perspective

Astrocytic uncoupling has profound implications for epileptogenesis. Prevention of the uncoupling has potential therapeutic benefits. Therefore, it would be appropriate to identify the exact molecular pathways responsible for uncoupling at various stages of epilepsy.

The present study has identified altered phosphorylation of Cx43 as a probable mechanism leading to uncoupling. Phosphorylation of Cx43 at S262, which in the present study was observed to be increased in the ipsilateral hippocampus, is known to reduce gap junctional coupling. In this context, a proof of principle study ascertaining the contribution of S262 phosphorylation to seizure-induced uncoupling in astrocytes is very much desirable. Such a proof can be obtained by evaluating the post seizure astrocytic coupling in mice in which S262 of Cx43 has been replaced either by glutamate (mimicking phosphorylation) or by alanine (mimicking dephosphorylation). If the latter mice are resistant to uncoupling, causal relationship between S262 phosphorylation and post seizure astrocytic uncoupling can be established.

The next step would be then to identify the kinase or kinases responsible for this phosphorylation. MAPKs and CDK-2 are known to phosphorylate Cx43 at S262 (and also at some other sites) (Thévenin et al., 2013). Inhibitors of these kinases can be employed to impede S262 phosphorylation and subsequent astrocytic uncoupling. In this case, MAPKs are particularly of importance as they are known to be activated in inflammatory conditions. TLR-4 stimulation in astrocytes has been shown to create a proinflammatory environment involving MAPKs activation (Gorina et al., 2011). MAPKs are also activated by cytokines for example TNFα (Takada and Aggarwal, 2004). Indeed, the data in the present study implicated a role of the inflammatory cytokines TNFα and IL-1β in phosphorylation of Cx43 at S262. Although various previous reports have shown upregulation of these cytokines after seizures (Vezzani and Granata, 2005), their contribution to astrocytic uncoupling is not clearly known. This contribution can be determined by assessing post seizure S262 phosphorylation and astrocytic coupling in mice deficient in TNFα and/or IL-1β. Alternatively, inhibitors of these cytokines can be employed to judge their role in uncoupling. Furthermore, phosphorylation of S262 can be checked in TLR-4 knock out mice, which have already been shown to be resistant to seizure-induced uncoupling (Bedner et al., 2015).

Another important finding from the present study is the abundance of plasma membrane Cx43 in the human sclerotic hippocampus and also in the ipsilateral hippocampus of mice 3 months after kainate injection. Expansion microscopy further revealed the presence of Cx43 puncta in between GFAP-positive processes in the human sclerotic hippocampus. It could not be deduced whether these puncta represented fully formed gap junctions (dodecamers) or undocked connexons (hexamers). Extracellular loop antibodies, which bind only to undocked connexons (and also to connexin monomers) can be used to distinguish between gap junctions and other Cx43 structures by immunohistochemistry (Riquelme et al., 2013). The opening of connexons known as hemichannel activity can be assessed ex-vivo by ethidium bromide uptake. The configuration of Cx43 into hexamers and dodecamers can also be determined based on their molecular weight in native conditions. Another approach to unravel the Cx43 configuration would be visualization of Cx43 at higher resolution obtained by techniques like atomic force microscopy. It is also probable that the abundant Cx43 immunolabelling in sclerotic conditions might represent fully formed but closed gap junctions. The permanent closure of gap junctions implies drastic reduction in its open probability and /or unitary conductance. Interestingly, both of these properties are influenced by phosphorylation. Indeed, in the present study phosphorylation at S255 of Cx43 has been found to be increased in human sclerotic hippocampus. On the other hand, in the mouse model employed in this study, phosphorylations at both S255 and S368 were found to be augmented. Therefore, it will be pertinent to assess the global changes in Cx43 phosphorylation in the chronic phase of epilepsy. Such an assessment can be done either by using phospho-specific antibodies or by using mass spectrometry.

Bibliography

Aasen T, Mesnil M, Naus CC, Lampe PD, Laird DW. 2016. Gap junctions and cancer: communicating for 50 years. Nat Rev Cancer 16:775–788.

Abbott NJ, Rönnbäck L, Hansson E. 2006. Astrocyte–endothelial interactions at the blood–brain barrier. Nat Rev Neurosci 7:41–53.

Ai X, Pogwizd SM. 2005. Connexin 43 Downregulation and Dephosphorylation in Nonischemic Heart Failure Is Associated With Enhanced Colocalized Protein Phosphatase Type 2A. Circ Res 96:54–63.

Alexopoulos AV. 2013. Pharmacoresistant epilepsy: Definition and explanation. Epileptology 1:38–42.

Alvestad S, Hammer J, Hoddevik EH, Skare Ø, Sonnewald U, Amiry-Moghaddam M, Ottersen OP. 2013. Mislocalization of AQP4 precedes chronic seizures in the kainate model of temporal lobe epilepsy. Epilepsy Res 105:30–41.

Aronica E, Van Vliet EA, Mayboroda OA, Troost D, Da Silva FHL, Gorter JA. 2000. Upregulation of metabotropic glutamate receptor subtype mGluR3 and mGluR5 in reactive astrocytes in a rat model of mesial temporal lobe epilepsy. Eur J Neurosci 12:2333–2344.

Avignone E, Lepleux M, Angibaud J, Nägerl UV. 2015. Altered morphological dynamics of activated microglia after induction of status epilepticus. J Neuroinflammation 12:202.

Avignone E, Ulmann L, Levavasseur F, Rassendren F, Audinat E. 2008. Status Epilepticus Induces a Particular Microglial Activation State Characterized by Enhanced Purinergic Signaling. J Neurosci 28:9133–9144.

Axelsen LN, Calloe K, Holstein-Rathlou N-H, Nielsen MS. 2013. Managing the complexity of communication: regulation of gap junctions by post-translational modification. Front Pharmacol 4:1-18

Axelsen LN, Stahlhut M, Mohammed S, Larsen BD, Nielsen MS, Holstein-Rathlou N-H, Andersen S, Jensen ON, Hennan JK, Kjølbye AL. 2006. Identification of ischemia-regulated phosphorylation sites in connexin43: A possible target for the antiarrhythmic peptide analogue rotigaptide (ZP123). J Mol Cell Cardiol 40:790–798.

Bazargani N, Attwell D. 2016. Astrocyte calcium signaling: the third wave. Nat Neurosci 19:182–189.

Bazzigaluppi P, Weisspapir I, Stefanovic B, Leybaert L, Carlen PL. 2016. Astrocytic gap junction blockade markedly increases extracellular potassium without causing seizures in the mouse neocortex. Neurobiol Dis 101:1-7.

Beardslee MA, Laing JG, Beyer EC, Saffitz JE. 1998. Rapid Turnover of Connexin43 in the Adult Rat Heart. Circ Res 83:629–635.

Becker AJ, Chen J, Paus S, Normann S, Beck H, Elger CE, Wiestler OD, Blümcke I. 2002. Transcriptional profiling in human epilepsy: expression array and single cell real-time qRT-PCR analysis reveal distinct cellular gene regulation. Neuroreport 13:1327–1333.

Bedner P, Dupper A, Hüttmann K, Müller J, Herde M, Dublin P, Deshpande T, Schramm J, Häussler U, Haas C. 2015. Astrocyte uncoupling as a cause of human temporal lobe epilepsy. Brain J Neurol 138:1208–1222.

Bedner P, Steinhäuser C, Theis M. 2012. Functional redundancy and compensation among members of gap junction protein families? Biochim Biophys Acta BBA - Biomembr 1818:1971–1984.

Behrens E, Zentner J, Roost D van, Hufnagel A, Elger CE, Schramm J. 1994. Subdural and depth electrodes in the presurgical evaluation of epilepsy. Acta Neurochir (Wien) 128:84–87.

Bélanger M, Allaman I, Magistretti PJ. 2011. Brain Energy Metabolism: Focus on Astrocyte-Neuron Metabolic Cooperation. Cell Metab 14:724–738.

Bengzon J, Kokaia Z, Elmér E, Nanobashvili A, Kokaia M, Lindvall O. 1997. Apoptosis and proliferation of dentate gyrus neurons after single and intermittent limbic seizures. Proc Natl Acad Sci 94:10432–10437.

Beyer EC, Berthoud VM. 2009. The Family of Connexin Genes. In: Connexins A Guide. Springer 3–26.

Bezzi P, Volterra A. 2001. A neuron–glia signalling network in the active brain. Curr Opin Neurobiol 11:387–394.

Birbeck GL. 2010. Epilepsy Care in Developing Countries: Part I of II. Epilepsy Curr 10:75–79.

Blümcke I, Kistner I, Clusmann H, Schramm J, Becker AJ, Elger CE, Bien CG, Merschhemke M, Meencke H-J, Lehmann T, Buchfelder M, Weigel D, Buslei R, Stefan H, Pauli E, Hildebrandt M. 2009. Towards a clinico-pathological classification of granule cell dispersion in human mesial temporal lobe epilepsies. Acta Neuropathol (Berl) 117:535–544.

Blümcke I, Thom M, Aronica E, Armstrong DD, Bartolomei F, Bernasconi A, Bernasconi N, Bien CG, Cendes F, Coras R, Cross JH, Jacques TS, Kahane P, Mathern GW, Miyata H, Moshé SL, Oz B, Özkara Ç, Perucca E, Sisodiya S, Wiebe S, Spreafico R. 2013. International consensus classification of hippocampal sclerosis in temporal lobe epilepsy: A Task Force report from the ILAE Commission on Diagnostic Methods. Epilepsia 54:1315–1329.

Boitano S, Dirksen ER, Sanderson MJ. 1992. Intercellular propagation of calcium waves mediated by inositol trisphosphate. Science 258:292–295.

Bosco D, Haefliger J-A, Meda P. 2011. Connexins: Key Mediators of Endocrine Function. Physiol Rev 91:1393–1445.

Braganza O, Bedner P, Hüttmann K, von Staden E, Friedman A, Seifert G, Steinhäuser C. 2012. Albumin is taken up by hippocampal NG2 cells and astrocytes and decreases gap junction coupling. Epilepsia 53:1898–1906.

Brouns R, De Vil B, Cras P, De Surgeloose D, Mariën P, De Deyn PP. 2010. Neurobiochemical markers of brain damage in cerebrospinal fluid of acute ischemic stroke patients. Clin Chem 56:451–458.

Bushong EA, Martone ME, Jones YZ, Ellisman MH. 2002. Protoplasmic astrocytes in CA1 stratum radiatum occupy separate anatomical domains. J Neurosci Off J Soc Neurosci 22:183–192.

Carmignoto G, Haydon PG. 2012. Astrocyte calcium signaling and epilepsy. Glia 60:1227–1233.

Cavus I, Kasoff WS, Cassaday MP, Jacob R, Gueorguieva R, Sherwin RS, Krystal JH, Spencer DD, Abi-Saab WM. 2005. Extracellular metabolites in the cortex and hippocampus of epileptic patients. Ann Neurol 57:226–235.

Chen F, Tillberg PW, Boyden ES. 2015. Expansion Microscopy. Science 347:543–548.

Chen VC, Gouw JW, Naus CC, Foster LJ. 2013. Connexin multi-site phosphorylation: Mass spectrometry-based proteomics fills the gap. Biochim Biophys Acta BBA - Biomembr 1828:23–34.

Choi J-S, Kim SY, Park H-J, Cha J-H, Choi Y-S, Kang J-E, Chung J-W, Chun M-H, Lee M-Y. 2003. Upregulation of gp130 and differential activation of STAT and p42/44 MAPK in the rat hippocampus following kainic acid-induced seizures. Brain Res Mol Brain Res 119:10–18.

Chozinski TJ, Halpern AR, Okawa H, Kim H-J, Tremel GJ, Wong ROL, Vaughan JC. 2016. Expansion microscopy with conventional antibodies and fluorescent proteins. Nat Methods 13:485–488.

Chuquet J, Hollender L, Nimchinsky EA. 2007. High-resolution in vivo imaging of the neurovascular unit during spreading depression. J Neurosci Off J Soc Neurosci 27:4036–4044.

Collignon F, Wetjen NM, Cohen-Gadol AA, Cascino GD, Parisi J, Meyer FB, Marsh WR, Roche P, Weigand SD. 2006. Altered expression of connexin subtypes in mesial temporal lobe epilepsy in humans. J Neurosurg 105:77–87.

Cone AC, Cavin G, Ambrosi C, Hakozaki H, Wu-Zhang AX, Kunkel MT, Newton AC, Sosinsky GE. 2014. Protein Kinase Cδ-mediated Phosphorylation of Connexin43 Gap Junction Channels Causes Movement within Gap Junctions followed by Vesicle Internalization and Protein Degradation. J Biol Chem 289:8781–8798.

Cooper CD, Lampe PD. 2002. Casein kinase 1 regulates connexin-43 gap junction assembly. J Biol Chem 277:44962–44968.

da Costa Neves RS, Jardim AP, Caboclo LO, Lancellotti C, Marinho TF, Hamad AP, Marinho M, Centeno R, Cavalheiro EA, Scorza CA, Targas Yacubian EM. 2013. Granule cell dispersion is not a predictor of surgical outcome in temporal lobe epilepsy with mesial temporal sclerosis. Clin Neuropathol 32:24–30.

Coulter DA, Steinhäuser C. 2015. Role of Astrocytes in Epilepsy. Cold Spring Harb Perspect Med 5:a022434.

Crow DS, Beyer EC, Paul DL, Kobe SS, Lau AF. 1990. Phosphorylation of connexin43 gap junction protein in uninfected and Rous sarcoma virus-transformed mammalian fibroblasts. Mol Cell Biol 10:1754–1763.

Dallérac G, Chever O, Rouach N. 2013. How do astrocytes shape synaptic transmission? Insights from electrophysiology. Front Cell Neurosci 7: https://doi.org/10.3389/fncel.2013.00159:

Das S, Smith TD, Sarma JD, Ritzenthaler JD, Maza J, Kaplan BE, Cunningham LA, Suaud L, Hubbard MJ, Rubenstein RC, Koval M. 2009. ERp29 restricts Connexin43 oligomerization in the endoplasmic reticulum. Mol Biol Cell 20:2593–2604.

Davalos D, Grutzendler J, Yang G, Kim JV, Zuo Y, Jung S, Littman DR, Dustin ML, Gan W-B. 2005. ATP mediates rapid microglial response to local brain injury in vivo. Nat Neurosci 8:752–758.

De Simoni MG, Perego C, Ravizza T, Moneta D, Conti M, Marchesi F, De Luigi A, Garattini S, Vezzani A. 2000. Inflammatory cytokines and related genes are induced in the rat hippocampus by limbic status epilepticus. Eur J Neurosci 12:2623–2633.

Demetrius LA, Magistretti PJ, Pellerin L. 2015. Alzheimer's disease: the amyloid hypothesis and the Inverse Warburg effect. Front Physiol 5: https://doi.org/10.3389/fphys.2014.00522

Deng W, Aimone JB, Gage FH. 2010. New neurons and new memories: how does adult hippocampal neurogenesis affect learning and memory? Nat Rev Neurosci 11:339–350.

Doble BW, Dang X, Ping P, Fandrich RR, Nickel BE, Jin Y, Cattini PA, Kardami E. 2004. Phosphorylation of serine 262 in the gap junction protein connexin-43 regulates DNA synthesis in cell-cell contact forming cardiomyocytes. J Cell Sci 117:507–514.

Donato R, Cannon BR, Sorci G, Riuzzi F, Hsu K, Weber DJ, Geczy CL. 2013. Functions of S100 Proteins. Curr Mol Med 13:24–57.

Dunn CA, Lampe PD. 2014. Injury-triggered Akt phosphorylation of Cx43: a ZO-1-driven molecular switch that regulates gap junction size. J Cell Sci 127:455–464.

Dupper A. 2014. Entkopplung von Astrozyten als Ursache von Temporallappenepilepsie. Available from: http://hss.ulb.uni-bonn.de/2014/3675/3675.htm

During MJ, Spencer DD. 1993. Extracellular hippocampal glutamate and spontaneous seizure in the conscious human brain. The Lancet 341:1607–1610.

Eid T, Lee T-SW, Thomas MJ, Amiry-Moghaddam M, Bjørnsen LP, Spencer DD, Agre P, Ottersen OP, Lanerolle NC de. 2005. Loss of perivascular aquaporin 4 may underlie deficient water and K+ homeostasis in the human epileptogenic hippocampus. Proc Natl Acad Sci U S A 102:1193–1198.

Eid T, Thomas M, Spencer D, Rundén-Pran E, Lai J, Malthankar G, Kim J, Danbolt N, Ottersen O, de Lanerolle N. 2004. Loss of glutamine synthetase in the human epileptogenic

hippocampus: possible mechanism for raised extracellular glutamate in mesial temporal lobe epilepsy. The Lancet 363:28–37.

Ek-Vitorin JF, King TJ, Heyman NS, Lampe PD, Burt JM. 2006. Selectivity of Connexin 43 Channels Is Regulated Through Protein Kinase C–Dependent Phosphorylation. Circ Res 98:1498–1505.

Elger C, Hufnagel A, Schramm J. 1993. Presurgical evaluation protocol— University of Bonn. In: Surgical treatment of the epilepsies. New York: Raven Press. 740–742.

Elmore S. 2007. Apoptosis: A Review of Programmed Cell Death. Toxicol Pathol 35:495–516.

Eyo UB, Murugan M, Wu L-J. 2017. Microglia–Neuron Communication in Epilepsy. Glia 65:5–18.

Fahrner A, Kann G, Flubacher A, Heinrich C, Freiman TM, Zentner J, Frotscher M, Haas CA. 2007. Granule cell dispersion is not accompanied by enhanced neurogenesis in temporal lobe epilepsy patients. Exp Neurol 203:320–332.

Falk MM, Kells RM, Berthoud VM. 2014. Degradation of connexins and gap junctions. FEBS Lett 588:1221–1229.

Filosa JA, Morrison HW, Iddings JA, Du W, Kim KJ. 2016. Beyond neurovascular coupling, role of astrocytes in the regulation of vascular tone. Neuroscience 323:96–109.

Fink SL, Cookson BT. 2005. Apoptosis, Pyroptosis, and Necrosis: Mechanistic Description of Dead and Dying Eukaryotic Cells. Infect Immun 73:1907–1916.

Fischer R, Kontermann RE, Maier O. 2015. Targeting sTNF/TNFR1 Signaling as a New Therapeutic Strategy. Antibodies 4:48–70.

Fishman GI, Moreno AP, Spray DC, Leinwand LA. 1991. Functional analysis of human cardiac gap junction channel mutants. Proc Natl Acad Sci 88:3525–3529.

Gl W. 1992. Glutamate receptors and excitotoxicity. Res Publ - Assoc Res Nerv Ment Dis 71:35–50.

Glass M, Dragunow M. 1995. Neurochemical and morphological changes associated with human epilepsy. Brain Res Rev 21:29–41.

Goldberg EM, Coulter DA. 2013. Mechanisms of epileptogenesis: a convergence on neural circuit dysfunction. Nat Rev Neurosci 14:337–349.

Gonçalves JT, Schafer ST, Gage FH. 2016. Adult Neurogenesis in the Hippocampus: From Stem Cells to Behavior. Cell 167:897–914.

Gorina R, Font-Nieves M, Márquez-Kisinousky L, Santalucia T, Planas AM. 2011. Astrocyte TLR4 activation induces a proinflammatory environment through the interplay between MyD88-dependent NFκB signaling, MAPK, and Jak1/Stat1 pathways. Glia 59:242–255.

Gosejacob D, Dublin P, Bedner P, Hüttmann K, Zhang J, Tress O, Willecke K, Pfrieger F, Steinhäuser C, Theis M. 2011. Role of astroglial connexin30 in hippocampal gap junction coupling. Glia 59:511–519.

Haas CA, Frotscher M. 2010. Reelin deficiency causes granule cell dispersion in epilepsy. Exp Brain Res 200:141–149.

Hattiangady B, Rao MS, Shetty AK. 2004. Chronic temporal lobe epilepsy is associated with severely declined dentate neurogenesis in the adult hippocampus. Neurobiol Dis 17:473–490.

Häussler U, Bielefeld L, Froriep UP, Wolfart J, Haas CA. 2012. Septotemporal Position in the Hippocampal Formation Determines Epileptic and Neurogenic Activity in Temporal Lobe Epilepsy. Cereb Cortex 22:26–36.

Hellsten J, Wennström M, Bengzon J, Mohapel P, Tingström A. 2004. Electroconvulsive seizures induce endothelial cell proliferation in adult rat hippocampus. Biol Psychiatry 55:420–427.

Hester MS, Danzer SC. 2014. Hippocampal granule cell pathology in epilepsy — A possible structural basis for comorbidities of epilepsy? Epilepsy Behav 38:105–116.

Heuser K, Eid T, Lauritzen F, Thoren AE, Vindedal GF, Taubøll E, Gjerstad L, Spencer DD, Ottersen OP, Nagelhus EA, Lanerolle NC de. 2012. Loss of Perivascular Kir4.1 Potassium Channels in the Sclerotic Hippocampus of Patients With Mesial Temporal Lobe Epilepsy. J Neuropathol Exp Neurol 71:814–825.

Heuser K, Nagelhus EA, Taubøll E, Indahl U, Berg PR, Lien S, Nakken S, Gjerstad L, Ottersen OP. 2010. Variants of the genes encoding AQP4 and Kir4.1 are associated with subgroups of patients with temporal lobe epilepsy. Epilepsy Res 88:55–64.

Hinterkeuser S, Schröder W, Hager G, Seifert G, Blümcke I, Elger CE, Schramm J, Steinhäuser C. 2000. Astrocytes in the hippocampus of patients with temporal lobe epilepsy display changes in potassium conductances. Eur J Neurosci 12:2087–2096.

Hossain MZ, Sawchuk MA, Murphy LJ, Hertzberg EL, Nagy JI. 1994. Kainic acid induced alterations in antibody recognition of connexin43 and loss of astrocytic gap junctions in rat brain. Glia 10:250–265.

Hu J, Castets F, Guevara JL, Van Eldik LJ. 1996. S100 beta stimulates inducible nitric oxide synthase activity and mRNA levels in rat cortical astrocytes. J Biol Chem 271:2543–2547.

Hu J, Van Eldik LJ. 1996. S100 beta induces apoptotic cell death in cultured astrocytes via a nitric oxide-dependent pathway. Biochim Biophys Acta 1313:239–245.

Huang RY, Laing JG, Kanter EM, Berthoud VM, Bao M, Rohrs HW, Townsend RR, Yamada KA. 2011. Identification of CaMKII Phosphorylation Sites in Connexin43 by High-Resolution Mass Spectrometry. J Proteome Res 10:1098–1109.

Hüttmann K, Sadgrove M, Wallraff A, Hinterkeuser S, Kirchhoff F, Steinhäuser C, Gray WP. 2003. Seizures preferentially stimulate proliferation of radial glia-like astrocytes in the adult dentate gyrus: functional and immunocytochemical analysis. Eur J Neurosci 18:2769–2778.

Ivens S, Kaufer D, Flores LP, Bechmann I, Zumsteg D, Tomkins O, Seiffert E, Heinemann U, Friedman A. 2007. TGF-β receptor-mediated albumin uptake into astrocytes is involved in neocortical epileptogenesis. Brain 130:535–547.

Iyyathurai J, Decuypere J-P, Leybaert L, D'hondt C, Bultynck G. 2016. Connexins: substrates and regulators of autophagy. BMC Cell Biol 17:S20.

Kaminska B, Gozdz A, Zawadzka M, Ellert-Miklaszewska A, Lipko M. 2009. MAPK Signal Transduction Underlying Brain Inflammation and Gliosis as Therapeutic Target. Anat Rec Adv Integr Anat Evol Biol 292:1902–1913.

Kelly JJ, Shao Q, Jagger DJ, Laird DW. 2015. Cx30 exhibits unique characteristics including a long half-life when assembled into gap junctions. J Cell Sci 128:3947–3960.

Kettenmann H, Ranson BR. 1988. Electrical coupling between astrocytes and between oligodendrocytes studied in mammalian cell cultures. Glia 1:64–73.

Khakh BS, Sofroniew MV. 2015. Diversity of astrocyte functions and phenotypes in neural circuits. Nat Neurosci 18:942–952.

Koulakoff A, Mei X, Orellana JA, Sáez JC, Giaume C. 2012. Glial connexin expression and function in the context of Alzheimer's disease. Biochim Biophys Acta BBA - Biomembr 1818:2048–2057.

Koval M, Molina SA, Burt JM. 2014. Mix and match: Investigating heteromeric and heterotypic gap junction channels in model systems and native tissues. FEBS Lett 588:1193–1204.

Kriegstein A, Alvarez-Buylla A. 2009. The Glial Nature of Embryonic and Adult Neural Stem Cells. Annu Rev Neurosci 32:149–184.

Kuffler SW, Nicholls JG, Orkand RK. 1966. Physiological properties of glial cells in the central nervous system of amphibia. J Neurophysiol 29:768–787.

Kuga N, Sasaki T, Takahara Y, Matsuki N, Ikegaya Y. 2011. Large-scale calcium waves traveling through astrocytic networks in vivo. J Neurosci Off J Soc Neurosci 31:2607–2614.

Kunze A, Congreso MR, Hartmann C, Wallraff-Beck A, Hüttmann K, Bedner P, Requardt R, Seifert G, Redecker C, Willecke K, Hofmann A, Pfeifer A, Theis M, Steinhäuser C. 2009a. Connexin expression by radial glia-like cells is required for neurogenesis in the adult dentate gyrus. Proc Natl Acad Sci 106:11336–11341.

Kunze A, Congreso MR, Hartmann C, Wallraff-Beck A, Hüttmann K, Bedner P, Requardt R, Seifert G, Redecker C, Willecke K, Hofmann A, Pfeifer A, Theis M, Steinhäuser C. 2009b. Connexin expression by radial glia-like cells is required for neurogenesis in the adult dentate gyrus. Proc Natl Acad Sci U S A 106:11336–11341.

Kwak BR, Sáez JC, Wilders R, Chanson M, Fishman GI, Hertzberg EL, Spray DC, Jongsma HJ. 1995. Effects of cGMP-dependent phosphorylation on rat and human connexin43 gap junction channels. Pflüg Arch 430:770–778.

Kyriakis JM, Avruch J. 2012. Mammalian MAPK signal transduction pathways activated by stress and inflammation: a 10-year update. Physiol Rev 92:689–737.

Laird DW. 2006. Life cycle of connexins in health and disease. Biochem J 394:527–543.

Laird DW, Puranam KL, Revel JP. 1991. Turnover and phosphorylation dynamics of connexin43 gap junction protein in cultured cardiac myocytes. Biochem J 273:67–72.

Lampe PD, Cooper CD, King TJ, Burt JM. 2006. Analysis of Connexin43 phosphorylated at S325, S328 and S330 in normoxic and ischemic heart. J Cell Sci 119:3435–3442.

Lampe PD, Kurata WE, Warn-Cramer BJ, Lau AF. 1998. Formation of a distinct connexin43 phosphoisoform in mitotic cells is dependent upon p34cdc2 kinase. J Cell Sci 111 (Pt 6):833–841.

Lampe PD, Lau AF. 2004. The effects of connexin phosphorylation on gap junctional communication. Int J Biochem Cell Biol 36:1171–1186.

Lampe PD, TenBroek EM, Burt JM, Kurata WE, Johnson RG, Lau AF. 2000. Phosphorylation of Connexin43 on Serine368 by Protein Kinase C Regulates Gap Junctional Communication. J Cell Biol 149:1503–1512.

Lee SH, Kim WT, Cornell-Bell AH, Sontheimer H. 1994. Astrocytes exhibit regional specificity in gap-junction coupling. Glia 11:315–325.

Lee TS, Eid T, Mane S, Kim JH, Spencer DD, Ottersen OP, Lanerolle NC de. 2004. Aquaporin-4 is increased in the sclerotic hippocampus in human temporal lobe epilepsy. Acta Neuropathol (Berl) 108:493–502.

Li A-F, Sato T, Haimovici R, Okamoto T, Roy S. 2003. High glucose alters connexin 43 expression and gap junction intercellular communication activity in retinal pericytes. Invest Ophthalmol Vis Sci 44:5376–5382.

Ma B, Buckalew R, Du Y, Kiyoshi CM, Alford CC, Wang W, McTigue DM, Enyeart JJ, Terman D, Zhou M. 2016. Gap junction coupling confers isopotentiality on astrocyte syncytium. Glia 64:214–226.

Maeda S, Nakagawa S, Suga M, Yamashita E, Oshima A, Fujiyoshi Y, Tsukihara T. 2009. Structure of the connexin 26 gap junction channel at 3.5 Å resolution. Nature 458:597–602.

Malone P, Miao H, Parker A, Juarez S, Hernandez MR. 2007. Pressure induces loss of gap junction communication and redistribution of connexin 43 in astrocytes. Glia 55:1085–1098.

Marta A-M, John R. F, Jarogniew J. Ł. 2011. Neurogenesis in the epileptic brain: a brief overview from temporal lobe epilepsy. Pharmacol Rep 63:1316–1323.

McIntyre DC, Racine RJ. 1986. Kindling mechanisms: Current progress on an experimental epilepsy model. Prog Neurobiol 27:1–12.

Minogue PJ, Beyer EC, Berthoud VM. 2013. A connexin50 mutant, CX50fs, that causes cataracts is unstable, but is rescued by a proteasomal inhibitor. J Biol Chem 288:20427–20434.

Moreno AP, Lau AF. 2007. Gap junction channel gating modulated through protein phosphorylation. Prog Biophys Mol Biol 94:107.

Morquette P, Verdier D, Kadala A, Féthière J, Philippe AG, Robitaille R, Kolta A. 2015. An astrocyte-dependent mechanism for neuronal rhythmogenesis. Nat Neurosci 18:844–854.

Moser EI, Roudi Y, Witter MP, Kentros C, Bonhoeffer T, Moser M-B. 2014. Grid cells and cortical representation. Nat Rev Neurosci 15:466–481.

Moshrefi-Ravasdjani B, Dublin P, Seifert G, Jennissen K, Steinhäuser C, Kafitz KW, Rose CR. 2016. Changes in the proliferative capacity of NG2 cell subpopulations during postnatal development of the mouse hippocampus. Brain Struct Funct: 1–17.

Murphy BL, Danzer SC. 2011. Somatic translocation: a novel mechanism of granule cell dendritic dysmorphogenesis and dispersion. J Neurosci Off J Soc Neurosci 31:2959–2964.

Musil LS, Cunningham BA, Edelman GM, Goodenough DA. 1990. Differential phosphorylation of the gap junction protein connexin43 in junctional communication-competent and -deficient cell lines. J Cell Biol 111:2077–2088.

Mylvaganam S, Ramani M, Krawczyk M, Carlen PL. 2014. Roles of gap junctions, connexins, and pannexins in epilepsy. Front Physiol 5: https://doi.org/10.3389/fphys.2014.00172

Nakagawa S, Maeda S, Tsukihara T. 2010. Structural and functional studies of gap junction channels. Curr Opin Struct Biol 20:423–430.

Newton SS, Girgenti MJ, Collier EF, Duman RS. 2006. Electroconvulsive seizure increases adult hippocampal angiogenesis in rats. Eur J Neurosci 24:819–828.

Nimlamool W, Andrews RMK, Falk MM. 2015. Connexin43 phosphorylation by PKC and MAPK signals VEGF-mediated gap junction internalization. Mol Biol Cell 26:2755–2768.

Niquet J, Ben-Ari Y, Represa A. 1994. Glial reaction after seizure induced hippocampal lesion: immunohistochemical characterization of proliferating glial cells. J Neurocytol 23:641–656.

Nitta N, Heinrich C, Hirai H, Suzuki F. 2008. Granule cell dispersion develops without neurogenesis and does not fully depend on astroglial cell generation in a mouse model of temporal lobe epilepsy. Epilepsia 49:1711–1722.

Oberheim NA, Tian G-F, Han X, Peng W, Takano T, Ransom B, Nedergaard M. 2008. Loss of astrocytic domain organization in the epileptic brain. J Neurosci Off J Soc Neurosci 28:3264–3276.

Ochalski P a. Y, Sawchuk MA, Hertzberg EL, Nagy JI. 1995. Astrocytic gap junction removal, connexin43 redistribution, and epitope masking at excitatory amino acid lesion sites in rat brain. Glia 14:279–294.

Orkand RK, Nicholls JG, Kuffler SW. 1966. Effect of nerve impulses on the membrane potential of glial cells in the central nervous system of amphibia. J Neurophysiol 29:788–806.

Oshima A. 2014. Structure and closure of connexin gap junction channels. FEBS Lett 588:1230–1237.

Pannasch U, Vargová L, Reingruber J, Ezan P, Holcman D, Giaume C, Syková E, Rouach N. 2011. Astroglial networks scale synaptic activity and plasticity. Proc Natl Acad Sci 108:8467–8472.

Parent JM, Yu TW, Leibowitz RT, Geschwind DH, Sloviter RS, Lowenstein DH. 1997. Dentate Granule Cell Neurogenesis Is Increased by Seizures and Contributes to Aberrant Network Reorganization in the Adult Rat Hippocampus. J Neurosci 17:3727–3738.

Parpura V, Zorec R. 2010. Gliotransmission: Exocytotic release from astrocytes. Brain Res Rev 63:83–92.

Pavel Dublin. 2012. Role of astrocytic connexins in health and disease. Available from: http://hss.ulb.uni-bonn.de/2012/2975/2975.htm

Pellerin L, Magistretti PJ. 2012. Sweet sixteen for ANLS. J Cereb Blood Flow Metab 32:1152–1166.

Phares TW, Kean RB, Mikheeva T, Hooper DC. 2006. Regional Differences in Blood-Brain Barrier Permeability Changes and Inflammation in the Apathogenic Clearance of Virus from the Central Nervous System. J Immunol 176:7666–7675.

Pogoda K, Kameritsch P, Retamal MA, Vega JL. 2016. Regulation of gap junction channels and hemichannels by phosphorylation and redox changes: a revision. BMC Cell Biol 17:11.

Ralay Ranaivo H, Wainwright MS. 2010. Albumin activates astrocytes and microglia through mitogen-activated protein kinase pathways. Brain Res 1313:222–231.

Rash JE, Yasumura T, Dudek FE, Nagy JI. 2001. Cell-Specific Expression of Connexins and Evidence of Restricted Gap Junctional Coupling between Glial Cells and between Neurons. J Neurosci Off J Soc Neurosci 21:1983.

Remo BF, Qu J, Volpicelli FM, Giovannone S, Shin D, Lader J, Liu F, Zhang J, Lent DS, Morley GE, Fishman GI. 2011. Phosphatase-Resistant Gap Junctions Inhibit Pathological Remodeling and Prevent ArrhythmiasNovelty and Significance. Circ Res 108:1459–1466.

Retamal MA, Froger N, Palacios-Prado N, Ezan P, Sáez PJ, Sáez JC, Giaume C. 2007. Cx43 hemichannels and gap junction channels in astrocytes are regulated oppositely by proinflammatory cytokines released from activated microglia. J Neurosci Off J Soc Neurosci 27:13781–13792.

Rigau V, Morin M, Rousset M-C, Bock F de, Lebrun A, Coubes P, Picot M-C, Baldy-Moulinier M, Bockaert J, Crespel A, Lerner-Natoli M. 2007. Angiogenesis is associated with blood–brain barrier permeability in temporal lobe epilepsy. Brain 130:1942–1956.

Riquelme MA, Kar R, Gu S, Jiang JX. 2013. Antibodies targeting extracellular domain of connexins for studies of hemichannels. Neuropharmacology 75:525–532.

Rothermundt M, Peters M, Prehn JHM, Arolt V. 2003. S100B in brain damage and neurodegeneration. Microsc Res Tech 60:614–632.

Rouach N, Avignone E, Même W, Koulakoff A, Venance L, Blomstrand F, Giaume C. 2002. Gap junctions and connexin expression in the normal and pathological central nervous system. Biol Cell 94:457–475.

Rouach N, Koulakoff A, Abudara V, Willecke K, Giaume C. 2008. Astroglial Metabolic Networks Sustain Hippocampal Synaptic Transmission. Science 322:1551–1555.

Sáez JC, Berthoud VM, Brañes MC, Martínez AD, Beyer EC. 2003. Plasma Membrane Channels Formed by Connexins: Their Regulation and Functions. Physiol Rev 83:1359–1400.

Sakatani S, Seto-Ohshima A, Shinohara Y, Yamamoto Y, Yamamoto H, Itohara S, Hirase H. 2008. Neural-activity-dependent release of S100B from astrocytes enhances kainate-induced gamma oscillations in vivo. J Neurosci Off J Soc Neurosci 28:10928–10936.

Salameh A. 2006. Life cycle of connexins: regulation of connexin synthesis and degradation. Adv Cardiol 42:57–70.

Scemes E, Giaume C. 2006. Astrocyte calcium waves: What they are and what they do. Glia 54:716–725.

Scemes, E. and Spray, D.C., 2003. The astrocytic syncytium. In: Advances in Molecular and Cell Biology: Elsevier: 31: 165-179.

Scemes E, Spray DC. 2009. Connexin Expression (Gap Junctions and Hemichannels). In: Astrocytes in (Patho) Physiology of the Nervous System. Springer. 107–150.

Schmeiser B, Zentner J, Prinz M, Brandt A, Freiman TM. 2017. Extent of mossy fiber sprouting in patients with mesiotemporal lobe epilepsy correlates with neuronal cell loss and granule cell dispersion. Epilepsy Res 129:51–58.

Schwartzkroin PA. 1994. Role of the hippocampus in epilepsy. Hippocampus 4:239–242.

Serlin Y, Shelef I, Knyazer B, Friedman A. 2015. Anatomy and physiology of the blood–brain barrier. Semin Cell Dev Biol 38:2–6.

Shorvon SD. 2011. The etiologic classification of epilepsy. Epilepsia 52:1052–1057.

Sirnes S, Kjenseth A, Leithe E, Rivedal E. 2009. Interplay between PKC and the MAP kinase pathway in Connexin43 phosphorylation and inhibition of gap junction intercellular communication. Biochem Biophys Res Commun 382:41–45.

Söderqvist F, Carlberg M, Hardell L. 2015. Biomarkers in volunteers exposed to mobile phone radiation. Toxicol Lett 235:140–146.

Sofroniew MV, Vinters HV. 2010. Astrocytes: biology and pathology. Acta Neuropathol (Berl) 119:7–35.

Söhl G, Willecke K. 2003. An Update on Connexin Genes and their Nomenclature in Mouse and Man. Cell Commun Adhes 10:173–180.

Solan JL, Fry MD, TenBroek EM, Lampe PD. 2003. Connexin43 phosphorylation at S368 is acute during S and G2/M and in response to protein kinase C activation. J Cell Sci 116:2203–2211.

Solan JL, Lampe PD. 2007. Key Connexin 43 Phosphorylation Events Regulate the Gap Junction Life Cycle. J Membr Biol 217:35–41.

Solan JL, Lampe PD. 2008. Connexin43 in LA-25 Cells with Active v-src Is Phosphorylated on Y247, Y265, S262, S279/282, and S368 via Multiple Signaling Pathways. Cell Commun Adhes 15:75–84.

Solan JL, Lampe PD. 2009. Connexin43 phosphorylation: structural changes and biological effects. Biochem J 419:261–272.

Solan JL, Lampe PD. 2014. Specific Cx43 phosphorylation events regulate gap junction turnover in vivo. FEBS Lett 588:1423–1429.

Solan JL, Marquez-Rosado L, Sorgen PL, Thornton PJ, Gafken PR, Lampe PD. 2007. Phosphorylation at S365 is a gatekeeper event that changes the structure of Cx43 and prevents down-regulation by PKC. J Cell Biol 179:1301–1309.

Sommer W. 1880. Erkrankung des Ammonshorns als aetiologisches Moment der Epilepsie. Arch Für Psychiatr Nervenkrankh 10:631–675.

Sorci G, Bianchi R, Riuzzi F, Tubaro C, Arcuri C, Giambanco I, Donato R. 2010. S100β Protein, a Damage-Associated Molecular Pattern Protein in the Brain and Heart, and Beyond. Cardiovasc Psychiatry Neurol 2010: http://dx.doi.org/10.1155/2010/656481

Steiner J, Bernstein H-G, Bielau H, Berndt A, Brisch R, Mawrin C, Keilhoff G, Bogerts B. 2007. Evidence for a wide extra-astrocytic distribution of S100β in human brain. BMC Neurosci 8:2.

Steinhäuser C, Grunnet M, Carmignoto G. 2016. Crucial role of astrocytes in temporal lobe epilepsy. Neuroscience 323:157–169.

Steinhäuser C, Seifert G, Bedner P. 2012. Astrocyte dysfunction in temporal lobe epilepsy: K+ channels and gap junction coupling. Glia 60:1192–1202.

Stout CE, Costantin JL, Naus CCG, Charles AC. 2002. Intercellular Calcium Signaling in Astrocytes via ATP Release through Connexin Hemichannels. J Biol Chem 277:10482–10488.

Strange BA, Witter MP, Lein ES, Moser EI. 2014. Functional organization of the hippocampal longitudinal axis. Nat Rev Neurosci 15:655–669.

Sutula T, Cascino G, Cavazos J, Parada I, Ramirez L. 1989. Mossy fiber synaptic reorganization in the epileptic human temporal lobe. Ann Neurol 26:321–330.

Takada Y, Aggarwal BB. 2004. TNF activates Syk protein tyrosine kinase leading to TNF-induced MAPK activation, NF-kappaB activation, and apoptosis. J Immunol Baltim Md 1950 173:1066–1077.

Takuma K, Baba A, Matsuda T. 2004. Astrocyte apoptosis: implications for neuroprotection. Prog Neurobiol 72:111–127.

Tanaka K, Watase K, Manabe T, Yamada K, Watanabe M, Takahashi K, Iwama H, Nishikawa T, Ichihara N, Kikuchi T, Okuyama S, Kawashima N, Hori S, Takimoto M, Wada K. 1997. Epilepsy and exacerbation of brain injury in mice lacking the glutamate transporter GLT-1. Science 276:1699–1702.

Tatum WO. 2012. Mesial temporal lobe epilepsy. J Clin Neurophysiol Off Publ Am Electroencephalogr Soc 29:356–365.

Taupin P. 2007. BrdU immunohistochemistry for studying adult neurogenesis: Paradigms, pitfalls, limitations, and validation. Brain Res Rev 53:198–214.

Theis M, Jauch R, Zhuo L, Speidel D, Wallraff A, Döring B, Frisch C, Söhl G, Teubner B, Euwens C, Huston J, Steinhäuser C, Messing A, Heinemann U, Willecke K. 2003. Accelerated Hippocampal Spreading Depression and Enhanced Locomotory Activity in Mice with Astrocyte-Directed Inactivation of Connexin43. J Neurosci 23:766–776.

Thévenin AF, Kowal TJ, Fong JT, Kells RM, Fisher CG, Falk MM. 2013. Proteins and Mechanisms Regulating Gap-Junction Assembly, Internalization, and Degradation. Physiology 28:93–116.

Thom M. 2014. Review: Hippocampal sclerosis in epilepsy: a neuropathology review. Neuropathol Appl Neurobiol 40:520–543.

Thom M, Liagkouras I, Elliot KJ, Martinian L, Harkness W, McEvoy A, Caboclo LO, Sisodiya SM. 2010. Reliability of patterns of hippocampal sclerosis as predictors of postsurgical outcome. Epilepsia 51:1801–1808.

Tian G-F, Azmi H, Takano T, Xu Q, Peng W, Lin J, Oberheim N, Lou N, Wang X, Zielke HR, Kang J, Nedergaard M. 2005. An astrocytic basis of epilepsy. Nat Med 11:973–981.

Torres A, Wang F, Xu Q, Fujita T, Dobrowolski R, Willecke K, Takano T, Nedergaard M. 2012. Extracellular Ca2+ Acts as a Mediator of Communication from Neurons to Glia. Sci Signal 5:ra8.

VanSlyke JK, Musil LS. 2005. Cytosolic Stress Reduces Degradation of Connexin43 Internalized from the Cell Surface and Enhances Gap Junction Formation and Function. Mol Biol Cell 16:5247–5257.

Vezzani A, Granata T. 2005. Brain Inflammation in Epilepsy: Experimental and Clinical Evidence. Epilepsia 46:1724–1743.

Vliet EA van, Araújo S da C, Redeker S, Schaik R van, Aronica E, Gorter JA. 2007. Blood–brain barrier leakage may lead to progression of temporal lobe epilepsy. Brain 130:521–534.

Wallraff A, Köhling R, Heinemann U, Theis M, Willecke K, Steinhäuser C. 2006. The impact of astrocytic gap junctional coupling on potassium buffering in the hippocampus. J Neurosci 26:5438–5447.

Walz W. 2000. Role of astrocytes in the clearance of excess extracellular potassium. Neurochem Int 36:291–300.

Wennström M, Hellsten J, Ekdahl CT, Tingström A. 2003. Electroconvulsive seizures induce proliferation of NG2-expressing glial cells in adult rat hippocampus. Biol Psychiatry 54:1015–1024.

Wittig I, Braun H-P, Schagger H. 2006. Blue native PAGE : Abstract : Nature Protocols. Nat Protoc 1:418–428.

Wong M. 2009. The Window of Epileptogenesis: Looking Beyond the Latent Period. Epilepsy Curr 9:144–145.

Wu Y, Liu D, Song Z. 2015. Neuronal networks and energy bursts in epilepsy. Neuroscience 287:175–186.

Zádor Z, Weiczner R, Mihály A. 2008. Long-lasting dephosphorylation of connexin 43 in acute seizures is regulated by NMDA receptors in the rat cerebral cortex. Mol Med Rep 1:721–727.

Zhu H, Dahlström A, Hansson H-A. 2005. Characterization of cell proliferation in the adult dentate under normal conditions and after kainate induced seizures using ribonucleotide reductase and BrdU. Brain Res 1036:7–17.

Declaration

I hereby declare that this Doctoral Thesis is original and was written independently, using no other sources and aids than stated. This document - in the current or similar form - has not and will not be submitted to any other institution, apart from the University of Bonn.

Bonn, February 2017

Tushar Deshpande